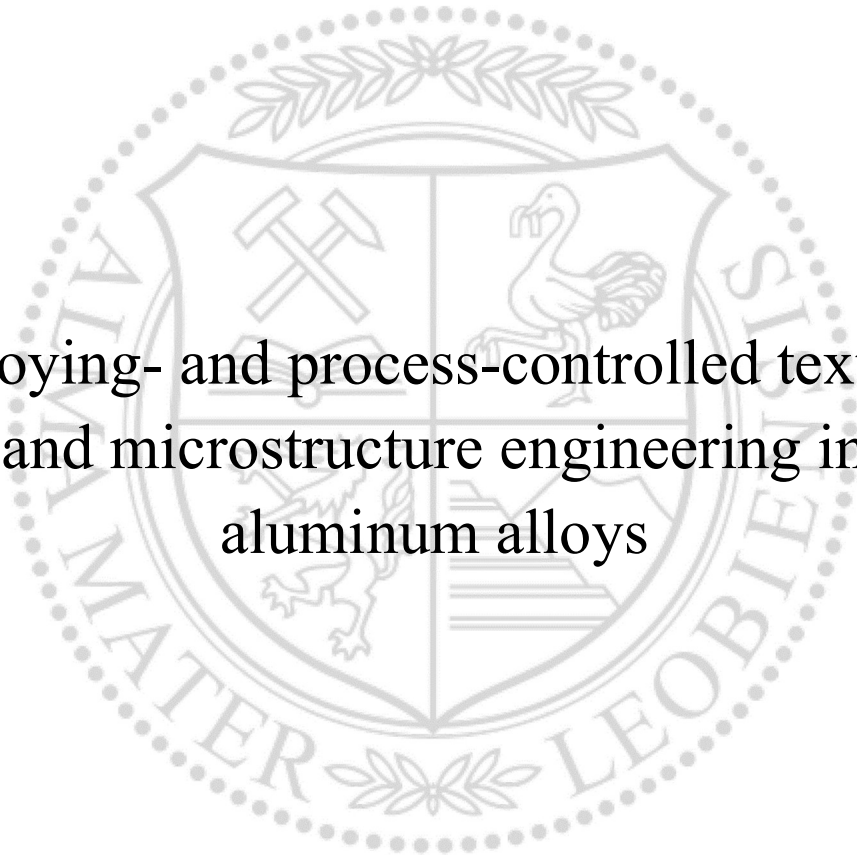




Chair of Nonferrous Metallurgy

Doctoral Thesis



Alloying- and process-controlled texture
and microstructure engineering in
aluminum alloys

Dipl.-Ing. Jakob Grasserbauer, BSc

July 2021



AFFIDAVIT

I declare on oath that I wrote this thesis independently, did not use other than the specified sources and aids, and did not use any unauthorized aids.

I declare that I have read, understood, and complied with the guidelines of the senate of the Montanuniversitaet Leoben for "Good Scientific Practice".

Furthermore, I declare that the electronic and printed version of the submitted thesis are identical, both, formally and with regard to content.

Date 06.07.2021

Signature Author
Jakob Grasserbauer

ACKNOWLEDGEMENTS

First of all, I would like to thank Prof. Stefan Pogatscher for his superior supervision and the chance to write my PhD thesis within the Christian Doppler Laboratory for Advanced Aluminum Alloys. I will never forget his invaluable input in the numerous discussions and the help he provided whenever needed. It was especially his ambition and exploratory spirit which inspired and motivated whenever I was stuck on unexpected results or difficult theories.

Next, I want to thank Prof. Helmut Antrekowitsch for the warm welcome at the Chair of Nonferrous Metallurgy at the Montanuniversität Leoben and the chance he provided to further improve my teaching skills. I would not have finished this thesis without his help and commitment at the beginning of my time as a PhD student.

Special thanks go to Prof. Peter Uggowitzer, who was never tired of discussing and explaining the most diverse theories on my results. It was also his unlimited enthusiasm for the field of metallurgy which motivated me throughout my entire time in Leoben.

Further thanks go to Irmgard Weißensteiner, Georg Falkinger, and Stefan Mitsche who helped me especially with their knowledge on texture and to put my results into the right light. All the publications would not have been possible without all the help they provided.

A big thanks goes to all my colleagues not only for their valuable input in discussions, but especially for making our workplace such a pleasant environment. I really enjoy(ed) coming to work (nearly) every day.

At last I would like to thank my family — especially my parents — for their unconditional love and enormous backing in all situations throughout my entire life and further for their financial support, without which I would never have achieved all my goals. Furthermore, my partner Birgit, who endured me all along these years and always supported my plans.

ABSTRACT

In recent decades, the usage of aluminum and its alloys has become an essential measure to reduce the CO₂ emissions in the automotive sector and to further promote electromobility by compensating the adverse weight increase of the battery-systems. To comply with the changing safety standards, a steady increase in the mechanical properties such as strength is required. In turn, modern car-body design demands enhanced formability of the used materials. As these properties are strongly defined by the microstructures and textures of the Al sheets, the control of those variables enables the desired property combination in optimized Al alloys.

The different impacts of the alloying elements in AlMg(Mn) and AlMgSi alloys, frequently used in the automotive industry, exhibit significant alterations in the microstructure and texture evolution throughout common sheet processing. The final sheet's properties are further controlled by various parameters such as the casting cooling rate, the degree of deformation, and the applied heat treatments, which makes sophisticated alloy and process design indispensable for the development of advanced aluminum alloys.

As the design of novel alloys or the application of alternative process parameters are initially realized on a laboratory scale, the comparability and transferability of promising results in microstructure and texture formation to the industrial scale is crucial. Therefore, laboratory- and industrial-fabricated sheets of the standard alloys EN AW-5182 and EN AW-6016 are analyzed after fundamental steps throughout the entire processing chain. The results indicate good conformity for the microstructures but reveal discrepancies in the strength of individual texture components especially in the deformed AlMgSi alloys. However, as the final annealed microstructures and textures are comparable, the established laboratory sheet processing has been approved for further microstructure and texture analyses.

In consideration of increasing amounts of recycled Al products, the influence of “impurity” elements such as Fe on the microstructure and texture formation of AlMg(Mn) alloys is investigated in a detailed laboratory scale study. The primary and secondary phase volume fraction, size, and composition is altered by various Fe/Mn ratios as well as different process parameters. The experimental results — using various characterization techniques — show good conformity with the performed thermodynamic calculations. The microstructures further indicate both effects of particle stimulated nucleation and Zener pinning, resulting in significant grain refinement for higher Fe and Mn alloying levels. In combination with the highly random textures of the final annealed sheets, the studied Fe and Mn alloyed Al sheets show beneficial microstructural features, which may also positively influence the mechanical properties of the alloys.

KURZFASSUNG

In den letzten Jahrzehnten wurde die Verwendung von Aluminium und Aluminiumlegierungen im Mobilitätssektor zu einer wesentlichen Maßnahme, um die CO₂-Emissionen zu reduzieren. Die Leichtbauweise kann weiters die Elektromobilität fördern, da dadurch die mit den Batteriesystemen einhergehende Massenzunahme teilweise kompensiert werden kann. Die stetig strenger werdenden Sicherheitsstandards verlangen zumeist eine Verbesserung der mechanischen Eigenschaften der Legierungen, allen voran der erreichbaren Festigkeit. Dies resultiert jedoch oftmals in einer verminderten Verformbarkeit der Aluminiumbleche und somit in Einschränkungen im modernen Karosseriedesign. Da viele grundlegende Eigenschaften stark von der Mikrostruktur und Textur abhängig sind, ermöglicht die Steuerung dieser Variablen die gewünschte Eigenschaftskombination in optimierten Aluminiumlegierungen.

Die unterschiedlichen Auswirkungen der Legierungselemente in AlMg(Mn)- und AlMgSi-Legierungen, die häufig in der Automobilindustrie verwendet werden, zeigen signifikante Veränderungen in der Mikrostruktur und der Texturentwicklung während der herkömmlichen Blecherzeugung. Die endgültigen Eigenschaften werden weiters durch verschiedene Parameter wie die Gussabkühlrate, den Verformungsgrad und die angewendeten Wärmebehandlungen gesteuert, was ein durchdachtes Legierungs- und Prozessdesign für die Entwicklung fortschrittlicher Aluminiumbleche unverzichtbar macht.

Da neuartige Legierungen oder die Anwendung alternativer Prozessparameter zumeist im Labormaßstab erprobt werden, ist die Vergleichbarkeit und Übertragbarkeit vielversprechender Ergebnisse bei der Mikrostruktur- und Texturbildung auf den industriellen Maßstab von entscheidender Bedeutung. Zur Charakterisierung dieses Verhaltens werden labor- und industriell-gefertigte Bleche der Standardlegierungen EN AW-5182 und EN AW-6016 über die gesamte Verarbeitungskette analysiert. Die Ergebnisse zeigen eine gute Vergleichbarkeit für die Mikrostrukturen, jedoch ergeben sich Diskrepanzen in der Stärke einzelner Texturkomponenten (insbesondere in den deformierten AlMgSi-Legierungen). Da jedoch die weich- oder lösungsgeglühten Mikrostrukturen und Texturen für Industrie und Labor grundsätzlich vergleichbar sind, kann der untersuchte Laborherstellungsprozess als annähernd repräsentativ betrachtet werden.

Weiters wird in Anbetracht der zunehmenden Mengen an recyceltem Aluminium der Einfluss von „Verunreinigungselementen“ wie Eisen auf die Mikrostruktur und Texturbildung in AlMg(Mn)-Legierungen in einer detaillierten Studie im Labormaßstab untersucht. Der Volumenanteil, die Größe und die Zusammensetzung der Primär- und Sekundärphasen werden durch Abwandlungen der Fe/Mn-Verhältnisse sowie verschiedene Prozessparameter modifiziert. Die unter Verwendung unterschiedlicher Charakterisierungstechniken erlangten experimentellen Ergebnisse weisen eine

gute Übereinstimmung mit den durchgeführten thermodynamischen Berechnungen auf. Die Mikrostrukturen zeigen sowohl die Effekte der partikelstimulierten Keimbildung als auch des Zener-Pinning, was zu einer signifikanten Kornfeinung für höhere Fe- und/oder Mn-Legierungsniveaus führt. In Kombination mit den sehr zufälligen Texturen im weichgeglühten Zustand ergeben sich für die untersuchten Fe- und Mn-legierten Al-Bleche vorteilhafte Merkmale, die auch die mechanischen Eigenschaften der Legierungen positiv beeinflussen können.

TABLE OF CONTENT

1	INTRODUCTION	1
2	STATE OF THE ART	4
2.1	Microstructure Evolution during Commercial Processing of Aluminum Alloys	4
2.1.1	Casting	4
2.1.2	Homogenization	7
2.1.3	Deformation	7
2.1.4	Recovery and Recrystallization	10
2.2	Microstructure Evolution in Two-Phase Alloys	13
2.2.1	Particle Stimulated Nucleation	14
2.2.2	Smith-Zener Pinning	15
2.3	Texture Evolution during Commercial Processing of Aluminum Alloys	16
2.3.1	Notation and Representation of Textures	17
2.3.2	Deformation Textures in Aluminum Alloys	20
2.3.3	Annealing Textures in Aluminum Alloys	21
2.3.4	Texture Related Effects in Aluminum Alloys	23
3	APPROACH	33
4	TEXTURE AND MICROSTRUCTURE EVOLUTION IN LABORATORY- AND INDUSTRIAL-SCALED ALUMINUM SHEET PROCESSING	35
4.1	Introduction	36
4.2	Materials and Methods	40
4.2.1	EBSD Data Processing	42
4.3	Results	44
4.3.1	Microstructure and Grain Parameters	44
4.3.2	Texture Analysis	48
4.4	Discussion	52
4.5	Conclusions	54
5	PRIMARY AND SECONDARY PHASE EVOLUTION IN FE AND MN CONTAINING 5XXX AL SHEETS	59
5.1	Introduction	60
5.2	Materials and Methods	63
5.3	Results	64
5.3.1	Microstructures and Intermetallic Phases in As-Cast State	65
5.3.2	Microstructural Evolution during Homogenization	68
5.3.3	Thermodynamic Calculations	77
5.3.4	Soft Annealed State	79
5.4	Discussion	83
5.5	Conclusions	87

6	GRAIN SIZE AND TEXTURE EVOLUTION IN FE AND MN CONTAINING 5XXX AL SHEETS	100
6.1	Introduction	101
6.2	Materials and Methods	104
6.3	Results	107
6.3.1	Microstructure Evolution and Resulting Grain Size	107
6.3.2	Zener Pinning Effect of Dispersoids	112
6.3.3	Grain Boundary Pinning by Primary Phase Particles	115
6.3.4	Texture Modifications by Primary and Secondary Phase Particles	115
6.4	Discussion	118
6.5	Conclusions	122
7	SUMMARY AND OUTLOOK	143
8	APPENDIX	145
8.1	Peer-reviewed publications	145
8.2	Talks	145

1 INTRODUCTION

With more and more noticeable consequences of climate change in the past decades and the technological ambitions to distinctly reduce the greenhouse gas emissions in the automotive sector, the usage of light-weight materials such as aluminum and its alloys has become essential to reach the ambitious aims [1]. Combining light weight, high strength, good formability, and high corrosion resistance, aluminum alloys have already established a leading position in some automotive applications, e.g. car body panels or engine blocks, and can furthermore compensate for the battery associated weight increase in upcoming electromobility. Thus, within the near future the demand for aluminum (alloys) will further increase and a profound knowledge of the material processing is indispensable [1–3].

As the properties of aluminum (sheet) products are strongly affected by the main and secondary alloying elements as well as the processing conditions, different classes of aluminum alloys require consideration in the automotive industry. The application of non-age-hardenable AlMg(Mn) (5xxx) alloys focuses mainly on chassis or structural components since for their use as exterior panels the effective suppression of surface quality diminishing “Lüders-bands” by microstructure control would be required [2, 4, 5]. In contrast, the class of age-hardenable AlMgSi (6xxx) alloys is often used as outer body sheet material, combining high strength in-service and adequate formability during processing operations [3]. The 6xxx alloys can exhibit insufficient surface appearance in terms of the roping (or ridging) phenomenon, which is connected to the microstructure and texture evolution of the material during rolling and recrystallization processes [6].

To further expand their field of application, the development of advanced aluminum alloys with a superior property spectrum concerning strength and ductility is targeted. Therefore, the systematic modification of microstructure and texture of the material is considered a possible approach. The implementation includes various strategies as for example novel alloying concepts and/or sophisticated processing, whereby both texture and microstructure will be affected concurrently [5].

While the general effects of microstructural parameters such as grain size and shape or the degree of cold deformation are already well-understood and considered in industrial manufacturing of Al sheets, the impact of additional phases in the aluminum matrix on the downstream processing and mechanical properties is still subject of intensive research [7, 8]. The complexity of the situation arises from the interaction of particle stimulated nucleation (PSN) in the vicinity of coarse particles and Smith-Zener pinning effects in the presence of small dispersoids. However, well-considered application of those mechanisms enables selective control of the microstructure [9].

In addition to the microstructural concerns, different studies highlighted the impact of the texture on the mechanical properties and forming behavior of the Al products [6]. In general, a random distribution of grain orientations is thought to account for uniform characteristics of the final sheets. While the high Mg level in the AlMg(Mn) alloys already favors texture randomization due to alterations in the deformation behavior, the pronounced formation of typical (banded) Cube recrystallization texture in AlMgSi alloys, which also accounts for the aforementioned surface roping phenomenon, demands for additional texture controlling mechanisms [1, 2, 6, 10]. The most notable effects were found for intermediate annealing treatments or, similar to the microstructure modifications, for the particle stimulated nucleation mechanism [11, 12].

The present thesis investigates the microstructure and texture evolution of well-established 5xxx and 6xxx alloys for the automotive industry within a laboratory- and industrial-scaled manufacturing process. The focus was placed on the comparability of the different processing scales in terms of microstructural features and the intensity of specific rolling and recrystallization texture components. Furthermore, the influence of primary and secondary phases on the resulting microstructure and texture was studied in modified Al4.5Mg0.1Si alloys with varying levels of Fe and Mn. Therefore, the laboratory-scaled manufacturing also involved different casting and homogenization processes as well as various degrees of cold deformation before final soft annealing.

References

- [1] Hirsch J.: Recent development in aluminium for automotive applications. *Transactions of Nonferrous Metals Society of China*, 24 (2014), 1995–2002.
- [2] Hirsch J. and T. Al-Samman: Superior light metals by texture engineering: Optimized aluminum and magnesium alloys for automotive applications. *Acta Materialia*, 61 (2013), 818–843.
- [3] Ostermann F.: *Anwendungstechnologie Aluminium*. Springer, Berlin, Germany (2014).
- [4] Ebenberger P. et al.: Processing-controlled suppression of Lüders elongation in AlMgMn alloys. *Scripta Materialia*, 166 (2019), 64–67.
- [5] Burger G. B. et al.: Microstructural Control of Aluminum Sheet Used in Automotive Applications. *Materials Characterization*, 35 (1998), 23–39.
- [6] Engler O. and J. Hirsch: Control of recrystallisation texture and texture-related properties in industrial production of aluminium sheet. *Int. J. Mat. Res.*, 100 (2009), 564–575.
- [7] Yu L. et al.: Influence of Fe-rich particles on microstructure evolution, texture and mechanical properties of Al–Mg–Si–Cu alloys. *Metallurgical Research & Technology*, 117 (2020), 508.
- [8] Engler O. and S. Miller-Jupp: Control of second-phase particles in the Al–Mg–Mn alloy AA 5083. *Journal of Alloys and Compounds*, 689 (2016), 998–1010.
- [9] Humphreys F. J., G. S. Rohrer and A. D. Rollett: *Recrystallization and related annealing phenomena*. Elsevier Science Ltd. (2017).
- [10] Bennett T. A., R. H. Petrov and L. A. I. Kestens: Texture-induced surface roping in an automotive aluminium sheet. *Scripta Materialia*, 61 (2009), 733–736.

- [11] Bennett T. A. et al.: The Effect of Intermediate Annealing on Texture Banding in Aluminum Alloy 6016. *Advanced Engineering Materials*, 12 (2010), 1018–1023.
- [12] Bennett T. A. et al.: The effect of particle-stimulated nucleation on texture banding in an aluminium alloy. *Scripta Materialia*, 63 (2010), 461–464.

2 STATE OF THE ART

The following chapter comprises general information on microstructure and texture formation in aluminum during sheet processing with a focus on AlMg(Mn) as well as AlMgSi alloys. Moreover, attention is paid to microstructure modifications by primary and secondary phase particles and the basic theories of particle stimulated nucleation and Smith-Zener pinning as well as their effects on the resulting texture [1].

2.1 Microstructure Evolution during Commercial Processing of Aluminum Alloys

The microstructure of a material is defined by its alloying elements, the processing parameters, and the applied heat treatments. Therefore, a profound knowledge of the basic concepts in physical metallurgy concerning crystal structures, plastic deformation, and recrystallization is indispensable. The following section describes the microstructural changes in consideration of different processing steps of aluminum alloys.

2.1.1 Casting

The primary solidification of a material is crucial for the further processing, the mechanical properties, and the texture. Various parameters such as the type of the casting process (e.g. continuous casting, die casting), the solidification, and the subsequent cooling conditions of the ingot significantly affect the resulting microstructure, which is basically comprised of casting grains and additional intermetallic primary phases [2–8].

Pure aluminum solidifies in the face-centered cubic crystal structure (**Fig. 2.1**). As a consequence of the casting process (and further thermomechanical processing), the crystal structure shows various defects, all of which affect the material's properties [9]. Furthermore, the addition of alloying elements induces different mechanisms of crystal lattice alterations. While small atoms can occupy interstitial sites in the crystal lattice, alloying elements with similar atomic radii substitute the matrix atoms on their regular positions [10].

Both effects of interstitial and substitutional atoms require a minimum solubility of the alloying elements in the aluminum matrix. As the solubility limit is exceeded, the precipitation of additional phases is initiated. Depending on the exact composition of the alloy and the thermodynamic processing conditions, alloying elements can either precipitate as primary phases during casting (intermetallic or pure alloying element crystals) or secondary phases in subsequent heat treatments

(see homogenization in section 2.1.2). However, both types of phases strongly distort the crystal lattice and therefore alter the further deformation and recrystallization behavior [9].

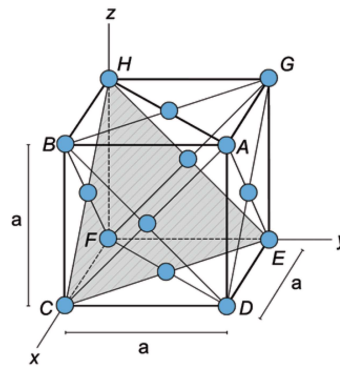


Fig. 2.1. Face-centered cubic unit cell of aluminum showing the densely packed (111) plane (containing the regular lattice points C, E, and H) and the [110] direction (running from lattice point F towards D) [9].

The formation of high angle grain boundaries (HAGBs) is initiated during casting. The strong impacts of the casting grain size on the resulting properties of various metals have been investigated for years and general relations like the strength increase related to grain refinement (described by the Hall-Petch equation) have been derived [9, 11]. In regards to aluminum wrought alloys, the reduction of the average casting grain size can further improve the toughness and ductility of the e.g. plate or sheet products [12]. Furthermore, the finer casting grain structures reduce segregation and porosity effects in the alloys, both of which can adversely affect the microstructure. Among the different methods for casting grain refinement available, commercial industrial processing focuses on the addition of grain refiners (to support heterogeneous nucleation) or accelerated cooling conditions [12–14], which can further influence the type, composition, and number density of the constituent primary phases [3, 5, 6]. The intermetallic phases and alloying elements may preferentially segregate to the grain boundaries during casting as accelerated diffusion is enabled in those regions due to higher atomic misarrangement [9, 11]. The formation of the primary phases during solidification occurs in all different commercial aluminum alloys as the solubilities of the alloying elements but also impurities such as Fe and other elements are relatively low.

In the non-age-hardenable AlMg(Mn) or 5xxx Al-alloys, which are widely used as construction material due to their medium to high strength, good fatigue properties, corrosion resistance and weldability, the main alloying element Mg shows a maximum solubility in the solid Al matrix of 17.4 wt.% at 450 °C [9]. The solubility decreases significantly with temperature and exhibits values around 0.2 wt.% at room temperature in thermodynamic equilibrium. The β -phase Al_8Mg_5 , which preferentially segregates to the interdendritic areas of the Al-Mg solid solution crystallites, adversely affects the corrosion resistance of the alloys due to the anodic potential to the Al matrix. However, as the diffusion of Mg in the matrix is limited because of the high binding potential of Mg/vacancy complexes in the 5xxx alloys [15], commercially used AlMg(Mn) alloys build supersaturated solid

solutions with Mg levels up to 4–5 wt.% (solid solution hardening) and show rather low tendencies of intergranular β -phase segregation [9].

The AlMgSi alloying system provides a basis for numerous different age-hardenable 6xxx Al alloys typically combining properties of medium to high strength, high fracture toughness as well as good corrosion resistance and formability [9, 16]. The phase equilibrium shows the intermetallic β -Mg₂Si phase existing alongside the α -Al solid solution matrix (Al-Mg₂Si pseudobinary phase diagram) [17]. The decreasing solubility of the phase at lower temperatures allows for precipitation hardening in consideration of specific processing sequences and therefore a superb combination of formability (T4 temper) and high strength after paint bake (T6 temper) in the automotive sheet production [17–19].

Besides the possible β -Al₃Mg₅ and the β -Mg₂Si primary phase precipitation in 5xxx and 6xxx alloys respectively, Fe-bearing constituent particle formation has been the topic of focused research for years now [2, 17, 20–22]. Typical formation of Al₃Fe (also reported as Al₁₃Fe₄) and Al₆Fe phases is observed for various alloying systems especially in the absence of other alloying elements like Mn, Si and Cu [20]. The Al₃Fe and Al₆Fe particles often exhibit needle-like morphologies and adversely affect the microstructure and properties as they cause stress concentrations and reduce the corrosion resistance of the alloy [23]. In commercial aluminum alloys, Mn is often added to modify the equilibrium composition and the morphology of the primary phases. Various types of intermetallic AlFeMn phases are observed, which show more plate-like structures with increasing Mn content and also Chinese-script (branched) morphology if casted under accelerated cooling conditions [5, 23].

While the AlFeMn phases are also found in AlMg(Mn) alloys, the consideration of the Si level is crucial for the AlMgSi alloys as the formation of Al(Fe,Mn)Si phases may be favored [20, 24–28]. Similar to the Al₃Fe phase, the plate-like monoclinic β -Al(Fe,Mn)Si is detrimental for the processing and mechanical properties of the alloys [24, 29]. Therefore, additional Mn alloying (lowering the Fe/Mn ratio) as well as higher cooling rates in the casting process are desirable as both favor the formation and thermodynamic stability of the α -Al(Fe,Mn)Si [5, 24, 30]. The α -Al(Fe,Mn)Si usually shows more compact or Chinese-script structures, is less detrimental to the final properties or can even beneficially affect the resulting microstructures by particle stimulated nucleation [3, 5, 9, 22, 29–32].

The formation of primary phases in the presence of higher Fe and Mn levels can also positively affect the microstructure and properties in the AlMg(Mn) alloys. Based on the interactions of Mg with dislocations during forming processes, the AlMg(Mn) alloys typically show stretcher-strain-marks and exhibit a strong Portevin-Le Chatelier (PLC) effect (Type A and B Lüders lines), making them unsuitable for outer body sheet applications [33, 34]. The Fe-bearing particles are of high interest in these engineering materials as they can suppress Lüdering (flow serrations), cause grain refinement and control the texture evolution (see section 2.2) [1, 5, 35].

2.1.2 Homogenization

High temperature (450–550 °C) casting ingot annealing treatments are generally implemented in the processing route to reduce the adverse effects of macro- and micro-segregations from the casting process [9]. Micro-segregations are typically balanced by enhanced diffusion processes at the elevated temperatures to result in a more homogenous solid solution of alloying elements [9]. The coarse primary constituent phases behave somewhat unpredictably as they may shrink, grow, or spheroidize with the homogenization treatment [36–38]. Furthermore, their composition may be altered as observed for the β - to α -AlFeSi transformation in the AlMgSi alloys [29, 39].

Another distinct microstructural effect during homogenisation is the formation of finely dispersed, thermally stable particles especially in Mn, Cr and Zr containing alloys [40]. The dispersoids (secondary phases) do not contribute to precipitation strengthening but crucially affect the further processing as they interact with grain boundaries and dislocations and thus strongly alter the deformation and recrystallization behavior [9, 41]. The size and number density of the emerging dispersoids depends on various parameters like time and temperature of the homogenization cycles as well as the content of dispersoid-forming alloying elements in solution after casting [9, 40–47].

Typical Mn containing (0–1.1 wt.%) AlMg alloys show the formation of $Al_6(Mn,Fe)$ dispersoid particles [9, 38, 42, 44, 48]. The size and volume fraction of those secondary phase particles typically increase with higher homogenization temperatures, longer annealing times, and higher Mn levels [38, 42, 43]. Furthermore, the formation of small α -AlFeSi dispersoids was observed for sufficiently high Si levels in both AlMg(Mn) and AlMgSi alloys. While in 6xxx alloys the typically high Si levels of >0.5 wt.% favor the formation of those particles anyway, the dissolution of coarse primary Mg_2Si phases and the related higher solute content of Si during homogenization are crucial for possible AlFeSi dispersoid precipitation in 5xxx alloys [38, 40–43, 47]. Furthermore, the precipitation behavior of hardening β - Mg_2Si phases may be altered in the AlMgSi alloys and therefore demands a more detailed consideration [49]. The interaction of the dispersoids with grain boundaries during recrystallization and grain growth further depends on their size, morphology, and total volume fraction. More details on the commonly known Smith-Zener pinning effects by dispersoids can be found in 2.2.2 [50].

2.1.3 Deformation

In general, as aluminum is considered a slip deforming metal due to its high stacking fault energy (γ_{SFE}) making twinning improbable, deformation processes are considered to occur almost exclusively by dislocation glide through the crystal [1]. For edge-dislocations, slip preferentially occurs in one of the twelve independent $\{111\}\langle 110\rangle$ glide systems referring to the four densely packed $\{111\}$ planes each including three $\langle 110\rangle$ directions (**Fig. 2.1**) (“planar glide”). A possible change of the slip system for edge-dislocations requires dislocation climb and therefore diffusion processes and vacancies

which predominantly occur at elevated temperatures [51–53]. Screw-dislocation movement is generally not restricted to particular glide planes as the distortion field of those dislocations shows cylindrical symmetry in an isotropic material [51]. In pure aluminum, the mechanism of cross-slip (“wavy glide”) is typically predominant since immobile dislocations as well as non-cuttable particles impede the planar glide [9] and the high stacking fault energy reduces the probability of dislocation dissociation [1, 54]. As deformation processes begin, new dislocations are generated at grain boundaries, crystal interfaces or stationary dislocation structures (“Frank-Read-source”) [9, 55]. With increasing strain during deformation the dislocations pile up and start the formation of network-like substructures. A heavy increase of the total stored energy and hence the driving force for following recrystallization is concomitant with the increasing dislocation density [1]. The typical hierarchy of structural elements in slip-deforming metals (with high γ_{SFE}) is schematically shown in **Fig. 2.2** [1].

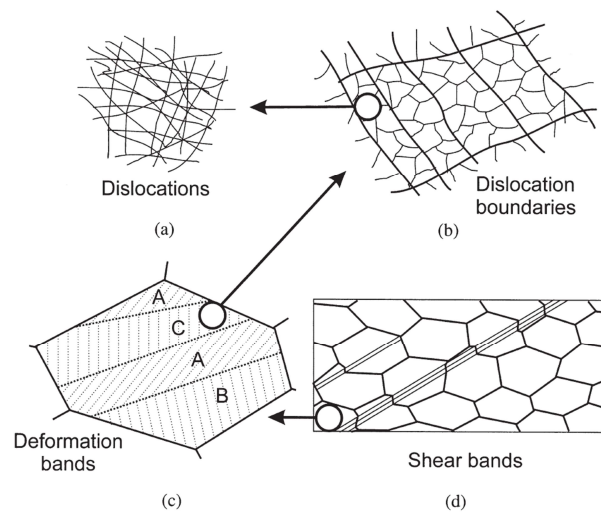


Fig. 2.2. Microstructural features in polycrystalline, slip-deforming metals [1].

In cell forming metals (such as aluminum alloys) the dislocations exist as random structures or tangles especially after rather low strains (**Fig. 2.2** (a)). With increasing strain, the dislocations arrange in narrow, high-dense boundaries to form (diffuse) cells and cell blocks in the deformed Al microstructures (**Fig. 2.2** (b)) [1, 56–58]. While further deformation occurs homogeneously within those cell blocks, the activation of other slip systems is required in the neighbouring blocks to meet the constraints of the overall strain [56, 59]. Especially in aluminum alloys, the banded structure of the cell blocks also proposes the term of “cell bands”, which are separated by dense dislocation walls (DDWs) or microbands [59, 60]. Whereas the misorientations between single cells within one cell block are in the range of $0.2\text{--}2^\circ$, the DDWs and the microbands exhibit orientation gradients of the adjacent regions up to 15° depending on the overall strain [1, 60]. For further increased strains, localized shear is observed over various microbands. These bands, often named S-bands or micro shear bands [1], typically align with the $\{111\}$ slip planes and therefore show distinct orientation changes compared to the microbands [61].

While the above-mentioned features represent the microstructure on a rather small scale, the deformation bands (**Fig. 2.2 (c)**) are considered the coarsest structural elements of grain subdivision [1]. The deformation bands result either from different active slip systems in different areas of the grain during deformation or from inhomogeneous strain distribution inside a single grain due to the orientation and plasticity of the adjacent grains [1, 62]. The narrow zones separating the deformation bands are termed transition bands, which consist of long cells or subgrains yielding a high cumulative orientation gradient [1]. The formation of deformation and transition bands is mostly observed in coarse grained microstructures [63]; the grain orientation is another critical factor affecting the deformation by banding or homogenous slip [64].

As already introduced on the microscopic scale as micro shear bands, the macroscopic equivalent of shear bands is observed after high plane strain deformations (**Fig. 2.2 (d)**) [1]. The shear bands, consisting of parallel bands over colonies of several grains, show typical inclining to the rolling plane between 20–40° (35° is illustrated) [1, 65] and arise independently of the grain structure and the general crystallographic considerations [1]. Especially in high stacking fault energy materials like aluminum, high deformation degrees can cause through-thickness shear bands degrading the final sheet quality [1]. The probability of shear banding depends on the grain size and orientation, solute content, and deformation temperature [65–67].

The deformation temperature generally impacts the formation of the different microstructural features and resulting grain orientations. As the strain distribution and deformation process become more homogeneous with the rising temperatures, the probability of deformation and shear banding decreases for the hot rolling process [63, 66, 68]. The grain subdivision is reduced with the activation of additional, non-octahedral slip systems [68, 69]. Simultaneously, the higher temperatures enable dynamic recovery and dynamic recrystallization processes (see section 2.1.4). In Al alloys, the dislocation climb and cross-slip strongly favor the microstructure restoration by the recovery process, in which the formation of low-angle boundaries and subgrains is observed [1]. However, higher temperatures generally promote more organized dislocation arrangements within the subgrains and overall more homogeneous microstructures [1].

The microstructures of (heavily) cold rolled fcc materials typically comprise all the features shown in **Fig. 2.2**. With the increase in strain and the amount of stored energy in the material, the substructures such as cells and subgrains experience significant refinement and usually show higher misorientations between adjacent regions [1]. The combination of the cold rolling degree (CRD) and the different microstructural features such as deformation bands, transition bands, and shear bands is pivotal in the subsequent recrystallization process, as they account for the driving pressure, represent preferential nucleation sites and therefore determine the resulting grain size and orientation [1, 70, 71].

Considering Al alloys, both the hot and cold deformation behavior are further affected by the alloying elements. For non-age-hardenable classes of aluminum alloys, the various strength levels are

determined by the amount of solid solution hardening elements added (in AlMg(Mn) typically 3–5 wt.% Mg;) and the degree of cold work (work hardening) [9]. During deformation the solute content of Mg in the AlMg(Mn) alloys can effectively suppress the formation of dislocation cells and cause stronger dislocation pinning/unpinning mechanisms [1, 15, 65]. (Dynamic) recovery is prevented as the typically wavy glide type of aluminum is transformed to more planar glide deformation behavior with increasing Mg content [15, 72]. A possible explanation is given by the higher equilibrium concentration of vacancies in the AlMg(Mn) alloys, which suppresses dislocation mushrooming and hence the formation of different dislocations which annihilate during recovery [15]. The dispersoid forming elements Mn and Cr can positively affect the plastic deformation behavior as they modify the increasing tendency of AlMg(Mn) alloys to deform by planar slip, resulting in a more homogeneous distribution of dislocations by planar and cross slip [9, 15]. With the alteration of the interaction of moving dislocations and the matrix as well as the reduction of γ_{SFE} with increasing Mg solute content, shear banding is favored [15, 65, 72]. Furthermore, with lower degrees of cold work before annealing and lower Mg levels, the surface appearance in regards to Lüders line formation can also be significantly improved [35, 73].

In both the AlMg(Mn) and AlMgSi alloys, the discussed microstructure evolution accounts for single phase crystals. However, as was introduced in 2.1.1 and 2.1.2, the primary and secondary phase particles alter the dislocation motion and hence the microstructure evolution. The discussion of those two-phase alloys is given in section 2.2.

2.1.4 Recovery and Recrystallization

Upon subsequent annealing treatments the distorted microstructures of the materials tend to return to the undeformed, “defect-free” crystal lattice. This tendency depends on the degree of (cold) deformation and the associated increase in stored energy as well as the annealing temperature. The short-range rearrangement of the dislocation structures during recovery and the formation and growth of completely new grains during recrystallization are the competing mechanisms in the microstructure reformation. Whether these processes occur during or after the deformation process is distinguished between dynamic and static recovery/recrystallization [1].

Recovery describes a series of events partially restoring the properties of the material before deformation and occurs only prior to recrystallization [1, 74]. A schematic overview of the ongoing microstructural processes is given in **Fig. 2.3**. The basic mechanisms of recovery are based on dislocation annihilation and rearrangement into stable, low energy sub-boundaries enabled by glide, climb and cross-slip of the edge- and screw-dislocations [1, 75]. The formation of dislocation cells (**Fig. 2.3 (a),(b)**) occurs in aluminum readily during deformation due to its high stacking fault energy [56, 57]. During annealing, the dislocations form more regular networks within the tangled cell-walls and diminish in the cell interior to form subgrains (**Fig. 2.3 (c),(d)**) [1, 74, 76]. The low angle subgrain boundaries, usually showing misorientations below 10–15°, can further decrease their energy (and

the stored energy of the material) through the formation of fewer, but higher misoriented boundaries by subgrain growth [1, 74]. The driving pressure is given by the misorientation of adjacent subgrains, which highly affects the mobility of the low angle grain boundaries (LAGBs, increased for high misorientations) and does not remain constant during the process [1].

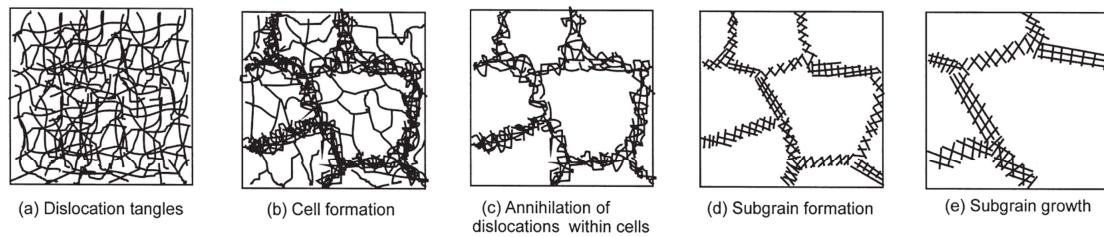


Fig. 2.3. Microstructure evolution during recovery in a cell forming material [1].

The extent of recovery during annealing is influenced by various factors such as strain, annealing temperature, and the intrinsic material properties. Commercial Al alloys exhibit recovery processes already during plastic deformation independent of the temperature, as the high stacking fault energy of the material facilitates dislocation climbing [15, 51]. Considering the impact of further alloying elements, the net effects are often difficult to predict [1]. Although Mg lowers γ_{SFE} , impedes the dislocation motion and therefore strongly retards dynamic recovery, static room temperature recovery takes place even faster in AlMg(Mn) alloys than in pure Al. The reason for this contradictory behavior is given by the higher equilibrium concentration of vacancies in AlMg(Mn) alloys at lower temperatures, which facilitate dislocation climb [15, 51, 76, 77]. Recovery also occurs between subsequent passes during rolling and therefore affects both the processing behavior and the final mechanical properties of the Al sheets [76–78]. Although recovery plays an important role in the annealing of AlMg(Mn) and AlMgSi sheets, up to now no adequate models exist fully describing the kinetics of the ongoing microstructural and mechanical property alterations [1].

While recovery likely occurs even at room temperature in the Al alloys [76], the additional energy in annealing treatments enables both faster recovery and subgrain growth as well as recrystallization. Recrystallization is indicated by the formation of new, strain-free grain nuclei and their growth at the expense of the deformed matrix during further annealing (**Fig. 2.4**) [74]. Once recrystallization sets in, there is no more recovery possible in the material [1].

The recrystallization process is affected by different variables. Generally, a minimum deformation (stored energy) is required to initiate nucleation and the smaller the degree of deformation, the higher the necessary temperature to induce recrystallization. The final grain size and shape in a fully recrystallized sample further depend on the annealing temperature and time as well as the heating rate [79–81]. Especially when considering Al alloys, the extent of recovery also affects the recrystallization behavior as the formation and growth of subgrains lowers the internal energy and therefore the driving force for recrystallization [1].

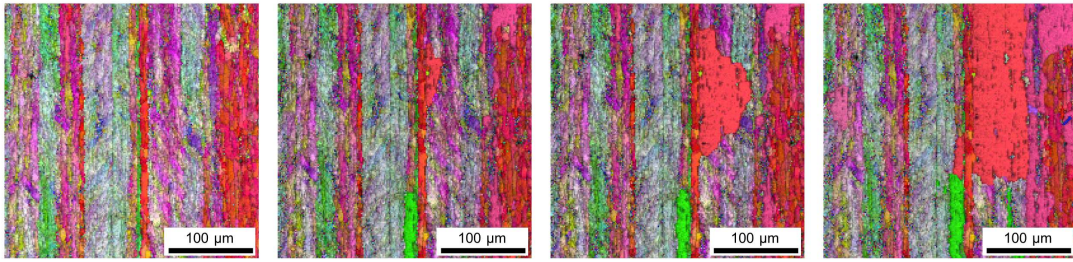


Fig. 2.4. Overlay of image quality and inverse pole figure of an in situ EBSD observation showing nucleation and grain growth in a cold rolled EN AW-6016 sheet during annealing at 325 °C [82].

The formal kinetics of the recrystallization process are commonly described in the Johnson-Mehl-Avrami-Kolmogorov (JMAK) model, which connects the recrystallized volume fraction to the nucleation and growth rates of the material [1, 80]. However, since the recrystallization nuclei (small crystallites of low energy, separated from the matrix by high angle grain boundaries (HAGB) showing different orientation than the surrounding matrix [1]) are not randomly distributed throughout the material as assumed in the JMAK model, the concordance with experimental results is rather poor [1, 74]. As will be discussed in more detail in section 2.3, the nuclei are supposed to already pre-exist in the deformed microstructure especially in the vicinity of large orientation gradients. Therefore, grain boundaries, deformation bands, transition bands, and shear bands represent preferential nucleation sites in contrast to the subgrain or cell interiors and nucleation depends on the strain and the microstructural features of the material [70, 81, 83].

The driving pressure for subsequent growth of the nuclei is related to the dislocation density in the surrounding area. A retarding force is generated by the curvature of the high angle grain boundary with a specific boundary energy [1, 79]. The nuclei must therefore reach a minimum critical radius to further lower the internal energy by continued growth. The growth rate of the recrystallized grains is also related to the mobility of the migrating boundary and hence to the grain orientation or the misorientation of the growing grain to the surrounding matrix [80].

Another (slightly) different recrystallization mechanism observed in aluminum alloys is the strain induced boundary migration (SIBM). Referring to Beck and Sperry [84], SIBM is considered as recrystallization not involving newly generated nuclei. The grains recrystallized by SIBM show orientations similar to the grains present in the as-deformed state. The direction of boundary migration differs for normal grain growth and SIBM, with the former moving opposite to the direction of the center of curvature and the latter towards the center of curvature [84]. Although SIBM is dominant in Al only up to strains of about 20%, it is crucial for the evolution of specific orientations (especially during hot rolling [85, 86]) and therefore of great industrial significance [87]. While SIBM is readily observed in Al, AlMn, AlMg, and AlFe alloys [64], the primary and secondary phases in AlMg(Mn) and AlMgSi alloys alter the recrystallization behavior and partly suppress the effects of SIBM in the commercial production of automotive Al sheets [16, 18, 79, 86, 88].

Upon completion of the recovery and recrystallization process and reaching the thermodynamic equilibrium conditions, the microstructure consists of (nearly) strain-free, equiaxed grains with the HAGBs perfectly meeting in an angle of 120° [1]. The experimentally obtained microstructures show significant alterations in grain size and grain shape. The microstructures and mechanical properties of rolled and annealed AlMg(Mn) and AlMgSi sheets are affected by the degree of deformation during hot and cold rolling as well as the time, temperature, and heating rate of the annealing treatment [9]. Both alloy systems tend to form smaller grains with increasing strains; smaller initial grain sizes further promote the formation of recrystallization nuclei and refine the final microstructure [81, 89]. Although solute atoms generally retain recrystallization mechanisms due to the solute drag [1], the higher Mg content in AlMg(Mn) alloys further enhances grain refinement as recovery at elevated temperatures is suppressed and the formation of dislocation clusters increases the number of nucleation sites for recrystallization [51, 90, 91]. The higher Mg levels also promote the formation of macroscopic shear bands and therefore again increase the nucleation rate [65]. In turn, the resulting grain size, size distribution, and morphology affect properties like strength, anisotropy, and Lüdering [19, 35, 73]. Therefore, sophisticated microstructural control is crucial throughout the processing of AlMg(Mn) alloys [9].

The recrystallization in AlMgSi alloys is further influenced by the possible precipitation state of the Mg₂Si hardening phases [9]. While [88] states that the recrystallization kinetics during final solution annealing are not affected by the dissolution of the Mg₂Si phase above 350 °C, the “post-dynamic” recrystallization at elevated temperatures after hot rolling impacts the further microstructure evolution [18]. As the level of solute elements is low compared to the AlMg(Mn) alloys, the nucleation rate is rather influenced by the heating rate in the final annealing treatment [92, 93]. However, a comprehensive discussion of the recrystallization behavior of both the AlMg(Mn) and AlMgSi alloys warrants the consideration of thermodynamically stable primary and secondary phase particles, which will be discussed in the following section 2.2.

2.2 Microstructure Evolution in Two-Phase Alloys

Whereas the basic mechanisms behind the microstructural evolution discussed in section 2.1 are generally applicable for the AlMg(Mn) and AlMgSi alloys, the effects of (coarse) primary and (fine) secondary phase alloys in those alloy systems are of high practical importance especially in sheet processing [18, 33, 70]. As the effects of particles on the deformation and recrystallization behavior are influenced by their size, volume fraction, shape, and spacing [1], the discussion of the two different effects of particle stimulated nucleation (PSN) and Smith-Zener pinning is realized separately in the following subsections.

2.2.1 Particle Stimulated Nucleation

Particle stimulated nucleation is readily observed in the vicinity of particles with diameters greater than $1\ \mu\text{m}$ in both the AlMg(Mn) and the AlMgSi alloys. [16, 94, 95]. During deformation, dislocations will accumulate around coarse non-deformable particles due to Orowan looping, generation of secondary dislocations and crystal rotations as shown in **Fig. 2.5 (a)** [96, 97]. Consequently, the overall dislocation density in particle containing alloys increases more rapidly with strain than it does in single phase alloys (**Fig. 2.5 (b)**). The higher dislocation density initiates recrystallization by subgrain boundary migration in the deformation zone, which stops as the energy of the zone is consumed [94, 98].

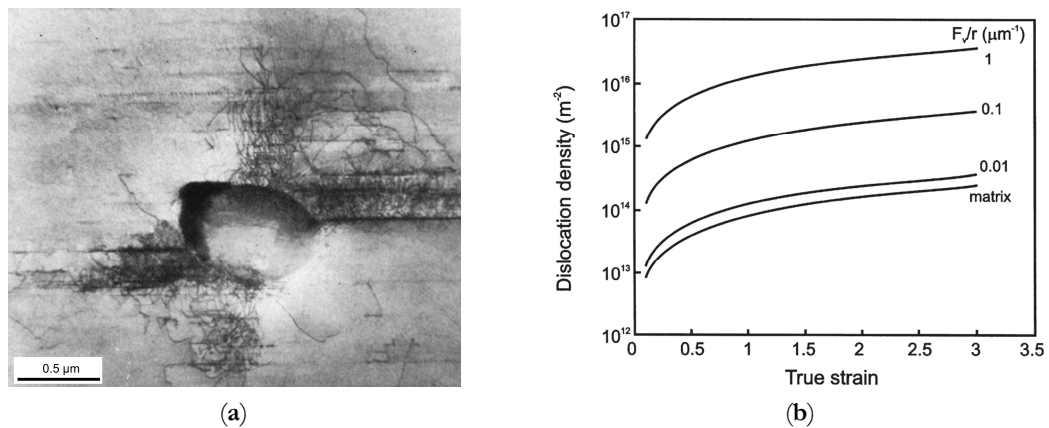


Fig. 2.5. (a) TEM observations of the deformation zone around a non-deformable particle by dislocation accumulation [97]; (b) influence of particles on the dislocation density in alloys (Fv/r : ratio of particle volume fraction and mean particle radius) [1].

The evolving grains are reported to show orientation relations to the deformed microstructure and as particle stimulated nucleation affects the nucleation rather than the growth rate of recrystallization, the final grain size is related to the interparticle distances [94]. The occurrence of PSN requires a minimum particle size ($>1\ \mu\text{m}$), which increases as the degree of deformation decreases [94]. The critical point is not found in the formation of PSN nuclei but in their conditions for growth, where the driving pressure (related to the particle radius) must exceed the counteracting pressure yielding from boundary curvature [1].

The probability to obtain PSN in the commercial production of Al sheets is influenced by the alloying elements as well as the relative degrees of hot and cold rolling [16, 70]. Considering AlMg(Mn) alloys, thermally stable and potential PSN particles are predominantly formed by impurity Fe in combination with Mn and Si [20, 23] and PSN is therefore readily observed during final soft annealing after cold rolling [99]. The large primary phase particles will decrease the resultant grain size and therefore positively affect the mechanical properties of the alloys. The tendency of Lüdering can further be reduced as non-aged dislocations can be generated in the vicinity of large primary phase particles upon quenching [35]. In a similar manner, the constituent AlFeSi phases in the AlMgSi alloys induce the PSN effects and can reduce plastic anisotropy and thus enhance the sheet formability [18].

However, the related microstructure modifications are often not observable as the formation of PSN nuclei is suppressed by finely dispersed stable secondary phases or hardening Mg_2Si precipitates in these alloys [18, 100].

2.2.2 Smith-Zener Pinning

In comparison to the coarse primary phase particles, the nanometer sized dispersoids, which formed during homogenization or upon heating for hot rolling, show complete contrary behavior as they impede recovery and recrystallization. The description of the retarding forces exerted on moving LAGBs and HAGBs was first given by Smith and Zener and is hence known as the Smith-Zener drag [50]. In general, the boundary is pinned by particles as the contact lowers the total boundary area and thus the energy of the system [50].

The Smith-Zener pinning is topic of research for decades now. Whereas earlier work focused on the accurate mathematical description of boundary energies, contact angle as well as particle size, morphology and fraction [101–104], the application of computer simulations on recrystallization in two-phase alloys resulted in numerous different formulations and resulting equations for the “correct” Smith-Zener drag forces [105–116]. As the detailed discussion of the basic formalism is beyond the scope of this thesis, this section will focus on the formulation of the Zener limiting grain size R_{lim} in relation to particle size r and volume fraction f_V (Equ. 2.1). The additional parameters K

$$R_{\text{lim}} = K \frac{r}{f_V^m} \quad (\text{Equ. 2.1})$$

and m account for the geometrical considerations and the random/non-random correlation of particles and boundaries. For a comprehensive overview on this topic, the reader is referred to [117] and [118].

For a given volume fraction and size of dispersoids, an equilibrium grain size after recrystallization will be obtained when the pinning pressure equals the driving pressure. While Smith and Zener only considered a given volume fraction of equally sized particles in their limiting grain size equation [50], Fullman incorporated the possible size distribution of particles yielding higher pinning forces for smaller particles [119]. Nes et al. showed that coherent particles will contribute higher pinning forces than noncoherent do and further implemented the effects of ellipsoidal particles on grain boundaries moving onwards in different angles [104, 117]. Another central parameter in all derivations of the Zener limiting grain size equation (Equ. 2.1) is the particle volume fraction. Whereas early theories state linear relations between the volume fractions and the resulting grain size with m equal to 1 [50, 117, 118], computer simulations in 2D and 3D systems suggest a dependency of m on the volume fraction changing from 1 or 0.5 to 0.33 with higher dispersoid fractions [108, 109], which is also supported by some experimental data (**Fig. 2.6**) [118].

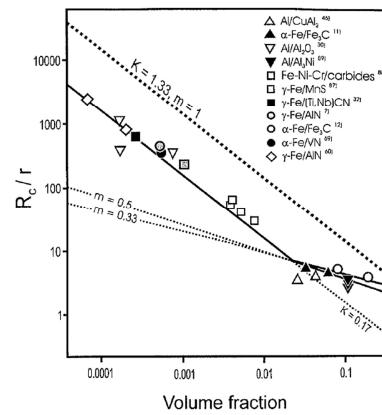


Fig. 2.6. Comparison of different values of the exponent m in the Zener limiting grain size ((Equ. 2.1) to experimental data [118]; R_c/r : ratio of the limiting grain radius R_c ($=R_{lim}$) to the mean particle radius.

In consideration of Al alloys, the Smith-Zener pinning is crucial in terms of grain size control [42, 43, 120, 121]. As mentioned in section 2.1.2, the Al_6Mn dispersoids in AlMg(Mn) and AlMgSi alloys retard grain growth during recrystallization and therefore result in overall grain refinement [9]. The grain size and morphology of the annealed Al sheets is further affected by the ellipsoidal shape of those particles, which impede grain growth more effectively in the sheet normal direction (ND) and may cause elongated, recrystallized grains in rolling direction (RD) [117]. In 6xxx Al sheets, the recrystallized grain size is also influenced by the size and distribution of the Mg_2Si phases as they can contribute to the Smith-Zener drag and therefore require sophisticated control during thermomechanical processing [18, 100].

To conclude on PSN and Zener pinning in Al alloys, both effects alter the resulting microstructure and are used for grain size control. In real alloys exhibiting a bimodal particle distribution, the effect of Smith-Zener pinning suppresses particle stimulated nucleation as it increases the critical size for PSN nuclei [122]. Therefore, the Smith-Zener drag more readily determines the final microstructures and textures as will be discussed in the subsequent section.

2.3 Texture Evolution during Commercial Processing of Aluminum Alloys

The influence of the grain orientations on the deformation and recrystallization behavior was already mentioned in the previous sections. The texture of a material is considered as the entirety of orientations of all grains within the sample [123] and affects the (an-)isotropy of the materials properties [1]. While in traditional approaches to texture analysis the texture and microstructure were discussed separately, the progress in electron microscopy over the last decades has enabled the simultaneous measurement of microstructural features and their corresponding orientations (microtexture) [123]. The following section gives a short overview on the representation of orientations and textures and discusses the evolution of texture throughout sample processing based on Al sheet manufacturing.

2.3.1 Notation and Representation of Textures

The unambiguous description of an orientation requires the definition of two sets of coordinate systems. The sample coordinate system usually refers to fundamental directions according to the external shape as for example rolling (RD), normal (ND) and transverse direction (TD) in rolled sheets. The second coordinate system is related to the crystal structure of the material and in cubic materials the orthogonal crystal axes [100], [010] and [001] are conventionally chosen as the crystal coordinate system [123]. An example of the position of the crystal system with respect to the sample coordinate system is given in **Fig. 2.7**. The depicted relative orientation can be described by means of a rotation matrix, containing the rotations necessary to make the sample system identically oriented to the crystal system [123]. The rotations are given by the cosines of the angles α , β , and γ , referring to the angles between one crystal axis and all three of the samples axes (see **Fig. 2.7**) [123]. However, although the resulting 3x3 matrix contains all necessary information, the practical description of orientations is usually realized by more descriptive and plain methods.

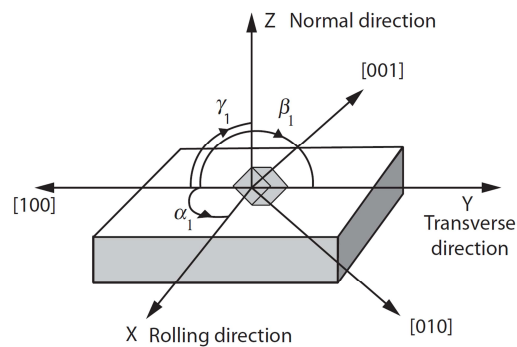


Fig. 2.7. Example of the relative orientation of sample and crystal coordinate system in a rolled material including the angles α_1 , β_1 , γ_1 between [100] and the sample axes RD, ND and TD [123].

One common method to further describe orientations is the ideal orientation notation using the Miller indices of planes and directions. The notation indicates the (hkl) plane of the crystal parallel to the sample surface (ND) and the [uvw] direction of the crystal parallel to RD [11, 123]. Therefore, the values from the orientation matrix are idealized and rounded and thus the ideal orientation notation usually does not describe an exact orientation but can be a few degrees away from it. An exemplary representation of the Goss orientation (110)[001] is given in **Fig. 2.8**, where the normal of the (110) plane is parallel to ND and the [001] direction is parallel to RD [11, 123].

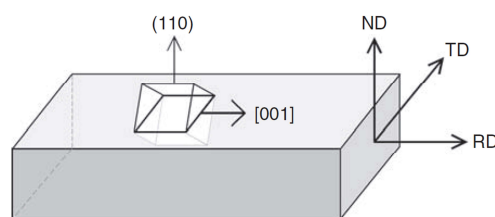


Fig. 2.8. Illustration of the Goss orientation in consideration of the ideal orientation notation of (110)[001] [123].

The representation of orientations by pole figures uses a stereographic projection. The oriented crystal unit cell is enclosed in a reference sphere, which is intersected by the plane normal directions (poles) [11]. The projection of this poles on the equatorial plane gives points including the relative orientation of the crystal by the angles α and β (see **Fig. 2.9 (a)**). If the equatorial plane is attached to the sample reference directions, the orientations can be fully described by a set of at least two different sample reference pole figures [123]. An example of a (111) pole figure of polycrystalline aluminum is given in **Fig. 2.9 (b)**. The significant accumulation of crystal orientations indicates a Cube textured material typical for recrystallized Al sheets.

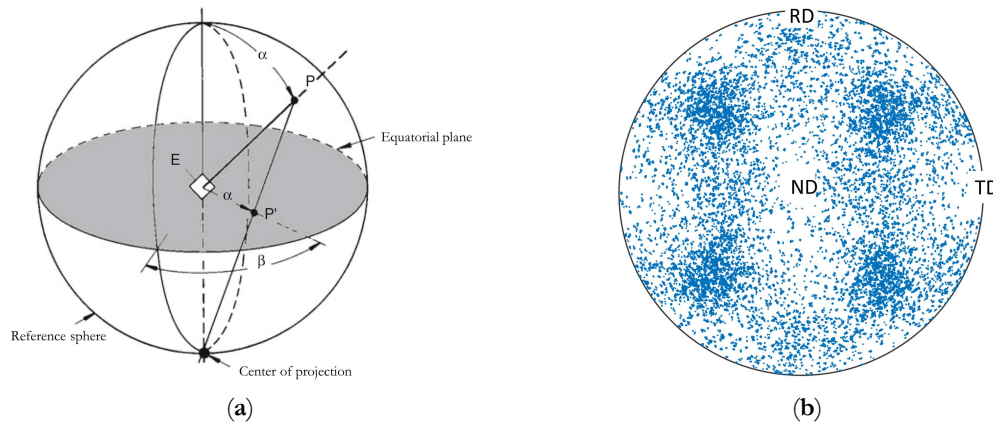


Fig. 2.9. (a) Stereographic projection of crystal orientations; E: crystallographic plane, P: pole, intersecting point of the plane normal and the reference sphere, P': intersection of the straight line connecting P and the center of projection (termed pole of the plane E), α : angle between P and the equatorial plane normal, β : azimuthal angle of P' [11]; (b) Resulting exemplary (111) pole figure including the original sample directions RD, TD and ND.

The most used representation method for texture data is the pole figure (PF), although the inverse pole figure (IPF) is often recommended for an easier interpretation (especially for fiber textures). In the inverse pole figure the distribution of a sample direction is represented with respect to the crystal coordinate system, which is why inverse pole figures are sometimes referred to as axis distribution diagrams [11]. **Fig. 2.10 (a)** depicts the (001) standard projection for a cubic crystal system with typical low indexed planes. Due to crystallographic symmetries in the cubic crystal, the representation of all orientations in an IPF can be reduced to the standard triangle connecting the directions $\langle 001 \rangle$, $\langle 011 \rangle$, and $\langle 111 \rangle$ (grey area in **Fig. 2.10 (a)**) [11]. A typical fiber texture is obtained for uniaxial deformation processes such as wire drawing. The corresponding inverse pole figure in **Fig. 2.10 (b)** shows a preferential alignment of the $\langle 111 \rangle$ and $\langle 100 \rangle$ direction parallel to the drawing axis [1].

The inverse pole figure notation is further used to create color coded micrographs (IPF mapping) directly from orientation data measured using electron backscatter diffraction. This form of representation is beneficial as it combines microstructure and texture information in one graph. An exemplary IPF mapping is shown in **Fig. 2.11 (a)**, where the grains are colored in dependence of their orientation relative to the sample normal direction (IPF Z or (001) IPF; **Fig. 2.11 (b)**).

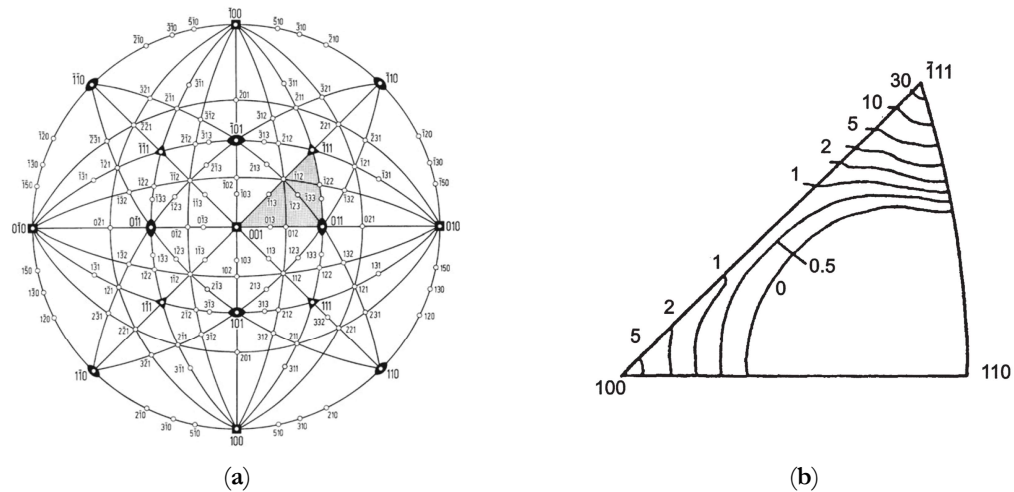


Fig. 2.10. (a) Standard (001)-projection including planes with low Miller indices in a cubic crystal system [11] and (b) Inverse pole figure of a drawn aluminum wire showing a strong preferential orientation of the $\langle 111 \rangle$ and $\langle 100 \rangle$ axis parallel to the drawing axis (numbers indicate texture intensities) [1].

However, for an exact representation of the orientational data another IPF representing a different sample direction is required, as the crystal unit cell can still be freely rotated around the axis parallel to the sample direction and hence the orientation is not fully determined by one IPF map.

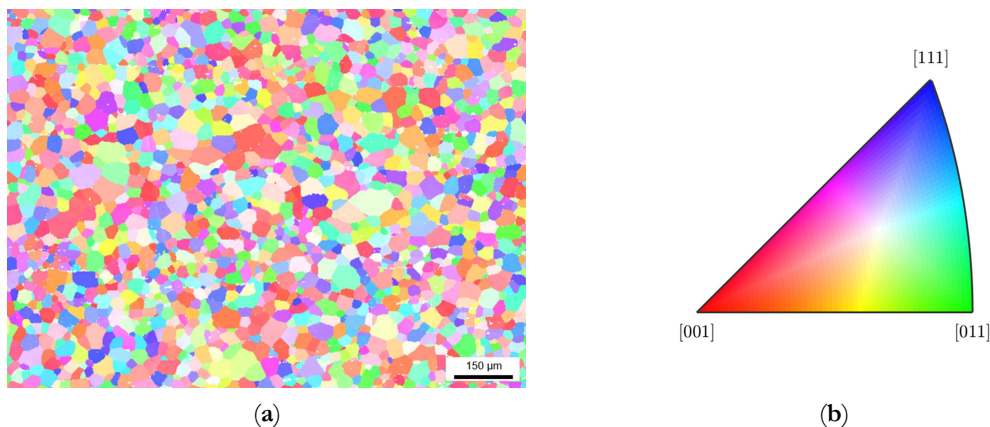


Fig. 2.11. (a) (001) inverse pole figure mapping of a soft annealed EN AW-5182 and (b) the corresponding color code indicating the orientations of the grains in relation to the sample normal direction.

An exact representation of the full orientation information can be realized by the means of Euler angles and the Euler space [1]. The Euler angles φ_1 , Φ , and φ_2 describe a set of three rotations necessary to rotate the sample system onto the crystal coordinate system (see **Fig. 2.12 (a)**) [123]. Euler angle orientations are commonly represented in the Euler space, which uses φ_1 , Φ , and φ_2 as orthogonal axes for a 3D coordinate system [1, 123]. For an easier two-dimensional representation, φ_1 and Φ are plotted in sections of φ_2 from 0° to 90° (reduced Euler space due to cubic crystal symmetry) [123].

From the orientation data, the orientation distribution function (ODF) can be used to quantify specific texture components. The ODF is a probability distribution function expressing the density of crystal orientations in a material and therefore the probability to find an orientation in an orientation interval around a specified orientation [123]. The results express the texture components

in multiples of the random distribution — hence comparing the intensity of the occurring component to its intensity in a completely random distribution of grain orientations. However, since the mathematical description is of high complexity, the reader is referred to [123] for more information on the ODF and its calculation. An exemplary 2D Euler plot in sections of φ_2 is given in **Fig. 2.12 (b)**, representing the calculated ODF from an aluminum sample using color coded orientation intensities.

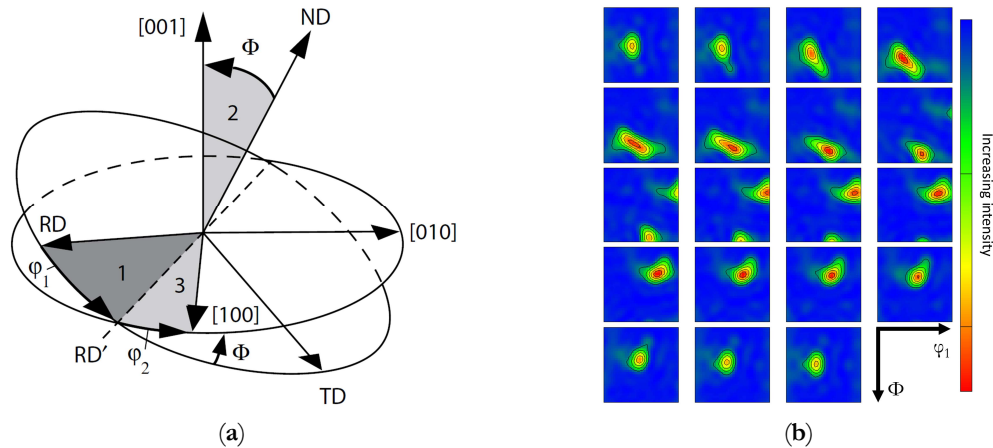


Fig. 2.12. (a) Graphical derivation of the Euler angles using the Bunge convention [123] and (b) Euler plot representing the calculated orientation distribution function by color coded orientation intensities, φ_2 sections from 0° (top, left) to 90° (bottom, right) in 5° steps.

2.3.2 Deformation Textures in Aluminum Alloys

The deformation texture of a material is directly influenced by its general deformation behavior. The almost exclusively occurring slip deformation in aluminum alloys yields specific grain orientations and thus texture components, which are governed by the deformation axes of the forming process [1, 124]. In typical aluminum sheet fabrication, the rolling process commonly results in a strong β -fiber texture [125]. During deformation the face-centered cubic unit cells rotate and find stable positions in orientations along the β -fiber running from Brass $\{011\}\langle 211\rangle$ over S $\{123\}\langle 634\rangle$ to the Copper $\{112\}\langle 111\rangle$ orientation (see **Fig. 2.13 (a)**).

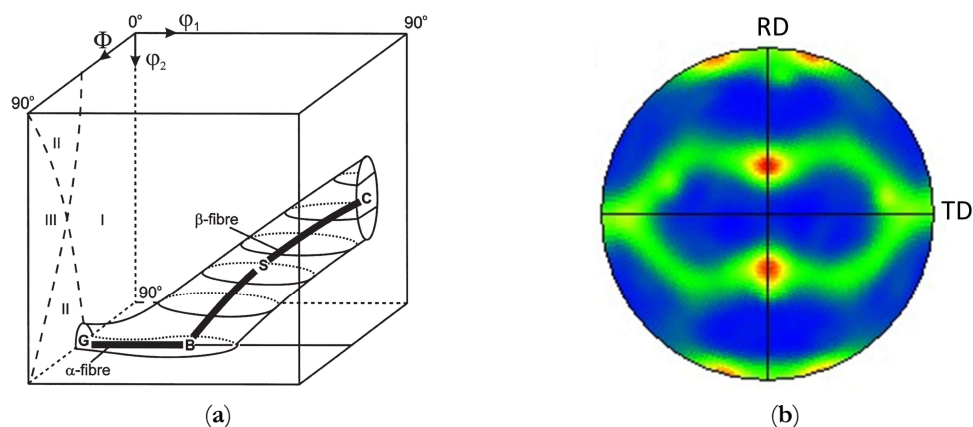


Fig. 2.13. (a) Position of the deformation texture components Goss (G), Brass (B), S, and Copper (C) in the reduced Euler space connected by the α - and β -fiber [125] and (b) (111) pole figure of the β -fiber rolling texture of a cold rolled AlMgSi alloy.

Additionally, the orientations along the fcc- α -fiber (running from Goss $\{011\}\langle 100\rangle$ to Brass) are readily observed in metals with high γ_{SFE} [125]. The relative intensities of the rolling texture components are strongly influenced by the degree of deformation, the rolling geometry, temperature, and friction, the initial orientation, and the alloying elements [126]. As the deformation conditions may vary over the sheet thickness (especially in hot bands), different deformation layers and texture components can be observed [69, 127].

During hot rolling, the elevated temperatures cause the activation of additional non-octahedral slip systems (see 2.1.3) [69, 128]. Those can intensify Brass and also stabilize the Cube $\{001\}\langle 100\rangle$ component, which is commonly observed in recrystallized materials' textures [69, 129–131]. An additional intensification of Brass is obtained because of enhanced α -fiber stability at elevated temperatures [126]. The hot band texture is the starting condition for further deformation and recrystallization steps, affects the final properties of the material and is therefore crucial to be controlled in Al sheet fabrication [18].

During cold rolling, the intensities of fcc metals strongly vary along the α -fiber and β -fiber with the degree of deformation [125]. The α -fiber vanishes with increasing thickness reductions. Although the β -fiber shows enhanced stability with cold deformation, the intensities tend to peak at the ideal orientations of S and Copper [1, 125]. Moreover, Hirsch et al. [8] highlighted the influence of the initial texture of the material on the resulting orientations showing the strong tendency of Cube grains to rotate towards the Copper or S orientation.

The alloying elements modify the deformation mechanisms and hence the deformation texture of Al alloys. As a solute element in Al, Mg promotes the formation of shear bands, which intensify the Brass orientation at the expense of Copper [65, 126, 131]. Consequently the AlMg(Mn) alloys can exhibit a balanced spectrum of orientations after cold rolling and recrystallization [16]. In the AlMgSi alloys, the size and distribution of the Mg_2Si precipitates is crucial. Although those phases do not strongly impact the deformation behavior, they can impede post dynamic recrystallization during subsequent hot rolling passes or after coiling of the finished hot band and therefore significantly alter the resulting cold-rolling and final annealing textures [18].

2.3.3 Annealing Textures in Aluminum Alloys

During annealing of the deformed Al sheets, recovery and recrystallization will significantly alter the texture of the material. Recovery (or dynamic recovery) usually does not transform the rolling texture components but sharpens their intensities [70, 99]. In the presence of small pinning particles new HAGBs may also form during recovery yielding a globular grain structure with retained rolling texture [70]. Similar microstructures are also obtained for dynamically recrystallized materials [1].

In regards to classical recrystallization by nucleation and growth, the nuclei in Al alloys are small, highly deformed zones already present in the as-deformed microstructure (see 2.1.4) [1]. However, the required conditions for growth are mostly satisfied in the vicinity of deformation inhomogeneities

where the misorientations between substructures are sufficiently large resulting in four common nucleation sites in aluminum: grain boundaries, transition bands, shear bands, and Cube bands [1, 70].

Earlier works often discussed which of the competing mechanisms of oriented nucleation or oriented growth is accountable for the classical recrystallization textures. The former theory describes the occurrence of only specific oriented nuclei and their growth during recrystallization, whereas the latter states the existence of randomly oriented nuclei but preferred growth conditions for the typical recrystallization texture components at the expense of others [70, 79, 132]. However, it is nowadays widely accepted that a combination of both theories will affect the evolution of the recrystallization texture components [1, 70, 71, 132].

The recrystallization texture of aluminum typically involves an intense and sometimes problematic Cube fraction [70, 133–136]. The Cube oriented grains nucleate at Cube bands, which are either transition bands or deformed grains in Cube orientation [70, 134, 137–139]. In addition to the size advantage of Cube oriented nuclei [137], the Cube orientations show growth advantages into various deformation texture components based on the high mobility of 40° $\langle 111 \rangle$ boundaries or the lower surface energy of the boundaries [137, 140]. While the Cube component is dominant in pure aluminum recrystallization textures, the alloying elements and particle distributions significantly alter the textures in aluminum alloys [70].

The nucleation of recrystallization at shear bands occurs favorably in aluminum alloys with high amounts of solute elements and for high cold rolling degrees [141]. The related texture components are the Goss and the Q $\{013\}\langle 231 \rangle$ orientation — both showing favorable growth conditions into the deformed matrix [70, 139, 140]. The increasing amounts of shear components in the recrystallized microstructures of AlMg(Mn) and AlCu alloys can modify the final textures to a more balanced orientation distribution [16, 142].

Another frequently observed component in pure aluminum textures is the R $\{124\}\langle 211 \rangle$ orientation [70]. Its nucleation occurs primarily on the HAGBs of the deformed grains, which also provides favorable growth conditions due to the large misorientations in the surrounding area [16]. As the R orientation is close to the deformation texture component S, its appearance is promoted by dynamic recrystallization and SIBM mechanisms, which do not strongly modify the orientations of the deformed microstructures. However, the formation of the R component is not readily observed in AlMg(Mn) and AlMgSi alloys, which again indicates the suppression of the dynamic recrystallization and SIBM mechanism [16].

Further different recrystallization texture components are obtained in two-phase alloys capable of PSN [16, 70]. The nuclei emerging and growing in the vicinity of large particles show slightly preferred P $\{011\}\langle 122 \rangle$ or Cube_{ND-22} $\{001\}\langle 310 \rangle$ orientations, although PSN textures are usually rather weak [70]. The PSN related texture components can thus be used for texture randomization in AlMg(Mn) and especially AlMgSi alloys, where the PSN nuclei suppress the formation of detrimental

Cube bands in the final recrystallized sheets [16, 70, 143–145]. During commercial Al sheet processing, the PSN effects on texture are strongly inhibited by the Zener pinning forces exerted by small secondary phase dispersoids or Mg_2Si precipitates, as those particles more effectively retard the nucleation in PSN zones than in Cube bands [146, 147]. Therefore, sophisticated thermomechanical processing is required for a careful texture and microstructure control.

2.3.4 Texture Related Effects in Aluminum Alloys

The recrystallization textures in Al alloys critically affect the forming behavior of the annealed sheets in terms of the plastic anisotropy or r - and Δr -value [16]. During subsequent processing (e.g. deep drawing) the sheets may exhibit a strong earing tendency, as the observed orientations (especially Cube) show distinctly different flow behavior with the direction of forming relative to the original rolling direction [70]. The typical flow behavior of rolling and recrystallization textures in dependence on the overall strain is given by the earing profiles in **Fig. 2.14 (a)**.

The adverse effect on the forming behavior is reduced by texture randomization and Cube suppression, which is realized in AlMg(Mn) sheets by full or partial recrystallization during hot rolling or by an intermediate annealing (IA) treatment between the cold rolling passes [16]. The effects are shown by the graph in **Fig. 2.14 (b)**, where the inter(mediate) annealed sheets show superior earing profiles [70].

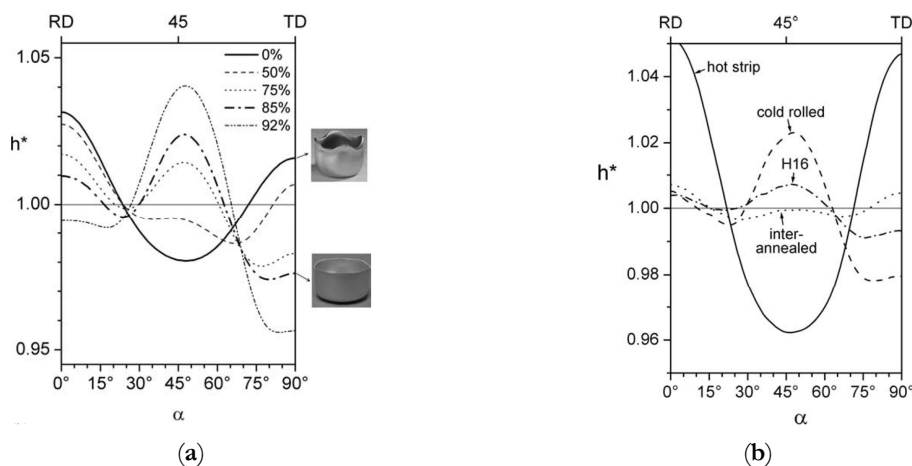


Fig. 2.14. (a) Earing profiles in dependence on the rolling strain, 0% strain depicts the retained 0°/90° earing from hot-rolling recrystallization textures, 92% strain shows the transformation to weaker 0°/90° earing with additional 45° ears, h^* : relative wall height of the drawn cup, α : drawing angle relative to the original rolling direction [70]; (b) Symmetrized earing profiles of AA 3105 measured at different stages of the processing line, h^* : relative wall height of the drawn cup, α : drawing angle relative to the original rolling direction [70].

A similar IA heat treatment is applied to suppress the Cube texture banding in AlMgSi alloys, although it does not reduce the total amount of the Cube fraction [148]. Improved formability of AlMgSi alloys demands the PSN effect to randomize the texture of the final annealed sheets and hence requires control of the primary and secondary phase particles as well as the Mg_2Si precipitates throughout the entire process chain [18].

Another frequently observed effect related to texture is the roping (or ridging) phenomenon of solution annealed 6xxx Al sheets [70]. Specific orientations like Cube and Goss form bands along the former rolling direction [149–151], which result in ridges and valleys after subsequent forming operations in TD and therefore insufficient surface finish (see **Fig. 2.15 (a)–(c)**) [16, 18, 70]. Again PSN and intermediate annealing are suitable remedial measures [144, 152, 153] and further alternative rolling processes can beneficially alter the recrystallization texture in these Al sheets [154, 155].

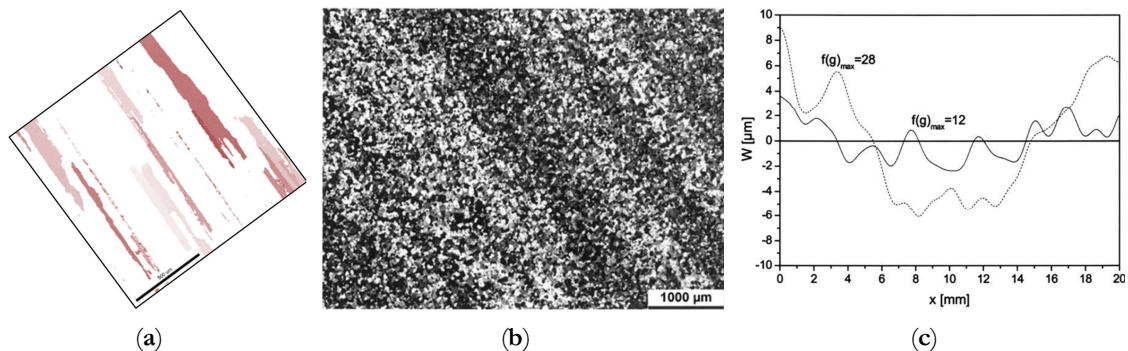


Fig. 2.15. (a) Observed (Cube) texture bands in an *in situ* EBSD investigation of an EN AW-6016 sheet; (b) optical micrograph showing strong texture banding [18]; (c) the waviness of the sheet surface after 20% tensile deformation in TD for two different texture intensities (dotted and continuous line) [18].

On the other hand, distinct textures can also lead to improvements in component properties. High-voltage capacitors are often manufactured with an anode made of high-purity aluminum foil (99.99%) including aluminum oxide as a dielectric. The capacitance of these electrolytic capacitors depends on the surface area of the aluminum foil, which can be greatly increased by an etching process [70, 136, 156]. During etching, narrow channels are formed through the $\langle 001 \rangle$ direction in the foil. Consequently, for optimal etching, a highly textured material with the $\langle 001 \rangle$ direction parallel to the foil normal is indispensable. In practice, this behavior is achieved best by a high fraction of Cube oriented grains, which are only accessible in thin foils by strongly Cube textured hot rolling microstructures [70, 136, 156]. During further cold rolling the Cube grains fragment and can thus provide a sufficient high number of Cube nuclei during final recrystallization [70, 136, 156].

References

- [1] Humphreys F. J., G. S. Rohrer and A. D. Rollett: Recrystallization and related annealing phenomena. Elsevier Science Ltd. (2017).
- [2] Algendy A. Y., K. Liu and X.-G. Chen: Formation of intermetallic phases during solidification in Al-Mg-Mn 5xxx alloys with various Mg levels. MATEC Web of Conferences, 326 (2020), 2002.
- [3] Belmares-Perales S.: Effect of Cooling Rate and Fe/Mn Weight Ratio on Volume Fractions of α -AlFeSi and β -AlFeSi Phases in Al-7.3Si-3.5Cu Alloy. Metals and Materials International, 14 (2008), 307–314.
- [4] Li Y. J. and L. Arnberg: Solidification structures and phase selection of iron-bearing eutectic particles in a DC-cast AA5182 alloy. Acta Materialia, 52 (2004), 2673–2681.

-
- [5] Liu Y. et al.: Effect of Fe, Si and Cooling Rate on the Formation of Fe- and Mn-rich Intermetallics in Al–5Mg–0.8Mn Alloy. *Journal of Materials Science & Technology*, 32 (2016), 305–312.
- [6] Seifeddine S., S. Johansson and I. L. Svensson: The influence of cooling rate and manganese content on the β -Al₅FeSi phase formation and mechanical properties of Al–Si-based alloys. *Materials Science and Engineering: A*, 490 (2008), 385–390.
- [7] Turmezey T.: AlFe and AlFeSi Intermetallic Phases in Aluminium Alloys. *Age-Hardenable Aluminium Alloys*, 13-14 (1987), 121–132.
- [8] Hirsch J., E. Nes and K. Lücke: Rolling and recrystallization textures in directionally solidified aluminium. *Acta Metallurgica*, 35 (1987), 427–438.
- [9] Ostermann F.: *Anwendungstechnologie Aluminium*. Springer, Berlin, Germany (2014).
- [10] Gobrecht J.: *Werkstofftechnik - Metalle*. In: Oldenbourg-Lehrbücher für Ingenieure. Oldenbourg, München (2009).
- [11] Gottstein G.: *Materialwissenschaft und Werkstofftechnik*. Springer, Berlin, Germany (2014).
- [12] Guan R.-G. and D. Tie: A Review on Grain Refinement of Aluminum Alloys: Progresses, Challenges and Prospects. *Acta Metallurgica Sinica (English Letters)*, 30 (2017), 409–432.
- [13] Liang G. et al.: Effect of cooling rate on grain refinement of cast aluminium alloys. *Materialia*, 3 (2018), 113–121.
- [14] Schmid F. et al.: Industry-oriented sample preparation of 6xxx and 5xxx aluminum alloys in laboratory scale. *Proceedings of EMC 2019* (2019), 639–652.
- [15] Kuhlmann-Wilsdorf D.: The Connection between Recovery and Glide Type in Aluminum and Al-Mg. *Aluminium Alloys - Their Physical and Mechanical Properties*, 331-337 (2000), 689–702.
- [16] Hirsch J. and T. Al-Samman: Superior light metals by texture engineering: Optimized aluminum and magnesium alloys for automotive applications. *Acta Materialia*, 61 (2013), 818–843.
- [17] Zhang J. et al.: Equilibrium pseudobinary Al–Mg₂Si phase diagram. *Materials Science and Technology*, 17 (2001), 494–496.
- [18] Engler O. and J. Hirsch: Texture control by thermomechanical processing of AA6xxx Al–Mg–Si sheet alloys for automotive applications—a review. *Materials Science and Engineering: A*, 336 (2002), 249–262.
- [19] Burger G. B. et al.: Microstructural Control of Aluminum Sheet Used in Automotive Applications. *Materials Characterization*, 35 (1998), 23–39.
- [20] Allen C. M. et al.: Intermetallic phase selection in 1XXX Al alloys. *Progress in Materials Science*, 43 (1998), 89–170.
- [21] Skjerpe P.: Intermetallic phases formed during DC-casting of an Al–0.25 Wt Pct Fe–0.13 Wt Pct Si alloy. *Metallurgical Transactions A*, 18 (1987), 189–200.
- [22] Khalifa W., F. H. Samuel and J. E. Gruzleski: Iron intermetallic phases in the Al corner of the Al-Si-Fe system. *Metallurgical and Materials Transactions A*, 34 (2003), 807–825.
- [23] Liu Y. et al.: Effect of Mn and Fe on the Formation of Fe- and Mn-Rich Intermetallics in Al-5Mg-Mn Alloys Solidified Under Near-Rapid Cooling. *Materials (Basel, Switzerland)*, 9 (2016), 88.
- [24] Belmares-Perales S. and A. A. Zaldívar-Cadena: Addition of iron for the removal of the β -AlFeSi intermetallic by refining of α -AlFeSi phase in an Al–7.5Si–3.6Cu alloy. *Materials Science and Engineering: B*, 174 (2010), 191–195.
- [25] Davignon G. et al.: An isothermal section at 550 °C in the Al-Rich corner of the Al-Fe-Mn-Si system. *Metallurgical and Materials Transactions A*, 27 (1996), 3357–3361.

- [26] Chakrabarti D. and D. E. Laughlin: Phase relations and precipitation in Al–Mg–Si alloys with Cu additions. *Progress in Materials Science*, 49 (2004), 389–410.
- [27] Sweet L. et al.: The Effect of Iron Content on the Iron-Containing Intermetallic Phases in a Cast 6060 Aluminum Alloy. *Metallurgical and Materials Transactions A*, 42 (2011), 1737–1749.
- [28] Uttarasak K. et al.: Evolution of Fe-containing intermetallic phases and abnormal grain growth in 6063 aluminum alloy during homogenization. *Results in Physics*, 15 (2019), 102535.
- [29] Kuijpers N. et al.: The dependence of the β -AlFeSi to α -Al(FeMn)Si transformation kinetics in Al–Mg–Si alloys on the alloying elements. *Materials Science and Engineering: A*, 394 (2005), 9–19.
- [30] Ji S. et al.: Effect of iron on the microstructure and mechanical property of Al–Mg–Si–Mn and Al–Mg–Si diecast alloys. *Materials Science and Engineering: A*, 564 (2013), 130–139.
- [31] Que Z., Y. Wang and Z. Fan: Formation of the Fe-Containing Intermetallic Compounds during Solidification of Al-5Mg-2Si-0.7Mn-1.1Fe Alloy. *Metallurgical and Materials Transactions A*, 49 (2018), 2173–2181.
- [32] Minoda T., H. Hayakawa and H. Yoshida: Effect of iron content on the surface quality of 6063 aluminum alloy extrusion. *Keikinzoku*, 50 (2000), 491–494.
- [33] Hirsch J.: Aluminium Alloys for Automotive Application. *Aluminium Alloys - Supplement of ICAA5*, 242 (1997), 33–50.
- [34] Hirsch J.: Automotive trends in aluminium - The European Perspective. *Materials Forum*, 28 (2004), 15–23.
- [35] Ebenberger P. et al.: Processing-controlled suppression of Lüders elongation in AlMgMn alloys. *Scripta Materialia*, 166 (2019), 64–67.
- [36] Sheppard T. and N. Raghunathan: Modification of cast structures in Al–Mg alloys by thermal treatments. *Materials Science and Technology*, 5 (1989), 268–280.
- [37] Claves S. R., D. L. Elias and W. Z. Misiolek: Analysis of the Intermetallic Phase Transformation Occurring during Homogenization of 6xxx Aluminum Alloys. *Materials Science Forum*, 396 (2002), 667–674.
- [38] Engler O., K. Kuhnke and J. Hasenclever: Development of intermetallic particles during solidification and homogenization of two AA 5xxx series Al-Mg alloys with different Mg contents. *Journal of Alloys and Compounds*, 728 (2017), 669–681.
- [39] Li Y. and L. Arnberg: A eutectoid phase transformation for the primary intermetallic particle from Alm(Fe,Mn) to Al3(Fe,Mn) in AA5182 alloy. *Acta Materialia*, 52 (2004), 2945–2952.
- [40] Lodgaard L. and N. Ryum: Precipitation of dispersoids containing Mn and/or Cr in Al–Mg–Si alloys. *Materials Science and Engineering: A*, 283 (2000), 144–152.
- [41] Strobel K. et al.: Dispersoid Phases in 6xxx Series Aluminium Alloys. *Age-Hardenable Aluminium Alloys*, 654-656 (2010), 926–929.
- [42] Engler O., Z. Liu and K. Kuhnke: Impact of homogenization on particles in the Al–Mg–Mn alloy AA 5454 – Experiment and simulation. *Journal of Alloys and Compounds*, 560 (2013), 111–122.
- [43] Engler O. and S. Miller-Jupp: Control of second-phase particles in the Al-Mg-Mn alloy AA 5083. *Journal of Alloys and Compounds*, 689 (2016), 998–1010.
- [44] Li Y. J., W. Z. Zhang and K. Marthinsen: Precipitation crystallography of plate-shaped Al6(Mn,Fe) dispersoids in AA5182 alloy. *Acta Materialia*, 60 (2012), 5963–5974.
- [45] Liu S. et al.: Effects of Combined Additions of Mn and Zr on Dispersoid Formation and Recrystallization Behavior in Al-Zn-Mg Alloys. *Metallurgical and Materials Transactions A*, 50 (2019), 4877–4890.

- [46] Osman M. et al.: Effect of homogenisation conditions on recrystallisation in Al–Mg–Mn alloy AA 5454. *Materials Science and Technology*, 23 (2007), 688–698.
- [47] Rakhmonov J. et al.: Effects of Al(MnFe)Si dispersoids with different sizes and number densities on microstructure and ambient/elevated-temperature mechanical properties of extruded Al–Mg–Si AA6082 alloys with varying Mn content. *Journal of Alloys and Compounds*, 861 (2021), 157937.
- [48] Ratchev P., B. Verlinden and P. van Houtte: Effect of preheat temperature on the orientation relationship of (Mn,Fe)Al₆ precipitates in an AA 5182 Aluminium—Magnesium alloy. *Acta Metallurgica et Materialia*, 43 (1995), 621–629.
- [49] Qian X., N. Parson and X.-G. Chen: Effect of post-homogenisation cooling rate and Mn addition on Mg₂Si precipitation and hot workability of AA6060 alloys. *Canadian Metallurgical Quarterly*, 59 (2020), 189–200.
- [50] Smith C. S.: Grains, phases, and interfaces: An introduction of microstructure. *Trans.AIME*, 175 (1948), 15–51.
- [51] Altenpohl D.: Aluminium und Aluminiumlegierungen. In: *Reine und angewandte Metallkunde in Einzeldarstellungen, Band: 19*. Springer, Berlin, Heidelberg, Germany (1965).
- [52] Kannan V. C. and G. Thomas: Dislocation Climb and Determination of Stacking-Fault Energies in Al and Al-1% Mg. *Journal of Applied Physics*, 37 (1966), 2363–2370.
- [53] Mott N. F.: The Mechanical Properties of Metals. *Proceedings of the Physical Society. Section B*, 64 (1951), 729–741.
- [54] Kuhlmann-Wilsdorf D., H. G. F. Wilsdorf and J. A. Wert: LEDS theory of workhardening stages and planar versus distributed glide. *Scripta Metallurgica et Materialia*, 31 (1994), 729–734.
- [55] Frank F. C. and W. T. Read: Multiplication Processes for Slow Moving Dislocations. *Physical Review*, 79 (1950), 722–723.
- [56] Bay B. et al.: Overview no. 96 evolution of f.c.c. deformation structures in polyslip. *Acta Metallurgica et Materialia*, 40 (1992), 205–219.
- [57] Kuhlmann-Wilsdorf D.: Theory of plastic deformation: - properties of low energy dislocation structures. *Materials Science and Engineering: A*, 113 (1989), 1–41.
- [58] Liu Q., D. Juul Jensen and N. Hansen: Effect of grain orientation on deformation structure in cold-rolled polycrystalline aluminium. *Acta Materialia*, 46 (1998), 5819–5838.
- [59] Bay B., N. Hansen and D. Kuhlmann-Wilsdorf: Deformation structures in lightly rolled pure aluminium. *Materials Science and Engineering: A*, 113 (1989), 385–397.
- [60] Bay B., N. Hansen and D. Kuhlmann-Wilsdorf: Microstructural evolution in rolled aluminium. *Materials Science and Engineering: A*, 158 (1992), 139–146.
- [61] Rosen G. I. et al.: Microstructure and local crystallography of cold rolled aluminium. *Acta Metallurgica et Materialia*, 43 (1995), 2563–2579.
- [62] Lee C. S. and B. J. Duggan: Deformation banding and copper-type rolling textures. *Acta Metallurgica et Materialia*, 41 (1993), 2691–2699.
- [63] Kuhlmann-Wilsdorf D.: The theory of dislocation-based crystal plasticity. *Philosophical Magazine A*, 79 (1999), 955–1008.
- [64] Somerday M. and F. J. Humphreys: Recrystallisation behaviour of supersaturated Al–Mn alloys Part 2 – Al–0.3 wt-%Mn. *Materials Science and Technology*, 19 (2003), 30–35.
- [65] Duckham A., R. Knutsen and O. Engler: Influence of deformation variables on the formation of copper-type shear bands in Al–1Mg. *Acta Materialia*, 49 (2001), 2739–2749.

-
- [66] Morii K., H. Mecking and Y. Nakayama: Development of shear bands in f.c.c. single crystals. *Acta Metallurgica*, 33 (1985), 379–386.
- [67] Ridha A. A. and W. B. Hutchinson: Recrystallisation mechanisms and the origin of cube texture in copper. *Acta Metallurgica*, 30 (1982), 1929–1939.
- [68] Hughes D. A. and N. Hansen: A comparison of the evolution of cold and hot deformation microstructures and textures in fcc metals. Proceedings of the TMS Symposium on "Advances in Hot Deformation Textures and Microstructures" (SAND-94-8487C, CONF-9310260-1), Sandia National Laboratories, Livermore, CA (United States) (1993), 1-18.
- [69] Maurice C. and J. H. Driver: Hot rolling textures of f.c.c. metals—Part I. Experimental results on Al single and polycrystals. *Acta Materialia*, 45 (1997), 4627–4638.
- [70] Engler O. and J. Hirsch: Control of recrystallisation texture and texture-related properties in industrial production of aluminium sheet. *Int. J. Mat. Res.*, 100 (2009), 564–575.
- [71] Engler O. and K. Lücke: Mechanisms of recrystallization texture formation in aluminium alloys. *Scripta Metallurgica et Materialia*, 27 (1992), 1527–1532.
- [72] Drury M. R. and F. J. Humphreys: The development of microstructure in Al-5% Mg during high temperature deformation. *Acta Metallurgica*, 34 (1986), 2259–2271.
- [73] Ebenberger P. et al.: Effect of Compositional and Processing Variations in New 5182-Type AlMgMn Alloys on Mechanical Properties and Deformation Surface Quality. *Materials* (Basel, Switzerland), 12 (2019), 1645.
- [74] Beck P. A.: Annealing of cold worked metals. *Advances in Physics*, 3 (1954), 245–324.
- [75] Hull D. and D. J. Bacon: Introduction to dislocations. In: *Materials science*. Butterworth-Heinemann, Oxford (2001).
- [76] Nes E.: Recovery revisited. *Acta Metallurgica et Materialia*, 43 (1995), 2189–2207.
- [77] Verdier M. et al.: Microstructural evolution during recovery in Al–2.5%Mg alloys. *Materials Science and Engineering: A*, 248 (1998), 187–197.
- [78] Falkinger G. and P. Simon: Static recovery of an AlMg4.5Mn aluminium alloy during multi-pass hot-rolling. *Procedia Engineering*, 207 (2017), 31–36.
- [79] Doherty R. D.: Recrystallization and Texture. *Progress in Materials Science*, 42 (1997), 39–58.
- [80] Burke J. E. and D. Turnbull: Recrystallization and grain growth. *Progress in Metal Physics*, 3 (1952), 220–292.
- [81] Bay B. and N. Hansen: Recrystallization in Commercially Pure Aluminum. *Metallurgical and Materials Transactions A*, 15 (1984), 287–297.
- [82] Grasserbauer J.: In situ electron backscatter diffraction: Recrystallization behavior and microstructural evolution in Al-Mg-Si alloys during heating. Master's Thesis, Graz University of Technology, Graz (2018).
- [83] Hirsch J.: Recent development in aluminium for automotive applications. *Transactions of Nonferrous Metals Society of China*, 24 (2014), 1995–2002.
- [84] Beck P. A. and P. R. Sperry: Strain Induced Grain Boundary Migration in High Purity Aluminum. *Journal of Applied Physics*, 21 (1950), 150–152.
- [85] Theyssier M. C. and J. H. Driver: Recrystallization nucleation mechanism along boundaries in hot deformed Al bicrystals. *Materials Science and Engineering: A* (1999), 73–82.
- [86] Vatne H. E. et al.: Modelling recrystallization after hot deformation of aluminium. *Acta Materialia*, 44 (1996), 4463–4473.

- [87] Bellier S. P. and R. D. Doherty: The structure of deformed aluminium and its recrystallization—investigations with transmission Kossel diffraction. *Acta Metallurgica*, 25 (1977), 521–538.
- [88] Poletti C. et al.: Microstructure Evolution in a 6082 Aluminium Alloy during Thermomechanical Treatment. *Materials (Basel, Switzerland)*, 11 (2018), 1319.
- [89] Hurley P. J. and F. J. Humphreys: A study of recrystallization in singlephase aluminium using insitu annealing in the scanning electron microscope. *Journal of Microscopy*, 213 (2004), 225–234.
- [90] Morishige T. et al.: Effect of Mg content on the minimum grain size of Al–Mg alloys obtained by friction stir processing. *Scripta Materialia*, 64 (2011), 355–358.
- [91] Sheppard T., N. C. Parson and M. A. Zaidi: Dynamic recrystallization in Al–7Mg alloy. *Metal Science*, 17 (1983), 481–490.
- [92] Wang X. et al.: Effect of heating rate on mechanical property, microstructure and texture evolution of Al–Mg–Si–Cu alloy during solution treatment. *Materials Science and Engineering: A*, 621 (2015), 8–17.
- [93] Gao G. et al.: Influence of different solution methods on microstructure, precipitation behavior and mechanical properties of Al–Mg–Si alloy. *Transactions of Nonferrous Metals Society of China*, 28 (2018), 839–847.
- [94] Humphreys F. J.: The nucleation of recrystallization at second phase particles in deformed aluminium. *Acta Metallurgica*, 25 (1977), 1323–1344.
- [95] Furu T., K. Marthinsen and E. Nes: Particle Effects on Recrystallization of Metals. *Materials Science Forum*, 113-115 (1993), 41–54.
- [96] Orowan E.: Zur Kristallplastizität. III. *Zeitschrift für Physik*, 89 (1934), 634–659.
- [97] Humphreys F. J. and A. T. Stewart: Dislocation generation at SiO₂ particles in an α -brass matrix on plastic deformation. *Surface Science*, 31 (1972), 389–421.
- [98] Hansen N. and B. Bay: Initial stages of recrystallization in aluminium containing both large and small particles. *Acta Metallurgica*, 29 (1981), 65–77.
- [99] Engler O. et al.: Effect of pretreatment and texture on recovery and recrystallisation in Al–4.5Mg–0.7Mn alloy. *Materials Science and Technology*, 10 (1994), 771–782.
- [100] Engler O. and J. Hirsch: Recrystallization Textures and Plastic Anisotropy in Al–Mg–Si Sheet Alloys. *Materials Science Forum*, 217 (1996), 479–486.
- [101] Doherty R. D.: Role of interfaces in kinetics of internal shape changes. *Metal Science*, 16 (1982), 1–14.
- [102] Gladman T.: On the theory of the effect of precipitate particles on grain growth in metals. *Proceedings of the Royal Society of London. Series A. Mathematical and Physical Sciences*, 294 (1966), 298–309.
- [103] Hillert M.: Inhibition of grain growth by second-phase particles. *Acta Metallurgica*, 36 (1988), 3177–3181.
- [104] Ryum N., O. Hunderi and E. Nes: On grain boundary drag from second phase particles. *Scripta Metallurgica*, 17 (1983), 1281–1283.
- [105] Anderson M. P. et al.: Inhibition of grain growth by second phase particles: Three dimensional Monte Carlo computer simulations. *Scripta Metallurgica*, 23 (1989), 753–758.
- [106] Chakrabarti T. and S. Manna: Zener pinning through coherent precipitate: A phase-field study. *Computational Materials Science*, 154 (2018), 84–90.
- [107] Chang K., W. Feng and L.-Q. Chen: Effect of second-phase particle morphology on grain growth kinetics. *Acta Materialia*, 57 (2009), 5229–5236.

-
- [108] Hazzledine P. M. and R. D. J. Oldershaw: Computer simulation of Zener pinning. *Philosophical Magazine A*, 61 (1990), 579–589.
- [109] Kad B. K. and P. M. Hazzledine: Monte Carlo simulations of grain growth and Zener pinning. *Materials Science and Engineering: A*, 238 (1997), 70–77.
- [110] Li Z., J. Wang and H. Huang: Influences of grain/particle interfacial energies on second-phase particle pinning grain coarsening of polycrystalline. *Journal of Alloys and Compounds*, 818 (2020), 152848.
- [111] Li Z., J. Wang and H. Huang: Influences of particle fractions on second-phase particles pinning grain coarsening processes. *Journal of Materials Science*, 55 (2020), 3434–3449.
- [112] Phaneesh K. R. et al.: On the Zener limit of grain growth through 2D Monte Carlo simulation. *Computational Materials Science*, 58 (2012), 188–191.
- [113] Phaneesh K. R. et al.: 3D MC Simulation of Grain Growth Kinetics and the Zener Limit in Polycrystals. *Applied Mechanics and Materials*, 598 (2014), 8–12.
- [114] Srolovitz D. J. et al.: Computer simulation of grain growth-III. Influence of a particle dispersion. *Acta Metallurgica*, 32 (1984), 1429–1438.
- [115] Wang N. et al.: Two modes of grain boundary pinning by coherent precipitates. *Acta Materialia*, 135 (2017), 226–232.
- [116] Zhou J. et al.: Zener pinning by coherent particles: pinning efficiency and particle reorientation mechanisms. *Modelling and Simulation in Materials Science and Engineering*, 25 (2017), 65008.
- [117] Nes E., N. Ryum and O. Hunderi: On the Zener drag. *Acta Metallurgica*, 33 (1985), 11–22.
- [118] Manohar P. A., M. Ferry and T. Chandra: Five Decades of the Zener Equation. *ISIJ International*, 38 (1998), 913–924.
- [119] Fullman R. L.: *Metal interfaces*. American Society for Metals, Metals Park, OH (1952).
- [120] Vetrano J. S. et al.: Influence of the particle size on recrystallization and grain growth in Al-Mg-X alloys. *Materials Science and Engineering: A*, 238 (1997), 101–107.
- [121] Hu R. et al.: Dispersoid Formation and Recrystallization Behavior in an Al-Mg-Si-Mn Alloy. *Journal of Materials Science & Technology*, 26 (2010), 237–243.
- [122] Engler O.: On the Influence of Dispersoids on the Particle Stimulated Nucleation of Recrystallization in an Al-Fe-Si Model Alloy. *International Conference On Textures and Anisotropy of Polycrystals*, Clausthal (1997).
- [123] Engler O. and V. Randle: *Introduction to texture analysis*. CRC Press, Boca Raton (2010).
- [124] Dillamore I. L. and W. T. Roberts: Preferred Orientation In Wrought And Annealed Metals. *Metallurgical Reviews*, 10 (1965), 271–380.
- [125] Hirsch J. and K. Lücke: Overview no. 76: Mechanism of deformation and development of rolling textures in polycrystalline f.c.c. metals—I. Description of rolling texture development in homogeneous CuZn alloys. *Acta Metallurgica*, 36 (1988), 2863–2882.
- [126] Li S. et al.: A Review of Texture Evolution Mechanisms During Deformation by Rolling in Aluminum Alloys. *Journal of Materials Engineering and Performance*, 27 (2018), 3350–3373.
- [127] Mishin O. V. et al.: Recovery and recrystallization in commercial purity aluminum cold rolled to an ultrahigh strain. *Acta Materialia*, 61 (2013), 5354–5364.
- [128] Alvi M. H. et al.: Cube texture in hot-rolled aluminum alloy 1050 (AA1050)—nucleation and growth behavior. *Acta Materialia*, 56 (2008), 3098–3108.
- [129] Maurice C. and J. H. Driver: High temperature plane strain compression of cube oriented aluminium crystals. *Acta Metallurgica et Materialia*, 41 (1993), 1653–1664.

- [130] Weiland H. and J. Hirsch: Microstructure and Local Texture in Hot Rolled Aluminum. *Textures and Microstructures*, 14 (1991), 647–652.
- [131] Bate P. and A. Oscarsson: Deformation banding and texture in hot rolled Al–1.0Mn–1.2Mg alloy. *Materials Science and Technology*, 6 (1990), 520–527.
- [132] Engler O., H. E. Vatne and E. Nes: The roles of oriented nucleation and oriented growth on recrystallization textures in commercial purity aluminium. *Materials Science and Engineering: A*, 205 (1996), 187–198.
- [133] de La Chapelle S.: Cube recrystallization textures in a hot deformed Al–Mg–Si alloy. *Scripta Materialia*, 45 (2001), 1387–1391.
- [134] Dons A. L. and E. Nes: Nucleation of cube texture in aluminium. *Materials Science and Technology*, 2 (1986), 8–18.
- [135] Gatti J. R. and P. P. Bhattacharjee: Nucleation behavior and formation of recrystallization texture in pre-recovery treated heavily cold and warm-rolled Al–2.5wt.%Mg alloy. *Materials Characterization*, 106 (2015), 141–151.
- [136] Kobayashi M., Y. Takayama and H. Kato: Preferential Growth of Cube-Oriented Grains in Partially Annealed and Additionally Rolled Aluminum Foils for Capacitors. *Materials Transactions*, 45 (2004), 3247–3255.
- [137] Kashyap K. T. and R. George: Mechanism of cube grain nucleation during recrystallization of deformed commercial purity aluminium. *Bulletin of Materials Science*, 29 (2006), 197–200.
- [138] Dillamore I. L. and H. Katoh: The Mechanisms of Recrystallization in Cubic Metals with Particular Reference to Their Orientation-Dependence. *Metal Science*, 8 (1974), 73–83.
- [139] Hjelen J., R. Ørsund and E. Nes: On the origin of recrystallization textures in aluminium. *Acta Metallurgica et Materialia*, 39 (1991), 1377–1404.
- [140] Lücke K. and O. Engler: Effects of particles on development of microstructure and texture during rolling and recrystallisation in fcc alloys. *Materials Science and Technology*, 6 (1990), 1113–1130.
- [141] Wagner P., O. Engler and K. Lücke: Formation of Cu-type shear bands and their influence on deformation and texture of rolled f.c.c. $\{112\}\langle 111\rangle$ single crystals. *Acta Metallurgica et Materialia*, 43 (1995), 3799–3812.
- [142] Engler O., J. Hirsch and K. Lücke: Texture Development in Al-1.8 wt% Cu Depending on the Precipitation State - II. Recrystallization Textures. *Acta Metallurgica et Materialia*, 43 (1995), 121–138.
- [143] Bennett T. A., R. H. Petrov and L. A. I. Kestens: Effect of particles on texture banding in an aluminium alloy. *Scripta Materialia*, 62 (2010), 78–81.
- [144] Bennett T. A. et al.: The effect of particle-stimulated nucleation on texture banding in an aluminium alloy. *Scripta Materialia*, 63 (2010), 461–464.
- [145] Yu L. et al.: Influence of Fe-rich particles on microstructure evolution, texture and mechanical properties of Al–Mg–Si–Cu alloys. *Metallurgical Research & Technology*, 117 (2020), 508.
- [146] Vatne H. E., O. Engler and E. Nes: The Effect of Precipitates on Texture Development. *Textures of Materials - ICOTOM 10*, 157-162 (1994), 1501–1506.
- [147] Vatne H. E., O. Engler and E. Nes: Influence of particles on recrystallisation textures and microstructures of aluminium alloy 3103. *Materials Science and Technology*, 13 (1997), 93–102.
- [148] Bennett T. A. et al.: The Effect of Intermediate Annealing on Texture Banding in Aluminum Alloy 6016. *Advanced Engineering Materials*, 12 (2010), 1018–1023.
- [149] Jin H. and D. J. Lloyd: Roping in 6111 aluminum alloys with various iron contents. *Materials Science and Engineering: A*, 403 (2005), 112–119.

- [150] Schäfer C. et al.: Quantification of roping in aluminium sheet alloys for car body applications by combining 3D surface measurements with Fourier analysis. *International Journal of Materials Research*, 106 (2015), 248–257.
- [151] Wu P. D. et al.: Analysis of roping in AA6111 automotive sheet. *Acta Materialia*, 51 (2003), 1945–1957.
- [152] Bennett T. A., R. H. Petrov and L. A. I. Kestens: Texture-induced surface roping in an automotive aluminium sheet. *Scripta Materialia*, 61 (2009), 733–736.
- [153] Bennett T. A., R. H. Petrov and L. A. I. Kestens: Surface Texture Modification for Improved Roping Behaviour of Aluminium Alloy 6016. *Solid State Phenomena*, 160 (2010), 197–202.
- [154] Sidor J. et al.: Controlling the plastic anisotropy in asymmetrically rolled aluminium sheets. *Philosophical Magazine*, 88 (2008), 3779–3792.
- [155] Duan X. et al.: Reduce the Planar Anisotropy of AA6016 Aluminum Sheets by Texture and Microstructure Control. *Crystals*, 10 (2020), 1027.
- [156] Engler O. and M.-Y. Huh: Evolution of the cube texture in high purity aluminum capacitor foils by continuous recrystallization and subsequent grain growth. *Materials Science and Engineering: A* (1999), 371–381.

3 APPROACH

The subsequent chapters of the present thesis are based on the results of the research conducted by the author, which were published before in peer-reviewed journals. The structure of the following sections hence follows the original journal articles. The aim of this thesis was the investigation of microstructure and texture evolution in 5xxx and 6xxx Al sheets. Whereas Chapter 4 gives a general overview and comparison of texture and microstructure evolution during industrial and laboratory scale processing of AlMg(Mn) and AlMgSi sheets, the Chapters 5 and 6 represent a two-part study on the effects of Fe and Mn on texture and microstructure in the 5xxx alloys. A detailed description of the intentions underlying the experimental work in the present research studies is given in the following passages.

The increasing demands in formability and strength of Al alloys as well as specific texture effects like roping require sophisticated texture and microstructure engineering as was addressed in the Chapters 1 and 2 [1–3]. However, although both are already topic of research over decades now, the strive for further optimization is still high. As the consequential design of novel aluminum alloys or the modification of processing parameters is often realized in laboratory facilities on smaller production scales, the comparability of the resulting microstructures and textures to the later industry samples is crucial. Therefore, Chapter 4 — Texture and Microstructure Evolution in Laboratory- and Industrial-scaled Aluminum Sheet Processing — comprises an extensive study on the occurring differences in the laboratory- and industrial-scaled processing of 5xxx and 6xxx Al sheets.

Another important aspect is the formation and impact of additional phases in the aluminum matrix on the microstructure and texture as the previous chapters highlighted the effects of PSN and Zener pinning, but also mentioned the often detrimental or beneficial impacts of the particles on the resulting mechanical properties. In combination with the increasing fraction of recycling material for Al alloys and the often concomitant rising level of impurity elements as for example Fe, the two-part study presented in the Chapters 5 and 6 focused on the impact of four different combinations of Fe and Mn on the resulting microstructures and textures in AlMg(Mn) alloys.

The in Chapter 5 presented Part I — Primary and Secondary Phase Evolution in Fe and Mn Containing 5xxx Al Sheets — followed the ideas of the beneficial impacts of Mn on the morphology of Fe bearing primary phases and the dispersoid formation in 5xxx alloys [4]. As it was shown in earlier studies, various processing parameters like the casting cooling rate [5] and homogenization time/temperature [6] can affect the equilibrium phase formation and therefore further alter the resulting phase structures. The experimental approach followed thermodynamic calculations of the alloying systems using the Pandat software. A comprehensive investigation of various processing

parameters on the formation, modification, and evolution of Fe, Mn, and Si containing primary and secondary phases within 5xxx aluminum sheet processing was included.

The subsequent Part II — Grain Size and Texture Evolution in Fe and Mn containing 5xxx Al Sheets — comprises the detailed analysis of the microstructure and texture of the alloys. Based on the variable fractions of (coarser) primary and finely dispersed secondary particles the focus was turned on the effects of PSN and Zener pinning. While the mechanism and amount of PSN were investigated in terms of occurring texture randomizations in the alloys as described in [7], an extensive study on the Zener pinning effects was carried out with the ultimate goal to obtain the true values of the parameters K and m in equation 2.1 [8]. Therefore, comprehensive experimental characterization, involving light optical microscopy, scanning electron microscopy as well as electron backscatter diffraction, was performed to derive the necessary data on grain size, phase fraction, and the texture of the final Al sheets.

References

- [1] Engler O. and J. Hirsch: Control of recrystallisation texture and texture-related properties in industrial production of aluminium sheet. *Int. J. Mat. Res.*, 100 (2009), 564–575.
- [2] Hirsch J.: Recent development in aluminium for automotive applications. *Transactions of Nonferrous Metals Society of China*, 24 (2014), 1995–2002.
- [3] Hirsch J. and T. Al-Samman: Superior light metals by texture engineering: Optimized aluminum and magnesium alloys for automotive applications. *Acta Materialia*, 61 (2013), 818–843.
- [4] Liu Y. et al.: Effect of Mn and Fe on the Formation of Fe- and Mn-Rich Intermetallics in Al-5Mg-Mn Alloys Solidified Under Near-Rapid Cooling. *Materials (Basel, Switzerland)*, 9 (2016), 88.
- [5] Liu Y. et al.: Effect of Fe, Si and Cooling Rate on the Formation of Fe- and Mn-rich Intermetallics in Al-5Mg-0.8Mn Alloy. *Journal of Materials Science & Technology*, 32 (2016), 305–312.
- [6] Engler O., K. Kuhnke and J. Hasenlever: Development of intermetallic particles during solidification and homogenization of two AA 5xxx series Al-Mg alloys with different Mg contents. *Journal of Alloys and Compounds*, 728 (2017), 669–681.
- [7] Engler O. et al.: Effect of pretreatment and texture on recovery and recrystallisation in Al-4.5Mg-0.7Mn alloy. *Materials Science and Technology*, 10 (1994), 771–782.
- [8] Manohar P. A., M. Ferry and T. Chandra: Five Decades of the Zener Equation. *ISIJ International*, 38 (1998), 913–924.

4 TEXTURE AND MICROSTRUCTURE EVOLUTION IN LABORATORY- AND INDUSTRIAL-SCALED ALUMINUM SHEET PROCESSING

The following chapter compares the microstructure and texture evolution of EN AW-5182 and EN AW-6016 on laboratory- and industrial-scaled sheet processing. The study addressed the potentially occurring differences on various processing scales and the importance of sophisticated laboratory process design. It will be shown that the obtained microstructural features are similar for the different processing scales for both investigated alloys. Whereas the strength of specific texture components and the grain size and fragmentation differ for the laboratory and industrial scale especially after rolling, the final soft- and solution annealed microstructures and textures indicate high accordance. Therefore, the established laboratory sheet processing has been approved for further microstructure and texture analyses.

Evolution of Microstructure and Texture in Laboratory- and Industrial-scaled Production of Automotive Al-Sheets*

With the rising importance of aluminium sheets for automotive applications, the influence of microstructure and texture on mechanical properties and on forming behavior has gained re-increased interest in recent years. This paper provides an introduction to the topic and demonstrates the evolution of microstructure and texture in the standard alloys EN AW-5182 and EN AW-6016 for different processing scales. Moreover, strategies for texture and microstructure characterization of automotive Al-sheets are discussed. As the development of alloys or processes usually starts in laboratory facilities, the transferability to the industrial scale of the results thereof is studied. A detailed analysis of the entire processing chain shows good conformity of careful laboratory production with the industrial production concerning microstructure as well as qualitative and quantitative texture evolution for EN AW-5182. While comparable grain sizes can be achieved in final annealed sheets of EN AW-6016, quantitative discrepancies in texture occur between the different production scales for some sample states. The results are discussed in light of the basics of plasticity and recrystallisation including the effect of solutes, primary phases, and secondary phases in the alloys.

4.1 Introduction

In recent decades, the use of aluminium components has increased, particularly in the automotive industry, as the associated weight reduction leads to a reduction in CO₂ emissions and can further promote the use of electromobility. In order to meet the increasing demands on safety standards and mechanical properties, a deep understanding of the mechanisms underlying the various application-relevant properties is required [1–4]. Alloys for automotive body applications often belong to one of the two aluminum classes, 5xxx (AlMg(Mn)) or 6xxx (AlMgSi). The Mg and Mn containing 5xxx Al-alloys fall into the category of non-age-hardenable Al-alloys and show good formability, high strength, corrosion resistance, and weldability. The mechanical properties are controlled by the Mg content and the degree of cold forming. Owing to age-hardenability of 6xxx Al-alloys, controlled thermo-mechanical processing is crucial in these alloys. The various possible strength levels, together with high fracture toughness and good corrosion resistance, open a wide field of applications [3]. Over the last decades, the influence of crystal orientation on the mechanical properties and on the forming

* Published in *Materials* 13 (2020), 469 written by Jakob Grasserbauer, Irmgard Weißensteiner, Georg Falkinger, Stefan Mitsche, Peter J. Uggowitzer and Stefan Pogatscher.

Author contributions:

JG: Conceptualization, methodology, validation, investigation, original draft, visualization.

ability of the Al-components has been intensively investigated and has recently gained eminent interest with the rising importance of Al-sheet materials for automotive applications [5–7].

As far as the orientation distribution of the grains within forming operations is concerned, the texture of a material describes the entirety of the crystallographic orientations. However, textured materials are commonly understood to exhibit intensified orientations that are characteristic of the strain conditions of previous forming operations. The progress in measurement techniques over the last decades provides a variety of possible methods for texture characterization. In general, the most prominent techniques are X-ray diffraction (XRD) and electron backscattered diffraction (EBSD), both having beneficial aspects. X-ray diffraction texture measurements show improved statistics when compared with those of EBSD, because of larger sampled areas. However, with the lack of microstructural information in the X-ray measurements (only macrotexture measurements are possible), EBSD is superior in terms of achieving meaningful results concerning microstructure and texture simultaneously (microtexture). In any case, the usage of these techniques provides reliable information concerning texture analysis and the suitability of XRD or EBSD depends at least on the sample processing conditions and the information sought [8].

Owing to the face-centered cubic crystal structure of Al, typical deformation structures occur in the rolling process. The basic deformation mechanism of dislocation slip, which is also relevant in other crystal structures, occurs on twelve independent $\{111\}\langle 110\rangle$ slip systems and generally results in structural features of different dimensions, namely, cells or subgrains, deformation bands, and shear bands [9–11]. In addition to these structures, the influence of alloying elements and their interaction with precipitation is crucial. The automotive alloys EN AW-5182 and EN AW-6016 examined in this study exhibit some typical characteristics, the detailed discussion of which we consider to be essential.

The investigation of the microstructure and texture of Al-sheets first requires a very precise description of the parameters regarding the position within the sheet thickness. The different strain conditions within the sheet result in a variety of microstructural features. The resulting texture components can be completely different, which also affects the final sheet properties. While high-strained near-surface layers often show distinct shear components, the microstructure in the center of a sheet often suffers more typical plane-strain conditions [12, 13]. A stronger formation of substructure and thus more stored energy will be found closer to the surface of the sheets. Another feature typical for highly strained areas is a 25° – 40° inclining of the subgrain dislocation networks and band-like structures to the rolling direction (RD) [14].

The complex interactions of all these phenomena can lead to a large diversity of annealed sheet grain structures. As far as EN AW-5182 is concerned, the chemical composition facilitates the formation of shear bands owing to the slightly reduced stacking fault energy and the enhanced solute drag. In addition, Mn-containing dispersoids limit grain growth. For EN AW-6016, the systematic control of second-phase particles is crucial as the age-hardening phases can readily form in earlier stages of the

processing route and affect the microstructure of the final sheet. These basic mechanisms form the backbone for understanding microstructure development in such alloys [6, 15].

Intense research in the field of texture and the related properties of Al-sheets lead to a common understanding of the typical mechanisms for rolling- and recrystallization-texture evolution [16–19]. Typical cold-rolling processes for standard fcc-alloys form components such as Brass, Copper, and S (see also **Fig. 4.1**), also referred to as β -fiber [20, 21]. These stable orientations are prominent for the active octahedral slip systems at cold-rolling temperatures; however, hot-rolling conditions including elevated temperatures above 320 °C tend to activate non-octahedral slip. Publications on this topic show in this case the stabilization of Brass, but also Cube orientation $\{001\}\langle 100\rangle$ [22].

Typical recrystallization textures in Al are dominated by the Cube component, which arises from Cube nuclei in the deformation zones [23–28]. Earlier theories of texture evolution stated the controversy between oriented nucleation and oriented growth. Concerning Cube grains, one can find coincidences of both theories, as they nucleate from preserved Cube bands and show favorable growth conditions in to typical deformation texture components [29–32]. Major influences on Cube texture are given by the degree of cold-rolling and annealing temperatures as well as solute elements [33]. However, especially in EN AW-5182, the Mg in solid solution can readily reduce the dominance of the cube texture by influencing the dislocation cell formation, especially at lower strains [5, 34].

In EN AW-6016, second phase particles show potential to modify occurring textures by various mechanisms. In general, the influence of particles on the final texture can be divided into two main mechanisms. Small, closely spaced particles with sizes below 500 nm are able to increase the Smith–Zener pinning on grain boundaries, and thus delay recrystallization [35]. Depending on the time of particle formation during processing, the resulting texture may have an enhanced or retained Cube component [36, 37]. Additionally, existing particles with a size $>1\ \mu\text{m}$ act as favorable nucleation sites. The mechanism of particle stimulated nucleation (PSN) is based on heavier deformation substructures in the vicinity of these particles, which provide higher driving force for recrystallization. Investigations indicate the formation of rather random texture components or at least a reduction of the predominant Cube orientation in the vicinity of these particles [38–40].

Exemplary textures of annealed EN AW-5182 and EN AW-6016 are shown in **Fig. 4.1**. While **Fig. 4.1 (b)** indicates typical recrystallization texture dominated by the Cube component for the EN AW-6016; the orientation distribution for the EN AW-5182 appears more random and weaker.

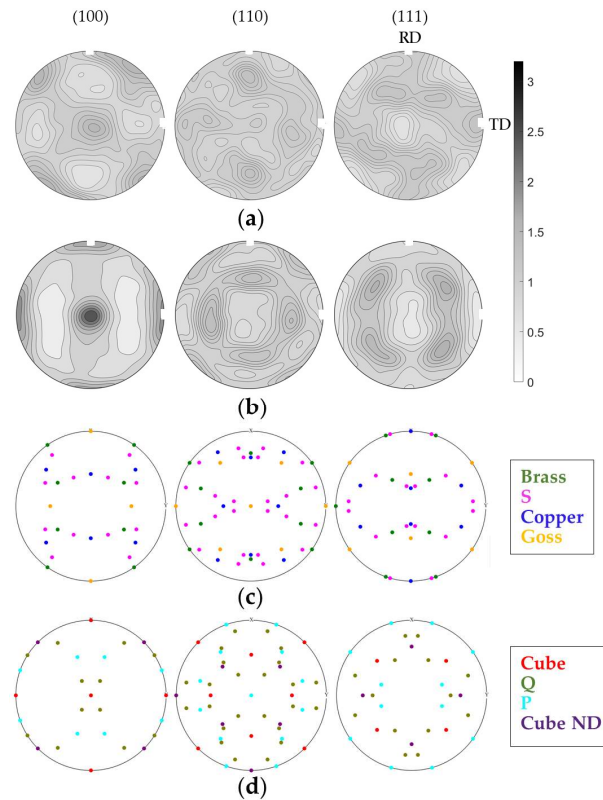


Fig. 4.1. Typical textures of annealed (a) EN AW-5182 and (b) EN AW-6016; ideal orientations of main (c) rolling texture components and (d) recrystallization texture components. RD, rolling direction; TD, transverse direction; ND, normal direction.

As new alloys or process changes are often only implemented in laboratory facilities, the further development of aluminum alloys is very often based on small series production. However, difficulties can arise in the transferability of the results to industrial scale, and the comparability of laboratory and industrial products must always be guaranteed. The first difficulties in the casting process can already be observed in the typical processing of wrought aluminum alloys.

In particular, the Al-series AlMg(Mn) (5xxx) and AlMgSi (6xxx) both require precise knowledge of the parameters in casting, as micro- and macro-segregations have to be controlled. As the distribution of the alloying elements as primary phases or dissolved elements can have a significant influence on the subsequent deformation process, controlled cooling conditions upon casting are indispensable [41]. In the case of age-hardenable Al-alloys, a homogenization treatment should generally be carried out to homogeneously distribute the hardening phase-forming elements and counteract segregations [15, 42–44]. In addition, the rolling geometries can influence the overall texture and microstructure development. The most important factors in this case are the diameter and friction of the rolls. As these two parameters differ for laboratory and industrial rolling mills, the final textures may show a significant inconsistency [9].

In this study, we evaluate the microstructure and texture evolution in the two Al-alloys EN AW-5182 and EN AW-6016 on different processing scales. Particular attention is paid to individual processing steps and the underlying changes in microstructure and texture in laboratory scale. The results will

be discussed in the light of well-established theories and will demonstrate the need for careful consideration of the differences between laboratory and industrially produced Al-sheets.

4.2 Materials and Methods

The alloys EN AW-5182 and EN AW-6016 were studied. The chemical composition is given in

Tab. 4.1.

Tab. 4.1. Chemical composition of the studied alloys EN AW-5182 and EN AW-6016 (in wt %).

Alloy	Mg	Mn	Fe	Si	Al
EN AW-5182	4.83	0.41	0.16	0.09	Bal.
EN AW-6016	0.35	0.07	0.19	1.14	Bal.

Sample production is based on a conventional production process of 5xxx and 6xxx alloys, as shown schematically in **Fig. 4.2** [45, 46]. The usual industrial processing parameters [4, 15] were used for the industrially scaled path, the aluminum sheets produced by Austria Metall AG (AMAG) rolling GmbH. For the laboratory production route, the complete processing of both alloys – consisting of alloy production, casting, rolling and annealing – was carried out in the small laboratory facilities described below (see also the work of [47] for further details).

Casting: The ingot material for both alloys was provided by AMAG rolling GmbH company, Ranshofen, Austria. Initially, the ingot material was remelted in a resistance-heated furnace (Nabertherm K20/13/S, Lilienthal, Germany), degassed using an impeller with Ar gas, and finally casted into laboratory-scaled molds [45]. After milling to block sizes of $80 \times 80 \times 40 \text{ mm}^3$, samples of EN AW-6016 were homogenized in an air-circulated furnace for 10 h at $565 \text{ }^\circ\text{C}$ with subsequent air cooling, while EN AW-5182 remained untreated.

Rolling: For the laboratory scaled rolling process, a small-scale laboratory rolling mill with roll diameter of 250 mm was used. Both alloys were hot-rolled and cold-rolled (HR and CR), including an intermediate soft annealing (IA) heat treatment at $370 \text{ }^\circ\text{C}$ in between the cold-rolling passes. Maximum reductions per pass were 2 mm for hot-rolling and 1 mm for cold-rolling. From the initial thickness of 40 mm, the EN AW-5182 was hot-rolled to a thickness of about 2.5 mm, and subsequently cold-rolled to 1.5 mm before intermediate annealing. EN AW-6016 was hot-rolled to 7.3 mm, cold-rolled to 3.1 mm, and intermediate annealed. For the IA heat treatment, an air-circulated furnace (Nabertherm N60/85SHA, Lilienthal, Germany) was used. Relatively low heating and cooling rates are intended to mimic large scale processing of coils in a batch furnace. The final sheet thickness was specified to be 1.20 mm and 1.25 mm for the 5182 and 6016 alloys, respectively. The dimensions were achievable within a tolerance of 0.03 mm in thickness.

Heat treatment: The final heat treatments, meaning soft annealing (SA) for EN AW-5182 and solution annealing (also SA) for EN AW-6016, were performed in a salt bath for 5 min at

temperatures of 500 °C and 530 °C, respectively, to mimic an industrial continuous heat treatment line. Subsequently, the samples were water quenched.

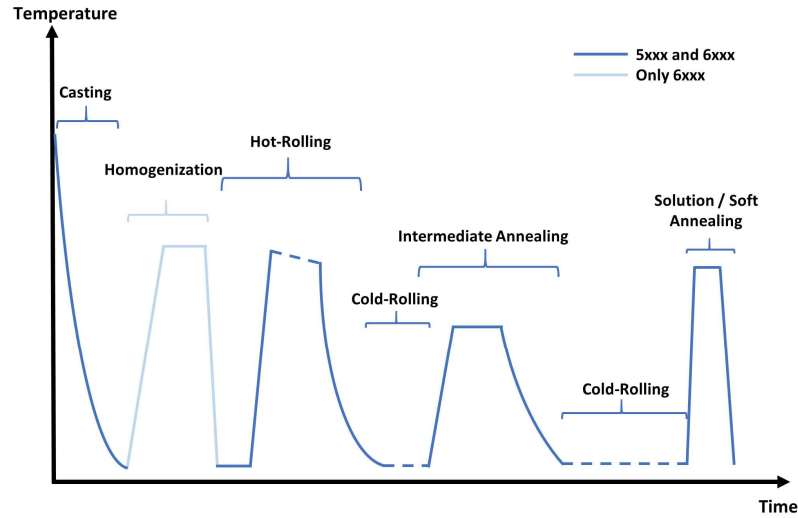


Fig. 4.2. Schematically illustrated process route for EN AW-5182 (no homogenization) and EN AW-6016.

As the aim of this work was to acquire a sound knowledge of texture and microstructure evolution, samples were examined at different stages of the production process. In addition to the information given in **Fig. 4.2**, cast and homogenized microstructures were prepared by means of metallographic methods, but only briefly investigated for the quality of the casting and homogenization process.

The material of the designated processing steps was further processed by means of standard metallographic preparation in two sample orientations: (1) the cross-section spanned between rolling direction (RD) and normal direction (ND); (2) position at $s = 0.5$ (equation 4.1) as metallographic samples in the sheet plane comprising the RD and transverse direction (TD) where D_t represents the distance from center and t_0 represents the initial thickness [15].

$$s = \frac{2D_t}{t_0} \quad (\text{Equ. 4.1})$$

The sample preparation included cutting, embedding, grinding, and polishing, as well as polishing with an oxide polishing suspension (OPS, Struers) at relatively high contact forces of up to 50 N for at least 18 s. In addition to the OPS-polishing reactant, unperfumed liquid soap was used to improve lubrication during preparation.

Measurements of both alloys required further treatment for sufficient surface quality. For EBSD, electropolishing (EP) was performed on a Struers Lectro-Pol 5 electropolishing unit with electrolyte A2 (provided by Struers) for 4–8 s at 36 V and 10 °C.

Microstructure and texture were investigated using scanning electron microscope (SEM) (JEOL 7200F FEG-SEM, Tokyo, Japan) equipped with an EBSD-measurement system (Nordlys Nano detector, Oxford Instruments, Abingdon, UK). For qualitative analysis, backscattered electron (BSE) images of the prepared sections were also collected. The EBSD-measurements were done using a 70°

pre-tilt specimen holder and accelerating voltage of 20 kV. Acquisition and analysis of the diffraction patterns required a large variation in parameters, as deformed and annealed sample states were measured.

4.2.1 EBSD Data Processing

The post processing and evaluation of EBSD data were done by means of the Matlab based toolbox MTEX 5.2.beta3 [48].

Grain size analysis: The linear intercept length (LIL) is calculated for the data from EBSD measurements. For the grain reconstruction, a tolerance angle of 5° was chosen and larger areas of connected, not-indexed pixels (e.g. primary phases) were excluded from the dataset. The rest of the EBSD data were smoothed by applying a half-quadratic filter [49].

Texture Analysis: The raw data were rotated manually and centered by means of stereographic projections of the discrete orientations. For a sound representation of a materials' texture, the orientation information of a minimum number of 1000 [50, 51] to 3000 spatially independent grains [52, 53] is required. In the present study, at least 3000 grains were analyzed for all sample conditions of EN AW-5182. For EN AW-6016, the analysis was more challenging. The large grain size of the as-cast condition leads to large, similarly oriented areas after hot-rolling and even after the first cold-rolling cycles. However, at least 7.5 mm^2 of the hot-rolled and at least 1.5 mm^2 of the cold-rolled material were analyzed by EBSD with step sizes depending on the amount of stored deformation. Note that XRD measurements of the hot-rolled material did not lead to better results, although a beam of 1 cm^2 was applied to measure samples of $23 \times 23 \text{ mm}^2$.

To quantify changes in texture and to compare it to the XRD data, orientation distribution functions (ODF) were calculated from the EBSD data in the mtext toolbox. The ODF best represents the entirety of discrete orientations when combining the calculation via a direct kernel density estimation and the kernel density estimation via Fourier series. The semi-automatic half width selection algorithm was applied on discrete orientations as well as on the mean orientation (weighted by area) from "orientation clusters", which are grains defined by a misorientation threshold of 2° . The half widths for the kernel density estimation were confined between 6° and 10° for the individual orientations (the resulting ODF is shown in **Fig. 4.3 (a)**) and between 6° and 11.5° for the orientation clusters (ODF in **Fig. 4.3 (b)**). The ODFs calculated via both methods (without any symmetrization) were finally averaged (**Fig. 4.3 (c)**), which, in the present study, reduces the under-smoothing of the data and still conserves the maxima of the data sets. This procedure also leads to the lowest deviation of the volume fractions of ideal orientations derived from the ODF to the volume fractions directly extracted from the EBSD data (**Fig. 4.3 (d)**).

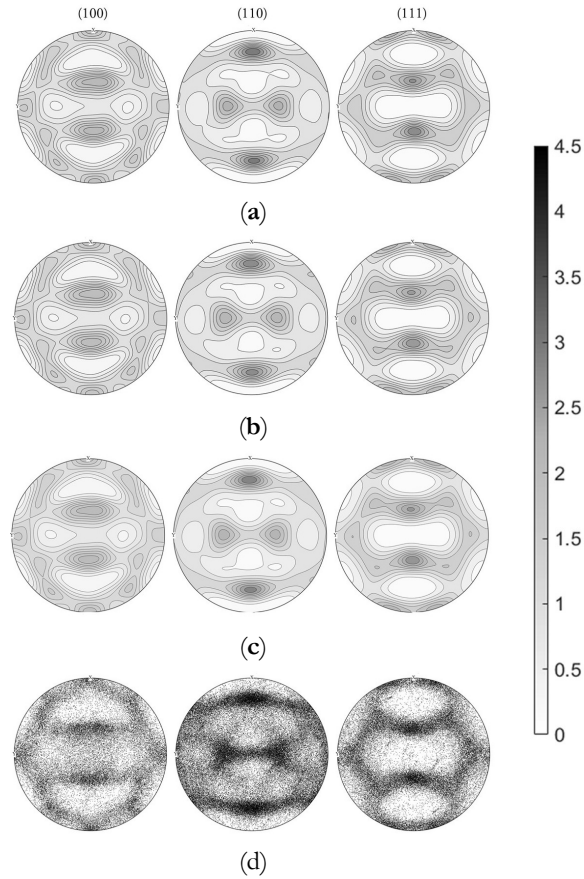


Fig. 4.3. (a) Orientation distribution function (ODF) calculated from orientation clusters; (b) ODF calculated from individual orientations; (c) the final averaged ODF compared to (d) the stereographic projections of the individual orientations.

Statistical methods to correctly determine the accuracy of the ODF calculated from measured pole figures were shown in the work of [54], and error estimations on ODFs calculated from individual orientations are presented in the works of [53] or [55]. The works of [54] and [53] have in common an artificial variation of the input data and a subsequent comparison of the mean of the input data to estimate the relative uncertainty. As the EBSD data in the present study have a high number of random orientations that cannot be assigned to ideal orientations, we did not perturbate simulated textures to compare the outcome of the ODF but compared the evaluated volume fractions with the directly evaluated ones from EBSD data of very large datasets. Then, 3000 ODF calculations on parts of the dataset (50000 individual orientations and 2500 mean orientations of areas with max. 2° misorientation) were performed to evaluate the standard deviation between these ODFs and the ODF calculated from the whole dataset. The maximum standard deviation of the intensity was 7×10^{-7} , which proves a reliable representation of the individual orientations by means of the ODF. The standard deviation correlates with the intensity; however, the relative error is highest in areas with low intensity.

The texture of the material was quantified by evaluating the respective volume fractions of the ideal components (orientations listed in **Tab. 4.2**) for including the symmetric equivalents) from the ODF. Therefore, the tolerance angle of the ideal orientations was chosen as 10° , which comprises

orientations with a certain angular spread on the one hand and almost completely avoids overlapping between the ideal components on the other hand, as the minimum angle between them is 19.38°.

Tab. 4.2. Ideal orientations of analyzed texture components and corresponding Euler angles (Bunge convention) [8].

Component		Phi1	Phi	Phi2
Cube	{001}<100>	0	0	0
Cub _{ND-45}	{001}<110>	45	0	0
Goss	{011}<100>	0	45	0
Copper	{112}<111>	180	21.8	0
		289.5	45	0
S	{123}<634>	121	36.7	26.6
		302.3	18.4	0
		301	36.7	26.6
		122.3	18.4	0
Brass	{011}<211>	35.3	45	0
		90	144.7	225
Q	{013}<231>	239	143.3	206.6
		237.7	161.6	180
		59	143.3	206.6
		57.7	161.6	180
P	{011}<122>	90	35.3	45
		0	21.8	360

4.3 Results

The following sections present the evolution of microstructure and texture in 5182 and 6016 Al-alloys on the different processing scales. The microstructural evolution is discussed based on micrographs as well as on grain size analyses. The change of texture during processing is presented in the form of pole figures based on ODF calculations and volume fractions of ideal texture components extracted from these ODFs.

4.3.1 Microstructure and Grain Parameters

4.3.1.1 Microstructure Evolution of EN AW-5182

The micrographs in **Fig. 4.4 (a)–(f)** show the microstructure of laboratory produced alloy 5182 for the three different process steps: hot-rolling, cold-rolling (after IA), and soft annealing. For better recognition of all structural details, both backscattered electron (BSE) images and band-contrast (BC) images are shown.

First of all, the upcoming aspects of deformation in the hot-rolled state can be recognized in **Fig. 4.4 (a),(b)**. In the laboratory process, the material was hot-rolled to 2.5 mm from an initial thickness of

40 mm. The corresponding microstructure shows slightly elongated grains in the rolling direction, an increasing dislocation network at the grain boundaries (red arrow **Fig. 4.4 (b)**) with typical inclining of cell-band boundaries (slip bands) to RD (green arrow **Fig. 4.4 (b)**), as well as a linear alignment of fragmented primary phases and secondary phases (blue arrow in **Fig. 4.4 (a)**; secondary phases are hardly visible at this magnification). Black areas result from a preferential dissolution during preparation, which does not affect the quality of the statements. The BC image given in **Fig. 4.4 (b)** indicates some grain boundaries, which enables first estimations of the grain sizes in the process states.

Fig. 4.4 (c),(d) show the microstructure after the final cold-rolling pass (according to CR after IA). The cold-rolling degree of 20% with a final sheet-thickness of 1.20 mm leads to a typical rolling structure, which, in this special case, appears somewhat comparable to the hot-rolling microstructure. On closer look, it reveals a more pronounced subgrain formation and a tendency for reduced grain size in the CR state. Again, the band-contrast images give a good overview of the grade of deformation and the associated grain size, although shadowing of primary phases occurs.

Fig. 4.4 (e),(f) show the soft annealed microstructure of the laboratory sheet. Owing to the orientation contrast and the absence of subgrain structures, the different grains are clearly recognizable already in the BSE image. It is striking that a relatively coarse-grained microstructure appears in the final state, even though some grains still show an elongation in the rolling direction, and thus have no balanced aspect ratio. The BC image also reveals preferential attack of specific grain orientations by electrolyte during EP.

The comparison of the BSE and BC images highlights the importance of the usage of EBSD for microstructural investigations, especially in the deformed states.

Additional Energy-dispersive X-ray spectroscopy (EDS) analysis of particles identified the formation of (primary-)Al-(Fe,Mn) constituents and small (secondary-) particles — dispersoids with higher Fe and Mn concentrations compared with the matrix. During processing, the primary phase particles align to the rolling direction and easily fragment owing to the stress conditions during rolling. A more detailed analysis of dispersoids composition is not concerned in this study.

More information on the microstructure is given by the grain linear intercept length illustrated in **Tab. 4.3**, deduced from large area EBSD mappings. In order to allow an initial comparison, the parameters for the industrially processed Al-sheets are added.

Tab. 4.3 compares the linear intercept lengths of the industrially and laboratory produced sheets of EN AW-5182. Particularly noticeable are the differences in the mean linear intercept length in the individual process steps. Especially, the results after the individual cold-rolling steps open a discussion about the deformation energies introduced in industry and laboratory production, as the linear intercept length for the lab-scale products shows a significant increase compared with the industrial

material. In addition to the large differences in LIL after the cold-rolling stages, however, a common tendency to form a very similar grain size after the annealing stages can be observed.

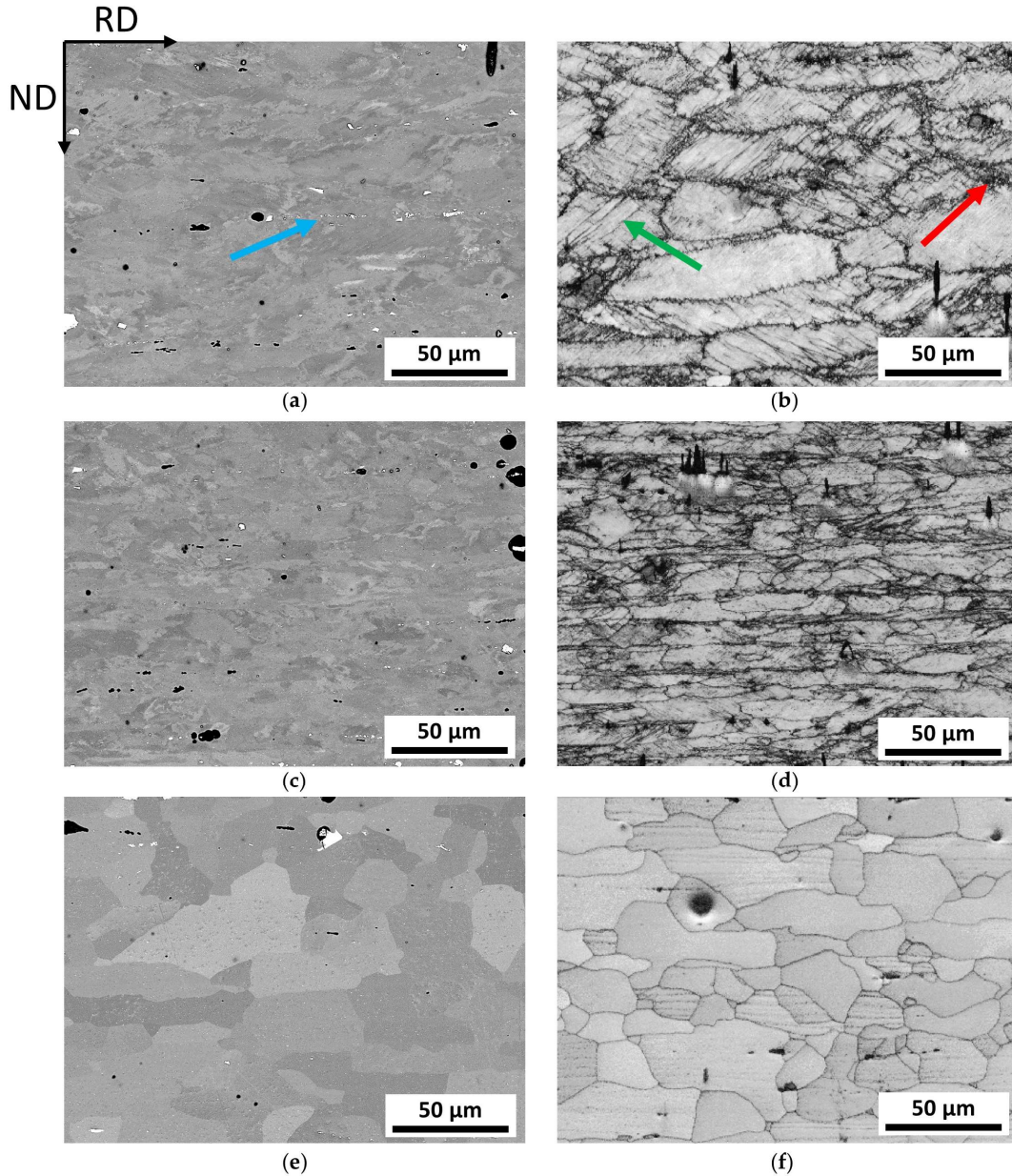


Fig. 4.4. Microstructure evolution of the laboratory processed EN AW-5182 plotted in the TD-plane; (a), (c), and (e) show (a) backscattered electron (BSE) images of the hot-rolled, (c) cold-rolled (after IA), and (e) soft annealed state, respectively; (b), (d), and (f) show (b) band contrast maps of the hot-rolled, (d) cold-rolled (after intermediate annealing (IA)), and (f) soft annealed state, respectively.

Tab. 4.3. Microstructural parameter for laboratory and industrially produced EN AW-5182 sheets.

Scale of Production	Direction	HR	CR1	IA	CR2	SA
Laboratory	$l_{RD}/\mu\text{m}$	14 ± 11	22 ± 24	13 ± 9	17 ± 11	22 ± 13
Industry	$l_{RD}/\mu\text{m}$	18 ± 12	12 ± 7	10 ± 4	10 ± 6	20 ± 11

HR: hot-rolling; CR1: cold-rolling before intermediate annealing; IA: intermediate annealing; CR2: cold-rolling after intermediate annealing; SA: soft annealing; $l_{RD}/\mu\text{m}$: linear intercept length in rolling direction.

4.3.1.2 Microstructure Evolution of EN AW-6016

The micrographs in **Fig. 4.5 (a)–(f)** display the results for EN AW-6016. For the hot-rolled condition (**Fig. 4.5 (a),(b)**), one pronounced aspect is the extremely large grain size. With grains potentially exceeding the image- and scan-size limits, the assessment of texture and microstructural evolution is affected by larger errors in this processing state. The orientation contrast in the BSE images shows less and heavier deformed subgrain structures within the grains. Preferential attack of electrolyte in EP and shadowing by primary phases again is recognizable in the BC images.

The cold-rolled microstructure in **Fig. 4.5 (c),(d)** shows noticeable subgrain development and heavily deformed microstructure. Moreover, a band-like deformation structure with directional alignment to RD of the sub-cells is observable. A comparison to EN AW-5182 in **Fig. 4.5 (c),(d)** indicates stronger deformation structures within the grains of EN AW-6016, which is because of the higher cold-rolling degree for EN AW-6016.

In the solution annealed EN AW-6016, BSE and BC images show good accordance regarding the qualitative microstructure and occurring features. Overall, the microstructure shows polygonal, almost equiaxed grains with only a slight remaining stretch in RD.

A comparison of the LIL deduced from large area EBSD mappings for laboratory and industrial products is given in **Tab. 4.4**. As mentioned above, the hot-rolled images in **Fig. 4.5** indicate grains far in excess of the scanned range, meaning that the LIL values for hot-rolled conditions should not be taken into account. Nevertheless, as the grain sizes greatly exceed the expectations on both scales, these results should not be connected to differences in lab- and industry-processing. Starting from IA, the data exhibit better accordance. The following cold-rolling steps suggest differences in the underlying deformation states for laboratory and industry, as the disagreement in LIL is more pronounced. Concerning the linear intercept length in the recrystallized sample states IA and SA, both show a much better accordance. Particularly, the final solution annealed samples exhibit comparable LIL.

Tab. 4.4. Microstructural parameter for laboratory and industrially produced EN AW-6016 sheets.

Scale of Production	Direction	HR	CR1	IA	CR2	SA
Laboratory	$l_{RD}/\mu\text{m}$	$68 \pm 147^*$	$27 \pm 45^*$	22 ± 25	14 ± 18	22 ± 15
Industry	$l_{RD}/\mu\text{m}$	$73 \pm 112^*$	$16 \pm 22^*$	37 ± 34	13 ± 11	19 ± 10

*The large error results from a low number of analyzed grains, partially exceeding scan size in the EBSD measurements. HR: hot-rolling; CR1: cold-rolling before intermediate annealing; IA: intermediate annealing; CR2: cold-rolling after intermediate annealing; SA: soft annealing; $l_{RD}/\mu\text{m}$: linear intercept length in rolling direction.

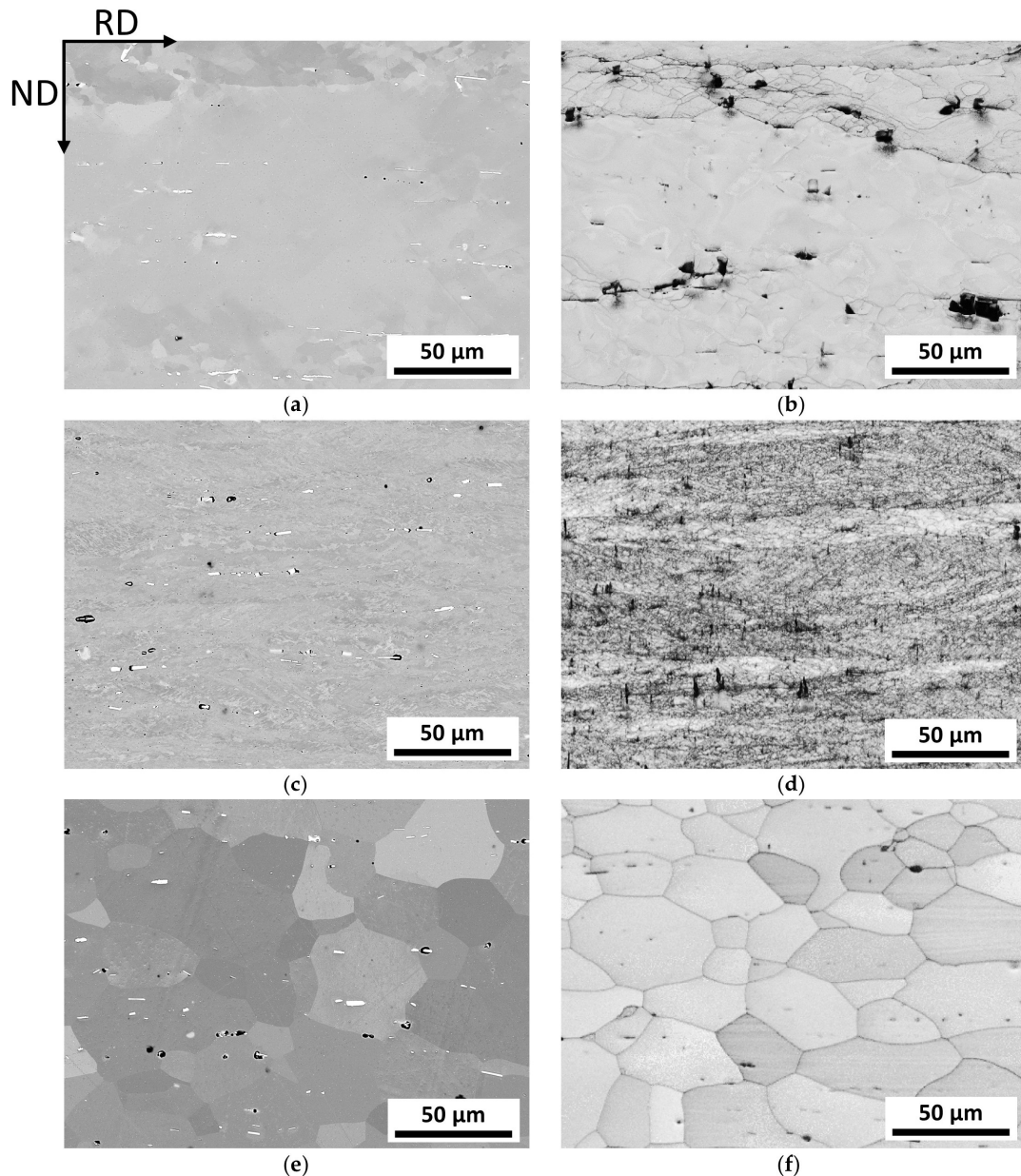


Fig. 4.5. Microstructure evolution of the laboratory processed EN AW-6016 plotted in the TD-plane; (a), (c), and (e) show BSE-images of the (a) hot-rolled, (c) cold-rolled (after IA), and (e) soft annealed state, respectively; (b), (d), and (f) show band contrast maps of the (b) hot-rolled, (d) cold-rolled (after IA), and (f) solution annealed state, respectively.

4.3.2 Texture Analysis

4.3.2.1 Texture Evolution in EN AW-5182

A description of the results regarding the orientation distribution during the process steps in the alloy EN AW-5182 is made based on the illustrations shown in **Fig. 4.6**. First, in **Fig. 4.6** (a)–(f), pole figures calculated from ODF data are shown for the processing states HR, CR2, and SA (laboratory: **Fig. 4.6** (a),(c),(e); industry: **Fig. 4.6** (b),(d),(f)). A more comprehensive quantification of the texture evolution for specific components is shown in **Fig. 4.6** (g)–(j), where the diagrams depict either rolling or recrystallization texture components.

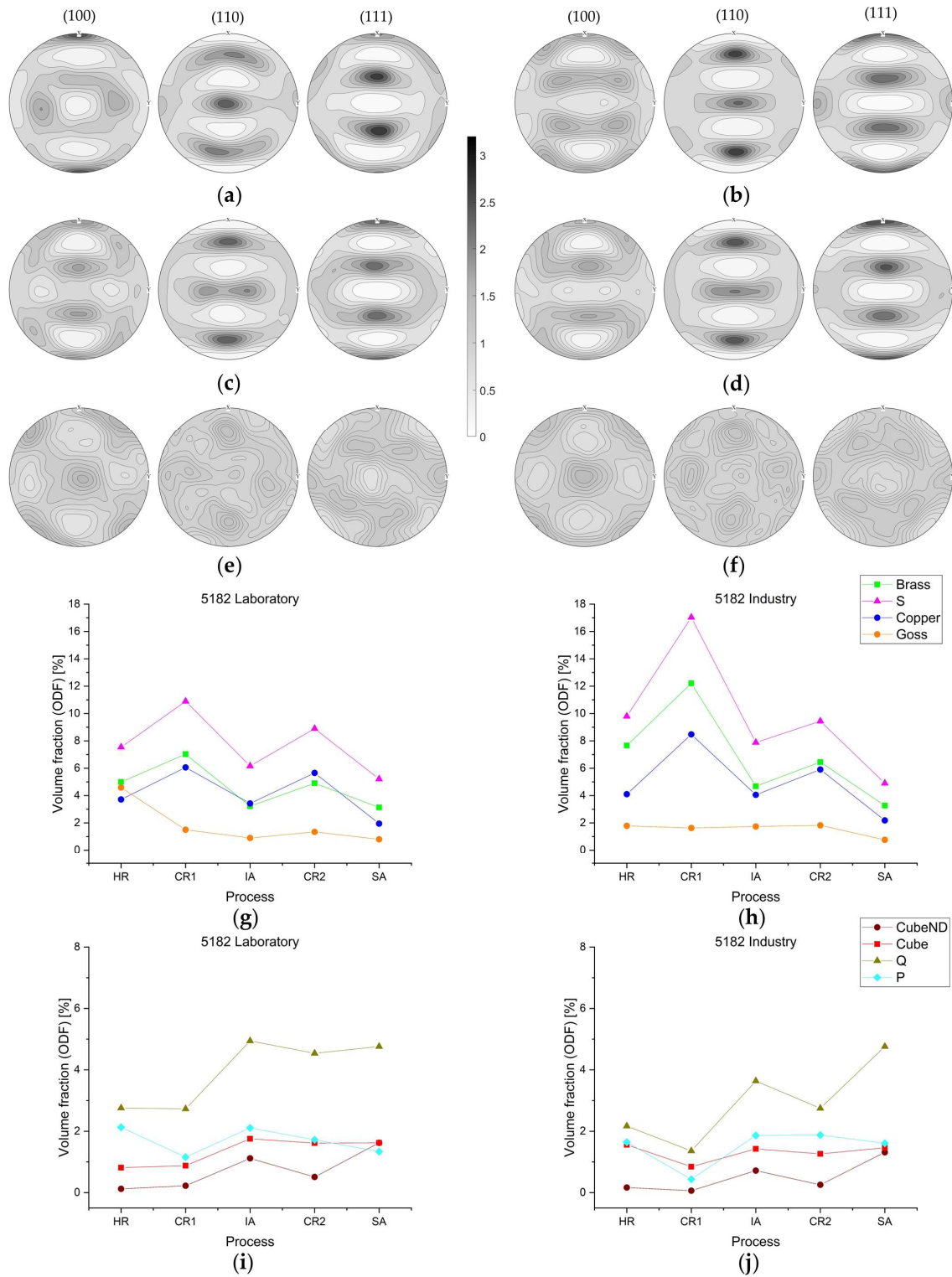


Fig. 4.6. Evolution of texture components within sheet processing for EN AW-5182; (001), (110), and (111) pole figures based on ODF data for (a) hot rolling (HR) laboratory, (b) HR industry, (c) cold rolling (CR)2 laboratory, (d) CR2 industry, (e) soft annealing (SA) laboratory, and (f) SA industry; diagrams (g) to (j) show the evolution of specific texture components over the entire processing route.

Starting with hot-rolled conditions, pole figures **Fig. 4.6 (a),(b)** show the typical β -fiber formation in both laboratory and industry samples, although the total intensities are not equal. Owing to the elevated temperatures, the entire rolling texture is rather weak, but still shows pronounced Brass and S components. Comparing laboratory and industry samples, the pole figures show good accordance

of the orientations occurring. During further processing, cold-rolling leads to intensified β -fiber components, especially in the industrially produced samples. Therefore, the pole figures in **Fig. 4.6 (c),(d)** illustrate typical orientation distribution for cold-rolled fcc-materials. The results given in **Fig. 4.6 (e),(f)** clarify the obvious differences in rolling and recrystallization texture formation. The β -fiber components are significantly reduced and the volume fraction of typical orientations of recrystallized grains (Cube, Q, P) increases; however, the overall intensity of recrystallization texture is weak for both laboratory and industry samples.

The representation of proportions of some specific texture components, given in **Fig. 4.6 (g)–(j)**, enables an easier comparison of the entire process. The evolution of rolling texture components in **Fig. 4.6 (g),(h)** verifies the presumptions based on the pole figures. Typical β -fiber components dominate the texture after rolling processes and are weakened by recrystallization (heat treatments). The good agreement of the texture components, not only qualitatively, but for most of the sample states also quantitatively, is emphasized with these diagrams.

The components of the recrystallization texture in **Fig. 4.6 (i),(j)** also confirm theoretical considerations from the literature [12]. Strengthening of these components occurs with heat treatments and recrystallization, while they develop at the expense of the rolling components. Although the evolution of recrystallization components generally still shows conformity for laboratory and industry, the Q component is intensified in laboratory samples throughout the entire process. Additionally, the cube component does not dominate the final sheet structure in contrast to classical recrystallization textures of low alloyed fcc-systems.

4.3.2.2 Texture Evolution in EN AW-6016

The results on texture evolution in EN AW-6016 are presented in **Fig. 4.7 (a)–(j)**. The orientation distribution for hot-rolled sample states shown in the pole figures in **Fig. 4.7 (a),(b)** reveal only a few different orientations. While formation of typical β -fiber is expected during hot-rolling of Al-alloys, both laboratory and industrially hot-rolled samples exhibit higher Cube fractions. The higher amount of deformation energy introduced during cold-rolling tends to form the β -fiber in both laboratory and industry sheets. **Fig. 4.7 (c)** indicates more typical S and Copper components in the laboratory sample, while the industrial sample (**Fig. 4.7 (d)**) also shows Brass orientations.

The pole figures of the solution annealed sample states in **Fig. 4.7 (e),(f)** show good accordance for laboratory and industry. Theoretical aspects of texture formation are observable, particularly as Cube component domination is indicated on both scales of sample processing.

The entire texture evolution in **Fig. 4.7 (g)–(j)** confirms most of the indications based on the pole figures. While the typical trend of rolling texture components over process is found for the industrial sample, the Brass component in the laboratory sample vanishes for the first cold-rolling process. Although quantitative differences are evident, both industry as well as laboratory follow expected behavior during the rolling process.

The trend of recrystallization texture components for the industrial sample in **Fig. 4.7 (j)** depicts the classical fcc-texture evolution. The dominating Cube component is accompanied by lower volume fractions of Q, P, and CubeND in the annealed sample states. Laboratory samples show similar behavior for the evolution of recrystallization components, and even though the Q component dominates the final texture of the sheet, the overall texture development is qualitatively and, for specific sample states, also quantitatively comparable for industry and laboratory.

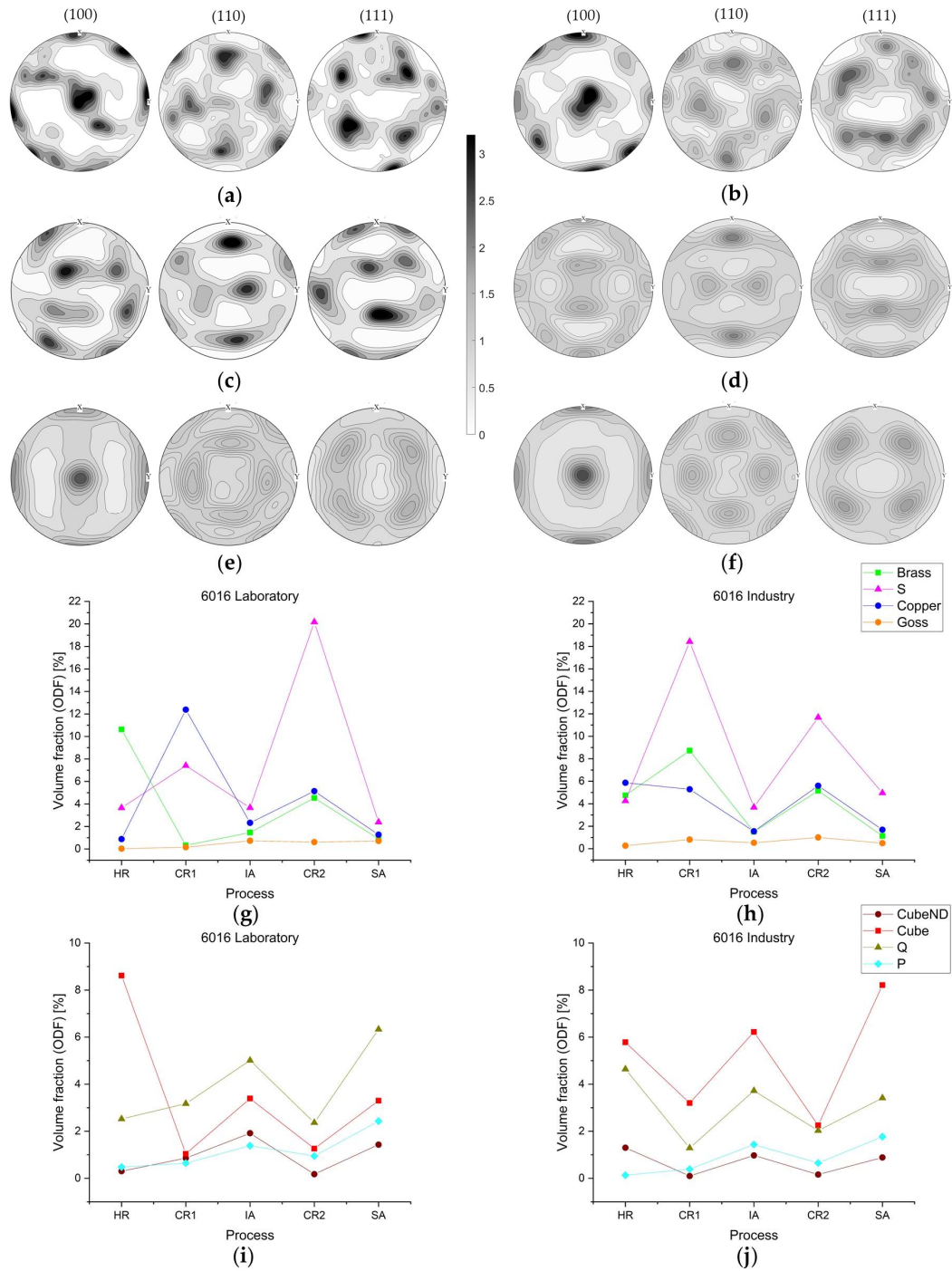


Fig. 4.7. Evolution of texture components within sheet processing for EN AW-6016; (001), (110), and (111) pole figures based on ODF data for (a) HR laboratory, (b) HR industry, (c) CR2 laboratory, (d) CR2 industry, (e) SA laboratory, and (f) SA industry; diagrams (g) to (j) show the evolution of specific texture components over the entire processing route.

4.4 Discussion

In the following, the comparability of texture and microstructure development in industrial and laboratory samples will be discussed, including some considerations on general texture evolution in Al alloys.

The microstructure evolution of the EN AW-5182 laboratory-sheets generally confirms the results and theories of previous publications [9]. While typical microstructural features such as subgrain dislocation networks can be observed in both laboratory and industrial scaled processing [14, 56], it should be noted that the deformation energy introduced during rolling is generally expected to be lower in the laboratory sheets. A comparison of the hot-rolled microstructure with the industrial samples reveals the absence of a strong deformation substructure on laboratory scale, which can be attributed to reduced rolling forces in the laboratory mill. Subsequent cold-rolling increases the deformation structure, but still, based on the linear intercept length for both CR1 and CR2 given in **Tab. 4.3**, energy input and grain fragmentation are higher in the industrial process. The less fragmentation of grains may also result in the increment of linear intercept length in both CR states, as the elongation of the grains in RD is not suppressed. After intermediate annealing and soft annealing, however, similar results in grain size and microstructure are observed for the EN AW-5182. The differences of about 10% can be attributed to the deformation energy input during rolling as well as to impacts from differences during laboratory and industrial heat treatments.

As far as the influence of particles on the overall microstructure development is concerned, different mechanisms must be considered. As shown in **Fig. 4.4 (a)**, various types and sizes of particles are present. Coarse (also fragmented), non-shearable particles enhance the misorientation of the grain in their nearest surrounding by accumulation of dislocations, which can result in grain refinement around those particles after annealing. Secondary phases in the nanometer range often hinder the recrystallization process (grain boundary pinning) [9, 57]. A comparison of BSE images of laboratory and industrial sheets shows a similar phase distribution owing to sophisticated processing (especially casting). Although potential particles are present in the studied alloys on both scales, there is no clear evidence for specifically related microstructure transformations. Despite this, as both laboratory and industrial sheets exhibit equivalent behavior concerning particle-related phenomena, the overall comparability of the production process with respect to microstructure development shows satisfactory results.

Moreover, regarding texture evolution in EN AW-5182, **Fig. 4.6 (a)–(j)** shows good agreement between laboratory and industrial sheets. **Fig. 4.6 (a)–(d)** highlight the strong development of β -fiber texture components, most prominently the S and Brass orientations [5, 58, 59]. Additionally, the comparison of the intensities in the pole figures for laboratory and industry indicates fewer rolling structures in laboratory processing. The quantification of texture components from ODFs over the

process in **Fig. 4.6 (g)–(j)** also emphasizes the promising results for the comparability of laboratory and industry alloy production in terms of microstructure and texture.

General minor intensities of the recrystallization texture components, including Cube orientation, suggest randomization of texture to a certain degree (especially in the laboratory alloy). Concerning the strengthening of the Q component during recrystallization, the sometimes-stated origin near to shear bands (reported in some Mg-containing heavily-rolled Al-alloys) could not be verified due to the absence of attendant microstructural features and the rarely emerging Goss component, which can also indicate features of shear during deformation [6, 11, 37, 60]. As the entire texture development does not show any influence of PSN, a minor significance of microstructural changes based on coarse particles can be assumed; however, a more detailed analysis of the primary and secondary phase distribution will nevertheless be the subject of future investigations.

The comparison of the microstructure development of EN AW-6016 in laboratory and industrial samples shows similarities for individual processing steps. Starting from hot-rolling, fragmented grains with enormous elongation show typical characteristics of the rolling process in the laboratory sheets (**Fig. 4.5 (a),(b)**). Additionally, the linear intercept length listed in **Tab. 4.4** indicates comparable grain sizes for industrial products. As high standard deviations of the linear intercept length in hot-rolled and CR1 sample states emphasize the imbalance of present grains, further discussion of measured grain size is only useful for a qualitative comparison of laboratory and industrial samples beginning at the IA process step.

The hot-rolled microstructure shows the alignment of subgrain structures in specific angles to RD, as well as inhomogeneous distribution of deformation structures over the sampled area. These inhomogeneities arise from the different orientations and sizes of the grains, which causes an unbalanced stress propagation over the whole sample [9]. The higher deformation energy introduced during cold-rolling forms massively distorted grains with elongations in RD in both laboratory and industry. While there are some discrepancies occurring between laboratory and industry for the linear intercept length in HR and CR1, better comparability of the average linear section length for EN AW-6016 can be observed from IA onwards. Possible explanations are inequalities in the rolling process for laboratory and industry regarding forces and roll gap geometries. As the stored energy is also the driving force for recrystallization, intermediate annealing transfers existing differences to annealed sheets as well. Nevertheless, the final sheet microstructure and the linear intercept length show good accordance on laboratory and industrial scale. Originating from good agreements in CR2 state, the final annealing tends to produce comparable microstructures, confirming in particular the comparability of these heat treatments in terms of time and heating rate.

Interesting behavior can be seen in the texture evolution of EN AW-6016 samples. Owing to the already discussed problem of giant grains in the hot-rolled condition, the pole figures depicted in **Fig. 4.7 (a),(b)** indicate highly textured Al-sheets in both laboratory and industry. As this data are based only on the orientations of a few grains, the validity of the plots is strongly restricted; however,

laboratory and industrial samples both show the appearance of Cube orientation, while the tendency of β -fiber formation is not clearly noticeable in the evaluated data. As mentioned in the work of [15], enhancement of the Cube component in hot-rolled sheets can occur by post-dynamic recrystallization, which also constitutes a possible process in our laboratory production.

Following the pole figures in **Fig. 4.7 (c),(d)** as well as the texture evolution for rolling components, typical β -fiber formation can be noticed in every rolling process step. The extinction of Brass component in the initial cold-rolled laboratory sample is not comprehensible, as fundamental publications report its occurrence in (cold-)rolled fcc-materials [9, 12], though the industrially processed material does adhere to theoretical predictions. Overall, the trends in texture formation are again comparable for laboratory and industry scale production.

Solution annealed samples show typical recrystallization components in **Fig. 4.7 (e),(f)** as well as **Fig. 4.7 (i),(j)** [6, 7]. The dominant Cube component is accompanied by other stable orientations in recrystallized industrial sheets, namely, Q, P, and CubeND. Laboratory sheets show minor Cube intensities, but more distinct formation of Q component in **Fig. 4.7 (i)**. The evolution of these specific components does not highlight specific mechanisms concerning texture modifications. The absence of the Goss component and missing microstructural features suggest the absence of shear banding in the present alloys, although slightly intensified P and Q texture components are noticeable in the annealed sheets [57, 61, 62].

Another possible explanation for the balanced distribution of recrystallization components in **Fig. 4.7** may lie in the presence of particles. However, as stated in various publications [35, 36, 38, 39], the PSN connected texture transformation is generally not clearly observable, as in **Fig. 4.7 (e),(f)** or **Fig. 4.7 (i),(j)**. The slightly higher volume fractions of components P, CubeND, and Q suggest that particles capable of PSN may only be present in the laboratory produced sheets. These possible inequalities in particle distribution for laboratory and industry sheets may result from scale effects during thermomechanical processing, which affects the precipitation of the hardening phases, and thus impacts the texture formation.

As qualitative conformity in microstructure and texture evolution for the EN AW-6016 is found for the entire process, the comparability of laboratory and industrial processes can be endorsed. However, while the microstructure shows good quantitative agreements in the term of final grain size, the quantitative texture development is not comparable for all processing steps.

4.5 Conclusions

This work provides a comprehensive overview on microstructure and texture evolution of the Al-alloys EN AW-5182 and EN AW-6016. Moreover, it investigates the influences of different processing scales and highlights the importance of carefully designed laboratory experiments. The following conclusions can be made:

- Texture and microstructure evolution throughout the process shows good conformity for EN AW-5182, both qualitatively and quantitatively. Typical rolling and recrystallization behavior of fcc-metals is found.
- For EN AW-6016, results from laboratory and industrial scale can be compared qualitatively over the process chain, although quantitative differences do occur. Slight differences in both rolling and recrystallization texture components emphasize the necessity of more detailed analysis of some sample states.
- Final annealed sheets show highly comparable microstructure and texture in both laboratory and industrially produced sheets for both alloys.
- Although EN AW-5182 and EN AW-6016 both include alloying elements forming primary and secondary phases, the influences of particle stimulated nucleation or intensified Zener-pinning are not clearly observable in either of these alloys.

In general, careful design of laboratory production of automotive aluminum sheets is necessary to study new alloys or processes. However, at least qualitative comparison to industrially processed sheets should be possible.

Acknowledgments

The authors gratefully thank Prof. Dierk Raabe and his group (Max-Planck-Institut für Eisenforschung, Düsseldorf, Germany) for their valuable input. Furthermore, we thank the involved colleagues at AMAG rolling GmbH, the Christian Doppler Laboratory for Advanced Aluminum Alloys, and Lehrstuhl für Nichteisenmetallurgie, Montanuniversität Leoben.

References

- [1] Cole G. S. and A. M. Sherman: Lightweight Materials for Automotive Applications. *Materials Characterization*, 35 (1995), 3–9.
- [2] Müller W. et al.: Recent development in aluminium alloys for the automotive industry. *Materials Science and Engineering: A*, 280 (2000), 37–49.
- [3] Ostermann F.: *Anwendungstechnologie Aluminium*. Springer, Berlin, Germany (2014).
- [4] Burger G. B. et al.: Microstructural Control of Aluminum Sheet Used in Automotive Applications. *Materials Characterization*, 35 (1998), 23–39.
- [5] Engler O.: Texture and anisotropy in cold rolled and recovery annealed AA 5182 sheets. *Materials Science and Technology*, 31 (2015), 1058–1065.
- [6] Engler O. and J. Hirsch: Control of recrystallisation texture and texture-related properties in industrial production of aluminium sheet. *Int. J. Mat. Res.*, 100 (2009), 564–575.
- [7] Engler O. and J. Hirsch: Recrystallization Textures and Plastic Anisotropy in Al-Mg-Si Sheet Alloys. *Materials Science Forum*, 217 (1996), 479–486.

- [8] Engler O. and V. Randle: Introduction to texture analysis. CRC Press, Boca Raton (2010).
- [9] Humphreys F. J., G. S. Rohrer and A. D. Rollett: Recrystallization and related annealing phenomena. Elsevier Science Ltd. (2017).
- [10] Bay B., N. Hansen and D. Kuhlmann-Wilsdorf: Microstructural evolution in rolled aluminium. *Materials Science and Engineering: A*, 158 (1992), 139–146.
- [11] Engler O. and K. Lücke: Mechanisms of recrystallization texture formation in aluminium alloys. *Scripta Metallurgica et Materialia*, 27 (1992), 1527–1532.
- [12] Dillamore I. L. and W. T. Roberts: Preferred Orientation In Wrought And Annealed Metals. *Metallurgical Reviews*, 10 (1965), 271–380.
- [13] Mishin O. V., B. Bay and D. Juul Jensen: Through-Thickness Texture Gradients in Cold-Rolled Aluminum. *Metallurgical and Materials Transactions A*, 31 (2000), 1653–1662.
- [14] Hurley P. J. and F. J. Humphreys: The application of EBSD to the study of substructural development in a cold rolled single-phase aluminium alloy. *Acta Materialia*, 51 (2003), 1087–1102.
- [15] Engler O. and J. Hirsch: Texture control by thermomechanical processing of AA6xxx Al–Mg–Si sheet alloys for automotive applications—a review. *Materials Science and Engineering: A*, 336 (2002), 249–262.
- [16] Doherty R. D.: Recrystallization and Texture. *Progress in Materials Science*, 42 (1997), 39–58.
- [17] Engler O., J. Hirsch and K. Lücke: Texture Development in Al-1.8 wt% Cu Depending on the Precipitation State - II. Recrystallization Textures. *Acta Metallurgica et Materialia*, 43 (1995), 121–138.
- [18] Hirsch J. and T. Al-Samman: Superior light metals by texture engineering: Optimized aluminum and magnesium alloys for automotive applications. *Acta Materialia*, 61 (2013), 818–843.
- [19] Li S. et al.: A Review of Texture Evolution Mechanisms During Deformation by Rolling in Aluminum Alloys. *Journal of Materials Engineering and Performance*, 27 (2018), 3350–3373.
- [20] Hirsch J. and K. Lücke: Overview no. 76: Mechanism of deformation and development of rolling textures in polycrystalline f.c.c. metals—I. Description of rolling texture development in homogeneous CuZn alloys. *Acta Metallurgica*, 36 (1988), 2863–2882.
- [21] Hirsch J., E. Nes and K. Lücke: Rolling and recrystallization textures in directionally solidified aluminium. *Acta Metallurgica*, 35 (1987), 427–438.
- [22] Bate P. and A. Oscarsson: Deformation banding and texture in hot rolled Al–1.0Mn–1.2Mg alloy. *Materials Science and Technology*, 6 (1990), 520–527.
- [23] Alvi M. H. et al.: Cube texture in hot-rolled aluminum alloy 1050 (AA1050)—nucleation and growth behavior. *Acta Materialia*, 56 (2008), 3098–3108.
- [24] Dons A. L. and E. Nes: Nucleation of cube texture in aluminium. *Materials Science and Technology*, 2 (1986), 8–18.
- [25] Hurley P. J. and F. J. Humphreys: A study of recrystallization in singlephase aluminium using insitu annealing in the scanning electron microscope. *Journal of Microscopy*, 213 (2004), 225–234.
- [26] de La Chapelle S.: Cube recrystallization textures in a hot deformed Al-Mg-Si alloy. *Scripta Materialia*, 45 (2001), 1387–1391.
- [27] Kashyap K. T. and R. George: Mechanism of cube grain nucleation during recrystallization of deformed commercial purity aluminium. *Bulletin of Materials Science*, 29 (2006), 197–200.
- [28] Samajdar I. and R. D. Doherty: Cube recrystallization texture in warm deformed aluminum: Understanding and prediction. *Acta Materialia*, 46 (1998), 3145–3158.

- [29] Engler O., H. E. Vatne and E. Nes: The roles of oriented nucleation and oriented growth on recrystallization textures in commercial purity aluminium. *Materials Science and Engineering: A*, 205 (1996), 187–198.
- [30] Engler O.: On the influence of orientation pinning on growth selection of recrystallisation. *Acta Materialia*, 46 (1998), 1555–1568.
- [31] Mao W. and P. Yang: Formation mechanisms of recrystallization textures in aluminum sheets based on theories of oriented nucleation and oriented growth. *Transactions of Nonferrous Metals Society of China*, 24 (2014), 1635–1644.
- [32] Kobayashi M., Y. Takayama and H. Kato: Preferential Growth of Cube-Oriented Grains in Partially Annealed and Additionally Rolled Aluminum Foils for Capacitors. *Materials Transactions*, 45 (2004), 3247–3255.
- [33] Bennett T. A. et al.: The Effect of Intermediate Annealing on Texture Banding in Aluminum Alloy 6016. *Advanced Engineering Materials*, 12 (2010), 1018–1023.
- [34] Ridha A. A. and W. B. Hutchinson: Recrystallisation mechanisms and the origin of cube texture in copper. *Acta Metallurgica*, 30 (1982), 1929–1939.
- [35] Bennett T. A., R. H. Petrov and L. A. I. Kestens: Effect of particles on texture banding in an aluminium alloy. *Scripta Materialia*, 62 (2010), 78–81.
- [36] Humphreys F. J.: A unified theory of recovery, recrystallization and grain growth, based on the stability and growth of cellular microstructures—II. The effect of second-phase particles. *Acta Materialia*, 45 (1997), 5031–5039.
- [37] Daaland O. and E. Nes: Recrystallization texture development in commercial Al-Mn-Mg alloys. *Acta Materialia*, 44 (1996), 1413–1435.
- [38] Vatne H. E., O. Engler and E. Nes: Influence of particles on recrystallisation textures and microstructures of aluminium alloy 3103. *Materials Science and Technology*, 13 (1997), 93–102.
- [39] Humphreys F. J.: The nucleation of recrystallization at second phase particles in deformed aluminium. *Acta Metallurgica*, 25 (1977), 1323–1344.
- [40] Humphreys F. J. and D. Juul Jensen: Structure and Texture Evolution during the Recrystallisation of Particle Containing Materials. 7th Risø International Symposium on Metallurgy and Materials Science, 7 (1986), 93–106.
- [41] Liu Y. et al.: Effect of Mn and Fe on the Formation of Fe- and Mn-Rich Intermetallics in Al-5Mg-Mn Alloys Solidified Under Near-Rapid Cooling. *Materials (Basel, Switzerland)*, 9 (2016), 88.
- [42] Sidor J. J., R. H. Petrov and L. Kestens: Microstructural and texture changes in severely deformed aluminum alloys. *Materials Characterization*, 62 (2011), 228–236.
- [43] Claves S. R., D. L. Elias and W. Z. Misiolek: Analysis of the Intermetallic Phase Transformation Occurring during Homogenization of 6xxx Aluminum Alloys. *Materials Science Forum*, 396 (2002), 667–674.
- [44] Ratchev P., P. Verinden and P. van Houtte: Effect of preheat temperature on the orientation relationship of (Mn,Fe)Al₆ precipitates in an AA 5182 aluminium-magnesium alloy. *Acta Metallurgica et Materialia*, 43 (1995), 621–629.
- [45] Ebenberger P. et al.: Effect of Compositional and Processing Variations in New 5182-Type AlMgMn Alloys on Mechanical Properties and Deformation Surface Quality. *Materials (Basel, Switzerland)*, 12 (2019), 1645.
- [46] Prillhofer R. et al.: Property Criteria for Automotive Al-Mg-Si Sheet Alloys. *Materials (Basel, Switzerland)*, 7 (2014), 5047–5068.

- [47] Schmid F. et al.: Industry-oriented sample preparation of 6xxx and 5xxx aluminum alloys in laboratory scale. *Proceedings of EMC 2019* (2019), 639–652.
- [48] Bachmann F., R. Hielscher and H. Schaeben: Texture Analysis with MTEX - Free and Open Source Software Toolbox. *Solid State Phenomena*, 160 (2010), 63–68.
- [49] Hielscher R. et al.: Denoising of crystal orientation maps. *Journal of Applied Crystallography*, 52 (2019), 984–996.
- [50] Schwarzer R. A. and J. Sikkau: Electron Back Scattered Diffraction : Current State, Prospects and Comparison with X-Ray Diffraction Texture Measurement. *The Banarast Metallurgist*, 18 (2013), 1–11.
- [51] Contrepois Q., C. Maurice and J. H. Driver: Hot rolling textures of Al–Cu–Li and Al–Zn–Mg–Cu aeronautical alloys: Experiments and simulations to high strains. *Materials Science and Engineering: A*, 527 (2010), 7305–7312.
- [52] Engler O.: Comparison of X-ray and electron backscatter diffraction textures for back-annealed Al–Mg alloys. *Journal of Applied Crystallography*, 42 (2009), 1147–1157.
- [53] Van den Boogart, G. K.: Statistical Errors of Texture Entities Based on EBSD Orientation Measurements. *Materials Science Forum*, 495 (2005), 179–184.
- [54] Creuziger A., K. Syed and T. Gnäupel-Herold: Measurement of uncertainty in orientation distribution function calculations. *Scripta Materialia*, 72 (2014), 55–58.
- [55] Pospiech J., J. Jura and G. Gottstein: Statistical Analysis of Single Grain Orientation Data generated from Model Textures. *Materials Science Forum*, 157 (1994), 407–412.
- [56] Liu Q., D. Juul Jensen and N. Hansen: Effect of grain orientation on deformation structure in cold-rolled polycrystalline aluminium. *Acta Materialia*, 46 (1998), 5819–5838.
- [57] Lücke K. and O. Engler: Effects of particles on development of microstructure and texture during rolling and recrystallisation in fcc alloys. *Materials Science and Technology*, 6 (1990), 1113–1130.
- [58] Weiland H. and J. Hirsch: Microstructure and Local Texture in Hot Rolled Aluminum. *Textures and Microstructures*, 14 (1991), 647–652.
- [59] Liu W. C. and J. G. Morris: Quantitative Analysis of Texture Evolution in Cold-Rolled, Continuous-Cast AA 5xxx-Series Aluminum Alloys. *Metallurgical and Materials Transactions A*, 35 (2004), 267–277.
- [60] Gatti J. R. and P. P. Bhattacharjee: Nucleation behavior and formation of recrystallization texture in pre-recovery treated heavily cold and warm-rolled Al–2.5wt.%Mg alloy. *Materials Characterization*, 106 (2015), 141–151.
- [61] Liu W.: Quantification of recrystallization texture evolution in cold rolled AA 5182 aluminum alloy. *Scripta Materialia*, 49 (2003), 539–545.
- [62] Sidor J. J., R. H. Petrov and L. A. Kestens: Modeling the crystallographic texture changes in aluminum alloys during recrystallization. *Acta Materialia*, 59 (2011), 5735–5748.

5 PRIMARY AND SECONDARY PHASE EVOLUTION IN FE AND MN CONTAINING 5XXX AL SHEETS

Based on the influence of additional phases on the microstructure and texture evolution in Al alloys (see Chapter 2), the following section comprehensively analyses and discusses the influence of Fe and Mn additions on the intermetallic phase formation in 5xxx Al alloys. The detrimental effects of Fe bearing phases on the resulting mechanical properties of those alloys can be counteracted by the appropriate choice of Mn contents, i.e. altering the Fe/Mn ratio. The primary intermetallic phases change from needle-shaped $Al_3(Fe,Mn)$ (high Fe/Mn ratios) to blocky or Chinese-script $Al_6(Fe,Mn)$ or $Al_{15}(Fe,Mn)_3Si_2$ (high Fe/Mn ratios) and further exhibit impacts of the processing parameters. The secondary phase dispersoid formation is initiated during homogenization and the particles show variant volume fractions, sizes, and morphologies with the Fe and Mn content as well as the homogenization time/temperature. Therefore, a broadly based two-part study involved four different alloys and systematic variations of the processing parameters during commercial sheet processing. The variations in primary and secondary phase evolution are presented in the following Part I of this research.

Influence of Fe and Mn on the Microstructure Formation in 5xxx Alloys—Part I: Evolution of Primary and Secondary Phases*

The increasing demands for Al sheets with superior mechanical properties and excellent formability require a profound knowledge of the microstructure and texture evolution in the course of their production. The present study gives a comprehensive overview on the primary- and secondary phase formation in AlMg(Mn) alloys with varying Fe and Mn additions, including variations in processing parameters such as solidification conditions, homogenization temperature, and degree of cold rolling. Higher Fe alloying levels increase the primary phase fraction and favor the needle-shaped morphology of the constituent phases. Increasing Mn additions alter both the shape and composition of the primary phase particles, but also promote the formation of dispersoids as secondary phases. The size, morphology, and composition of primary and secondary phases is further affected by the processing parameters. The average dispersoid size increases significantly with higher homogenization temperature and large primary particles tend to fragment during cold rolling. The microstructures of the final soft annealed states reflect the important effects of the primary and secondary phase particles on their evolution. The results presented in this paper regarding the relevant secondary phases provide the basis for an in-depth discussion of the mechanisms underlying the microstructure formation, such as Zener pinning, particle stimulated nucleation, and texture evolution, which is presented in Part II of this study.

5.1 Introduction

In the past decades, the use of aluminum as a construction material strongly increased in various fields of application. Depending on the alloying and micro-alloying elements, a wide range of combinations of materials properties exist. Especially with regard to improving sustainability and reducing CO₂ emissions of processes and technical applications, the use of aluminum alloys as replacement for materials with higher density is a common approach. With the growing importance of weight reductions in the automotive sectors, amongst other alloying systems, attention was focused on the aluminum 5xxx (AlMg(Mn)) alloys. The non-age-hardenable alloys typically show superb combinations of medium strength, corrosion resistance, and good formability [1]. Control of the mechanical properties is predominantly realized by the amount of Mg in solid solution and the degree of cold work prior to soft annealing [1]. Additionally, the secondary alloying element Mn plays a key

* Published in *Materials* 14 (2021), 3204 written by Jakob Grasserbauer, Irmgard Weißensteiner, Georg Falkinger, Thomas M. Kremmer, Peter J. Uggowitzer and Stefan Pogatscher.

Author contributions:

JG: Conceptualization, methodology, validation, investigation, original draft, visualization.

role in intermetallic phase formation. It therefore affects both the processing and final properties of the alloys.

The importance of primary phase distribution in the AlMg(Mn) alloys is highlighted by their capability of reducing the Lüders elongation and the resulting undesired strain marks, which are a common problem of those alloys [2]. In this context, the industrial casting process is crucial as the different cooling rates in ingot casting, continuous casting, and twin-roll casting strongly influence the primary phase size and number density [1]. Overall, the development of advanced aluminum alloys hence requests both a sophisticated process design and deep knowledge on microstructural relations in these alloys [1, 3–5].

The primary and secondary phase formation in 5xxx Al alloys is in general a very complex process and controlled by Mg and secondary alloying elements such as Mn, Fe, and Si [6]. Although a large variety of intermetallic phases can form during solidification, and also during subsequent heat-treatments, the most typically found phases include: Al₃Fe (or Al₁₃Fe₄), Al₆Mn, (α-)Al(Fe,Mn)Si, and Mg₂Si [6–18].

The Fe-rich intermetallic Al₃Fe tends to form in alloys showing higher Fe/Mn ratios and lower amounts of Si or Mg. This phase, appearing needle-like in 2D micrographs, is highly implicated with disadvantageous effects of Fe containing intermetallics in Al. Because of their characteristic shape, those precipitates cause stress concentrations and, additionally, the phase is reported to negatively influence the corrosion resistance of the alloys [14, 19, 20]. According to thermodynamic calculations and experimental observations, the Al₃Fe phase is often found as Al₁₃Fe₄. Because of the interchangeability of Fe and Mn especially at lower ratios of Fe/Mn and higher temperatures, Al₃(Fe,Mn) or Al₁₃(Fe,Mn)₄ is recommended as a more precise designation [6, 9, 10, 16]. In the following we stick to this notation.

The intermetallic phase Al₆Mn, well known from the group of 3xxx (AlMn) alloys, shows a stronger formation with low Fe/Mn ratio and low Si contents. Due to the inter-changeability of Fe and Mn, the Al₆(Fe,Mn) phase is formed which mostly appears in the form of irregularly shaped plate- or block-like particles, but sometimes also exhibits Chinese-script structure [16]. The exact stoichiometry of those phases in the Mg-containing 5xxx alloys is hence not totally clarified, e.g., the authors of [9] and [21] report on the formation of Al_m(Fe,Mn) with m being in the range of 4.0 to 4.4. They additionally mention the influence of higher Mg content in promoting the formation of Al₃(Fe,Mn) at the expense of Al₆(Fe,Mn) [9, 12, 21].

Regarding the influence of Si on the formation of Fe and Mn containing phases in Al alloys, the two different types of α- and β-AlFeSi must be considered. In the case of lower amounts of Fe impurities and the absence of Mn especially in AlMgSi alloys, typically β-Al₁₅FeSi formation is favored. This generally faceted and needle-shaped phase shows similar effects on the alloys mechanical properties as the Al₃(Fe,Mn). The tendency of formation or transformation from β- to α-AlFeSi is promoted by higher Fe/Si ratios and re-quires a minimum amount of Mn for phase stabilization. While the hexagonal αh-Al₈FeSi is more often found in Mn free alloys, cubic αc-Al₁₅(Fe,Mn)₃Si₂ is formed by

peritectic reactions and is mostly affected by the Mn content. In contrast to β -Al₁₅FeSi, their globular or Chinese-script morphology can reduce the adverse effects of the intermetallic particles on the mechanical properties [6–8, 11, 15, 22, 23].

In addition to the Fe and Mn bearing primary phases, Mg₂Si particles can form during solidification as an equilibrium phase. The phase fraction of these particles largely depends on Si and Mg contents as well as on the cooling rates. During subsequent heat-treatments, those Mg₂Si precipitates can be dissolved and/or modified in size and shape to meet their intended purpose as hardening phases in (especially 6xxx) Al alloys [1, 6].

The cooling rates during solidification are crucial for the phase formation in AlMg(Mn) alloys. Distinguishing between slow cooling (S-C, ~0.5–3 K/s) and near-rapid cooling (NR-C, ~50 K/s), the stabilities of the aforementioned phases can change considerably [12]. Moreover, the network of intermetallic phases is significantly refined with higher cooling rates. Furthermore, the amount of solutes of especially Fe, Mn, and Si is affected by the solidification rate, which in turn plays a decisive role in the subsequent homogenization treatment and the formation of secondary phase particles [7, 12, 14, 16, 23].

Depending on the particular time and temperature of the heat-treatments in Fe and Mn containing 5xxx Al alloys, three different types of particles are involved in the precipitation behavior of secondary phases: Al₆(Fe,Mn), α -Al₁₅(Fe,Mn)₃Si₂, and Mg₂Si. The rod- or platelet-shaped Al₆(Fe,Mn) dispersoids are widely used as pinning particles in those alloys and therefore have significant influence on the recrystallization behavior and the microstructure. Different studies highlight the importance of maximum homogenization temperature and holding time on the volume fraction and size distribution of the particles [24–26], indicating that higher temperatures result in a higher fraction of coarsened Al₆(Fe,Mn) particles for example. Additionally, the higher temperatures affect the level of solute Si as Mg₂Si starts to dissolve at temperatures above 500 °C, and β - to α -AlFeSi transformations of primary phases can occur [10, 22]. As a consequence, the likelihood of α -Al₁₅(Fe,Mn)₃Si₂ dispersoid formation increases. The nucleation and growth of those particles is interdependent of the Al₆(Fe,Mn) dispersoid formation, which highlights the importance of well-considered thermomechanical processing for these Al alloys [24–29].

In recent decades, the usage of thermodynamic calculations was established in alloy design. With different commercially distributed software packages (e.g., FactSage, Thermo-Calc, MatCalc, and Pandat), the design of novel alloy compositions or modified thermomechanical processing is more easily accessible. Calculations of equilibrium and non-equilibrium conditions allow careful predictions of the occurring phases, although the validation by experimental characterizations is still indispensable [8, 10, 26].

The present study investigates the influence of secondary alloying elements Fe and Mn in a near 5182 aluminum alloy produced in laboratory scale. Attention is paid to primary and secondary phase formation in dependence on alloy composition and cooling rate during solidification as well as precipitation and phase transformation during homogenization. Additionally, a comparison to

thermodynamic calculations highlights the importance of combining experimental work with simulation studies.

5.2 Materials and Methods

The present study involved four modifications of Fe and Mn contents on a Al4.5Mg alloy produced within a laboratory scaled process. The compositions of the alloys can be found in **Tab. 5.1**.

Tab. 5.1. Chemical composition of the investigated alloys (wt. %).

Alloy	Mg	Si	Fe	Mn
LFe-LMn	4.51	0.12	0.10	0.22
LFe-HMn	4.40	0.12	0.11	0.94
HFe-LMn	4.48	0.11	0.40	0.22
HFe-HMn	4.56	0.11	0.39	1.04

The laboratory sample production followed the manufacturing process of 5xxx Al alloys as described in [30] and [31]. Casting at two different scales resulted in two different cooling rates during solidification to approximately simulate the cooling rates in twin-roll casting (with laboratory near rapid cooling, NR-C) and continuous casting (with laboratory slow cooling, S-C).

After milling of the cast blocks to sizes of $60 \times 40 \times 14 \text{ mm}^3$, two different homogenization treatments were performed (maximum temperatures of 500 and 550 °C). The heat treatment cycle, using an air-circulated furnace (Nabertherm N60/85SHA, Lilienthal, Germany), included heating from room temperature within five hours to the different maximum temperatures and holding for two hours.

The following rolling process was performed on a laboratory rolling mill with non-heatable rolls measuring 80 mm in diameter. For hot rolling (HR), the samples were first heated to the rolling temperature of 430 °C in the air-circulated furnace and put back into it after each rolling step for about 10 min to avoid critical losses in temperature. The final hot rolling thickness was varied to allow different degrees of cold rolling (CRD) while keeping the final sheet thickness unchanged. Therefore, the hot rolling process comprises reductions from 14 to 3.20 mm as well as 14 to 1.85 mm. The following intermediate annealing with a maximum temperature of 370 °C and a total cycle-time of about 72 h was again done in the air-circulated furnace. Subsequent cold rolling at room temperature was carried out on the aforementioned rolling mill. Reaching the final sheet thickness of about 1.20 mm resulted in two different cold rolling degrees (CRD) of 35% and 63%, respectively.

The final soft annealing was performed in a salt bath, which provides faster heating than conventional air-circulated furnaces. The annealing time was 5 min at a temperature of 500 °C, after which the samples were quenched in water.

Metallographic sample preparation for microstructure analyses comprised gentle grinding and polishing with diamond and oxide polishing suspensions. Preparation for transmission electron microscopy was finished by electropolishing of discs having 3 mm in diameter and approximately 100 μm in thickness. An electrolyte composing of $\frac{1}{3}$ HNO_3 and $\frac{2}{3}$ methanol was used in a Struers TenuPol twin-jet electropolishing unit at temperatures around -25 $^\circ\text{C}$.

The as-cast homogenized and soft annealed sample states were investigated using a scanning electron microscope (SEM) (JEOL 7200F FEG-SEM, Tokyo, Japan) equipped with an energy dispersive X-ray (EDX) detector (XMax-80, Oxford Instruments, Abingdon, UK) including automatic particle feature analysis of backscattered electron images using threshold limits. The feature analysis was carried out for as-cast and homogenized samples containing at least 1000 particles per scan for statistically representative results. For characterization Fe/Mn-ratios as well as shape factor ($\text{SF} = \frac{\text{Perimeter}^2}{4\pi \cdot \text{Area}}$) were used directly from feature mapping data. Focus was placed on primary phase distribution and composition in the as cast and homogenized sample states as well as the distribution and composition of dispersoids in the homogenized samples. Additionally, transmission electron microscopy (Thermo Scientific™ Talos™ F200X G2, ThermoFisher Scientific, Hillsboro, OR, USA) was used to clarify the composition of the second phase particles.

The evaluation of the primary and secondary phase fraction was carried out with the help of the free software tool ImageJ (version 1.53e). The calculations of the dispersoid volume fractions followed the method of Österreicher et al. [32], analyzing SEM images of higher magnifications (10,000 \times ; at least a total area of 325 μm^2) recorded using an accelerating voltage of 5 kV. The results were recorded including the average radii (r) and aspect ratios (AR; shorter divided by longer aspect of the particles) of the particles. Note that the related tables display the average data of all evaluated images per sample, while the images of the individual samples shown in the respective figures may show slight deviations thereof.

The thermodynamic calculations for this study followed the CALPHAD approach using the integrated computational software tool Pandat, database PanAl2019 (CompuTherm LLC, Middleton, WI, USA). The simulation involved calculations for non-equilibrium as-cast (Scheil approach [33]) as well as equilibrium conditions. The results are discussed and evaluated by contrast with the experimental findings.

5.3 Results

This section presents the evolution of primary and secondary phases in the alloys described above using micrographs as well as phase fraction analysis. Additional thermodynamic calculations using Pandat are shown in comparison and for experimental validation. Primary and secondary phase fractions and composition were derived by the evaluation of multiple SEM pictures and feature (EDX) mappings.

5.3.1 Microstructures and Intermetallic Phases in As-Cast State

5.3.1.1 Slow Cooling during Solidification (S-C)

The as-cast microstructures of the four different alloys were analyzed in terms of particle size and distribution of the primary phases using SEM and EDX. **Fig. 5.1 (a)–(d)** illustrate sizes and arrangement of the microstructural features as well as the casting defects in the alloys according to **Tab. 5.1**. Depending on the alloy's Fe and Mn contents, different primary phase structures can be observed, mainly segregated to the casting cell boundaries. To illustrate the phase evolution during cooling, a thermodynamic simulation for equilibrium and nonequilibrium solidification (Scheil) for the HFe-HMn alloy is given in **Fig. A5.1**.

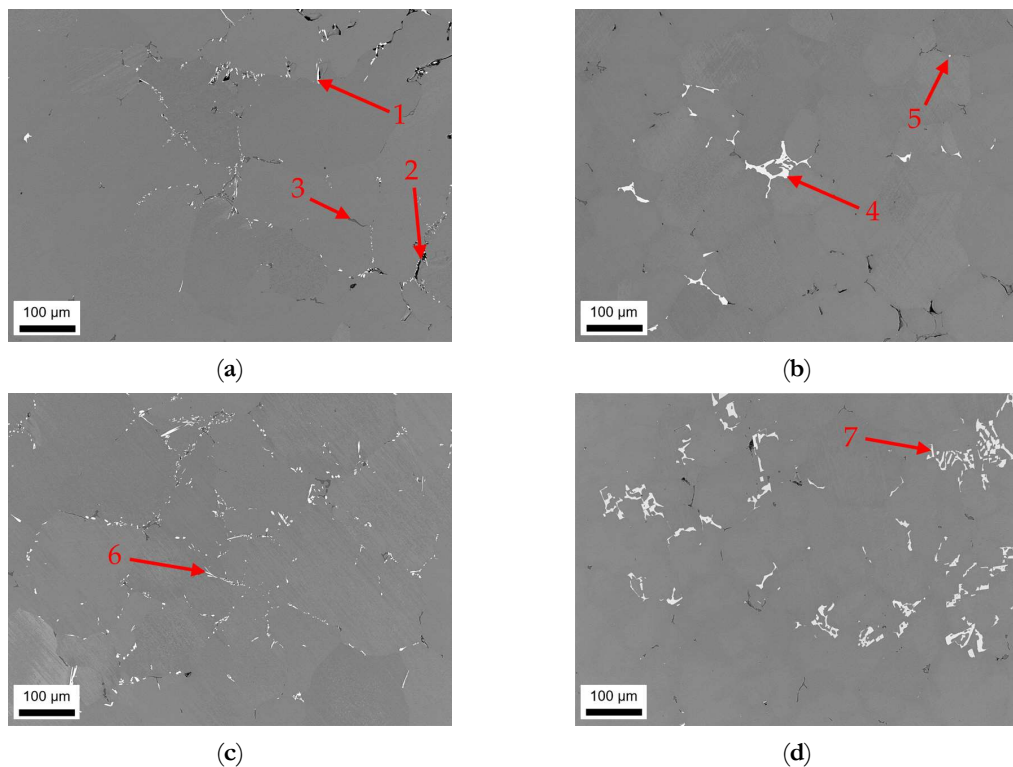


Fig. 5.1. Casting microstructure of S-C cast samples; (a) LFe-LMn, (b) LFe-HMn, (c) HFe-LMn, and (d) HFe-HMn; (1) $\text{Al}_3(\text{Fe},\text{Mn})$ phase, (2) casting defect (pore), (3) Mg_2Si phase, (4) $\text{Al}_6(\text{Fe}, \text{Mn})$ phase, (5) $\text{Al}_{15}(\text{Fe},\text{Mn})_3\text{Si}_2$ phase, (6) $\text{Al}_3(\text{Fe},\text{Mn})$ phase, (7) Chinese-script $\text{Al}_6(\text{Fe},\text{Mn})$ phase.

In the samples with low Mn content (LFe-LMn and HFe-LMn) in **Fig. 5.1 (a)–(c)**, the size and density of the intermetallic network obviously differs. While LFe-LMn shows looser structured, typically needle-shaped bright phases, an increase in Fe content results in a higher number density and slight coarsening of those intermetallics. The characteristic shape of the phases (**Fig. 5.1 (a)** (1) and **Fig. 5.1 (c)** (6)) is not altered with the change in Fe contents. EDX analysis of the particles (features) indicates $\text{Al}_3(\text{Fe},\text{Mn})$ type for the phases (see **Fig. A5.2–Fig. A5.5** for the EDX spectra).

Additionally, **Fig. 5.1 (a)** (2) indicates occurring casting defects (pores). The dark appearing primary Mg_2Si phase in the LFe-LMn alloy (**Fig. 5.1 (a)** (3)) is also found in the other alloys. Particle feature analysis of both samples shows no indications for $\alpha-Al_{15}(Fe,Mn)_3Si_2$ phases nor denotes the $Al_6(Fe,Mn)$ phase. Details on area fraction and shape as well as the types of occurring phases are summarized in **Tab. 5.2**.

Tab. 5.2. Fraction, shape, and type of the primary phases in S-C cast samples, evaluated by automated feature analysis.

	f_{total} [%]	f_{bright} [%]	f_{dark} [%]	Fe/Mn	SF	$Al_3(Fe,Mn)$	$Al_6(Fe,Mn)$	$Al_{15}(Fe,Mn)_3Si_2$
LFe-LMn	0.90 ± 0.12	0.42 ± 0.24	0.48 ± 0.12	5.0 ± 1.0	1.78 ± 1.24	yes	no	no
LFe-HMn	1.48 ± 0.26	0.96 ± 0.33	0.52 ± 0.07	0.6 ± 0.4	3.06 ± 2.81	little	little	yes
HFe-LMn	1.46 ± 0.43	1.00 ± 0.34	0.46 ± 0.09	7.9 ± 2.4	2.08 ± 1.37	yes	no	no
HFe-HMn	4.09 ± 0.78	3.49 ± 0.93	0.60 ± 0.15	0.8 ± 0.5	3.37 ± 2.80	little	yes	no

f_{total} , f_{bright} , f_{dark} : total area fraction of primary phases or area fractions of bright and dark phases respectively; Fe/Mn: Ratio of iron to manganese contents of the bright phase particles; SF: shape factor.

Fig. 5.1 (b),(d) show the resulting primary phase distribution for LFe-HMn and HFe-HMn. With an increase in Mn contents (while keeping the Fe at 0.1 wt.%) the intermetallic particles show a significant change in shape and size (comparing **Fig. 5.1 (a),(b)**). The above-mentioned needle-shaped, bright phase coarsens and tends to form structures of more complex geometry (**Fig. 5.1 (b)** (4)). EDX feature analysis also shows weak Si concentration (about 3 wt.%) in some of the primary phases of the LFe-HMn alloy. While the Si level is still too low to indicate a formation of the stoichiometric $Al_{15}(Fe,Mn)_3Si_2$ phase, it implies the formation of some different AlFeSi-phase type.

The behavior of shape alteration is even more distinct in the HFe-HMn sample, where the primary intermetallics form networks of coarse phases. The platelet-like or Chinese script structures are uniformly found throughout the sample (**Fig. 5.1 (d)** (7)). Chemical analysis of the bigger primary phases using EDX indicates exclusively the $Al_6(Fe,Mn)$ phase forms because of the enhanced Mn content HFe-HMn.

The analysis of the dark phase shows Mg_2Si particles for both LFe-HMn and HFe-HMn. Besides the majority of particles, some small high Fe containing particles with composition closer to $Al_3(Fe,Mn)$ were found in both alloys. As apparent in **Fig. 5.1 (b)** (5), the shape and size of those precipitates is different to the samples LFe-LMn and HFe-LMn.

The data given in **Tab. 5.2**, including over 1000 particles per sample, confirm the visual trend of primary phase formation in the samples. While the amount of dark appearing Mg_2Si phases is not much different in all four samples, the total phase fraction is influenced only by the Fe- and Mn-containing phases. Surprisingly, both samples with either increased Fe or Mn contents show approximately equal fractions of Al-Fe or Al-Mn particles. Only the combined increase of Fe and Mn in sample HFe-HMn results in stronger primary precipitation and, therefore, a higher area fraction.

The Fe/Mn-ratio of the intermetallics is in good agreement with the samples alloying contents. Moreover, the higher Fe bearing phases show a clear tendency to form elongated phases, which is indicated by SF to a certain degree. However, since the $\text{Al}_6(\text{Fe,Mn})$ particles in higher Mn containing alloys are also irregularly shaped, the shape factors can only be considered in combination with the micrographs.

5.3.1.2 Near Rapid Cooling during Solidification (NR-C Cast),

The results of the NR-C cast samples are shown in **Fig. 5.2**. The faster cooling clearly results in a smaller casting cell size and smaller primary phase particles by a factor of approximately 5 to 10. Beside this refinement there are lower area fractions of Mg_2Si phase observable (compared to the S-C samples), which is also stated in **Tab. 5.3**. For an easier comparison see **Tab. A5.1**, which contains the fundamental data on the primary phases of various sample states.

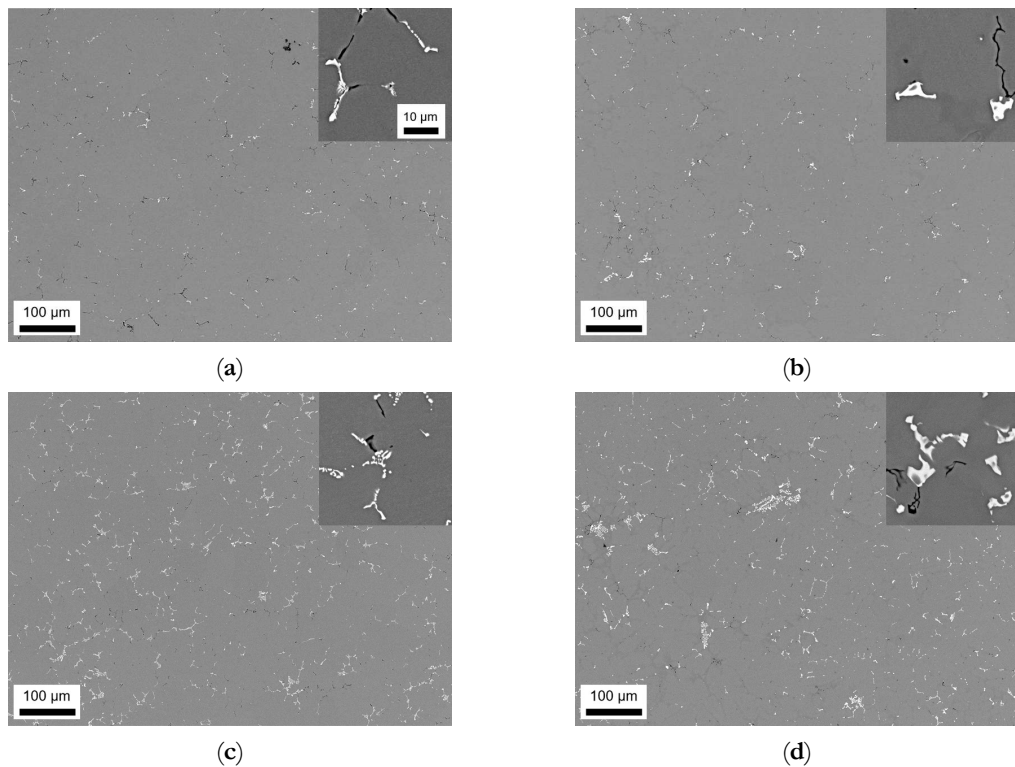


Fig. 5.2. Casting microstructure of NR-C cast samples; (a) LFe-LMn, (b) LFe-HMn, (c) HFe-LMn, (d) HFe-HMn; the insert scale bar in (b–d) is the same as for (a).

Tab. 5.3. Fraction, shape, and type of the primary phases in S-C cast samples, evaluated by automated feature analysis.

	f_{total} [%]	f_{bright} [%]	f_{dark} [%]	Fe/Mn	SF	$\text{Al}_3(\text{Fe,Mn})$	$\text{Al}_6(\text{Fe,Mn})$	$\text{Al}_{15}(\text{Fe,Mn})_3\text{Si}_2$
LFe-LMn	0.83 ± 0.16	0.39 ± 0.02	0.44 ± 0.14	6.1 ± 2.5	1.57 ± 1.01	yes	no	no
LFe-HMn	1.23 ± 0.21	0.73 ± 0.14	0.50 ± 0.07	0.7 ± 0.3	1.54 ± 1.06	no	little	yes
HFe-LMn	2.24 ± 0.42	1.89 ± 0.29	0.35 ± 0.13	8.6 ± 3.5	2.30 ± 2.42	yes	no	no
HFe-HMn	2.31 ± 0.13	1.90 ± 0.18	0.41 ± 0.05	1.3 ± 0.3	2.56 ± 2.17	no	yes	yes

f_{total} , f_{bright} , f_{dark} : total area fraction of primary phases or area fractions of bright and dark phases respectively; Fe/Mn: Ratio of iron to manganese contents of the bright phase particles; SF: shape factor.

The general trend of phase formation in LFe-LMn alloy is similar to the results for the S-C conditions during casting. The microstructure shows small needle-shaped phases with a higher Fe/Mn ratio (**Tab. 5.3**) and a netlike structure. Since the total area fraction of primary precipitates for this NR-C sample do not very much differ from the S-C numbers given in **Tab. 5.2**, the increase in Fe/Mn ratio of the particles implicates a higher Mn concentration in the aluminum matrix. The EDX data denote again the $\text{Al}_3(\text{Fe,Mn})$ phase in the NR-C cast conditions.

For the LFe-HMn alloy in **Fig. 5.2 (b)**, a slight alteration of the microstructure is found with increased cooling rate. The primary phases tend to form more compact and spherical blocks without the dense netlike structure. Some particles seem disconnected in the 2D micrographs (Chinese-script structures), which also affects the SF data given in **Tab. 5.3**. Closer analysis of the phases reveals the $\text{Al}_6(\text{Fe,Mn})$ phase in addition to $\text{Al}_{15}(\text{Fe,Mn})_3\text{Si}_2$ type, but the EDX analysis does not reflect the exact stoichiometry.

In HFe-LMn (**Fig. 5.2 (c)**), more Chinese-script phases instead of needles are found within the NR-C samples, whereas the chemical composition still points out $\text{Al}_3(\text{Fe,Mn})$ phase type. The HFe-HMn alloy in **Fig. 5.2 (d)** also shows, besides the mentionable refinement, a trend towards spheroidization of the features. The phases were identified to be most likely $\text{Al}_6(\text{Fe,Mn})$ with no remaining $\text{Al}_3(\text{Fe,Mn})$ phase. Interestingly, similar AlFeSi phases are found in HFe-HMn alloy and LFe-HMn.

The area fractions and Fe/Mn ratios of the samples show further interesting results. For both high Mn containing samples, the total area fractions are lower for the NR-C conditions, whereas the number of primary phases increases in the HFe-LMn alloy. Since the Fe/Mn ratio of all NR-C samples is higher compared to the S-C samples (**Tab. 5.2**), a clear trend of inhibited Mn precipitation or increased Mn in solid solution can be assumed.

5.3.2 Microstructural Evolution during Homogenization

This section describes the microstructural changes upon two different homogenization treatments (500 and 550 °C). Each subsection includes the description of both the primary and secondary phase evolution as well as phase fractions and micrographs.

5.3.2.1 Microstructure after Homogenization at 500 °C of S-C and NR-C Cast Samples

The homogenization leads to a slight decrease in total area fraction of the primary phases. In **Fig. 5.3**, coarsened Al-Fe or Al-Mn phases are observed compared to as-cast conditions. Especially LFe-LMn and HFe-HMn samples show distinct coarsening of the before fine $\text{Al}_3(\text{Fe,Mn})$ needles. For both high-Mn alloys (**Fig. 5.3 (b),(d)**), the smaller precipitates show more spherical shaped structures, but especially the HFe-HMn alloy shows some increase of the Chinese-script structures.

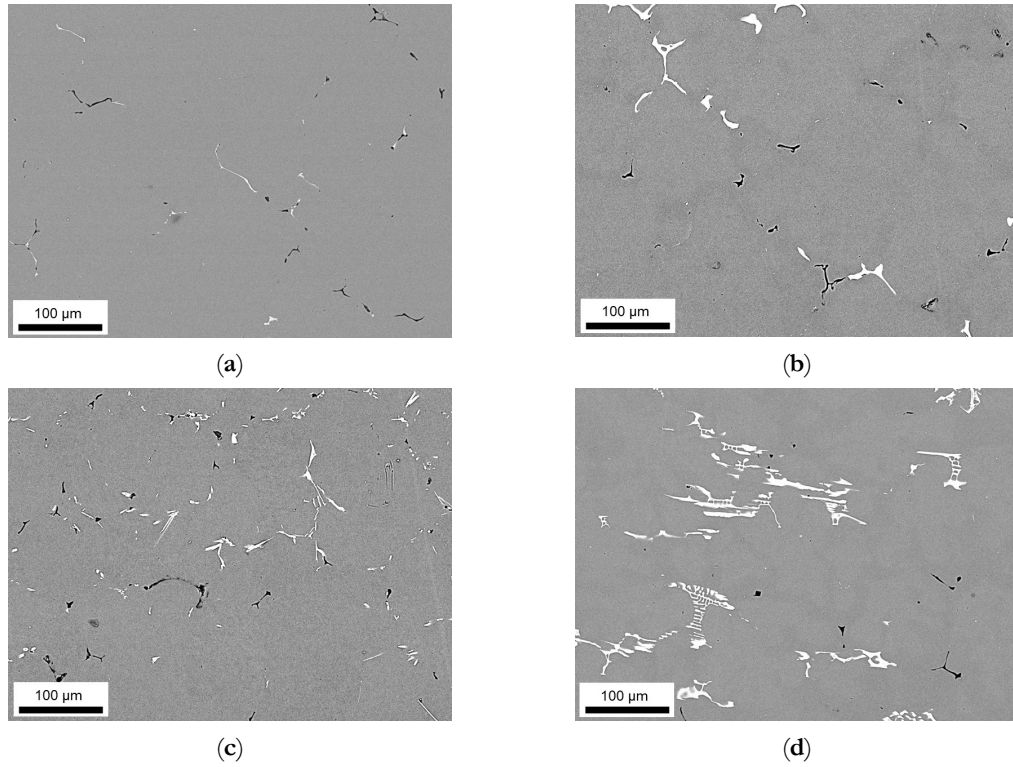


Fig. 5.3. Microstructure and primary phase distribution of S-C cast samples after homogenization at 500 °C; (a) LFe-LMn, (b) LFe-HMn, (c) HFe-LMn, (d) HFe-HMn.

The visible trends of phase alteration are confirmed by the data given in **Tab. 5.4**. In comparison to the as-cast samples, the total primary phase fraction and simultaneously both the Fe/Mn-bearing as well as Mg_2Si phases are decreased. Concerning the Fe/Mn-ratio, the high Mn containing alloys show no significant changes, although the standard deviation becomes significantly smaller. The two high Fe containing alloys show some slight increase in the Fe/Mn-ratio. Detailed consideration reveals the increase of average Fe contents in the primary phases but no significant change in Mn concentration. The EDX feature mapping indicates no transformation of primary phases. The changes in shape are also indicated by the slight decrease of SF comparing the results to the S-C cast samples in **Tab. 5.2** and **Tab. 5.4**.

Tab. 5.4. Fraction, shape, and composition of the primary phases after homogenization at 500 °C (S-C and NR-C samples).

		f_{total} [%]	f_{bright} [%]	f_{dark} [%]	Fe/Mn	SF
S-C cast	LFe-LMn	0.71 ± 0.11	0.30 ± 0.03	0.40 ± 0.08	5.7 ± 2.0	2.10 ± 1.73
	LFe-HMn	1.16 ± 0.36	0.79 ± 0.33	0.37 ± 0.03	0.6 ± 0.3	2.80 ± 2.84
	HFe-LMn	1.22 ± 0.08	0.87 ± 0.27	0.35 ± 0.19	8.5 ± 1.0	1.93 ± 1.40
	HFe-HMn	2.67 ± 0.27	2.25 ± 0.20	0.42 ± 0.07	0.8 ± 0.2	2.40 ± 1.88
NR-C cast.	LFe-LMn	0.74 ± 0.15	0.36 ± 0.12	0.38 ± 0.03	4.5 ± 1.7	1.88 ± 1.17
	LFe-HMn	0.91 ± 0.47	0.71 ± 0.37	0.20 ± 0.10	0.6 ± 0.2	1.51 ± 0.75
	HFe-LMn	1.53 ± 0.38	1.30 ± 0.30	0.33 ± 0.09	8.6 ± 2.7	2.00 ± 1.12
	HFe-HMn	2.82 ± 0.62	2.39 ± 0.52	0.42 ± 0.10	1.1 ± 0.3	2.27 ± 1.69

f_{total} , f_{bright} , f_{dark} : total area fraction of primary phases or area fractions of bright and dark phases respectively; Fe/Mn: ratio of iron to manganese contents of the bright phase particles; SF: shape factor.

Fig. 5.4 shows the micrographs for the NR-C cast samples homogenized at 500 °C. The microstructural characterization leads to results similar as for the S-C cast samples. However, the HFe-HMn sample shows coarsening and an increase in total primary phase fraction (**Fig. 5.4 (d)**). Additionally, the small number of Chinese-script phases found in the as-cast state is further reduced, since there are no such features observable anymore. The micrographs in **Fig. 5.4** (mainly HFe-HMn in **Fig. 5.4 (d)**) show small, circular black phases which were identified as pores using EDX (matrix signal).

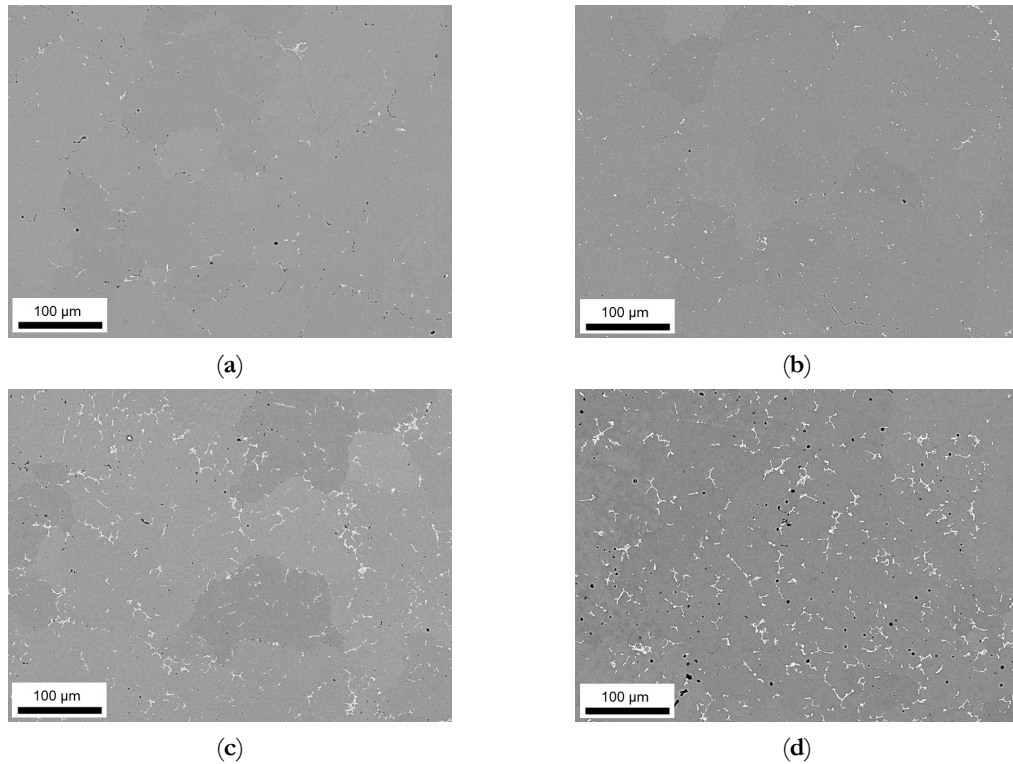


Fig. 5.4. Microstructure and primary phase distribution of NR-C cast samples after homogenization at 500 °C; (a) LFe-LMn, (b) LFe-HMn, (c) HFe-LMn, (d) HFe-HMn.

Comparing primary phase data of **Tab. 5.2** and **Tab. 5.4**, tendencies of reduction in total phase fraction can be observed for all samples except HFe-HMn. Interestingly, the Fe/Mn ratio of the precipitates is modified to lower values, which contrasts with S-C cast conditions. The EDX data denote slight concentrations of Mn in connection with reductions in Fe contents, but no phase transformations in general. Finally, the primary phases do not show the clear trend of spheroidization as noticeable before for the S-C cast and homogenized samples.

Besides the alteration of the primary phase number density and size, the homogenization initiates the formation of secondary phases. The analysis of dispersoids followed the methods described in section 5.2 using ImageJ software. **Fig. 5.5** and **Fig. 5.6** show the microstructural features after homogenization at high magnification for S-C cast and NR-C cast samples, respectively. In both figures, clear trends of dispersoid formation in dependence on the alloying contents are observable. The obtained blurred contrast variations in the background in **Fig. 5.5** are attributed to the

preparation and not to microstructural conditions in the sample. However, the emergence of the contrast is not yet clarified.

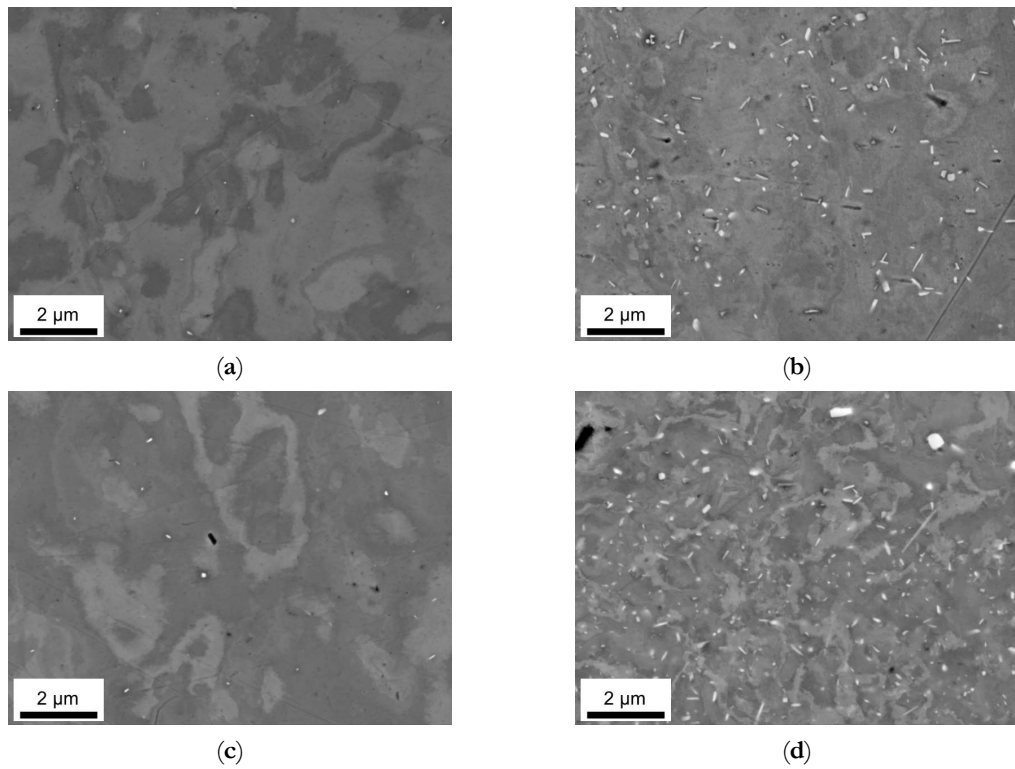


Fig. 5.5. Secondary phase distribution of S-C cast samples after homogenization at 500 °C; (a) LFe-LMn, (b) LFe-HMn, (c) HFe-LMn, (d) HFe-HMn.

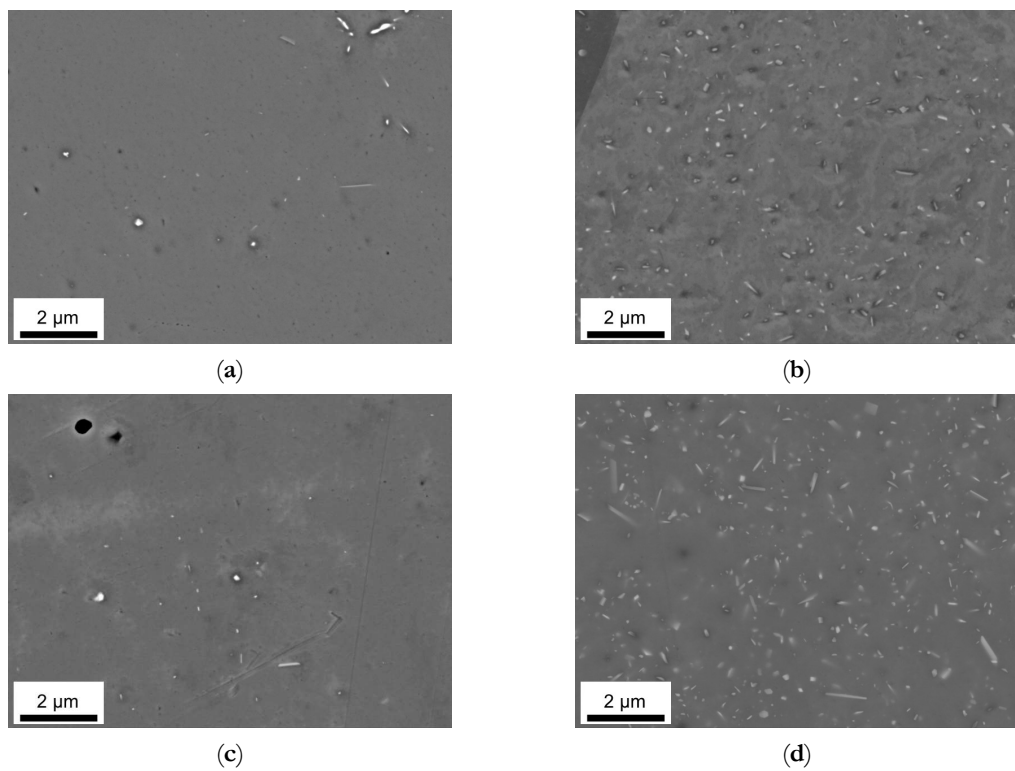


Fig. 5.6. Secondary phase distribution of NR-C cast samples after homogenization at 500 °C; (a) LFe-LMn, (b) LFe-HMn, (c) HFe-LMn, (d) HFe-HMn.

For both low Mn alloys, the number density of secondary particles (given in **Tab. 5.5**) is very low. While there is no difference in secondary phase precipitation perceivable with the change in Fe contents for LFe-LMn and HFe-LMn for the homogenized S-C cast samples, the total area fraction of dispersoids for the HFe-LMn alloy is approximately two times higher in the NR-C cast LFe-LMn alloy after homogenization. The micrographs in **Fig. 5.5** and **Fig. 5.6 (a),(c)** illustrate this trend. Furthermore, they show a slight modification of dispersoids shape from spheroidal to rod-shaped with the different casting conditions. This change is tabulated in the mean aspect ratio (AR) of the particles in **Tab. 5.5**, where an increase of AR is especially noticeable for LFe-LMn.

Tab. 5.5. Secondary phase morphology and volume fraction in S-C and NR-C cast samples homogenized at 500 °C.

		f_D [vol. %]	r [nm]	AR
S-C cast	LFe-LMn	0.021	59	0.65
	LFe-HMn	0.756	87	0.57
	HFe-LMn	0.024	74	0.55
	HFe-HMn	1.440	84	0.57
NR-C cast.	LFe-LMn	0.061	87	0.57
	LFe-HMn	0.620	71	0.58
	HFe-LMn	0.117	74	0.65
	HFe-HMn	2.341	86	0.57

f_D : volume fraction of dispersoids; r : average radius of the dispersoid particles; AR: aspect ratio of the dispersoids.

In both alloys with high Mn content, the dispersoid formation is clearly visible (**Fig. 5.5 (b),(d)**). Comparing the NR-C and S-C casting conditions (see **Fig. 5.5** and **Fig. 5.6**), the only clearly observable difference is a slight refinement of the secondary phase particles for the LFe-HMn alloy. This accords with the similar total area fraction of the differently casted samples, while r decreases significantly (**Tab. 5.5**). The ARs of the samples show no change and confirm the rod-shape of the particles.

The results for HFe-HMn are in good agreement with the statements for LFe-HMn above. The micrographs (**Fig. 5.5** and **Fig. 5.6 (d)**) depict high similarities of the dispersoids shape in dependence on the prior casting procedure, whereas the volume fraction is clearly higher for NR-C casting conditions, which is also verified by the data of the total volume fractions of dispersoids in **Tab. 5.5**. While there is no difference in the secondary phase morphology deducible from the AR data given, a small increase in the radius of the dispersoids is obtained for the NR-C conditions.

5.3.2.2 Microstructure after Homogenization at 550 °C of S-C and NR-C Cast Samples

Most of the typical primary phase particles found in **Fig. 5.1** persist the high temperature homogenization. However, a large extent of primary Mg_2Si is dissolved, evident in **Fig. 5.7 (a)–(d)**

by less dark appearing phases and **Tab. 5.6** showing a large reduction in the dark area fractions due to homogenization for samples cast under S-C conditions.

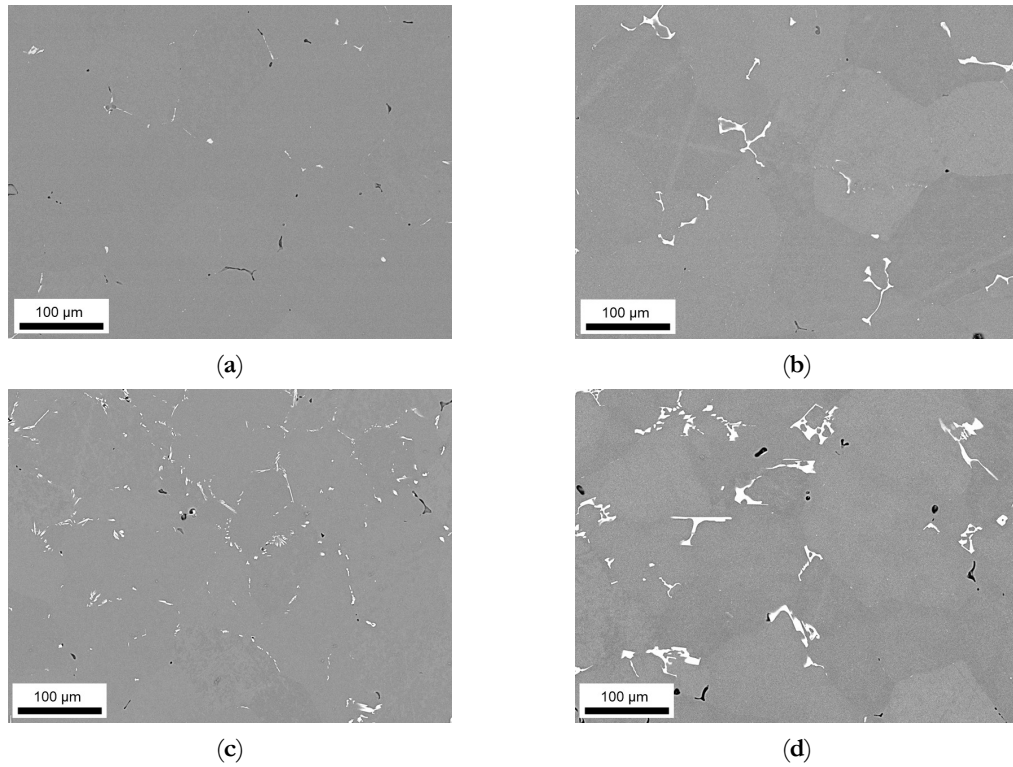


Fig. 5.7. Microstructure and primary phase distribution in S-C cast samples after homogenization at 550 °C; (a) LFe-LMn, (b) LFe-HMn, (c) HFe-LMn, (d) HFe-HMn.

Tab. 5.6. Fraction, shape, and composition of the primary phases after homogenization at 550 °C (S-C and NR-C samples).

		f_{total} [%]	f_{bright} [%]	f_{dark} [%]	Fe/Mn	SF
S-C cast	LFe-LMn	0.51 ± 0.14	0.28 ± 0.05	0.23 ± 0.09	4.3 ± 1.8	1.83 ± 1.38
	LFe-HMn	1.06 ± 0.05	0.90 ± 0.01	0.16 ± 0.04	0.3 ± 0.2	1.84 ± 1.57
	HFe-LMn	1.29 ± 0.21	1.00 ± 0.14	0.29 ± 0.07	7.9 ± 1.3	1.71 ± 1.46
	HFe-HMn	3.54 ± 0.32	3.22 ± 0.20	0.32 ± 0.12	0.8 ± 0.2	2.80 ± 2.68
NR-C cast	LFe-LMn	0.73 ± 0.20	0.43 ± 0.18	0.30 ± 0.02	3.1 ± 1.8	1.45 ± 0.67
	LFe-HMn	0.95 ± 0.05	0.86 ± 0.09	0.09 ± 0.04	0.3 ± 0.2	1.42 ± 0.73
	HFe-LMn	1.63 ± 0.50	1.37 ± 0.41	0.26 ± 0.10	7.1 ± 2.9	1.81 ± 1.17
	HFe-HMn	3.16 ± 0.68	2.90 ± 0.58	0.27 ± 0.11	0.5 ± 0.2	1.76 ± 1.15

f_{total} , f_{bright} , f_{dark} : total area fraction of primary phases or area fractions of bright and dark phases respectively; Fe/Mn: ratio of iron to manganese contents of the bright phase particles; SF: shape factor.

In the LFe-LMn alloy (**Fig. 5.7 (a)**), the $\text{Al}_3(\text{Fe},\text{Mn})$ precipitates do not show distinct alteration. The micrograph indicates the tendency of the primary phases to become finer and spheroidized with the homogenization. The data given in **Tab. 5.6** show, besides a reduction in overall primary phase fraction, a slight decrease in Fe/Mn ratio, whereas the shape factor of the particles remain nearly unchanged. This change in Fe/Mn ratio and the atomic ratios point towards a beginning phase transformation from $\text{Al}_3(\text{Fe},\text{Mn})$ to $\text{Al}_6(\text{Fe},\text{Mn})$.

In the LFe-HMn alloy (**Fig. 5.7**), the typical $\text{Al}_{15}(\text{Fe,Mn})_3\text{Si}_2$ primary phases are conserved. In addition to the original primary phases, some medium sized (few microns) secondary phases precipitate during homogenization. With its slightly raised Si concentration, these phases exhibit correlations to $\alpha\text{-Al}_{15}(\text{Fe,Mn})_3\text{Si}_2$. The data displayed in **Tab. 5.6** show, apart from the considerable decrease in Fe/Mn ratio, a modification of their shape in contrast to the as-cast state.

While the HFe-LMn alloy in **Fig. 5.7 (c)** shows some equivocal refinement of the needle-like $\text{Al}_3\text{F}(\text{Fe,Mn})$ precipitates, the network structure of phases in HFe-HMn becomes looser and particles less branched. As stated in **Tab. 5.6**, the phases merely change in shape and number density. In neither of both high Fe alloys are phase transformations traceable.

For the NR-C cast and homogenized alloys (**Fig. 5.8 (a)–(d)**), the trend of Mg_2Si dissolution is retained. The types of phases obtained conform with the initial situation in the samples, at which no transformations are perceived.

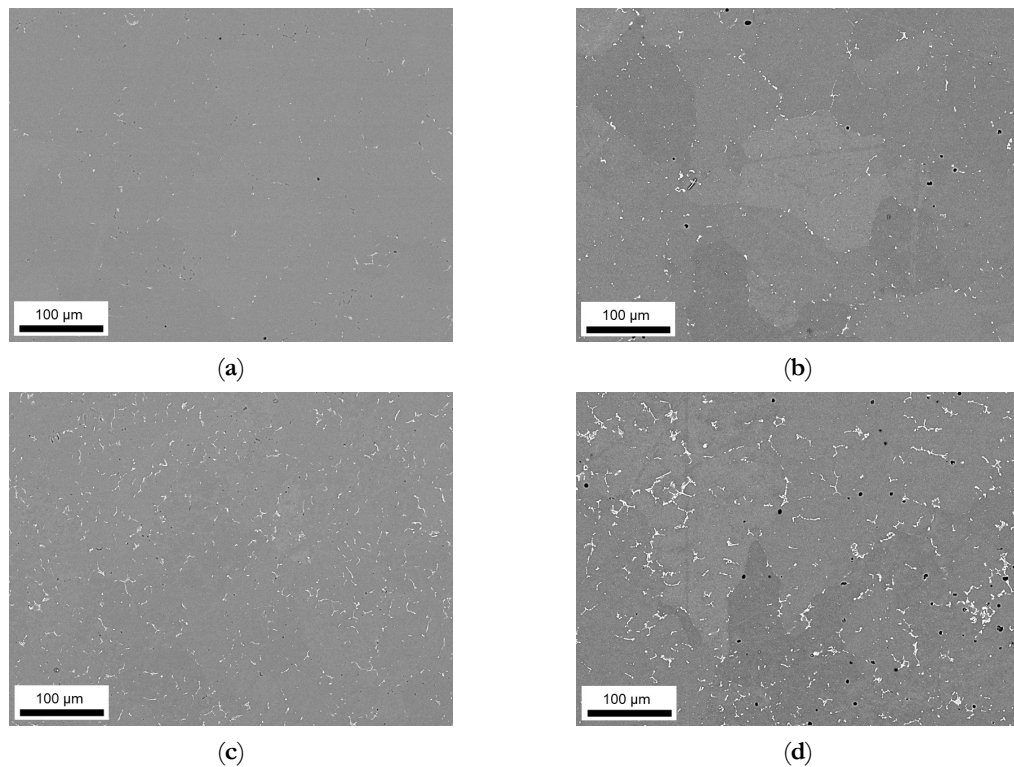


Fig. 5.8. Microstructure and primary phase distribution in NR-C cast samples after homogenization at 550 °C; (a) LFe-LMn, (b) LFe-HMn, (c) HFe-LMn, (d) HFe-HMn.

The LFe-LMn alloy does not show significant differences induced by the higher temperature homogenization, noticeable when comparing **Fig. 5.8 (a)** to **Fig. 5.2 (a)** or **Fig. 5.4 (a)**. According to **Tab. 5.6**, the Fe/Mn ratio decreases significantly, and the shape factor indicates weak spheroidization. The reduction of the total primary phase fraction can be attributed to Mg_2Si dissolution.

For the LFe-HMn alloy, refinement of the former plate-like structures can be observed. According to the change in Fe/Mn ratio (compare **Tab. 5.2** and **Tab. 5.6**), an integration of solute Mn from the matrix into the phases is to be assumed, as the average Mn level in the primary phases rises.

For both high-Fe variants, a looser structured network of intermetallic phases can be noticed. A reduction in Fe/Mn ratios is perceivable for both alloys. While the total fraction of primary phases is reduced or at least kept in the same range for HFe-LMn, the alloy with high Fe and high Mn contents exhibits an increase of the total area fraction. The reduction of the shape factor values for both alloys portends spheroidization of the particles (**Tab. 5.6**).

Fig. 5.9 and **Fig. 5.10** show the secondary phase evolution as a result of the 550 °C homogenization in high resolution for S-C and NR-C cast material, respectively. The precipitation of the dispersoids shows similar results concerning the dependence on Fe and Mn alloying contents as after the 500 °C homogenization. From the micrographs in **Fig. 5.9** and **Fig. 5.10**, coarsening of the secondary phases is perceptible at higher temperatures, while the block- or rod-shape for high Mn containing alloys is preserved.

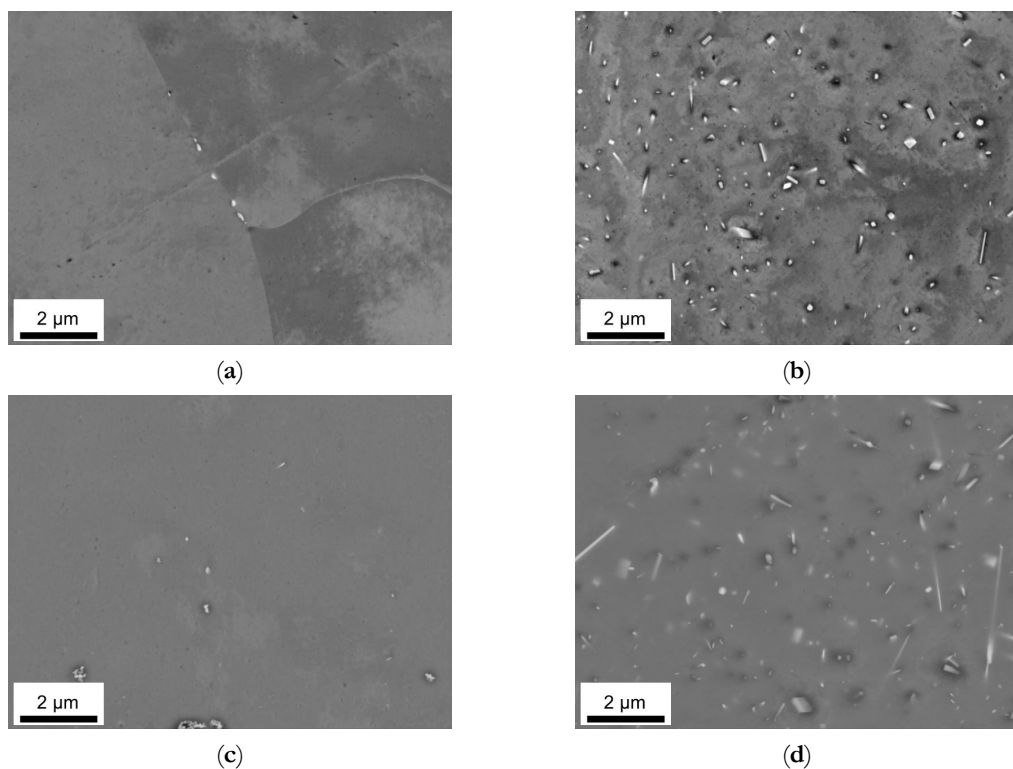


Fig. 5.9. Secondary phase distribution in S-C cast samples after homogenization at 550 °C; (a) LFe-LMn, (b) LFe-HMn, (c) HFe-LMn, (d) HFe-HMn.

Data on secondary phase number density as well as size and shape are given in **Tab. 5.7** (or in **Tab. A5.2** for easier comparison to the 500 °C homogenization). The total area fraction increases for the HFe-LMn alloy cast under NR-C conditions, while the area fractions of the other alloys do not show variations with the cooling rate.

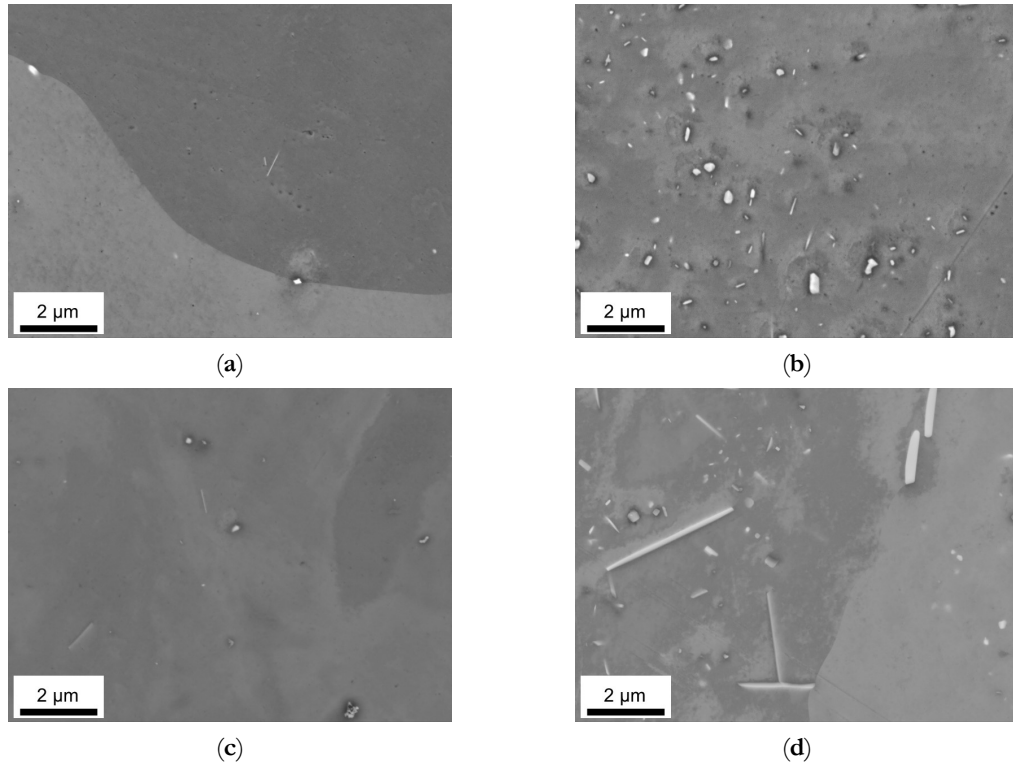


Fig. 5.10. Secondary phase distribution of NR-C cast samples after homogenization at 550 °C; (a) LFe-LMn, (b) LFe-HMn, (c) HFe-LMn, (d) HFe-HMn.

Tab. 5.7. Secondary phase morphology and volume fraction in S-C and NR-C cast samples homogenized at 550 °C.

		f_D [vol. %]	r [nm]	AR
S-C cast	LFe-LMn	0.047	144	0.56
	LFe-HMn	1.036	124	0.55
	HFe-LMn	0.108	74	0.58
	HFe-HMn	2.252	123	0.57
NR-C cast.	LFe-LMn	0.062	108	0.60
	LFe-HMn	0.741	105	0.54
	HFe-LMn	0.217	126	0.59
	HFe-HMn	2.293	158	0.51

f_D : volume fraction of dispersoids; r : average radius of the dispersoid particles; AR: aspect ratio of the dispersoids.

Coarsening of the dispersoids after homogenization at 550 °C is affirmed by the average radii (note the values in **Tab. 5.5**). Furthermore, the mix of high Fe and high Mn contents in combination with higher cooling rates results in the formation of micron sized, rod-shaped secondary phases, which is quantified by the reduced aspect ratio (**Fig. 5.10** (d)).

5.3.2.3 Phase Characterization Using TEM

To verify the composition and type of the obtained primary and secondary phases with the SEM-EDX feature mappings and point analyses, TEM measurements were performed on the HFe-HMn alloy. The resulting TEM EDX maps for the Fe, Mn and Si signal are shown in **Fig. 5.11**.

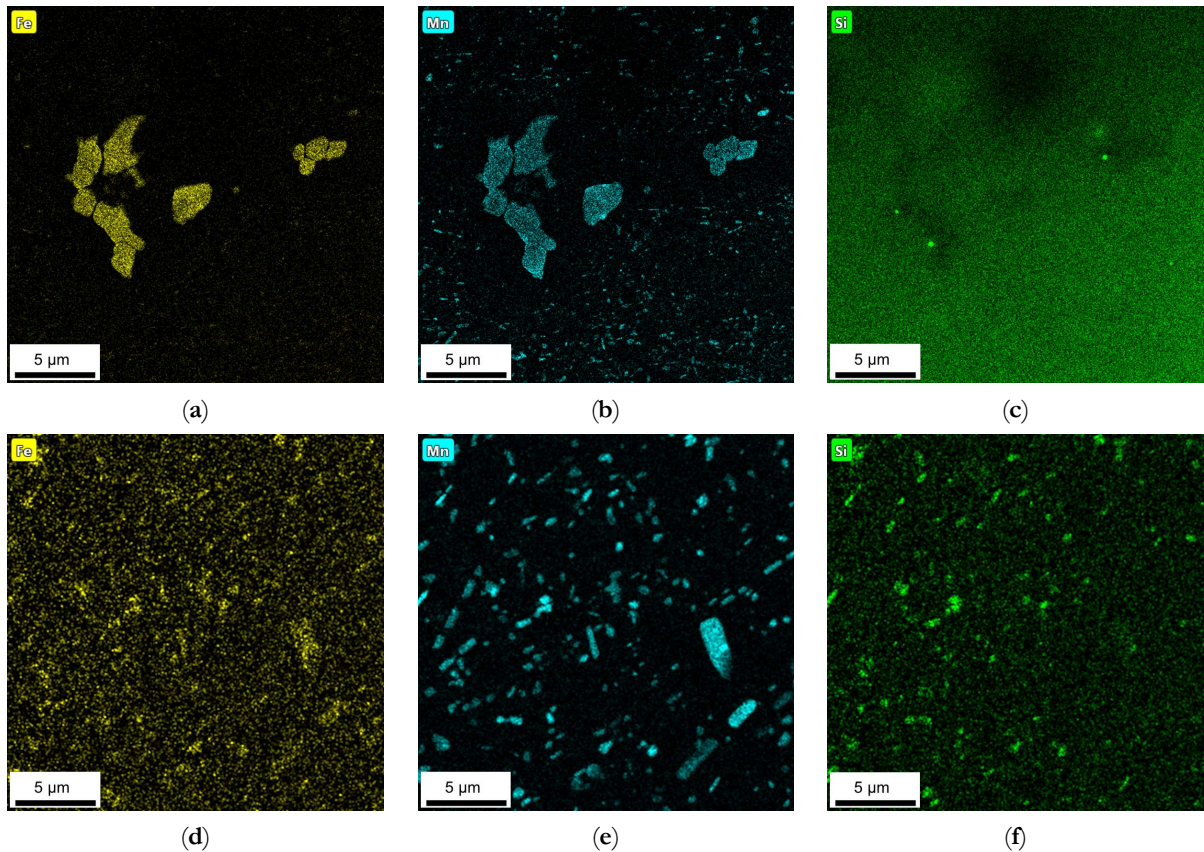


Fig. 5.11. EDX maps of the HFe-HMn alloys with NR-C (a–c) or S-C (d–f) casting conditions after homogenization at 500 °C from TEM measurements; (a,d): Fe map, (b,e) Mn map, (c,f) Si map.

The micron sized primary phase particles show enhanced intensities of Fe and Mn, while there is no evidence of Si. The Fe distributions shown in **Fig. 5.11** (a),(d) further indicate the integration of iron in secondary phase particles. However, as shown in **Fig. 5.11** (b),(e), the elemental allocation of manganese reveals a high number of dispersoids without Fe. Meanwhile, **Fig. 5.11** (c),(f) depict the general distribution of silicon in the sample's microstructural features. No indications for Si enrichment are visible in any of the primary or secondary phases in the NR-C cast HFe-HMn alloy (**Fig. 5.11** (c)). However, fine Si containing dispersoids are present in the homogenized S-C samples (**Fig. 5.11** (f)).

5.3.3 Thermodynamic Calculations

In addition to the experimental data given in Sections 5.3.1 and 5.3.2, this section provides information on the phase formation computed using the thermodynamic database PanAl2019. The simulation was performed for the four different alloys used in this study and the results are shown in **Tab. 5.8**. Each column and row give the fractions of elements (in wt.%) or phases (in vol.%) present after casting (approximated by a nonequilibrium Scheil calculation) and 550 °C homogenization (approximated by equilibrium calculation).

Tab. 5.8. Results of the thermodynamic calculations using Pandat software for the alloys investigated.

	Fe in Fcc $\times 10^{-3}$ [wt. %] Nonequi./Equi.	Mn in Fcc [wt. %] Nonequi./Equi.	$Al_{13}(Fe,Mn)_4$ [vol. %] Nonequi./Equi.	$Al_{15}(Fe,Mn)_3Si_2$ [vol. %] Nonequi./Equi.	$Al_6(Fe,Mn)$ [vol. %] Nonequi./Equi.
LF _{Fe} -LM _n	7.6/4.7	0.195/0.092	0.20/-	-	-/0.54
LF _{Fe} -HM _n	7.0/1.0	0.700/0.257	0.08/-	0.31/0.90	0.87/1.57
HFe-LM _n	17.0/6.7	0.165/0.066	0.77/0.56	-/0.51	-
HFe-HM _n	15.0/5.2	0.651/0.233	0.67/0.20	0.40/1.62	0.78/1.28

Fe,Mn in fcc: solute content of iron and manganese in the aluminum matrix; nonequi./equi.: calculated contents for nonequilibrium (Scheil) conditions/calculated contents for equilibrium conditions at 550 °C.

The first two columns of **Tab. 5.8** contain the information of solute elements Fe and Mn in the fcc matrix. Generally, the significantly higher solute content of manganese is evident in all alloys. The fractions of the dissolved elements change with the general alloying contents. Furthermore, there is an interdependent influence of Fe and Mn observed, since higher solution of one of the elements reduces the solubility of the other one. The comparison of nonequilibrium and equilibrium calculations shows the considerable reduction of solute contents, especially for the higher Mn alloyed samples.

Moreover, **Tab. 5.8** contains the information of primary and secondary phase evolution in terms of the thermodynamic aspects. The LF_{Fe}-LM_n alloy in as-cast state only shows occurrence of $Al_3(Fe,Mn)$ (considered as equivalent to $Al_{13}(Fe,Mn)_4$ in Pandat). With the homogenization the primary phases are either dissolved or transformed, since in the equilibrium state only $Al_6(Fe,Mn)$ is predicted to remain. The volume fraction data also include the fine dispersed secondary phase particles, which in turn shows a very low precipitation of phases during homogenization in this alloy. The transformation of primary phases or the precipitation of dispersoids is also concordant with the decrease in solute contents of Fe and Mn in the LF_{Fe}-LM_n alloy. Similar results are obtained for the HFe-LM_n alloy. Primary phases before homogenization only consist of type $Al_3(Fe,Mn)$, which are transformed to some extent into Si containing $Al_{15}(Fe,Mn)_3Si_2$ but not into $Al_6(Fe,Mn)$. The total volume fraction of phases increases from nonequilibrium to equilibrium conditions on the expense of solute elements due to the formation of dispersoids either of type $Al_3(Fe,Mn)$ or $Al_{15}(Fe,Mn)_3Si_2$.

Considering the higher Mn containing alloys, different types of primary phases can occur, although the majority consists of $Al_6(Fe,Mn)$ for the low Fe variant. For higher Fe additions the volume fractions are almost evenly distributed among the different types of phases. With homogenization of the LF_{Fe}-HM_n sample, all $Al_3(Fe,Mn)$ particles are dissolved or transformed into other types. The strong precipitation of $Al_{15}(Fe,Mn)_3Si_2$ and $Al_6(Fe,Mn)$ as dispersoids takes place mainly at the expense of the solute Fe and Mn. The HFe-HM_n alloy shows, besides the distinct transformation or degradation of $Al_3(Fe,Mn)$, a strong tendency of secondary $Al_{15}(Fe,Mn)_3Si_2$ phase precipitation, even though $Al_6(Fe,Mn)$ also represents a significant phase fraction.

5.3.4 Soft Annealed State

The primary phases of the different alloys in the final soft annealed state (500 °C/5 min/H₂O) are compared for S-C (**Fig. 5.12**) and NR-C (**Fig. 5.13**) conditions, homogenized at 500 °C, and cold rolled to a CRD of 63%. Further micrographs for the various homogenization temperatures and cold rolling degrees are shown in the appendix to Section 5 from **Fig. A5.6–Fig. A5.11**. The primary phases are now fragmented and arranged in bands. Following the results of analyzed casting and homogenization samples, the area fraction of the primary phases depicts equal trends of increased number density with high Mn contents (comparing **Fig. 5.12** and **Fig. 5.13 (a)** to **Fig. 5.12** and **Fig. 5.13 (b)** or **Fig. 5.12** and **Fig. 5.13 (c)** to **Fig. 5.12** and **Fig. 5.13 (d)**) and increased sizes with high Fe contents (comparing **Fig. 5.12** and **Fig. 5.13 (a)** to **Fig. 5.12** and **Fig. 5.13 (c)** or **Fig. 5.12** and **Fig. 5.13 (b)** to **Fig. 5.12** and **Fig. 5.13 (d)**), and does not indicate significant changes during further rolling and soft annealing.

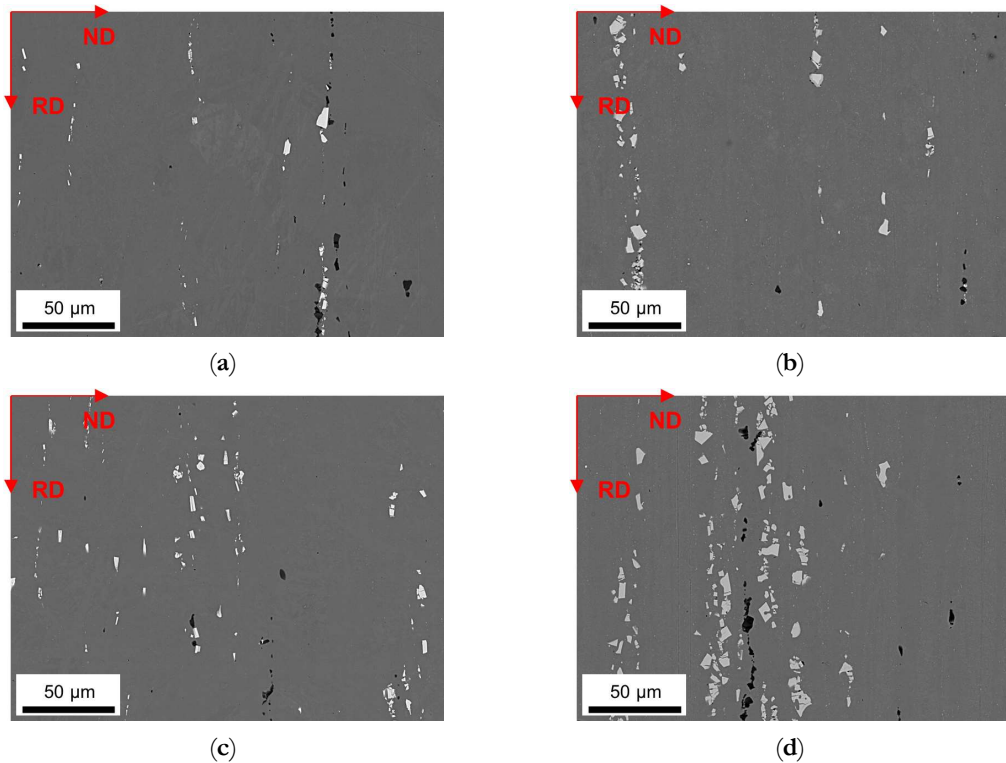


Fig. 5.12. Soft annealed microstructure of the alloys cast under S-C conditions, homogenized at 500 °C and cold rolled to a CRD of 63%; (a) LFe-LMn, (b) LFe-HMn, (c) HFe-LMn, (d) HFe-HMn; RD: rolling direction, ND: normal direction.

During rolling the rather needle- or rod-shaped particles in particular tend to align in the rolling direction. The initially different primary phase sizes (that result from the variations in the casting cooling rates) are retained even after final processing.

The alignment of the dispersoids in rolling direction is shown for exemplary sample states in **Fig. 5.14** and **Fig. 5.15**. The micrographs of the additional 24 sample states can be found in the appendix to Section 5 (**Fig. A5.12–Fig. A5.17**). The trends of favored dispersoid formation with increased Mn

contents (as observed after homogenization) are still clearly visible comparing **Fig. 5.14** or **Fig. 5.15** (a) to **Fig. 5.14** or **Fig. 5.15** (b). However, the figures indicate a slightly higher dispersoid number density with S-C cooling conditions in the soft annealed sample state.

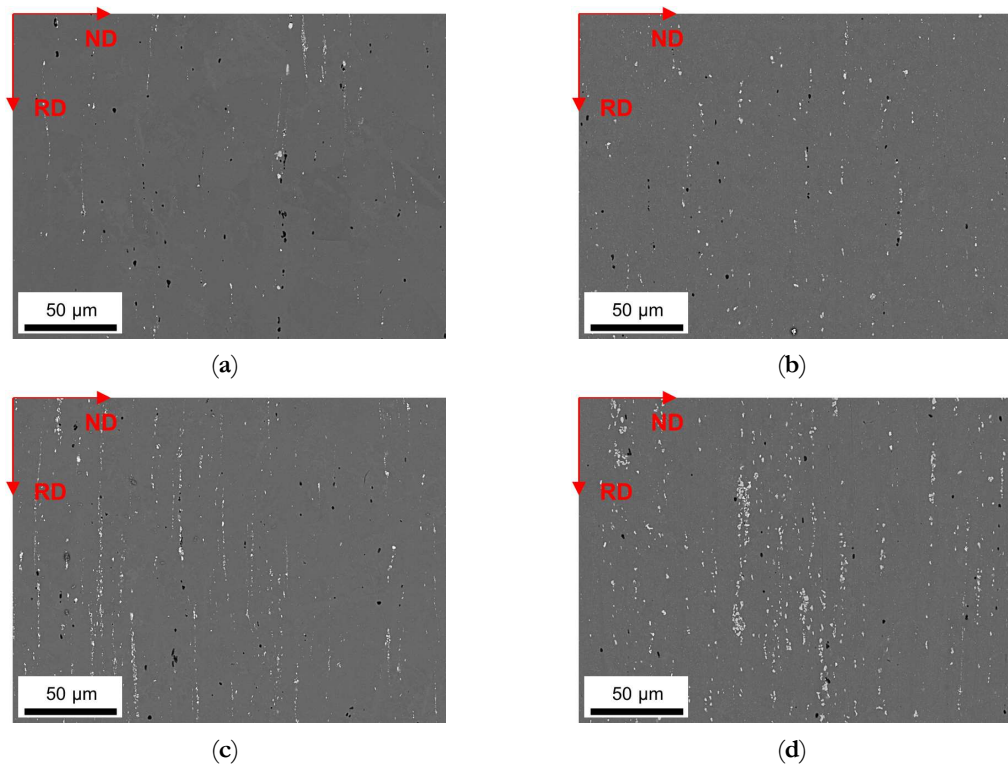


Fig. 5.13. Soft annealed microstructure of the alloys cast under NR-C conditions, homogenized at 500 °C and cold rolled to a CRD of 63%; (a) LFe-LMn, (b) LFe-HMn, (c) HFe-LMn, (d) HFe-HMn.

Additional information is given by the volume fractions and morphological parameters of the dispersoids in **Tab. 5.9** (S-C cast conditions; all sample states) and **Tab. 5.10** (NR-C cast conditions; all sample states). The higher average volume fraction for the S-C cast samples is verified. Comparing the data to the homogenized sample states (**Tab. 5.5** and **Tab. 5.7**), a clear trend towards lower volume fractions after further processing is obtained.

While the increase of the average dispersoid radius is still observed for the higher homogenization temperature, the total dispersoid radii are clearly shifted to lower values. The rod-shaped particle morphology is however still maintained as expressed by the AR data given in **Tab. 5.9** and **Tab. 5.10**.

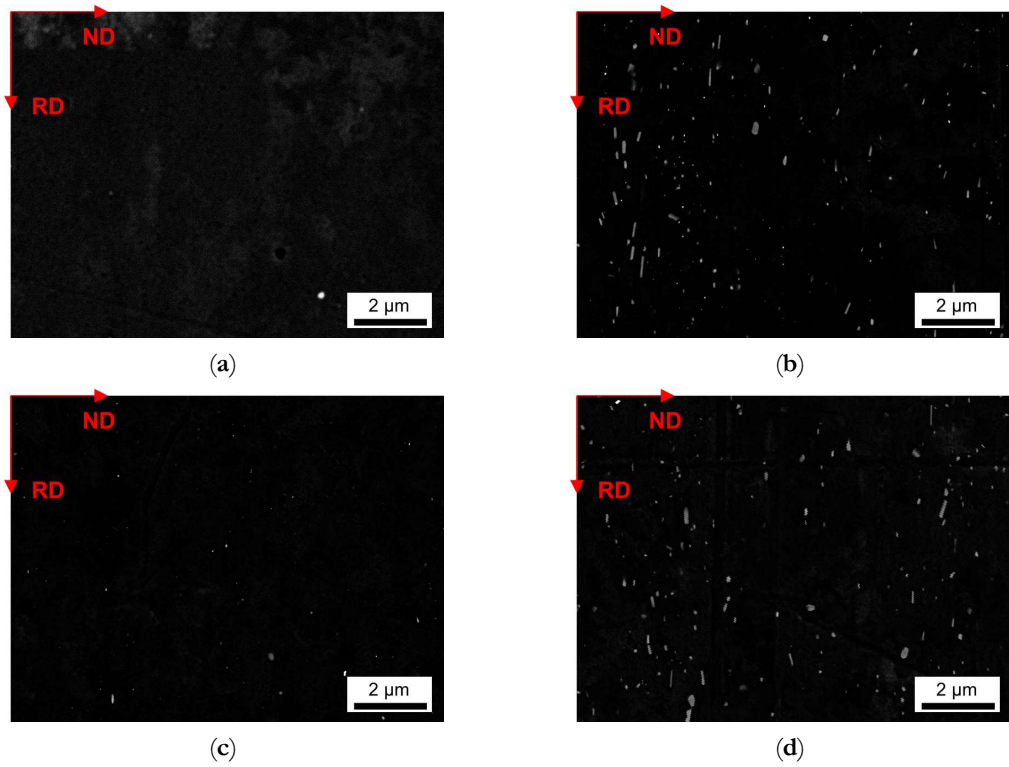


Fig. 5.14. Dispersoids in the soft annealed sample state cast under S-C conditions, homogenized at 500 °C and cold rolled to a CRD of 63%; (a) LFe-LMn, (b) LFe-HMn, (c) HFe-LMn, (d) HFe-HMn.

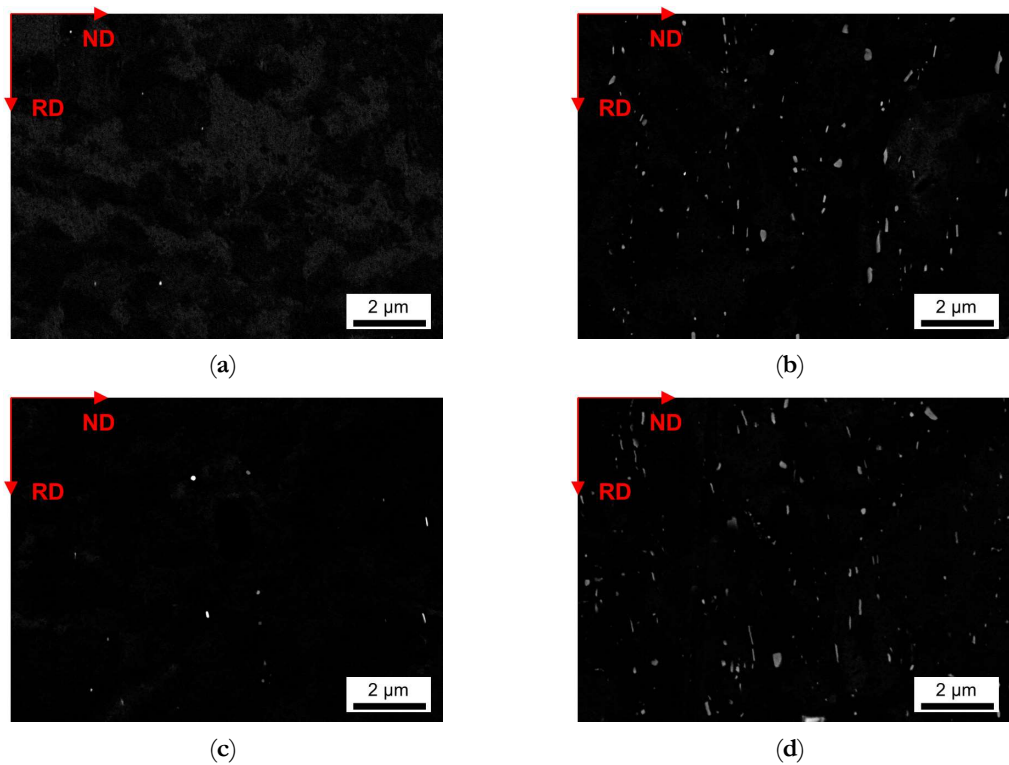


Fig. 5.15. Dispersoids in the soft annealed sample state cast under NR-C conditions, homogenized at 500 °C and cold rolled to a CRD of 63%; (a) LFe-LMn, (b) LFe-HMn, (c) HFe-LMn, (d) HFe-HMn.

Tab. 5.9. Secondary phase morphology and volume fraction in S-C cast, processed and soft annealed sample states.

Sample State		Alloy	f_D [vol. %]	r [nm]	AR
Homogenization	CRD				
500 °C	35%	LFe-LMn	0.01	78	0.60
		LFe-HMn	0.96	81	0.50
		HFe-LMn	0.01	45	0.57
		HFe-HMn	0.64	62	0.55
	63%	LFe-LMn	0.04	43	0.65
		LFe-HMn	0.75	61	0.51
		HFe-LMn	0.02	39	0.60
		HFe-HMn	0.63	58	0.55
550 °C	35%	LFe-LMn	0.03	75	0.55
		LFe-HMn	0.64	82	0.53
		HFe-LMn	0.01	72	0.59
		HFe-HMn	1.35	78	0.52
	63%	LFe-LMn	0.01	72	0.66
		LFe-HMn	1.27	91	0.51
		HFe-LMn	0.03	45	0.65
		HFe-HMn	1.63	92	0.47

f_D : volume fraction of dispersoids; r : average radius of the dispersoid particles; AR: aspect ratio of the dispersoids.

Tab. 5.10. Secondary phase morphology and volume fraction in NR-C cast, processed and soft annealed sample states.

Sample State		Alloy	f_D [vol. %]	r [nm]	AR
Homogenization	CRD				
500 °C	35%	LFe-LMn	0.02	54	0.68
		LFe-HMn	1.11	74	0.48
		HFe-LMn	0.05	62	0.49
		HFe-HMn	0.90	61	0.49
	63%	LFe-LMn	0.01	50	0.65
		LFe-HMn	1.01	73	0.47
		HFe-LMn	0.08	67	0.51
		HFe-HMn	1.07	63	0.48
550 °C	35%	LFe-LMn	0.01	58	0.65
		LFe-HMn	0.82	71	0.52
		HFe-LMn	0.03	77	0.58
		HFe-HMn	1.20	88	0.50
	63%	LFe-LMn	0.04	65	0.62
		LFe-HMn	0.58	81	0.47
		HFe-LMn	0.06	76	0.61
		HFe-HMn	1.00	79	0.52

f_D : volume fraction of dispersoids; r : average radius of the dispersoid particles; AR: aspect ratio of the dispersoids.

5.4 Discussion

In general, the types and fractions of the occurring intermetallic phases reflect the composition of the alloys. If one first looks at the S-C cast samples in **Fig. 5.1**, the primary phases of LFe-LMn and HFe-LMn only contain low concentrations of Mn. The characteristic needle-like shape and composition clearly indicate the $\text{Al}_3(\text{Fe},\text{Mn})$ phase, which is in good agreement with the results from other studies [6, 9, 10] and thermodynamic simulation. The stronger segregation of iron in comparison to Mn is based on the low solubility of Fe in the Al matrix [17, 18, 22]. Therefore, the increase in Fe alloying contents promotes higher number densities of primary phase nuclei, whereas the shape and structure of the phases remain unaltered.

With the increase in manganese alloying content, a significant change in shape of the primary phases can be observed. The needle-like intermetallic phases coarsen and form block-like structures in LFe-HMn or branched and Chinese-script structures in HFe-HMn, which was similarly observed by references [9, 12, 19]. With the change in Fe/Mn alloying ratio and due to the interchangeability of Fe and Mn, the stable eutectic component (precipitating as primary phase particles) becomes $\text{Al}_6(\text{Fe},\text{Mn})$ instead of $\text{Al}_3(\text{Fe},\text{Mn})$ [18]. While in [12] and [16] these changes were similarly observed especially in consideration of the increased Mn contents, Li and Arnberg [9] contradict this as high Mg contents in the alloys largely prevent the formation of the $\text{Al}_6(\text{Fe},\text{Mn})$ phase. The authors state preferred formation of $\text{Al}_3(\text{Fe},\text{Mn})$ and $\text{Al}_m(\text{Fe},\text{Mn})$ with m ranging from 4.1 to 4.4, but also suggest higher stability for $\text{Al}_6(\text{Fe},\text{Mn})$ with increasing Mn content. Since the Mn level in the investigated alloys is significantly higher, the described effects of Mg on the $\text{Al}_m(\text{Fe},\text{Mn})$ phase formation will presumably be retarded.

In addition to the $\text{Al}_6(\text{Fe}, \text{Mn})$ phases, particles with a higher Si concentration (classified as non-stoichiometric $\text{Al}_{15}(\text{Fe},\text{Mn})_3\text{Si}_2$) were found for the LFe-HMn alloy under S-C cast conditions. The alteration of phase stability is attributed to the very low Fe/Mn ratio of the LFe-HMn alloy, which was also observed in other studies for very similar compositions [6, 10].

Liu et al. [12] describe the effects of Mg and Si contents on the precipitation behavior of the Fe-Mn phases. The formation of (coarse) Mg_2Si , which was also observed in the present work in all alloys, subsequently affects the precipitation behavior of the Fe-Mn phases. With the decrease in average Si concentration in the matrix due to precipitation of Mg_2Si , the Si-containing Fe-Mn phases can hardly be formed. The absence of the non-stoichiometric $\text{Al}_{15}(\text{Fe},\text{Mn})_3\text{Si}_2$ phase for HFe-HMn results from both the change in Fe/Mn ratio and the Mg_2Si precipitation from the melt. A partial dissolution of Mg_2Si was observed for various alloys in the further homogenization processes at different temperatures [10, 21].

Numerous studies already mentioned the importance of the cooling rate in connection with the phases formed in a large variety of alloys [7, 9, 12, 14, 16]. Comparing **Fig. 5.1** and **Fig. 5.2**, a significant reduction in the casting cell size as well as the primary phase size by a factor of 5 to 10 is

observable for the NR-C conditions. Furthermore, especially for $\text{Al}_3(\text{Fe,Mn})$ containing alloys, an alteration of the needle shape can be observed (**Fig. 5.2 (a)**). The fast solidification decreases the casting cell size and therefore the final solidification zones, which become smaller but more branched [12, 16]. The near rapid cooling promotes therefore a higher number density of primary phases, whereas their total area fraction remains constant. As the mean area of the individual primary phases is reduced, the detectability of the lamellar structure is restricted. Furthermore, higher cooling rates favor the formation of Chinese-scripted phases also in low Mn containing alloys (**Fig. 5.2 (c)**).

In addition to the shape modifications of the intermetallic phases, the fractions of the primary phases for the different cooling conditions are compared in **Tab. 5.2** and **Tab. 5.3**. Like in [7, 12, 16], the clear increment in the total phase fraction is a result of the higher alloying contents of Fe and/or Mn. A trend of increased primary phase fractions with lower cooling rates can be noticed for most of the alloys and was also found by [7]. The contrary trend for the HFe-LMn alloy is again connected to the low solubility of Fe in the matrix, indicated by the change in Fe/Mn ratio of the primary phases with varied cooling conditions. Higher values for the Fe/Mn ratio indicate higher solute concentrations of Mn in the surrounding Al matrix or an increased segregation of Fe. Besides the alteration in Fe/Mn ratio, NR-C also stabilizes the non-stoichiometric $\text{Al}_{15}(\text{Fe,Mn})_3\text{Si}_2$ phase in the HFe-HMn alloy. A possible explanation might be the higher level of solute Si retained during solidification since the fraction of Mg_2Si is considerably lower in comparison to S-C conditions.

The homogenization heat treatment only induces a phase transformation for the S-C cast LFe-HMn at a temperature of 550 °C ($\text{Al}_3(\text{Fe,Mn})$ to $\text{Al}_6(\text{Fe,Mn})$) [21, 22]. The frequently examined phase transformation from disadvantageous Fe- and Mn-bearing phases to $\alpha\text{-Al}_{15}(\text{Fe,Mn})_3\text{Si}_2$ is not observed in the present alloys, most probably because of the low Si content [22]. The effect of the homogenization treatments on the total fraction of the primary phases can be noticed when comparing **Tab. 5.2–Tab. 5.6**. When considering the Fe-Mn bearing phases, the homogenization at 500 °C noticeably reduces the fraction of those phases. The higher temperature of 550 °C increases the maximum solubility of Fe and Mn in the matrix and diffusion enables slight dissolution. However, with higher homogenization temperatures, an increase in the area fraction is obtained for all alloys. Since this behavior contrasts with expectations, the fractions for the primary phases in **Tab. 5.4** and **Tab. 5.6** may also include parts of the secondary phase fractions.

Furthermore, as reported in [10], the homogenization can cause both shrinkage or growth of the constituent phases as well as spheroidization [26, 34], which is depicted in **Fig. 5.3**, **Fig. 5.4**, **Fig. 5.7**, and **Fig. 5.8** and quantified by the alteration of the corresponding shape factors in **Tab. 5.4** and **Tab. 5.6**. Additionally, stronger dissolution of Mg_2Si is clearly recognizable in all alloys after homogenization at the higher temperature of 550 °C [6].

Besides an alteration of the primary phases, the homogenization treatment results in the formation of finely dispersed second phase particles [1]. As shown in **Fig. 5.5** and **Fig. 5.6** for the 500 °C homogenization or **Fig. 5.9** and **Fig. 5.10** for the 550 °C homogenization, precipitates on the scale

of nano- up to micrometers can be observed. The influence of a homogenization time–temperature-cycle was already studied to some extent in [24, 26, 29, 34, 35]. The size, number density and composition of the thermodynamically stable phases varies with the alloying contents. In the present alloys, different stable dispersoid phases were found in the TEM measurements. **Fig. 5.11** highlights the formation of two different dispersoid types, $\text{Al}_6(\text{Fe},\text{Mn})$ and $\text{Al}_{15}(\text{Fe},\text{Mn})_3\text{Si}_2$, in dependence on the local solute Si level.

In the absence of high concentrations of solute elements, the low Mn alloys LFe-LMn and HFe-LMn do not show distinct secondary phase formation with fractions only around 0.05–0.11 vol.% for the 500 °C homogenization and 0.05–0.22 vol.% for the 550 °C homogenization, respectively (**Tab. 5.5** and **Tab. 5.7**). The differences for S-C and NR-C can be attributed to the increased solute Fe level for the higher cooling rates, resulting in increased driving forces for secondary phase precipitation. Concerning the size and aspect ratio of the dispersoids, the low Mn alloys do not depict clear trends.

With the increase in Mn content, the alloys show heavy precipitation of rod-shaped particles. As stated in [13], the 3D shape of the particles is rather plate-like than needle- or rod-shaped, and results after homogenization treatments at higher temperatures (550 °C). For lower temperatures also the formation of more spherical particles is mentioned in [13, 36], which can be found to some extent in the micrographs **Fig. 5.6** and **Fig. 5.10 (a)**. With longer times and higher homogenization temperatures, the bigger (plate-like) dispersoids can grow at the expense of the small (spherical) ones. This trend is clearly observed for the HFe-HMn alloy in **Fig. 5.6** and **Fig. 5.10 (d)** and found in the rise of the average radius from 86 nm to 158 nm [24].

Furthermore, the alloys show considerable influence of the Fe alloying content on the secondary phase formation. In [36] the interchangeability of Fe and Mn in the dispersoids of different types is reported, which is also confirmed in the present study. With the starting precipitation of Mn containing dispersoids, the remaining solute Fe atoms will attach to these particles and likely build long, drawn-out second phase particles. While the LFe-HMn alloy shows medium-high volume fractions of Al_6Mn type dispersoids, the higher Fe level in HFe-HMn, although usually not considered to be in solid solution to a large extent after casting, favors the formation of coarsened particles and raises the total volume fraction significantly. These considerations are highly affirmed since the behavior is more clearly found for the NR-C conditions. As an extremum, secondary phases of about 2.5 μm are found for the 550 °C homogenization of NR-C cast HFe-HMn alloy (**Fig. 5.10**). Those big phases also affect the significance of the dispersoid volume fractions, as there are also large regions without obtainable particles in those samples, though particle containing images are evaluated.

The thermodynamic calculations in the present study are in very good agreement with the results of the experimental work. The general considerations of Mn and Fe solute content in non-equilibrium and equilibrium conditions are concordant to the precipitation behavior of secondary phase particles. Whereas the amounts of phases computed for the particular conditions do not totally agree with the

experimental findings, they support current understanding of the trends of phase formation. Especially the for the high Fe containing alloys, the calculation underestimates the segregation of Fe in comparison to experimental data (e.g., HFe-LMn in **Tab. 5.3** and **Tab. 5.8**). Difficulties arise for equilibrium conditions, since the calculation only displays data for the absolute volume fractions of the stated phases including primary and secondary phases. However, consideration of the different fractions from **Tab. 5.6** and **Tab. 5.7** repeatedly show the disagreement of the data mainly for high Fe containing alloys.

In contrast to the calculation of volume fractions, the thermodynamic calculation clearly agrees with the experimentally found types of primary and secondary phases, in particular for the non-equilibrium state. However, the HFe-HMn alloy in the S-C conditions show a distinct discrepancy as the calculated $\text{Al}_{15}(\text{Fe},\text{Mn})_3\text{Si}_2$ phase is absent in the microstructure. The computed precipitation of both types of dispersoids, $\text{Al}_6(\text{Fe},\text{Mn})$ and $\text{Al}_{15}(\text{Fe},\text{Mn})_3\text{Si}_2$, is proved (**Fig. 5.11**) for the equilibrium conditions, although the verification of the given volume fractions of dispersoids goes beyond the scope of the experimental work. Finally, there are still difficulties in understanding the primary phase transformations tabulated in **Tab. 5.8**, since the experimental observations did not show major alterations of those intermetallics.

The final properties of the aluminum sheet after soft annealing are strongly influenced by the precipitation state of the intermetallics [1, 11, 24, 35]. The fragmentation of primary phases during rolling (as shown in **Fig. 5.12** and **Fig. 5.13** for the different casting cooling conditions) will certainly affect the recrystallization during annealing. In the vicinity of larger phase-fragments ($>1 \mu\text{m}$), the mechanism of particle stimulated nucleation might occur [37], whereas smaller primary phase particles can also contribute to the Zener pinning pressure usually exerted by dispersoids [38].

In this context, the rod-shape of the dispersoids and their alignment with RD (**Fig. 5.14** and **Fig. 5.15**) are crucial for the exerted pinning forces on grain boundaries growing in the different sample directions [38]. Comparing the dispersoids radii after homogenization and soft annealing, the significant reduction is attributed to a fragmentation of the particles during rolling. Since the probability is high that very small particles are not detected when evaluating the dispersoid fraction in the rolled and soft annealed condition, the decrease in the dispersoid volume fraction appears to be fairly plausible (compare **Tab. 5.5** or **Tab. 5.7** to **Tab. 5.9** or **Tab. 5.10**).

The present alloys cover a wide range of type, volume fraction, size, and distribution of the primary and secondary phases in the matrix. With the shown band-wise arrangement of primary phases and the preferred orientation of smaller rod-shaped dispersoids, a considerable influence on the final sheet recrystallization is to be expected. These effects will be discussed in the subsequent paper (Part II), including the discussion of the grain size, the grain morphology, and the texture of the alloys in the final sheet state.

5.5 Conclusions

The presented study investigates the evolution of primary and secondary phases in Al4.5Mg alloys with varied Fe and Mn levels as well as different casting and homogenization parameters at laboratory scaled production. The resulting microstructures are explained by micrographs, EDX phase characterization, and evaluated data on primary phase and dispersoid volume fractions. Furthermore, the experimentally observed occurrence and modification of primary and secondary phases are discussed in the light of thermodynamic calculations. Finally, the following conclusions can be drawn:

- High Fe/Mn ratios in the alloy contents favor the precipitation of $\text{Al}_3(\text{Fe},\text{Mn})$ primary phase in a characteristic needle-like shape. By increasing the Mn level, the primary phase coarsens and more likely forms $\text{Al}_6(\text{Fe},\text{Mn})$ or $\text{Al}_{15}(\text{Fe},\text{Mn})_3\text{Si}_2$, depending on the dissolved Si solute content and the primary precipitation of Mg_2Si , respectively.
- With near rapid cooling conditions in the casting process, the casting grain- and primary phase size are significantly reduced. The formation of different primary phase types in comparison to slow cooling conditions can be observed.
- The volume fractions of the primary phases considerably increase with the alloying contents, foremost by the Fe additions. The homogenization does not change the primary phases volume fractions nor compositions considerably.
- The homogenization heat treatment causes formation of secondary phases ($\text{Al}_6(\text{Fe},\text{Mn})$ or $\text{Al}_{15}(\text{Fe},\text{Mn})_3\text{Si}_2$), especially in the high Mn containing alloys. The influence of the cooling rate during casting is marginally visible. Higher homogenization temperatures and higher Fe contents clearly result in coarsening of the plate-like dispersoids.
- Thermodynamic calculations highly affirm the experimental results. Besides the good conformity in the observed primary and secondary phase intermetallic types, the trends of the computed volume fractions accord with evaluated data from the micrographs.
- The multitude of primary and secondary phase states created by this experimental work highly impacts the final aluminum sheets microstructure and properties, which will be discussed in part two of the present study.

Acknowledgments

The authors gratefully thank Lisa Zwitter for her valuable experimental work during her master thesis and further all involved colleagues at AMAG rolling GmbH, the Christian Doppler Laboratory for Advanced Aluminum Alloys, and Chair of Nonferrous Metallurgy, Montanuniversitaet Leoben for their input.

Appendix to Section 5

Tab. A5.1. Summarized data on primary phases of various sample states.

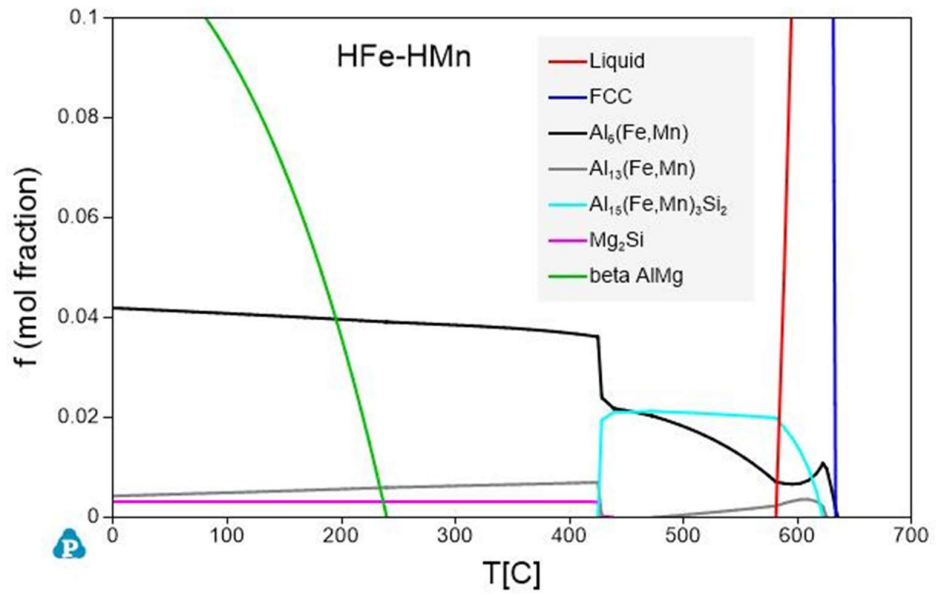
Sample State	Alloy	f_{bright} [%]	Fe/Mn	SF	Sample State	f_{bright} [%]	Fe/Mn	SF
S-C	LFe-LMn	0.42 ± 0.24	5.0 ± 1.0	1.78 ± 1.24	NR-C	0.39 ± 0.02	6.1 ± 2.5	1.57 ± 1.01
	LFe-HMn	0.96 ± 0.33	0.6 ± 0.4	3.06 ± 2.81		0.73 ± 0.14	0.7 ± 0.3	1.54 ± 1.06
	HFe-LMn	1.00 ± 0.34	7.9 ± 2.4	2.08 ± 1.37		1.89 ± 0.29	8.6 ± 3.5	2.30 ± 2.42
	HFe-HMn	3.49 ± 0.93	0.8 ± 0.5	3.37 ± 2.80		1.90 ± 0.18	1.3 ± 0.3	2.56 ± 2.17
S-C, 500 °C	LFe-LMn	0.30 ± 0.03	5.7 ± 2.0	2.10 ± 1.73	NR-C, 500 °C	0.36 ± 0.12	4.5 ± 1.7	1.88 ± 1.17
	LFe-HMn	0.79 ± 0.33	0.6 ± 0.3	2.80 ± 2.84		0.71 ± 0.37	0.6 ± 0.2	1.51 ± 0.75
	HFe-LMn	0.87 ± 0.27	8.5 ± 1.0	1.93 ± 1.40		1.30 ± 0.30	8.6 ± 2.7	2.00 ± 1.12
	HFe-HMn	2.25 ± 0.20	0.8 ± 0.2	2.40 ± 1.88		2.39 ± 0.52	1.1 ± 0.3	2.27 ± 1.69
S-C, 550 °C	LFe-LMn	0.28 ± 0.05	4.3 ± 1.8	1.83 ± 1.38	NR-C, 550 °C	0.43 ± 0.18	3.1 ± 1.8	1.45 ± 0.67
	LFe-HMn	0.90 ± 0.01	0.3 ± 0.2	1.84 ± 1.57		0.86 ± 0.09	0.3 ± 0.2	1.42 ± 0.73
	HFe-LMn	1.00 ± 0.14	7.9 ± 1.3	1.71 ± 1.46		1.37 ± 0.41	7.1 ± 2.9	1.81 ± 1.17
	HFe-HMn	3.22 ± 0.20	0.8 ± 0.2	2.80 ± 2.68		2.90 ± 0.58	0.5 ± 0.2	1.76 ± 1.15

Sample state: cast and homogenization conditions of the samples; f_{bright} : area fraction of bright phases; Fe/Mn: ratio of iron to manganese contents of the bright phase particles; SF: shape factor.

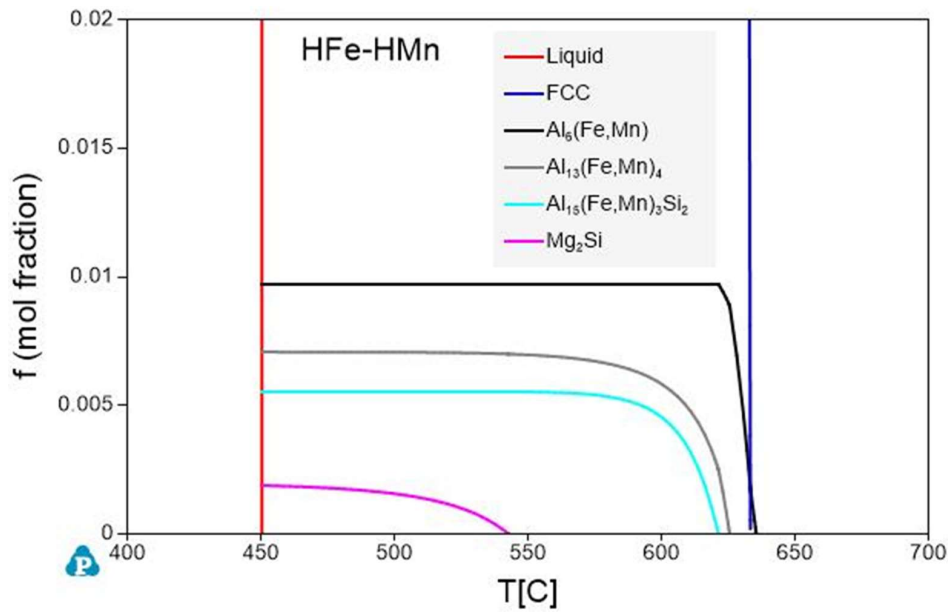
Tab. A5.2. Summarized data on secondary phases (dispersoids) of various sample states.

Sample State	Alloy	f_D [vol. %]	r [nm]	AR	Sample State	f_D [vol. %]	r [nm]	AR
S-C, 500 °C	LFe-LMn	0.021	59	0.65	NR-C, 500 °C	0.061	87	0.57
	LFe-HMn	0.756	87	0.57		0.620	71	0.58
	HFe-LMn	0.024	74	0.55		0.117	74	0.65
	HFe-HMn	1.440	84	0.57		2.341	86	0.57
S-C, 550 °C	LFe-LMn	0.047	144	0.56	NR-C, 550 °C	0.062	108	0.60
	LFe-HMn	1.036	124	0.55		0.741	105	0.54
	HFe-LMn	0.108	74	0.58		0.217	126	0.59
	HFe-HMn	2.252	123	0.57		2.293	158	0.51

Sample state: cast and homogenization conditions of the samples; f_{bright} : area fraction of bright phases; Fe/Mn: ratio of iron to manganese contents of the bright phase particles; SF: shape factor.



(a)



(b)

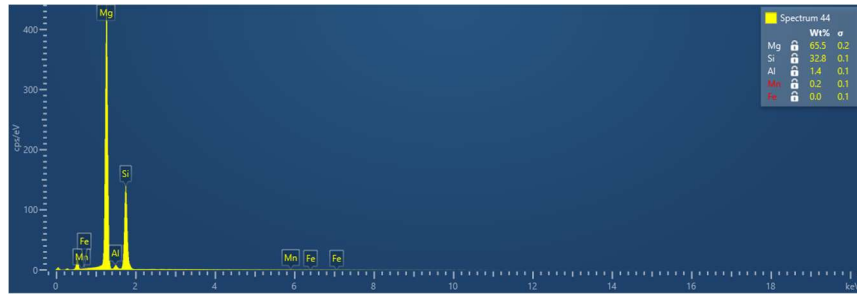
Fig. A5.1. Thermodynamic simulation of the phase evolution during cooling for (a) nonequilibrium (Scheil) and (b) equilibrium solidification for the HFe-HMn alloy.



(a)



(b)

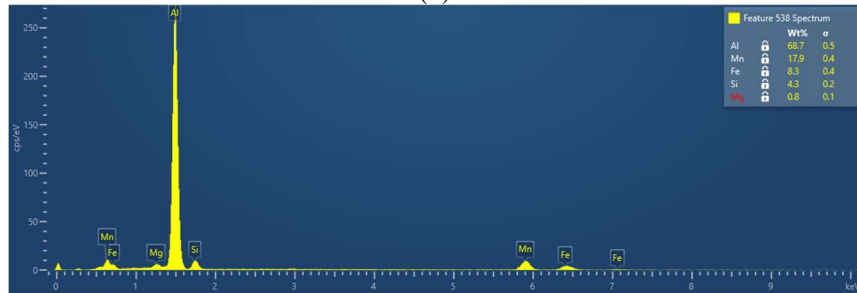


(c)

Fig. A5.2. EDX point analysis spectra indicated by the marked spots in Figure 1; (a) Fig. 5.1 (a) (1), $Al_3(Fe,Mn)$ particle, (b) Fig. 5.1 (a) (2), pore, (c) Fig. 5.1 (a) (3), Mg_2Si particle.



(a)



(b)

Fig. A5.3. EDX point analysis spectra indicated by the marked spots in Fig. 5.1; (a) Fig. 5.1 (b) (4), $Al_6(Fe,Mn)$ particle, (b) Fig. 5.1 (b) (5), $Al_{15}(Fe,Mn)_3Si_2$ particle.

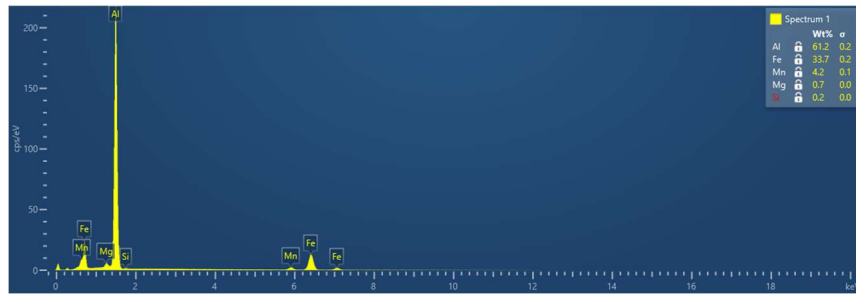


Fig. A5.4. EDX point analysis spectra indicated by the marked spots in Fig. 5.1 (c) (6), $Al_3(Fe,Mn)$ particle.

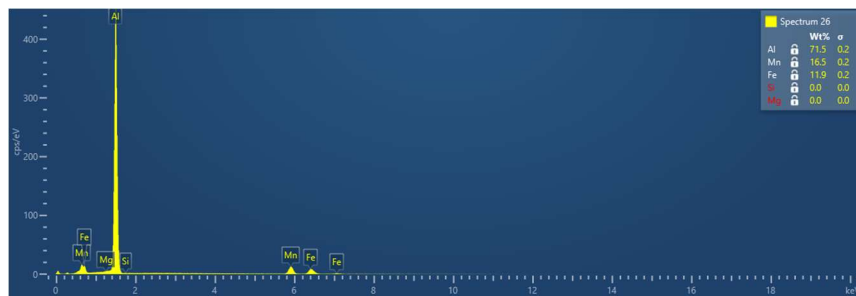


Fig. A5.5. EDX point analysis spectra indicated by the marked spots in Fig. 5.1 (d) (7), $Al_6(Fe,Mn)$ particle.

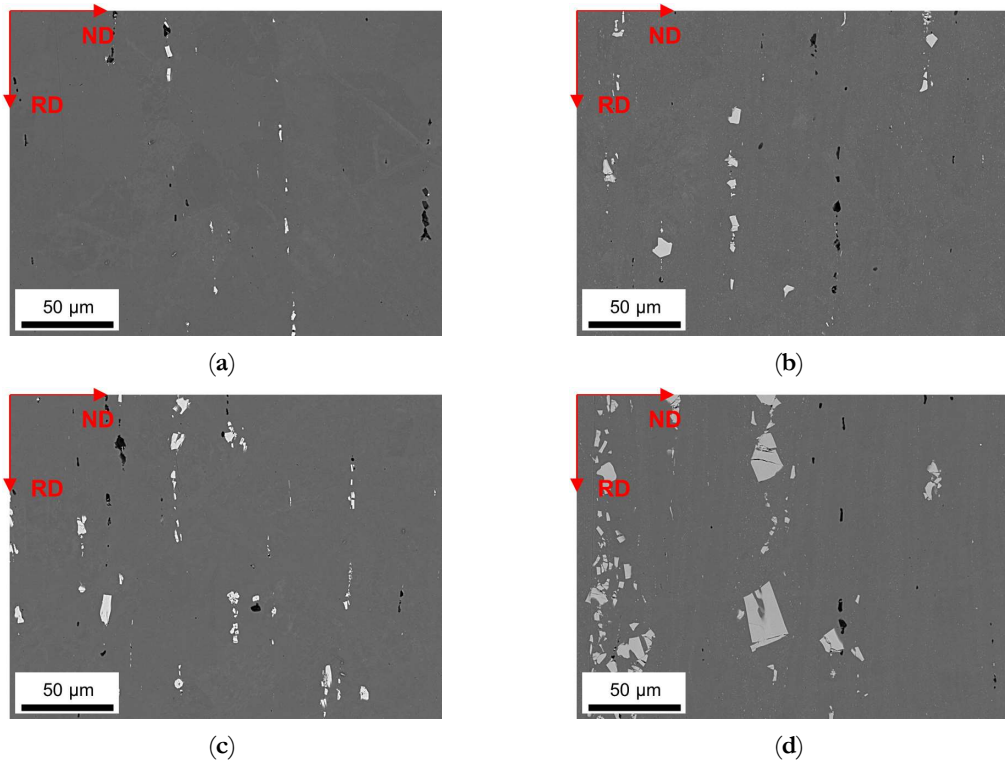


Fig. A5.6. Soft annealed microstructure of the alloys cast under S-C conditions, homogenized at 500 °C and cold rolled to a CRD of 35%; (a) LFe-LMn, (b) LFe-HMn, (c) HFe-LMn, (d) HFe-HMn.

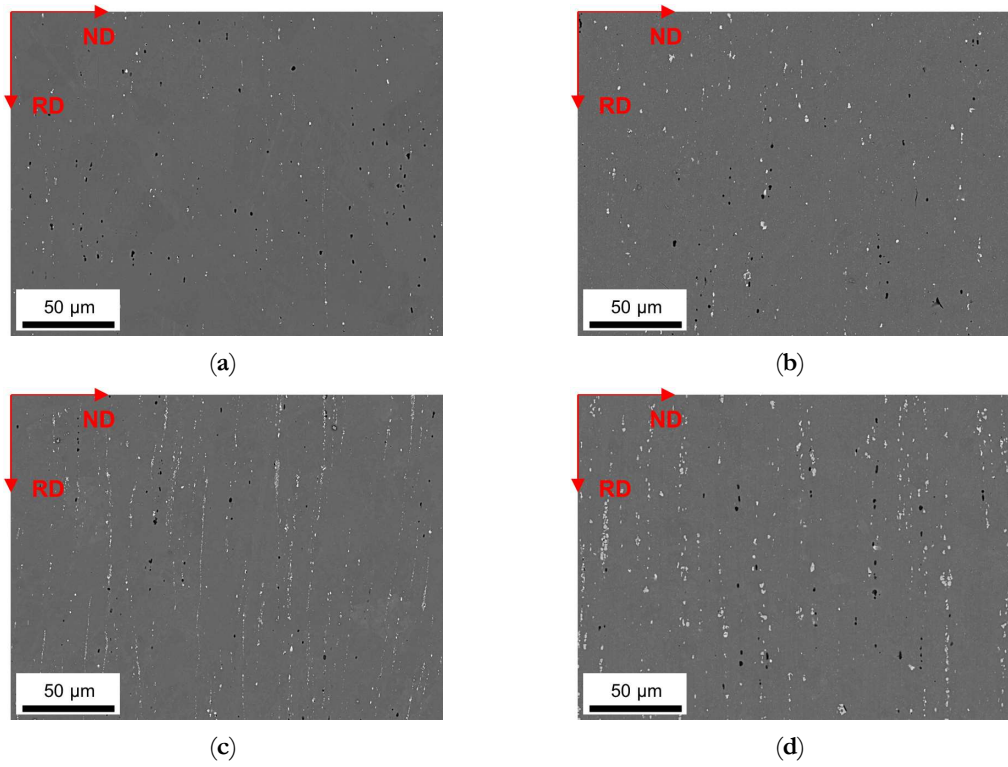


Fig. A5.7. Soft annealed microstructure of the alloys cast under NR-C conditions, homogenized at 500 °C and cold rolled to a CRD of 35%; (a) LFe-LMn, (b) LFe-HMn, (c) HFe-LMn, (d) HFe-HMn.

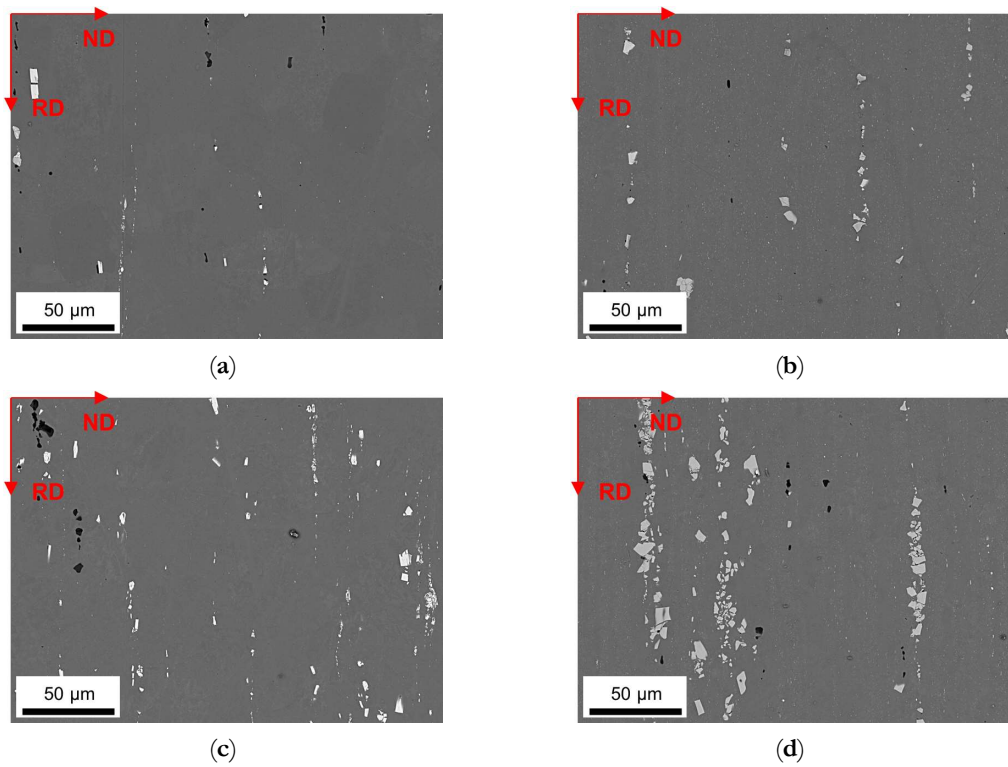


Fig. A5.8. Soft annealed microstructure of the alloys cast under S-C conditions, homogenized at 550 °C and cold rolled to a CRD of 63%; (a) LFe-LMn, (b) LFe-HMn, (c) HFe-LMn, (d) HFe-HMn.

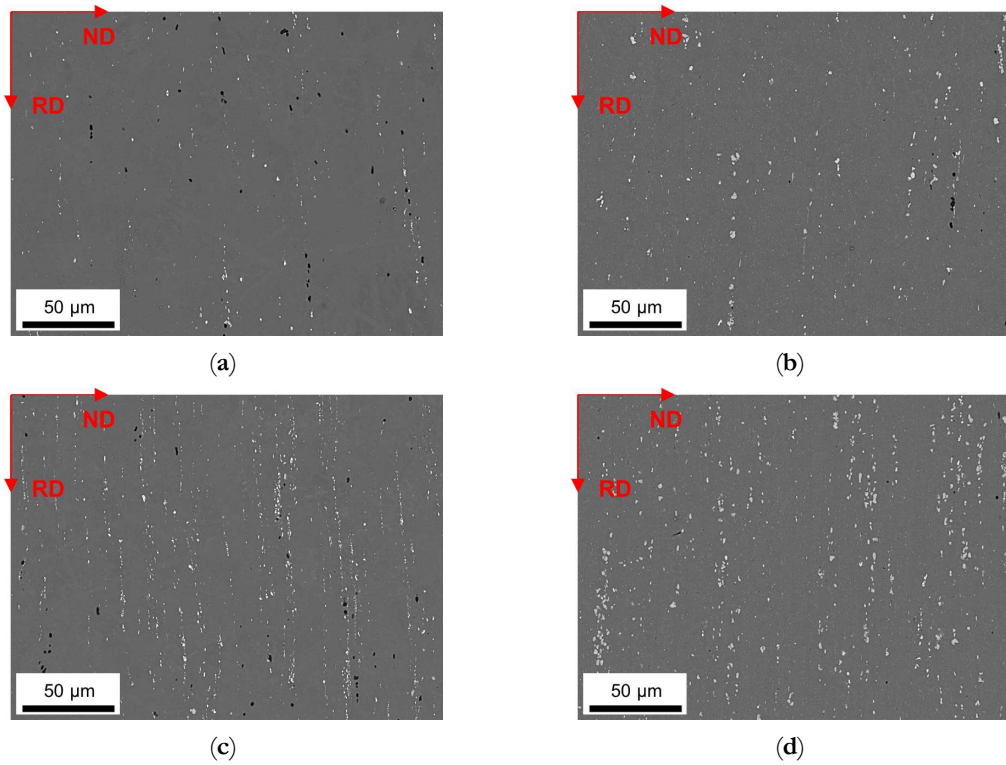


Fig. A5.9. Soft annealed microstructure of the alloys cast under NR-C conditions, homogenized at 550 °C and cold rolled to a CRD of 63%; (a) LFe-LMn, (b) LFe-HMn, (c) HFe-LMn, (d) HFe-HMn.

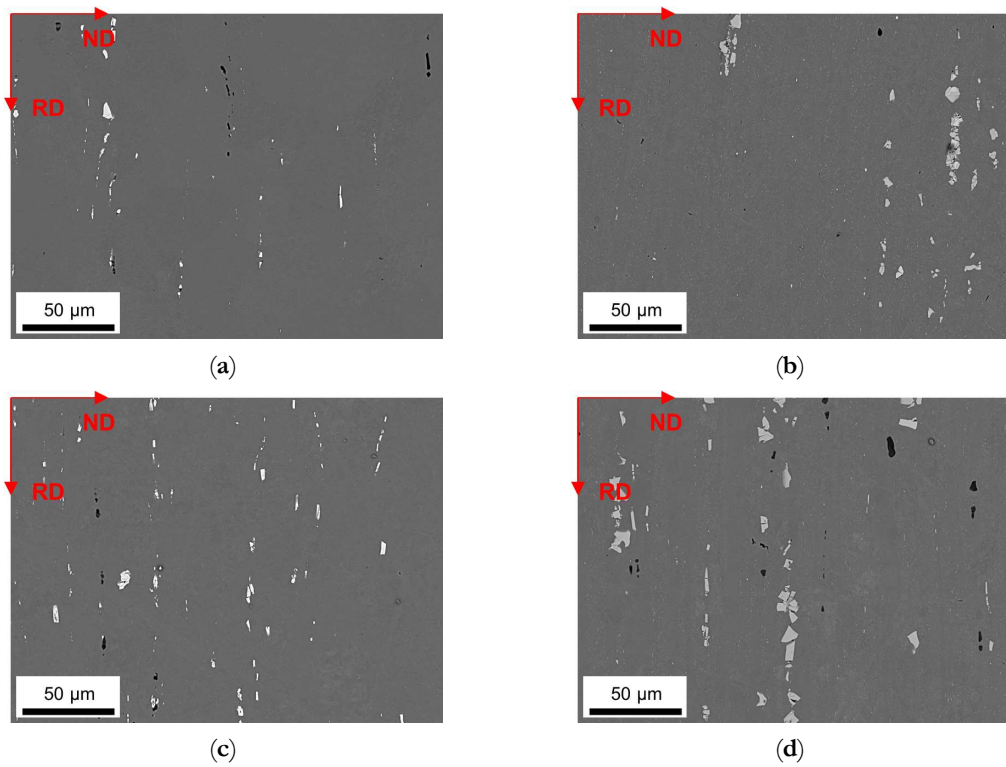


Fig. A5.10. Soft annealed microstructure of the alloys cast under S-C conditions, homogenized at 550 °C and cold rolled to a CRD of 35%; (a) LFe-LMn, (b) LFe-HMn, (c) HFe-LMn, (d) HFe-HMn.

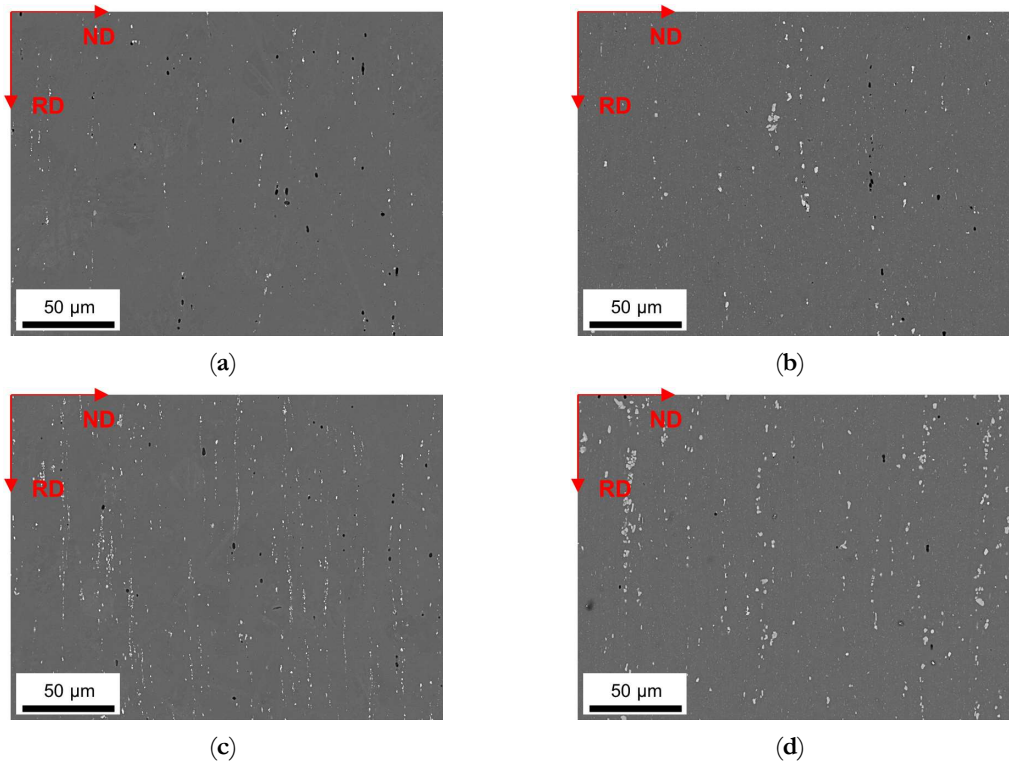


Fig. A5.11. Soft annealed microstructure of the alloys cast under NR-C conditions, homogenized at 550 °C and cold rolled to a CRD of 35%; (a) LFe-LMn, (b) LFe-HMn, (c) HFe-LMn, (d) HFe-HMn.

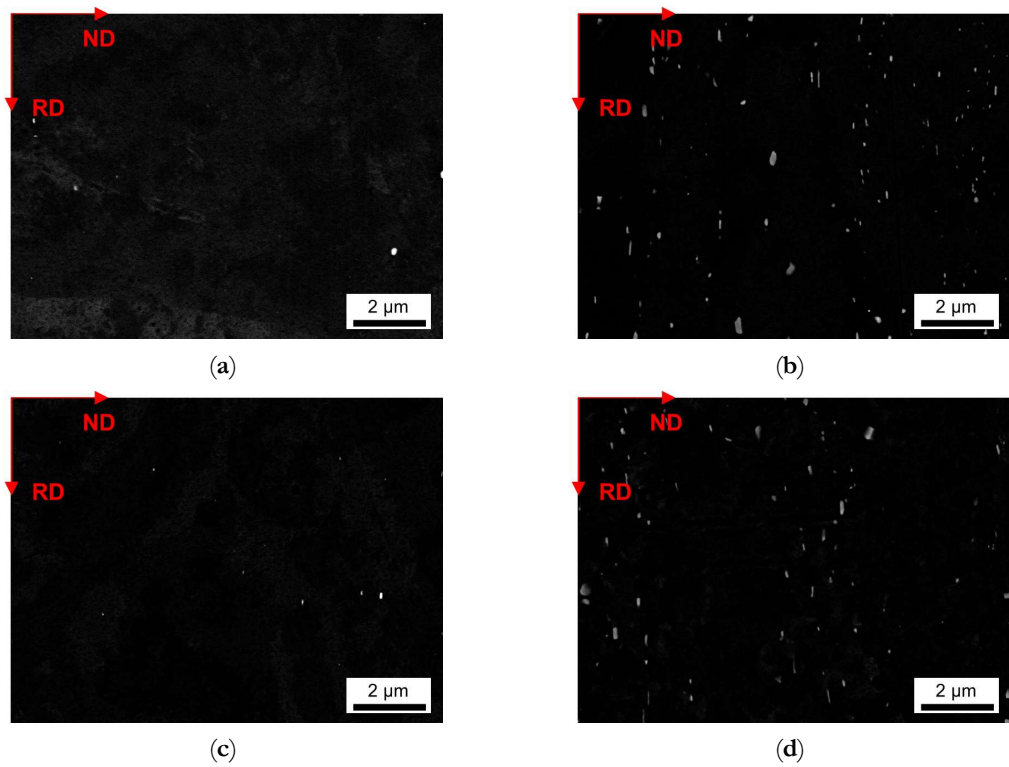


Fig. A5.12. Dispersoids in the soft annealed sample state cast under S-C conditions, homogenized at 500 °C and cold rolled to a CRD of 35%; (a) LFe-LMn, (b) LFe-HMn, (c) HFe-LMn, (d) HFe-HMn.

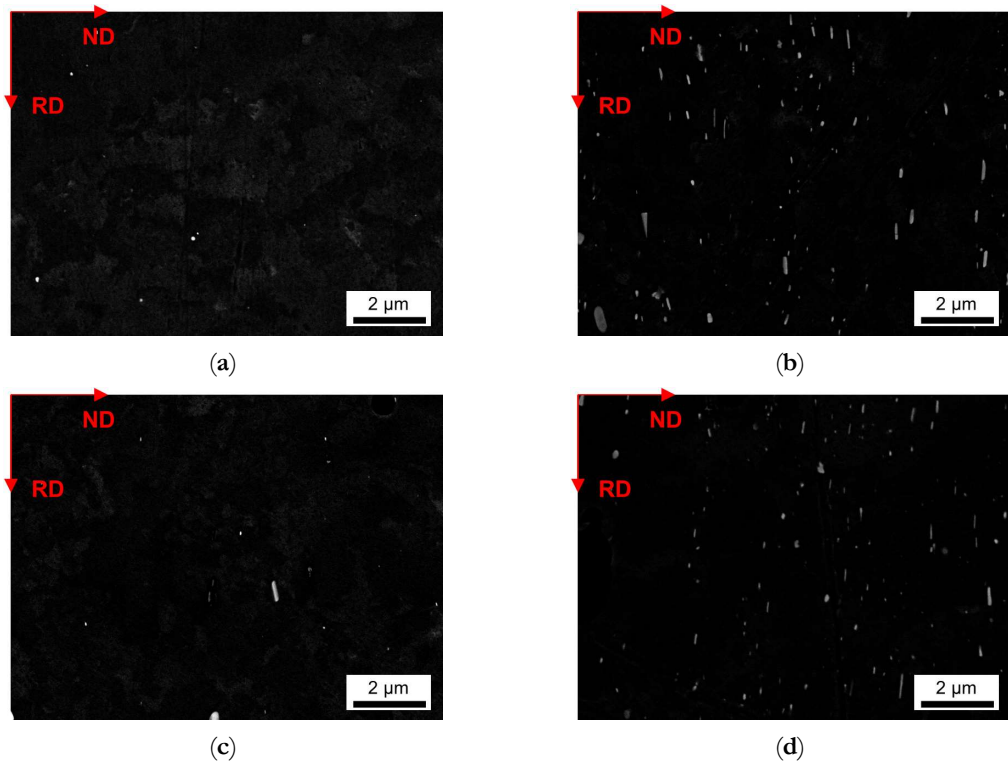


Fig. A5.13. Dispersoids in the soft annealed sample state cast under NR-C conditions, homogenized at 500 °C and cold rolled to a CRD of 35%; (a) LFe-LMn, (b) LFe-HMn, (c) HFe-LMn, (d) HFe-HMn.

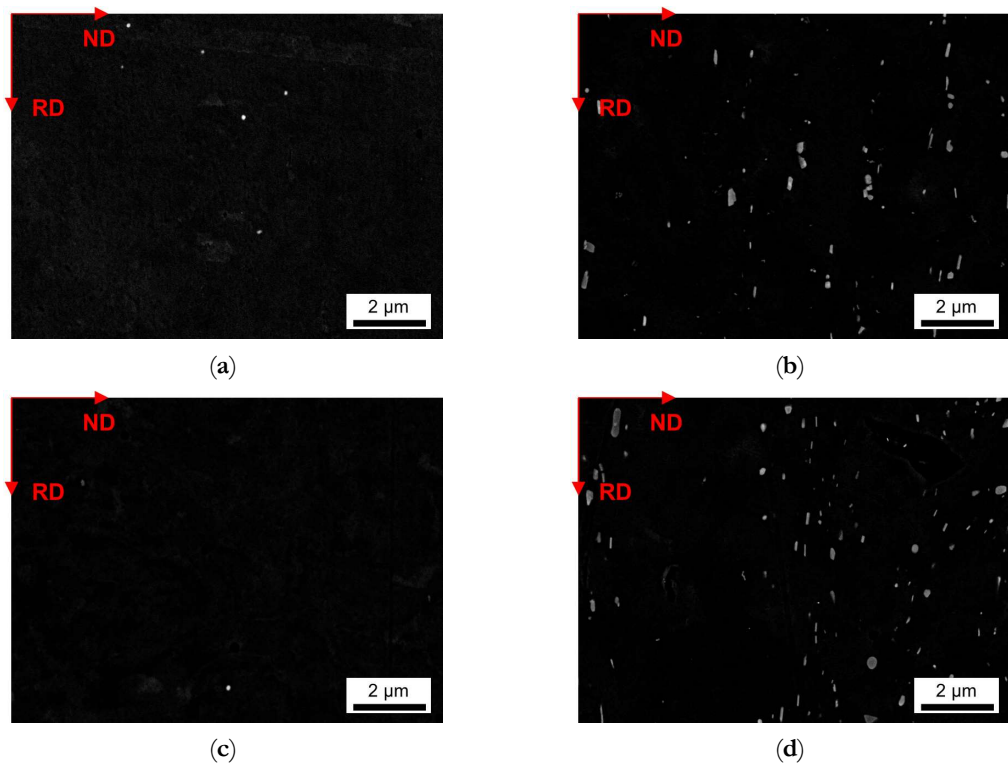


Fig. A5.14. Dispersoids in the soft annealed sample state cast under S-C conditions, homogenized at 550 °C and cold rolled to a CRD of 63%; (a) LFe-LMn, (b) LFe-HMn, (c) HFe-LMn, (d) HFe-HMn.

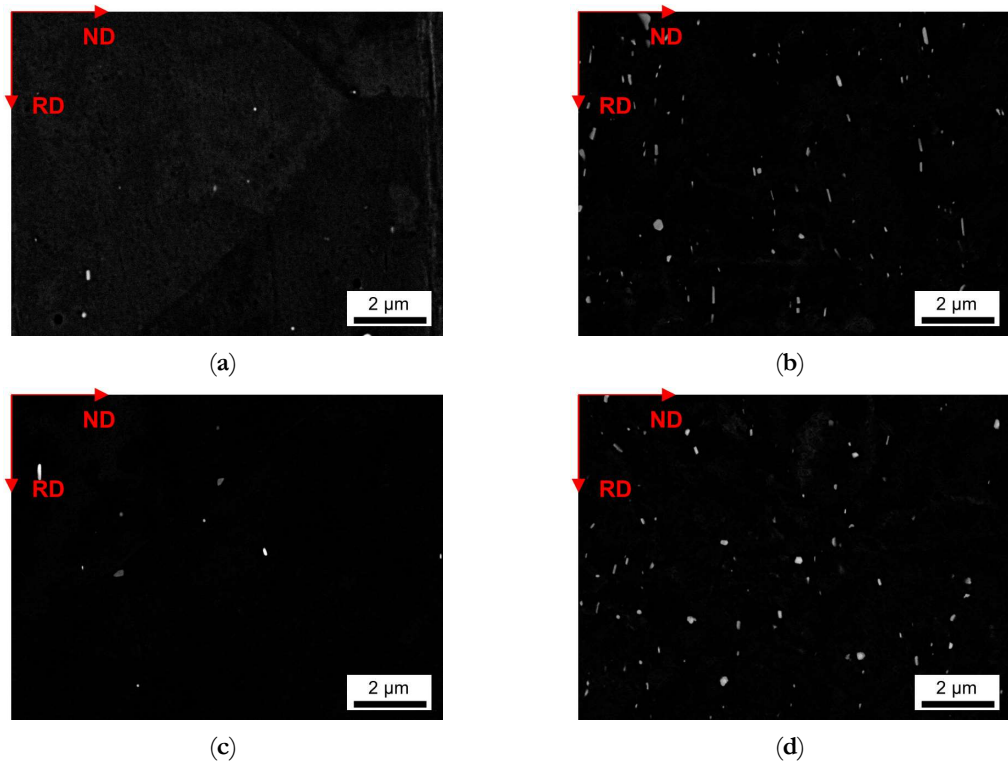


Fig. A5.15. Dispersoids in the soft annealed sample state cast under NR-C conditions, homogenized at 550 °C and cold rolled to a CRD of 63%; (a) LFe-LMn, (b) LFe-HMn, (c) HFe-LMn, (d) HFe-HMn.

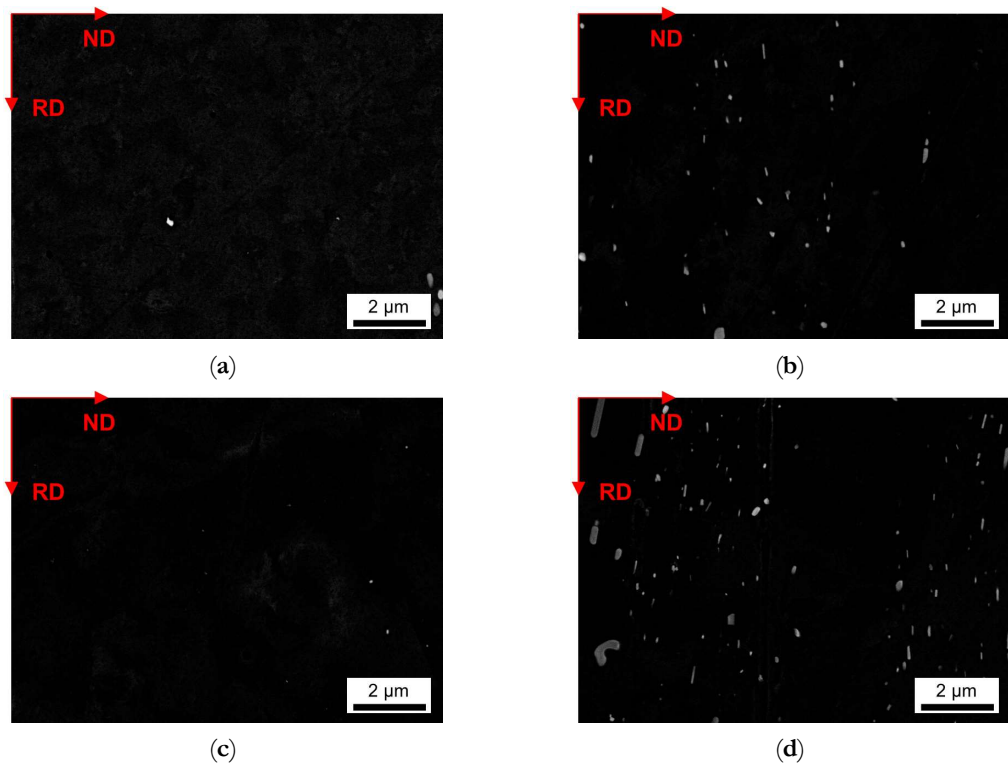


Fig. A5.16. Dispersoids in the soft annealed sample state cast under S-C conditions, homogenized at 550 °C and cold rolled to a CRD of 35%; (a) LFe-LMn, (b) LFe-HMn, (c) HFe-LMn, (d) HFe-HMn.

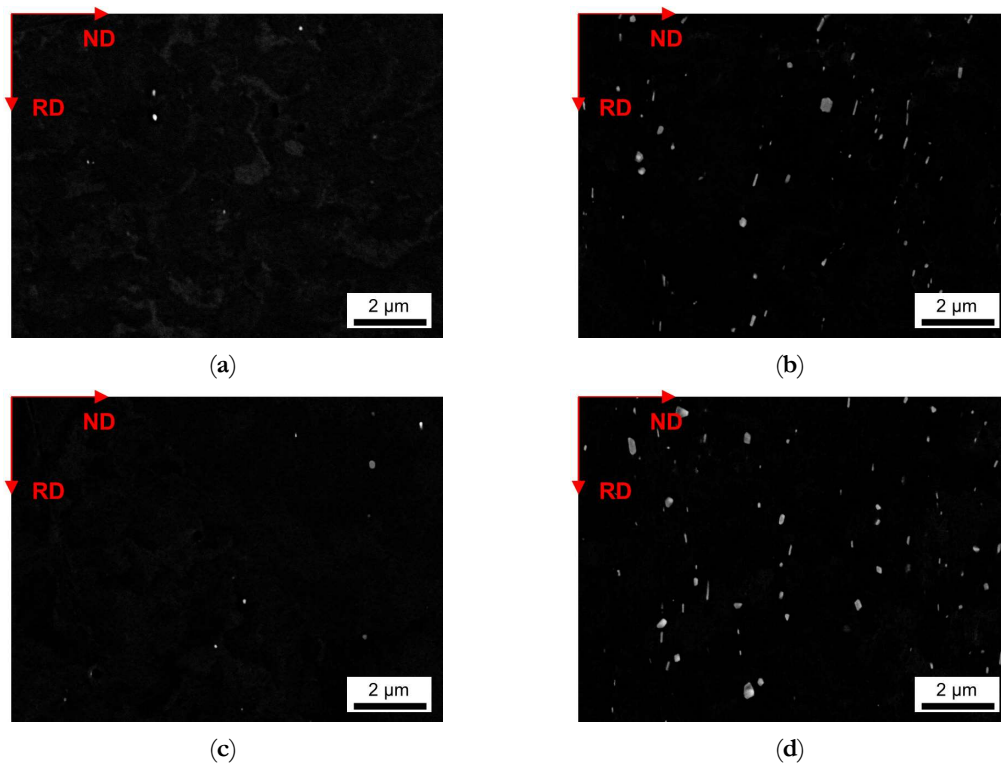


Fig. A5.17. Dispersoids in the soft annealed sample state cast under NR-C conditions, homogenized at 550 °C and cold rolled to a CRD of 35%; (a) LFe-LMn, (b) LFe-HMn, (c) HFe-LMn, (d) HFe-HMn.

References

- [1] Ostermann F.: *Anwendungstechnologie Aluminium*. Springer, Berlin, Germany (2014).
- [2] Ebenberger P. et al.: Processing-controlled suppression of Lüders elongation in AlMgMn alloys. *Scripta Materialia*, 166 (2019), 64–67.
- [3] Miller W. et al.: Recent development in aluminium alloys for the automotive industry. *Materials Science and Engineering: A*, 280 (2000), 37–49.
- [4] Burger G. B. et al.: Microstructural control of aluminum sheet used in automotive applications. *Materials Characterization*, 35 (1995), 23–39.
- [5] Cole G. S. and A. M. Sherman: Light weight materials for automotive applications. *Materials Characterization*, 35 (1995), 3–9.
- [6] Algendy A. Y., K. Liu and X.-G. Chen: Formation of intermetallic phases during solidification in Al-Mg-Mn 5xxx alloys with various Mg levels. *MATEC Web of Conferences*, 326 (2020), 2002.
- [7] Khalifa W., F. H. Samuel and J. E. Gruzleski: Iron intermetallic phases in the Al corner of the Al-Si-Fe system. *Metallurgical and Materials Transactions A*, 34 (2003), 807–825.
- [8] Belmares-Perales S. and A. A. Zaldívar-Cadena: Addition of iron for the removal of the β -AlFeSi intermetallic by refining of α -AlFeSi phase in an Al-7.5Si-3.6Cu alloy. *Materials Science and Engineering: B*, 174 (2010), 191–195.
- [9] Li Y.J. and Arnberg L.: Solidification structures and phase selection of iron-bearing eutectic particles in a DC-cast AA5182 alloy. *Acta Materialia*, 52 (2004), 2673–2681.
- [10] Engler O., K. Kuhnke and J. Hasenclever: Development of intermetallic particles during solidification and homogenization of two AA 5xxx series Al-Mg alloys with different Mg contents. *Journal of Alloys and Compounds*, 728 (2017), 669–681.

- [11] Ji S. et al.: Effect of iron on the microstructure and mechanical property of Al–Mg–Si–Mn and Al–Mg–Si diecast alloys. *Materials Science and Engineering: A*, 564 (2013), 130–139.
- [12] Liu Y. et al.: Effect of Fe, Si and Cooling Rate on the Formation of Fe- and Mn-rich Intermetallics in Al–5Mg–0.8Mn Alloy. *Journal of Materials Science & Technology*, 32 (2016), 305–312.
- [13] Ratchev P., B. Verlinden and P. van Houtte: Effect of preheat temperature on the orientation relationship of (Mn,Fe)Al₆ precipitates in an AA 5182 Aluminium–Magnesium alloy. *Acta Metallurgica et Materialia*, 43 (1995), 621–629.
- [14] Seifeddine S., S. Johansson and I. L. Svensson: The influence of cooling rate and manganese content on the β -Al₅FeSi phase formation and mechanical properties of Al–Si-based alloys. *Materials Science and Engineering: A*, 490 (2008), 385–390.
- [15] Sweet L. et al.: The Effect of Iron Content on the Iron-Containing Intermetallic Phases in a Cast 6060 Aluminum Alloy. *Metallurgical and Materials Transactions A*, 42 (2011), 1737–1749.
- [16] Liu Y. et al.: Effect of Mn and Fe on the Formation of Fe- and Mn-Rich Intermetallics in Al-5Mg-Mn Alloys Solidified Under Near-Rapid Cooling. *Materials (Basel, Switzerland)*, 9 (2016), 88.
- [17] Skjerpe P.: Intermetallic phases formed during DC-casting of an Al–0.25 Wt Pct Fe–0.13 Wt Pct Si alloy. *Metallurgical Transactions A*, 18 (1987), 189–200.
- [18] Allen C. M. et al.: Intermetallic phase selection in 1XXX Al alloys. *Progress in Materials Science*, 43 (1998), 89–170.
- [19] Sreeja Kumari S. S. et al.: Effects of individual and combined additions of Be, Mn, Ca and Sr on the solidification behaviour, structure and mechanical properties of Al–7Si–0.3Mg–0.8Fe alloy. *Materials Science and Engineering: A*, 460-461 (2007), 561–573.
- [20] Liu K., X. Cao and X.-G. Chen: Tensile Properties of Al-Cu 206 Cast Alloys with Various Iron Contents. *Metallurgical and Materials Transactions A*, 45 (2014), 2498–2507.
- [21] Li Y. and L. Arnberg: A eutectoid phase transformation for the primary intermetallic particle from Al_m(Fe,Mn) to Al₃(Fe,Mn) in AA5182 alloy. *Acta Materialia*, 52 (2004), 2945–2952.
- [22] Kuijpers N. et al.: The dependence of the β -AlFeSi to α -Al(FeMn)Si transformation kinetics in Al–Mg–Si alloys on the alloying elements. *Materials Science and Engineering: A*, 394 (2005), 9–19.
- [23] Narayanan L. A., F. H. Samuel and J. E. Gruzleski: Crystallization behavior of iron-containing intermetallic compounds in 319 aluminum alloy. *Metallurgical and Materials Transactions A*, 25 (1994), 1761–1773.
- [24] Engler O. and S. Miller-Jupp: Control of second-phase particles in the Al-Mg-Mn alloy AA 5083. *Journal of Alloys and Compounds*, 689 (2016), 998–1010.
- [25] Osman M. et al.: Effect of homogenisation conditions on recrystallisation in Al–Mg–Mn alloy AA 5454. *Materials Science and Technology*, 23 (2007), 688–698.
- [26] Engler O., Z. Liu and K. Kuhnke: Impact of homogenization on particles in the Al–Mg–Mn alloy AA 5454 – Experiment and simulation. *Journal of Alloys and Compounds*, 560 (2013), 111–122.
- [27] Liu S. et al.: Effects of Combined Additions of Mn and Zr on Dispersoid Formation and Recrystallization Behavior in Al-Zn-Mg Alloys. *Metallurgical and Materials Transactions A*, 50 (2019), 4877–4890.
- [28] Liu Z. et al.: Thermodynamics based modelling of the precipitation kinetics in commercial aluminium alloys. *Computational Materials Science*, 81 (2014), 410–417.
- [29] N. Raghunathan, M. A. Zaidi and T. Sheppard: Recrystallization kinetics of Al–Mg alloys AA 5056 and AA 5083 after hot deformation. *Mater. Sci. Technol.*, 2 (1986), 938–945.

- [30] Grasserbauer J. et al.: Evolution of Microstructure and Texture in Laboratory- and Industrial-Scaled Production of Automotive Al-Sheets. *Materials* (Basel, Switzerland), 13 (2020), 469.
- [31] Schmid F. et al.: Industry-oriented sample preparation of 6xxx and 5xxx aluminum alloys in laboratory scale. *Proceedings of EMC 2019, Düsseldorf, Germany, 24–26 June (2019)*, 639–652.
- [32] Österreicher J. A. et al.: Information depth in backscattered electron microscopy of nanoparticles within a solid matrix. *Materials Characterization*, 138 (2018), 145–153.
- [33] Scheil E.: Bemerkungen zur Schichtkristallbildung. *Z. Für Met.* 1942, 34, 70–72.
- [34] Sheppard T. and N. Raghunathan: Modification of cast structures in Al–Mg alloys by thermal treatments. *Materials Science and Technology*, 5 (1989), 268–280.
- [35] Rakhmonov J. et al.: Effects of Al(MnFe)Si dispersoids with different sizes and number densities on microstructure and ambient/elevated-temperature mechanical properties of extruded Al–Mg–Si AA6082 alloys with varying Mn content. *Journal of Alloys and Compounds*, 861 (2021), 157937.
- [36] Li Y. J., W. Z. Zhang and K. Marthinsen: Precipitation crystallography of plate-shaped Al₆(Mn,Fe) dispersoids in AA5182 alloy. *Acta Materialia*, 60 (2012), 5963–5974.
- [37] Humphreys F. J., G. S. Rohrer and A. D. Rollett: *Recrystallization and related annealing phenomena*. Elsevier Science Ltd. (2017).
- [38] Nes E., N. Ryum and O. Hunderi: On the Zener drag. *Acta Metallurgica*, 33 (1985), 11–22.

6 GRAIN SIZE AND TEXTURE EVOLUTION IN FE AND MN CONTAINING 5XXX AL SHEETS

Based on the results of Chapter 5, the effects of the primary and secondary phase volume fraction, particle size, and morphology on the resulting microstructures and textures in soft annealed sheets are discussed in this chapter. The resulting grain size is investigated deploying various characterization methods and discussed under consideration of pinning and PSN effects. The high Mn alloys exhibit strong Zener pinning and therefore significant grain refinement. The resulting grain sizes are compared to well-established models of the Zener limiting grain size indicating accordance to the original Smith-Zener approach. However, new parameters are found to best fit all the experimental data including the low dispersoid fraction containing alloys. Although the texture analysis of the samples verifies the highly random texture in the 5xxx Al alloys, trends of occurring PSN and pinning effects are observed by detailed examination.

Influence of Fe and Mn on the Microstructure Formation in 5xxx Alloys—Part II: Evolution of Grain Size and Texture*

In recent decades, microstructure and texture engineering has become an indispensable factor in meeting the rising demands in mechanical properties and forming behavior of aluminum alloys. Alloying elements such as Fe and Mn in AlMg(Mn) alloys affect the number density, size, and morphology of both the primary and secondary phases, thus altering the grain size and orientation of the final annealed sheet by Zener pinning and particle stimulated nucleation (PSN). The present study investigates the grain size and texture of four laboratory processed AlMg(Mn) alloys with various Fe and Mn levels (see Part I). Common models for deriving the Zener-limit grain size are discussed in the light of the experimental data. The results underline the significant grain refinement by dispersoids in high Mn alloys and show a good correlation with the Smith-Zener equation when weighting the volume fraction of the dispersoids with an exponent of 0.33. Moreover, for high Fe alloys certain reduction of the average grain size is obtained due to pinning effects and PSN of coarse primary phases. The texture analysis focuses on characteristic texture transformations occurring with pinning effects and PSN. However, the discussion of the texture and typical PSN components is only possible in terms of trends, as all alloys exhibit an almost random distribution of orientations.

6.1 Introduction

With the increasing demands on material recycling, especially in the field of lightweight materials, such as aluminum alloys, a profound knowledge of the effects of increased impurity levels (e.g., Fe) on the property profile of the manufactured products is of essential importance. The properties of the various aluminum alloys should be maintained even with increased content of impurity elements and meet the application requirements [1, 2]. In the category of AlMg(Mn) (5xxx) alloys, which unify medium strength and good formability, as well as good corrosion resistance, the final properties are largely determined by the solute content of Mg, the cold rolling degree (CRD) and the microstructure [3, 4]. Additionally, with superior deep-drawing properties, the AlMg(Mn) alloys are widely used in the automotive industry [5, 6].

With regard to the influence of secondary alloying elements Fe, Mn and Si, the aluminum alloys show distinct formation of various intermetallic phases [7–9] which affect the processing and microstructure of the material [10, 11]. For increased iron contents, typical formation of the needle-

* Published in *Materials* 14 (2021), 3312 written by Jakob Grasserbauer, Irmgard Weißensteiner, Georg Falkinger, Peter J. Uggowitzer and Stefan Pogatscher.

Author contributions:

JG: Conceptualization, methodology, validation, investigation, original draft, visualization.

like Al_3Fe (or $\text{Al}_{13}\text{Fe}_4$) phase is observed [12]. Various studies already accentuated the adverse effects of Fe on the materials properties, which can be partially counteracted by spheroidizing the phases by adding ‘Fe-corrector’ elements, such as Mn [12]. Furthermore, the main secondary alloying element Mn tends to coarsen and spheroidize the constituent Al-Fe(-Si) phases and initiates the formation of secondary phases (dispersoids) of type Al_6Mn during homogenization [12, 13]. These dispersoids play a crucial role in grain size control during subsequent rolling and recrystallization processes [14]. The Si content in the AlMg(Mn) alloys influences both the primary and secondary phase precipitation. During casting, Si can form stable Mg_2Si precipitates, as well as different types of Al(Fe,Mn)Si phases. Phase transformations and the precipitation of secondary $\alpha\text{-Al}_{15}(\text{Fe,Mn})_3\text{Si}_2$ dispersoids are likely to occur in the following homogenization treatment. Finally, the precipitation kinetics, grain size and, thus, the properties of Mn, Fe and Si containing 5xxx aluminum alloys are also strongly affected by the cooling rate in the casting process. In general, higher cooling rates during casting significantly refine the grain size, as well as constituent phases, and can further change the levels of solute Fe, Mn and Si [15–19]. A comprehensive overview on the details of primary and secondary phases formed in AlMg(Mn) alloys with varying Fe and Mn additions under different processing parameters, such as solidification conditions, homogenization temperature and degree of cold rolling, is given in Part I of this work [15].

With regard to the effects of primary and secondary phases on the recrystallization processes and, thus, on the evolution of microstructure, texture and the final properties, two fundamentally different mechanisms must be taken into account: particle stimulated nucleation (PSN) and grain boundary pinning [14, 20, 21]. In general, the PSN mechanism occurs in the vicinity of rather large (primary) particles ($>1\ \mu\text{m}$), where the accumulation of dislocations and the formation of recrystallization nuclei are favored. The resulting grain size is then related to the interparticle distances. Moreover, the PSN effect is commonly associated with changes in the typical recrystallization textures of aluminum alloys [14, 20, 22–25].

Meanwhile, the influence of small, nanometer sized (secondary phase) particles is described by the Smith–Zener pinning effect [26]. In the case of normal grain growth after primary recrystallization, the grain boundary movement is impeded by pinning forces of small dispersoid particles (“Zener drag”), which depend on the particle sizes, morphologies and volume fractions. Over several decades, numerous research groups improved the original Smith–Zener approach by taking various parameters, such as shape, orientation, or the constitution of the particle-matrix interface, into account [27–33]. Concerning the impact of dispersoid shape on the pinning efficiency, the authors of [27] derived formulas for the extreme cases of differently oriented spheroidal dispersoids and their restrictive forces on the moving grain boundary. However, the applicability of the formulas to experimentally derived data is still of high complexity.

With the progress in computational modelling in the last forty years, various simulations were performed on the interaction of particles and grain boundaries [34–46]. The simulation algorithms

resulted in a broad spectrum of possible parameters for the formulation of the Smith–Zener pinning. A comparison of experimental data to the various theoretical formulations for the Zener pinning pressure can be performed by the equation for the Zener limiting grain size R_{lim} (Equ. 6.1) [28],

$$\frac{R_{lim}}{r} = \frac{K}{f^m} \quad (\text{Equ. 6.1})$$

which represents the resulting grain size after recrystallization and grain growth till reaching equilibrium conditions (r , particle size; f , particle volume fraction). Over the years, not only the dimensionless constant K (considering geometric relations of boundary curvature and grain size) was altered in the various approaches, but also the exponent m , accounting for the pinning efficiency of the dispersoids. In general, it was found that for higher volume fractions the exponent m will be <1 . However, the exact definition of “higher” volume fractions differs in the various studies and ranges from 1 vol.% up to 3 vol.% of the secondary phase particles [28, 47].

In addition to the effects of primary and secondary phases on the grain size, the properties of the final aluminum sheets are also significantly influenced by the texture of the material [14, 48–52]. In typical aluminum rolling processes, the fcc crystal structure and the high stacking fault energy favor the formation of characteristic rolling textures in the deformed state. The orientations Brass $\{011\}\langle 211\rangle$, Copper $\{112\}\langle 111\rangle$ and S $\{123\}\langle 634\rangle$, typically referred to as β -fiber [6, 53–57], arise from the preferred dislocation slip systems in the material and represent rotations of the crystallites during cold deformation ending in this stable alignment [14].

During subsequent heat treatments, recrystallization, in terms of classical nucleation and growth mechanisms, rearranges the microstructure and the texture of the material. Whereas in earlier years the discussions focused on the differences between two common mechanisms of recrystallization texture formation—oriented nucleation and oriented growth—an implication of both effects is now the preferred approach [52, 58]. The main recrystallization texture component in the majority of aluminum alloys is the Cube orientation $\{001\}\langle 100\rangle$, which evolves from remaining Cube nuclei in the deformed state and was the subject of decades of research [49, 59–64]. Furthermore, frequently found accompanying recrystallization orientations, such as Goss $\{011\}\langle 100\rangle$ or Q $\{013\}\langle 231\rangle$, preferentially nucleate at shear bands, which were also found to occur particularly in AlMg(Mn) alloys [65].

The typical aluminum recrystallization texture can be altered by the presence of primary and secondary phases, due to the effects of PSN and Zener pinning. In the case of particle stimulated nucleation, the two specific texture components P $\{011\}\langle 122\rangle$ and Cub_{END} $\{001\}\langle 310\rangle$ are generally stated to preferentially evolve, together with a rather weak classical recrystallization texture [24, 66, 67]. Moreover, the Zener drag exerted by small dispersoid particles impedes the grain boundary movement and therefore changes the recrystallization texture by modifications of the oriented growth mechanisms. The resulting texture is in many cases still dominated by the Cube component, which is least affected by the drag forces due to low energy boundaries and the size

advantages of emerging Cube nuclei [25, 68]. In case of concurrent appearance of both effects, the Zener pinning dominates the recrystallization texture and effectively suppresses the growth of PSN nuclei [23, 66, 69].

In terms of the mechanical properties and forming behavior, the texture modifications due to particle related (recrystallization) effects can yield considerable improvements in the final sheet quality. For the AlMg(Mn) alloys, the combination of PSN and Cube texture components can optimize the resulting earing behavior and thus enhance the formability of the 5xxx Al sheets [52]. The number density and distribution of primary and secondary phases can further weaken the Portevin–Le Chatelier (PLC) effect in those alloys [70, 71]. Moreover, the PSN components can effectively suppress Cube banding in 6xxx alloys, therefore reducing the probability of the undesired roping phenomenon [6, 66, 72].

The present study focuses on the microstructure and texture evolution in 5xxx Al alloys with different Fe and Mn levels. A detailed description and discussion of the primary and secondary phase formation in alloys based on Al4.5Mg0.1Si with varying Fe (0.1 and 0.4 wt.%) and Mn (0.2 and 1.0 wt.%) contents is given in Part I of the study [15]. In this Part II, the effects of the mechanisms PSN and Zener pinning are discussed and the experimental data compared to established theories.

6.2 Materials and Methods

The studied alloys were based on Al4.5Mg0.1Si with varying Fe (0.1 or 0.4 wt.%) and Mn (0.2 or 1.0 wt.%) contents. Starting from four different alloys (low Fe, low Mn; low Fe, high Mn; high Fe, low Mn; high Fe, high Mn), the variations in casting cooling rate (NR-C: near-rapid cooling, ~ 50 K/s; S-C: slow-cooling, $\sim 1\text{--}2$ K/s), homogenization treatment (500 °C and 550 °C) and cold rolling degree (35% and 63%), before final soft annealing (salt bath at 500 °C for 5 min and water quenching), resulted in 32 different sample states (**Fig. 6.1**). Basically, while the high Fe contents resulted in higher volume fractions of primary phase particles, the high Mn favored the formation of dispersoids and resulted in high volume fractions, especially in the HFe-HMn alloy. Details of the casting and further processing steps of the alloys, as well as the analyses of the primary and secondary phases in terms of their composition, volume fraction and morphology, are presented in Part I of the study [15].

Investigations regarding the microstructure formation, such as grain size and Zener pinning, as well as texture analysis of the final soft annealed state, were performed on cross-sectional samples (looking in the transverse direction (TD) of the cold rolled sheet). Three different experimental methods were used for grain size analysis:

- High contrast backscattered electron (BSE) images from scanning electron microscopy;
- Light optical microscopy (LOM);
- Electron backscattered diffraction (EBSD).

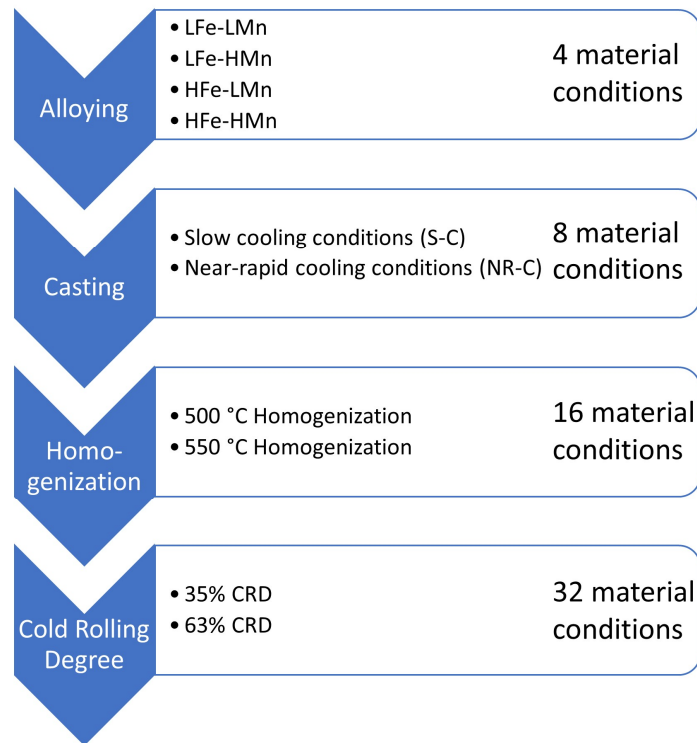


Fig. 6.1. Sample processing scheme, including all variations of the individual process steps.

The sample preparation for all characterization methods started with standard metallographic sample preparation, including cutting, embedding, grinding and polishing, plus oxide suspension (OPS, Struers) polishing on a Struers Tegramin 30 grinding and polishing machine. The BSE micrographs were recorded from these samples using a scanning electron microscope (SEM) (JEOL 7200F FEG-SEM, Tokyo, Japan) at an accelerating voltage of 10 kV or 5 kV at higher magnifications for dispersoid analysis. The EBSD measurements were performed on the SEM equipped with the EBSD-measurement system (Nordlys Nano detector, Oxford Instruments, Abingdon, UK) using 20 kV accelerating voltage and a 70° pre-tilt sample holder. Parameters and details on the necessary electropolishing surface treatment for the EBSD analysis can be found in [73]. For light optical microscopy, additional Barker etching of the OPS-polished samples with Barker etchant according to [74] using the Struers Lectro-Pol 5 unit at a temperature of 10 °C and a voltage of 25 V for 50 s accomplished the surface preparation. The LOM micrographs were recorded by utilizing polarized light in a reflected-light microscope Axio Imager M1m (Zeiss, Oberkochen, Germany).

The grain size analysis of the micrographs was carried out performing the line intercept method on LOM and BSE images of various sizes using the free software tool ImageJ. Each measurement contained a minimum of twelve lines (three in rolling direction (RD), three in normal direction (ND); two images per sample), with each line including at least 12 intercept points. Grain size analysis of the EBSD data of was performed by means of the Matlab based toolbox MTEX 5.2.beta3, which is described in detail in [73] and also used the line intercept method on two cross-sectional scans of size 1600 × 1200 μm² per sample (EBSD). The EBSD micrographs are presented in the form of inverse pole figure mappings (IPF) in the RD–ND plane.

The mean grain radius R was calculated from the mean intercept length, taking into account the proportionality constant of 0.75, as described in [75]. Grain-defining parameters, such as a minimum grain misorientation angle of 15° and a minimum grain size of $5 \mu\text{m}^2$, as well as grains situated on the sheet or scan edge and coarse primary particles, were considered as exclusion factors.

The calculation of the Zener limiting grain size follows Equation (Equ. 6.1) with the parameters K and m relating to the different models. The Manohar model used the parameters $K = 0.17$ and $m = 1$ [33], whereas the Smith–Zener model used $K = 4/3$ and $m = 1$ [26]. The implementation of the ellipsoidal particle morphology followed the derivations of Ryum [32] and yields the Equations (Equ. 6.2) and (Equ. 6.3) to calculate the limiting grain radii in RD and ND:

$$\frac{R_{\text{RD}}}{r} = \frac{2}{3f^m} \left(\frac{1}{\text{AR}}\right)^{0.47} \quad (\text{Equ. 6.2})$$

$$\frac{R_{\text{ND}}}{r} = \frac{1}{3f^m} \left(1 + \frac{1}{\text{AR}}\right) \frac{1}{\text{AR}}^{0.33} \quad (\text{Equ. 6.3})$$

with AR being the aspect ratio of the dispersoids. The calculation again used the exponent $m = 1$. More information on the mathematical considerations is given in [14] and [27].

The quantification of texture (using MTEX) focused on the relative intensity of ideal orientations (within 10° maximum deviation) extracted from the EBSD area fractions and normalized by the area fraction of a random orientation distribution, multiplied by the number of the respective symmetric equivalents. The quantification was based on the same cross-sectional scans as the grain size analysis including at least 4000 grains. The ideal orientations of the analyzed components are listed in **Tab. 6.1**.

Tab. 6.1. Analyzed texture components with respective ideal orientations and Euler angles [76, 77].

Component	{hkl}<uvw>	$\varphi_1, \Phi, \varphi_2$
Brass	{011}<211>	35.3, 45, 0
		90, 144.7, 225
Copper	{112}<111>	180, 21.8, 0
		289.5, 45, 0
		121, 36.7, 26.6
S	{123}<634>	302.3, 18.4, 0
		301, 36.7, 26.6
		122.3, 18.4, 0
Cube	{001}<100>	0, 0, 0
Goss	{011}<100>	0, 45, 0
P	{011}<122>	90, 35.3, 45
		0, 21.8, 360
Cub _{ND}	{001}<310>	22, 0, 0

6.3 Results

This section illustrates the evolution of the characteristic microstructural parameters and the texture as a function of the Fe and Mn content and the processing conditions.

6.3.1 Microstructure Evolution and Resulting Grain Size

As a result of the different conditions during casting, homogenization and cold rolling, a wide distribution of grain sizes of the final soft annealed samples was observed. **Fig. 6.2–Fig. 6.6** depict the microstructures of the LFe-LMn and HFe-HMn alloys by means of different micrographs. The selected sample states show the possible differences of the final microstructure for the casting conditions, the homogenization treatment and the degree of cold rolling. All other sample states and micrographs can be found in the Appendix to Section 6 (**Fig. A6.1–Fig. A6.27**). The general trends between composition, processing and microstructure and texture formation are given in the discussion.

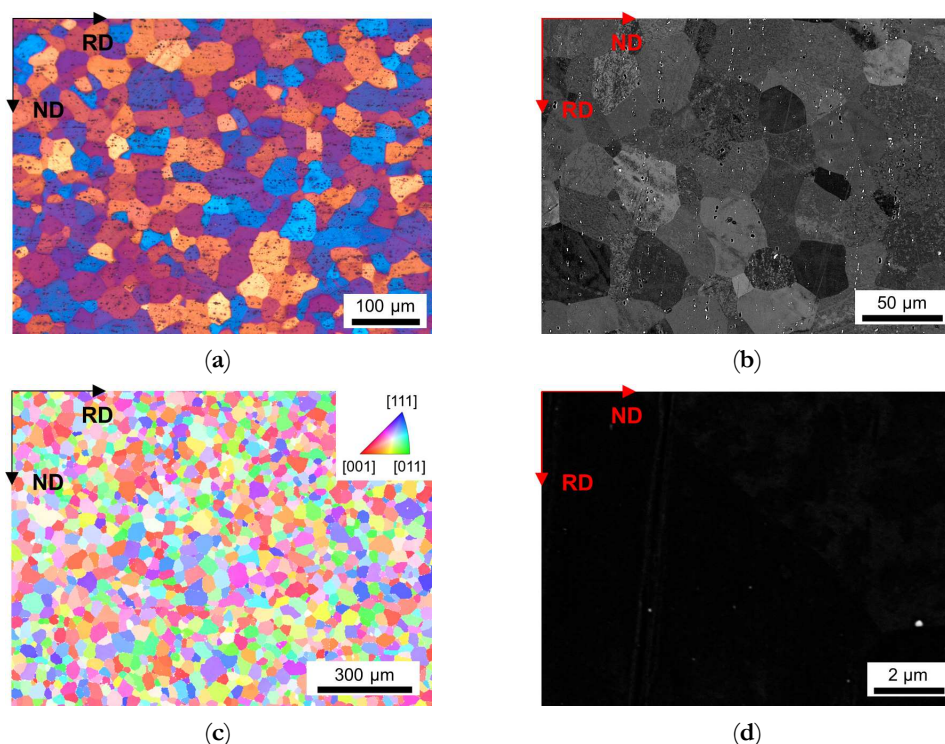


Fig. 6.2. Microstructure of the soft annealed LFe-LMn cast under NR-C condition, homogenized at 500 °C and cold rolled to a CRD of 35%. (a) LOM. (b) BSE image. (c) EBSD IPF map in RD–ND plane. (d) BSE micrograph showing dispersoids.

The LOM micrographs of the alloys in **Fig. 6.2** and **Fig. 6.3 (a)** provide a good general overview of the grain morphologies and sizes (note the different map scale bars). While for the LFe-LMn alloy almost equiaxed grains were observed, the HFe-HMn alloy indicates a slight stretch of the grains remaining in the former rolling direction. Furthermore, a significant refinement of the grains can be seen in **Fig. 6.3**, which is obviously associated with the higher number density of dispersoids. Apart from the dispersoids, the coarse Al-Fe-Mn(-Si) primary phases also seem to affect the microstructure.

The BSE images in **Fig. 6.2** and **Fig. 6.3 (b)** show band-wise arrangement of the primary phase precipitates and depict the distinct increase in primary phase fraction with the higher Fe and Mn contents.

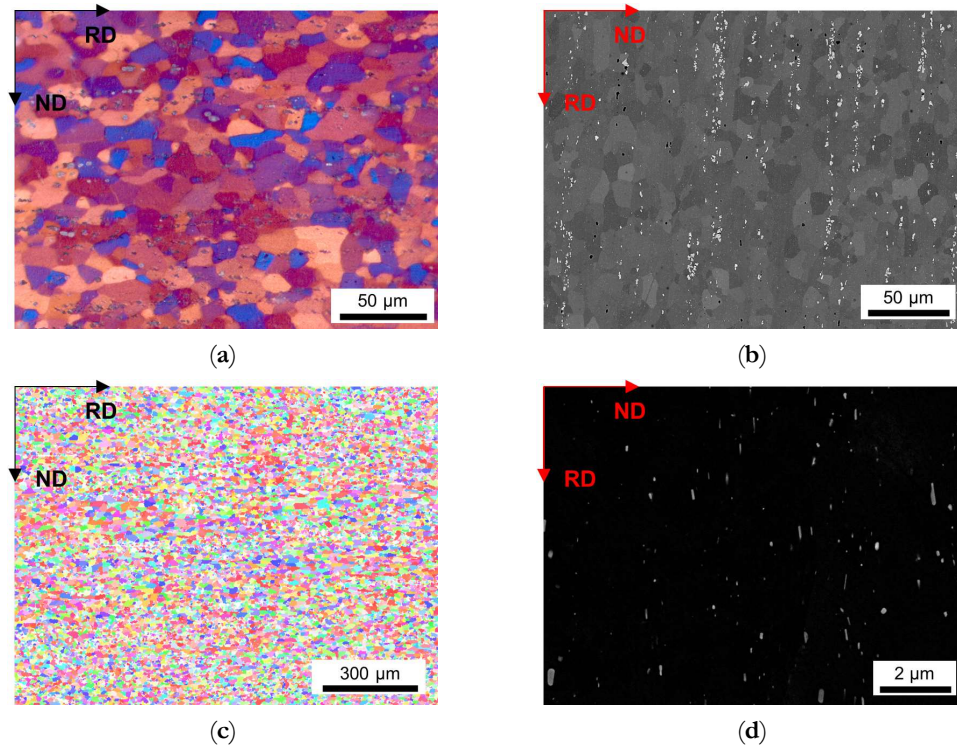


Fig. 6.3. Microstructure of the soft annealed HFe-HMn cast under NR-C condition, homogenized at 500 °C and cold rolled to a CRD of 35%. (a) LOM. (b) BSE image. (c) EBSD IPF map in RD–ND plane. (d) BSE micrograph showing dispersoids.

A higher cold rolling degree of 63% causes greater fragmentation and, therefore, refinement of the coarse phases in the HFe-HMn alloy (compare **Fig. 6.3** and **Fig. 6.4 (b)**). The BSE images will further be considered for grain size analysis, since the channeling contrast reveals the size and structure of the grains. A similar refinement as with the CRD is obtained for the NR-C in comparison to the S-C casting conditions for the HFe-HMn alloy (**Fig. 6.4** and **Fig. 6.5 (a),(b)**). Besides the grains, the primary phases are distinctly coarsened in the S-C casting samples (**Fig. 6.5 (b)**).

The inverse pole figure (IPF) maps of the presented figures indicate the absence of preferred orientations in both LFe-LMn and HFe-HMn samples (**Fig. 6.2** and **Fig. 6.3 (c)**). Furthermore, none of the processing conditions show significant alterations of the resulting grain orientations as the random texture character is preserved as shown for the HFe-HMn alloy in **Fig. 6.3–Fig. 6.6 (c)**. The color code legend inserted in **Fig. 6.2 (c)** applies to all IPF maps given in this study.

The typical dispersoid distribution and arrangement of the alloys is shown in **Fig. 6.2–Fig. 6.6 (d)**. While the low Mn containing alloy is nearly free of secondary phase particles (**Fig. 6.2 (d)**), the HFe-HMn shows spherical, as well as rod- or plate-shaped, dispersoids (**Fig. 6.3 (d)**). Similar to the findings in Part I [15], the nanometer sized particles align with the rolling direction. As explained later, the preferred orientation of the dispersoids results in unequal Zener pinning forces for RD and

ND growth directions, which is implemented in some of the calculations of the Zener limiting grain size.

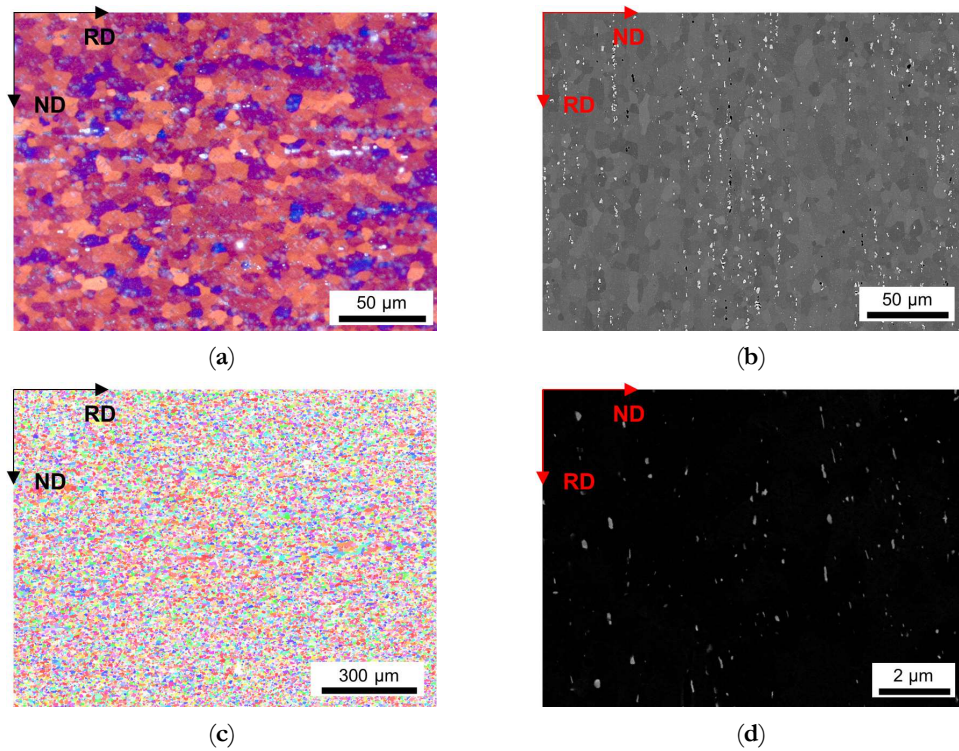


Fig. 6.4. Microstructure of the soft annealed HFe-HMn cast under NR-C condition, homogenized at 500 °C and cold rolled to a CRD of 63%. (a) LOM. (b) BSE image. (c) EBSD IPF map in RD–ND plane. (d) BSE micrograph showing dispersoids.

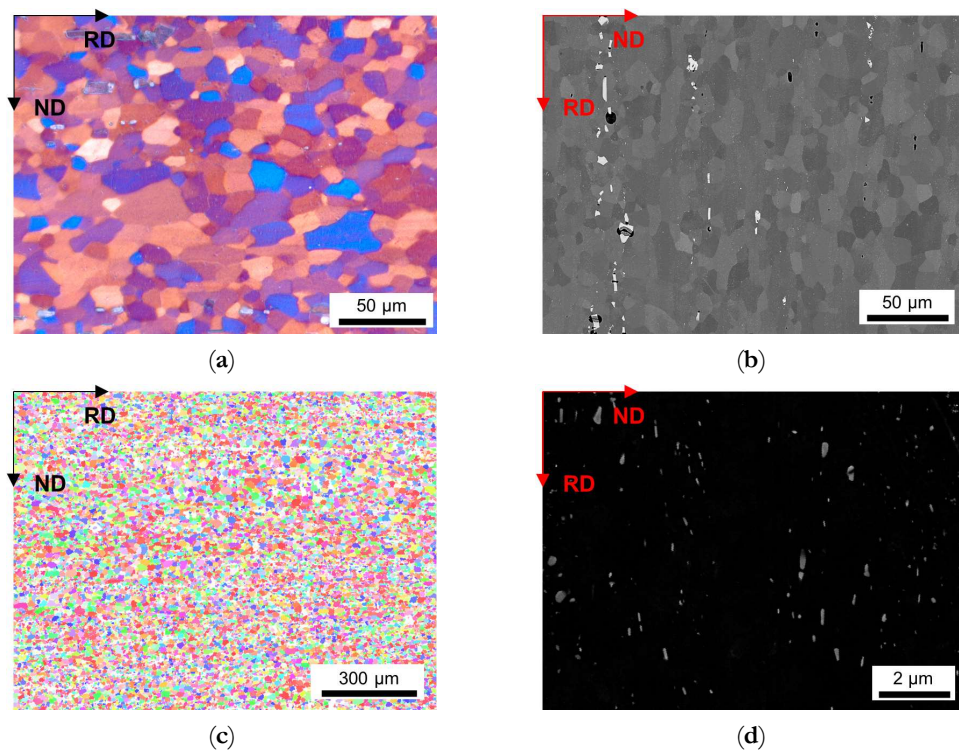


Fig. 6.5. Microstructure of the soft annealed HFe-HMn cast under S-C condition, homogenized at 500 °C and cold rolled to a CRD of 63%. (a) LOM. (b) BSE image. (c) EBSD IPF map in RD–ND plane. (d) BSE micrograph showing dispersoids.

As described in detail in Part I, neither the processing conditions as the given CRD (compare **Fig. 6.3** and **Fig. 6.4 (d)**), nor the casting cooling conditions (compare **Fig. 6.4** and **Fig. 6.5 (d)**) cause distinct alterations in the final dispersoid volume fraction and morphology. However, coarsening and more rod- or plate-shape morphology of the dispersoids is obtained for the higher homogenization temperature of 550 °C (compare **Fig. 6.5** and **Fig. 6.6 (d)**).

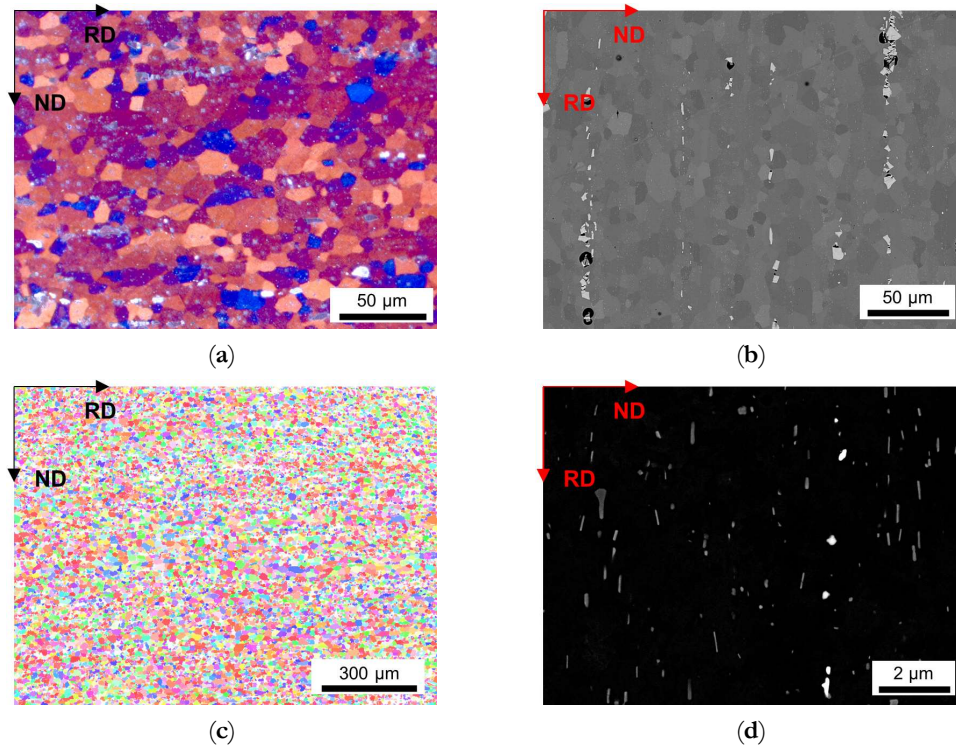


Fig. 6.6. Microstructure of the soft annealed HFe-HMn cast under S-C condition, homogenized at 550 °C and cold rolled to a CRD of 63%. (a) LOM. (b) BSE image. (c) EBSD IPF map in RD–ND plane. (d) BSE micrograph showing dispersoids.

The resulting grain sizes for the various 63% CRD sample states are listed in **Tab. 6.2**, including the data for the different characterization methods—LOM, BSE and EBSD. Because of the unbalanced aspect ratios for most of the samples, the results are given in terms of grain radii derived from line intercept measurements in RD, as well as ND, for all micrographs.

The data given in **Tab. 6.2** clearly show the influences of the different characterization methods. While the numbers of the mean grain radii from the LOM and BSE micrographs, R_{LOM} and R_{BSE} , are about the same, the mean grain size derived from EBSD measurements, R_{EBSD} , is significantly lower. Since EBSD measurement and processing are the least user affected, the true value will be closer to the numbers obtained for R_{EBSD} . The higher measurement errors for EBSD grain sizes result from different considerations than for LOM and BSE. For LOM and BSE images the measurement error (standard deviation) is given by the standard deviation of the mean value resulting from the measurements of the three different images, while the standard deviation for the EBSD data comprises the data of all individual grains. The basic discussion of the subsequent microstructure evolution will therefore be based on grain parameters obtained with the EBSD measurements.

Tab. 6.2 clearly illustrates the influence of sample processing on grain morphologies, i.e., the effects of casting cooling rate, homogenization, and cold rolling. For example, the NR-C cast samples show significantly finer grain structures in the final annealed sheets. Moreover, the faster cooling also results in a more balanced aspect ratio for most of the grains. The homogenization heat treatment results in a slight alteration of the microstructure since samples show reduction or increase in the mean grain radius with the higher maximum homogenization temperature of 550 °C in comparison to 500 °C.

Information on the resulting grain sizes for sample processing with a CRD of 35% is given in **Tab. 6.3**, where the comparison to **Tab. 6.2** reveals the influence of the cold rolling degree.

The alloying elements Fe and Mn differently impact the final microstructure. In general, the largest grains were observed for the LFe-LMn alloy. In the absence of dispersoid particles and with the low number density of primary phases, the recrystallization and grain growth are not effectively suppressed, resulting in grain sizes of around 20–25 μm for the S-C casting conditions.

Tab. 6.2. Grain size results for 63% CRD samples from LOM, BSE and EBSD images.

Alloy	Cast_Homogenization	R_{LOM} [μm]		R_{BSE} [μm]		R_{EBSD} [μm]	
		RD	ND	RD	ND	RD	ND
LFe-LMn	NR-C_500 °C	17.4 \pm 3.8	16.0 \pm 3.1	16.2 \pm 0.6	13.8 \pm 1.0	14.3 \pm 8.1	12.5 \pm 6.7
	S-C_500 °C	22.8 \pm 4.9	18.7 \pm 2.3	24.7 \pm 1.1	21.1 \pm 1.3	18.8 \pm 12.5	19.7 \pm 12.4
	NR-C_550 °C	19.6 \pm 1.4	13.7 \pm 1.1	14.2 \pm 0.3	14.1 \pm 0.5	13.5 \pm 7.9	11.6 \pm 6.3
	S-C_550 °C	18.8 \pm 1.5	16.4 \pm 3.0	18.4 \pm 0.8	17.7 \pm 1.2	16.3 \pm 9.9	15.8 \pm 9.3
LFe-HMn	NR-C_500 °C	6.5 \pm 0.7	5.5 \pm 0.5	6.7 \pm 0.2	5.3 \pm 0.3	6.0 \pm 2.8	5.5 \pm 2.3
	S-C_500 °C	12.1 \pm 1.3	7.5 \pm 0.5	10.2 \pm 0.6	7.3 \pm 0.5	11.5 \pm 8.3	7.1 \pm 3.8
	NR-C_550 °C	7.0 \pm 0.8	5.4 \pm 0.4	6.1 \pm 0.3	5.3 \pm 0.4	5.9 \pm 2.6	5.9 \pm 2.6
	S-C_550 °C	8.4 \pm 0.9	7.2 \pm 0.4	8.6 \pm 0.4	7.1 \pm 0.4	7.0 \pm 3.7	5.8 \pm 2.7
HFe-LMn	NR-C_500 °C	10.0 \pm 1.1	10.8 \pm 1.4	13.4 \pm 1.1	8.8 \pm 1.0	8.3 \pm 4.9	8.0 \pm 4.4
	S-C_500 °C	17.0 \pm 0.8	15.9 \pm 1.6	17.8 \pm 0.8	17.9 \pm 0.8	15.1 \pm 9.4	14.1 \pm 8.0
	NR-C_550 °C	10.4 \pm 0.9	9.5 \pm 1.1	8.4 \pm 0.8	9.3 \pm 0.6	9.1 \pm 5.1	9.3 \pm 5.1
	S-C_550 °C	14.7 \pm 2.7	15.0 \pm 2.6	13.8 \pm 0.8	15.0 \pm 0.8	11.5 \pm 7.1	12.8 \pm 8.6
HFe-HMn	NR-C_500 °C	8.8 \pm 1.4	5.6 \pm 0.7	6.7 \pm 0.9	5.3 \pm 0.2	6.3 \pm 3.1	5.0 \pm 2.0
	S-C_500 °C	10.7 \pm 1.4	7.1 \pm 0.7	9.1 \pm 0.2	6.4 \pm 0.3	7.3 \pm 4.1	5.9 \pm 2.7
	NR-C_550 °C	6.6 \pm 0.6	5.3 \pm 0.6	5.6 \pm 0.6	5.4 \pm 0.5	5.5 \pm 2.3	4.6 \pm 1.6
	S-C_550 °C	9.7 \pm 2.0	7.6 \pm 1.5	9.0 \pm 0.4	7.2 \pm 0.5	7.2 \pm 3.9	6.0 \pm 2.9

Cast_Homogenization: casting conditions and applied homogenization temperature; R_{LOM} , R_{BSE} , R_{EBSD} : calculated grain radii from results of the line intercept measurements and correction factors; RD, ND: grain size in rolling and normal direction.

With the increased Mn level in the LFe-HMn alloy and the strong formation of dispersoid particles, the grain growth is significantly retarded. Comparing the grain sizes in **Tab. 6.2** the average grain size decreases by more than a factor of 2, depending on the sample processing; however, as observed for the HFe-HMn alloy, the change in Fe contents with the high Mn level does not significantly alter the grain radii. Clearly, in the presence of high dispersoid density, the higher number density of the primary phases does not show any considerable effects.

Contrarily, the HFe-LMn alloy exhibits a refinement of the grains compared to the LFe-LMn alloy. Since the number density of dispersoids is comparably low in both alloys, the effect may be related to the higher number density of primary phase particles in this sample.

Tab. 6.3. Grain size results for 35% CRD samples from LOM, BSE and EBSD images.

Alloy	Cast_Homogenization	R_{LOM} [μm]		R_{BSE} [μm]		R_{EBSD} [μm]	
		RD	ND	RD	ND	RD	ND
LFe-LMn	NR-C_500 °C	18.6 ± 0.4	18.9 ± 3.2	19.5 ± 0.6	20.0 ± 0.6	17.2 ± 10.3	17.1 ± 9.9
	S-C_500 °C	21.5 ± 3.7	19.3 ± 2.3	25.1 ± 2.2	22.4 ± 2.0	20.7 ± 13.2	20.2 ± 12.5
	NR-C_550 °C	18.8 ± 1.5	18.2 ± 3.8	16.3 ± 0.9	16.4 ± 0.7	14.7 ± 8.6	14.0 ± 7.7
	S-C_550 °C	22.9 ± 3.2	19.5 ± 3.4	22.7 ± 1.7	21.9 ± 1.2	18.3 ± 10.6	16.8 ± 9.5
LFe-HMn	NR-C_500 °C	12.6 ± 2.3	10.9 ± 2.4	9.3 ± 0.5	7.0 ± 0.7	8.9 ± 5.5	6.4 ± 3.2
	S-C_500 °C	15.0 ± 2.6	10.2 ± 1.1	19.4 ± 2.5	14.2 ± 0.3	11.5 ± 8.3	7.1 ± 3.8
	NR-C_550 °C	12.5 ± 2.2	8.7 ± 0.6	10.0 ± 1.0	7.3 ± 0.7	8.9 ± 5.4	6.6 ± 3.4
	S-C_550 °C	13.7 ± 2.3	10.1 ± 0.7	12.4 ± 0.4	10.1 ± 0.4	10.2 ± 6.8	7.9 ± 4.5
HFe-LMn	NR-C_500 °C	12.1 ± 1.2	12.0 ± 1.9	13.2 ± 0.6	12.6 ± 1.0	10.4 ± 5.8	9.2 ± 4.8
	S-C_500 °C	18.4 ± 3.0	16.7 ± 2.5	20.9 ± 1.5	19.1 ± 1.4	17.3 ± 10.5	16.4 ± 9.9
	NR-C_550 °C	13.0 ± 2.2	13.6 ± 1.2	13.0 ± 0.8	13.9 ± 0.7	11.1 ± 6.3	9.9 ± 5.2
	S-C_550 °C	15.2 ± 3.2	15.6 ± 2.9	17.4 ± 0.6	17.4 ± 0.4	13.4 ± 7.8	12.1 ± 6.8
HFe-HMn	NR-C_500 °C	10.7 ± 1.6	7.2 ± 0.8	7.8 ± 1.1	6.0 ± 0.4	7.0 ± 3.8	5.4 ± 2.3
	S-C_500 °C	17.7 ± 3.8	9.6 ± 0.8	11.6 ± 1.8	9.0 ± 0.8	10.2 ± 7.2	7.4 ± 4.0
	NR-C_550 °C	9.1 ± 1.4	7.3 ± 0.4	9.0 ± 0.4	7.9 ± 0.6	7.2 ± 3.8	6.0 ± 2.8
	S-C_550 °C	14.9 ± 2.3	10.6 ± 1.4	11.1 ± 0.9	8.8 ± 1.0	9.2 ± 5.8	7.7 ± 4.2

Cast_Homogenization: casting conditions and applied homogenization temperature; R_{LOM} , R_{BSE} , R_{EBSD} : calculated grain radii from results of the line intercept measurements and correction factors; RD, ND: grain size in rolling and normal direction.

6.3.2 Zener Pinning Effect of Dispersoids

The importance of the Zener pinning effect is highlighted with the large differences in the resulting grain sizes shown in **Tab. 6.2**. With the dispersoids formation and the experimentally observed variations in the number density after homogenization (see Part I [15]), a wide range of the resulting pinning forces is to be expected. For accurate calculations of the limiting grain size, the volume fractions, as well as mean radii and aspect ratios of the dispersoids, were analyzed in all 32 different final sample states. **Tab. 6.4** and **Tab. 6.5** show the results of the analyses for the different alloys with NR-C cast conditions and 63% CRD at 500 °C and 550 °C homogenization, respectively.

Comparing the volume fractions of the secondary phase particles of the four alloys in **Tab. 6.4**, the trend of favored dispersoid formation in the high Mn alloys is obvious, whereas the Fe contents seem to have only little influence. Furthermore, the aspect ratio of the dispersoids is clearly more unbalanced in the higher volume fraction containing alloys LFe-HMn and HFe-HMn. Similar trends were observed for the samples with higher homogenization temperature (**Tab. 6.5**), although the volume fraction of dispersoids is significantly lower in the LFe-HMn alloy compared to HFe-HMn. Distinct coarsening of the secondary phase particles was observed with the higher homogenization

temperature comparing the values of the mean radii in **Tab. 6.4** and **Tab. 6.5**, whereas the aspect ratios remained almost unaffected, especially for the LFe-HMn and HFe-HMn alloys.

Tab. 6.4 and **Tab. 6.5** also contain the results of the Zener limiting grain size calculated according to (Equ. 6.1 with the experimentally evaluated particle sizes and volume fractions and different parameters from literature (see section “Materials and Methods”). Comparing the grain size predictions of the different models in **Tab. 6.4**, a wide range of possible values is obtained. Concerning the alloys containing low dispersoid volume fractions LFe-LMn and HFe-LMn, the approaches of Smith–Zener and Ryum both distinctly overestimate the resulting mean grain size in comparison to the experimentally obtained data in **Tab. 6.2**.

Tab. 6.4. Volume fractions and morphological parameters of the dispersoids for NR-C cast samples homogenized at 500 °C, cold rolled to a CRD of 63% and soft annealed; limiting grain sizes calculated using the models of Smith–Zener [26], Manohar [33] and Ryum [32].

Sample	Volume Fraction [vol. %]	r [nm]	AR	R _{lim} [μm]			
				Smith–Zener	Manohar	Ryum RD	Ryum ND
LFe-LMn	0.01	50	1.54	1207.0	153.9	1775.5	1094.5
LFe-HMn	1.01	73	2.13	9.6	1.2	19.42	7.95
HFe-LMn	0.08	67	1.95	105.8	13.5	195.3	89.7
HFe-HMn	1.07	63	2.06	7.9	1.0	15.4	6.6

r: average dispersoid radius; AR: aspect ratio of the ellipsoidal particles; R_{lim}: calculated limiting grain radius using different Zener pinning model parameters.

The calculations using the parameters of Manohar tend to accord with the mean grain radii from EBSD measurements, especially for the HFe-LMn alloy. Similar results are obtained for the higher homogenization temperature of 550 °C in **Tab. 6.5**, where the approach of Manohar roughly fits for LFe-LMn and HFe-LMn.

On the other hand, the calculations for LFe-HMn and HFe-HMn show contrary results. For the 500 °C homogenization temperature, the models of Smith–Zener and Ryum yield results which are in good accordance with the experimentally observed data.

Tab. 6.5. Volume fractions and morphological parameters of the dispersoids for NR-C cast samples homogenized at 550 °C, cold rolled to a CRD of 63% and soft annealed; limiting grain sizes calculated using the models of Smith–Zener [26], Manohar [33] and Ryum [32].

Sample	Volume Fraction [vol. %]	r [nm]	AR	R _{lim} [μm]			
				Smith–Zener	Manohar	Ryum RD	Ryum ND
LFe-LMn	0.04	65	1.60	199.6	25.5	304.2	179.2
LFe-HMn	0.58	81	2.15	18.6	2.4	37.8	15.3
HFe-LMn	0.06	76	1.65	169.0	21.5	264.4	150.5
HFe-HMn	1.00	79	1.93	10.5	1.34	19.2	8.9

r: average dispersoid radius; AR: aspect ratio of the ellipsoidal particles; R_{lim}: calculated limiting grain radius using different Zener pinning model parameters.

However, the grain size calculations using the ellipsoidal model of Ryum show better conformity for ND than for RD. Again, very similar relations were observed for the 550 °C homogenization in **Tab. 6.5**, although the calculated grain sizes are slightly higher than the average experimentally obtained data. The larger resulting grain size for the higher homogenization temperature can be attributed to the higher average radius of the dispersoids. Furthermore, the poor comparability of the resulting grain radii from Manohar's approach is noticeable for the two high manganese containing alloys.

Further experimental data can be found in **Tab. A6.1** and **Tab. A6.2** in the Appendix to Section 6, comparing other processing conditions, such as S-C cast and cold rolling degree of 35%.

The different Zener models and the effects of various parameters on the limiting grain radius in dependence on the dispersoid radius and the total volume fraction of the secondary phase particles are illustrated in **Fig. 6.7**. The experimental data points include the volume fractions and radii of the dispersoids, as well as the grain radii (from EBSD), of all sample states of the four alloys.

For the samples with low dispersoid volume fraction LFe-LMn and HFe-LMn, all models overestimate the experimentally obtained resulting grain size, but the analytical description according to Manohar is clearly better than that according to Smith–Zener. Conversely, the Smith–Zener model describes the measured mean grain sizes of the samples with high dispersoid volume fraction LFe-HMn and HFe-HMn quite well.

Numerous computational 3D simulations on the Zener limiting grain size derived values of the exponent m close to 0.33 for dispersoid volume fractions over 1% [34–36]. **Fig. 6.7** includes an optimized model fitting the experimental data. Although in fact only applicable for samples with high dispersoid volume fractions LFe-HMn and HFe-HMn, the constant factor K was adapted to best fit the data points for all alloys using $m = 0.33$. In general, a good conformity can be obtained for LFe-LMn, LFe-HMn and HFe-HMn; only in HFe-LMn is the obtained grain size in average lower than that predicted by the applied model.

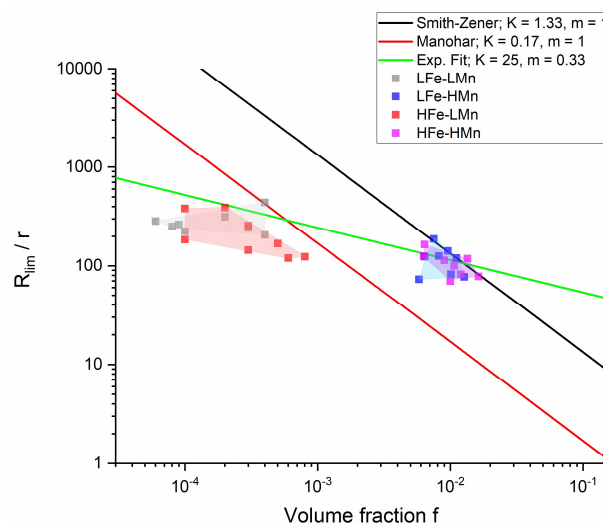


Fig. 6.7. Comparison of the Zener limiting grain size calculated from the models of Smith–Zener and Manohar [26, 28, 33] to the experimentally observed data for the four different alloys, including the best fit.

6.3.3 Grain Boundary Pinning by Primary Phase Particles

Besides the grain refinement observed in the high dispersoid fraction containing alloys LFe-HMn and HFe-HMn, the HFe-LMn alloy shows significant reduction in the mean grain radius in comparison to LFe-LMn. Since the number fraction of secondary phase particles is comparably low in both alloys, the effect must be connected to the higher Fe content, equivalent to higher primary phase fractions.

Fig. 6.8 shows the EBSD inverse pole figure map of NR-C cast HFe-HMn alloy, homogenized at 500 °C and cold rolled to 63%. While **Fig. 6.8 (a)** provides a more general overview of the microstructure and orientation distribution in the present alloy, **Fig. 6.8 (b)** gives more details on the primary phases in the marked area (red rectangle). The magnified IPF map (**Fig. 6.8 (b) top**) shows the dark appearing primary phases in band-wise arrangement situated at the edges of various grains. Closer consideration reveals many of these rather coarse particles located at triple points, already suggesting an impact on the grain boundary mobility and, therefore, the grain growth behavior. Although the suggested Zener pinning of coarse particles is low in comparison to the dispersoid pinning, the general pinning efficiency is increased with the particles situated at grain junctions. Therefore, for the high primary phase volume fraction containing alloys HFe-LMn and HFe-HMn, an additional pinning pressure is obtained resulting in grain refinement, especially for HFe-LMn. The grain size map in **Fig. 6.8 (b) (bottom)** depicts the color-coded grain size in the magnified area. From both the IPF and the size area map, a certain refinement of the average grain size is obtained around primary phases.

Fig. 6.8 (c),(d) show the band contrast and high angle grain boundaries ($>15^\circ$ misorientation) of the investigated sample section. Both indicated fully recrystallized microstructures and do not show remaining subgrains.

6.3.4 Texture Modifications by Primary and Secondary Phase Particles

The texture analysis concerns the orientation data from the EBSD measurements of the total cross sections of the samples including, in all cases, more than 4000 grains. With very low maximum intensities in the calculated orientation distribution functions, the results are presented in terms of bar charts on the EBSD area fractions of selected ideal texture components. Additionally, **Fig. A6.28** exemplary shows the ODF data of a HFe-HMn alloy plotted in sections of Euler angle φ_2 , including the ideal orientations of specific texture components. In general, as already observable in the IPF maps in **Fig. 6.2–Fig. 6.6** and **Fig. 6.8**, the grains do not show preferred orientations. No peculiarities regarding the interaction of differently sized particles with the surrounding grain orientations can be seen.

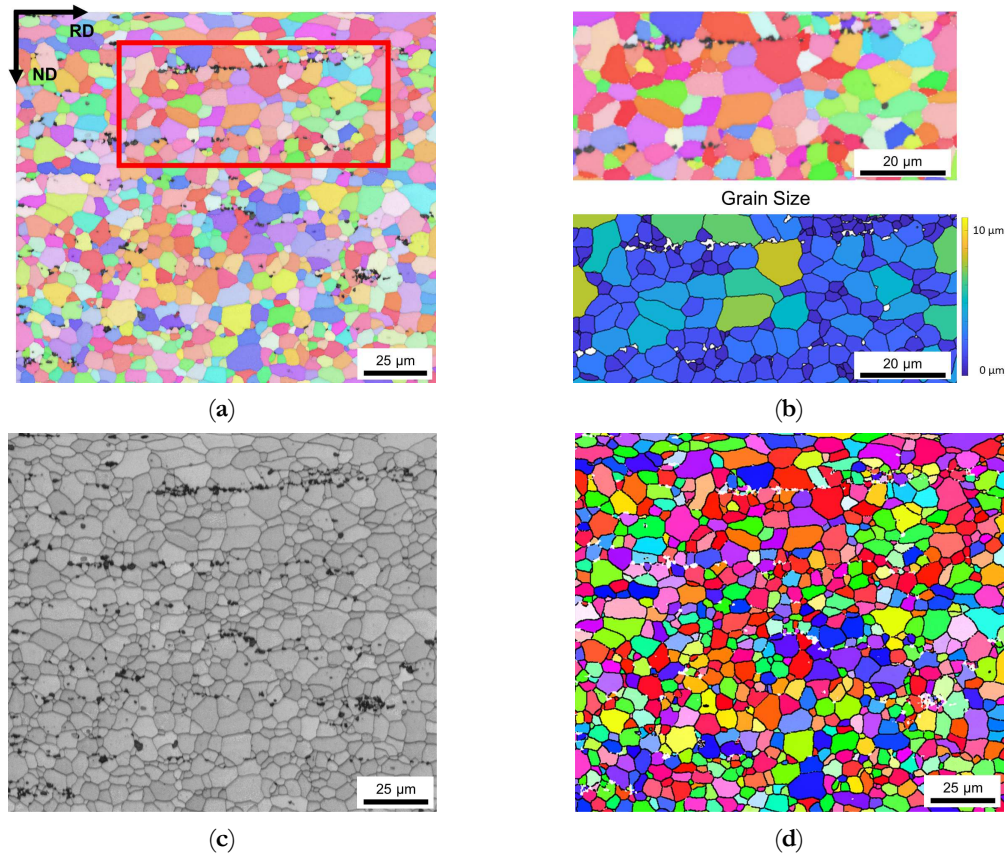


Fig. 6.8. (a) Inverse pole figure map in RD–ND plane of NR-C cast HFe-HMn alloy, homogenized at 500 °C and cold rolled to a CRD of 63%. (b) Magnified area showing the primary phase arrangement and the area equivalent grain radius of surrounding grains, respectively. (c) Band contrast image indicating the fully recrystallized microstructure. (d) Overlay of high angle grain boundaries ($>15^\circ$, black) on the IPF map shown in (a).

The influence of the various process parameters on the overall texture evolution in the different alloys is shown in **Fig. 6.9** (and **Fig. A6.29** for other sample states). The resulting texture for NR-C and S-C cast conditions (500 °C homogenization, 35% CRD; **Fig. 6.9** (a),(b)) demonstrates a generally low impact of the different casting conditions on the final texture. Besides the very low intensities obtained for both the rolling and recrystallization components, the NR-C samples show higher Cube_{ND} texture intensities for the different alloys on average (comparing **Fig. 6.9** (a),(b)).

The results obtained for the different homogenization temperatures (comparing **Fig. 6.9** (b),(c)) show a slightly higher persistence of the β -fiber rolling components, as well as a slightly higher content of the classical Cube and Cube_{ND} recrystallization textures for higher annealing temperatures.

In contrast to the casting and homogenization process, the degree of cold work prior to final sheet annealing controls the texture evolution of the sample in some part (comparing **Fig. 6.9** (c),(d)). Concerning the β -fiber components, **Fig. 6.9** (d) clearly shows the weakened intensities obtained for higher cold rolling. As expected, contrary behavior is obtained for the recrystallization components and the Goss orientation.

Furthermore, the texture evolution for the alloys and, thus, the different primary and secondary phase fractions can be derived from **Fig. 6.9** and **Fig. A6.29** for the various processing parameters. An

overall trend of retained β -fiber components in the final sheets was observed with the different secondary phase volume fractions of the alloys. With increasing dispersoid number density the rolling components favorably persist the annealing treatment.

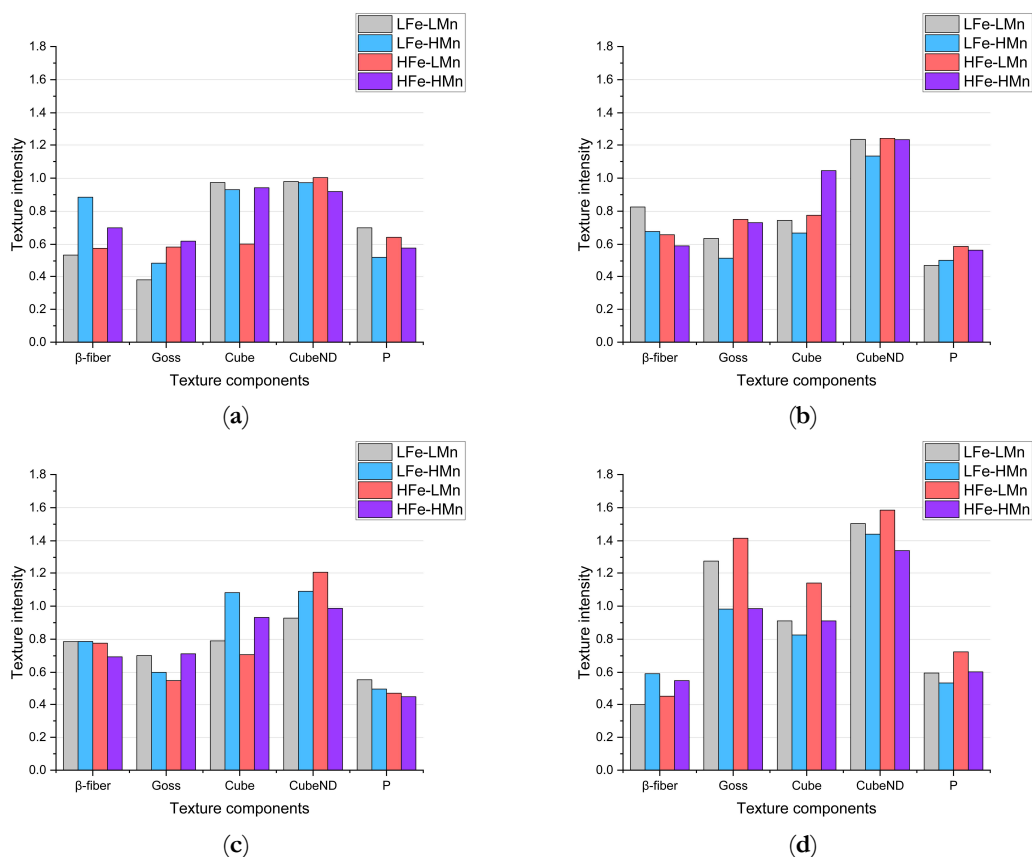


Fig. 6.9. Influence of the processing parameters on the resulting texture of the different alloys in the final soft annealed sheets. (a) S-C cast, 500 °C homogenized and 35% CRD. (b) NR-C cast, 500 °C homogenized and 35% CRD. (c) NR-C cast, 550 °C homogenized and 35% CRD. (d) NR-C cast, 550 °C homogenized and 63% CRD.

The Goss component, which can be found in typical rolling and recrystallization textures, exhibits an ambiguous progress, as the intensity is weakened or reinforced in the LFe-HMn and HFe-HMn alloys. The frequently observed Cube component shows low area fractions, which are on average slightly increased for the alloys with higher dispersoid volume fractions. The formation or growth of PSN component P is promoted in some of the LFe-LMn and HFe-LMn alloys. No effects of PSN can be seen in the very erratic CubeND area fractions. For a more detailed analysis of possible PSN effects, an additional evaluation of the areas around coarse primary phase particles was carried out and the occurring texture components analyzed. While the grain size was significantly reduced in the immediate vicinity of the particles (**Fig. 6.8 (b)**), no clear trend towards intensification of characteristic PSN texture components was obtained.

6.4 Discussion

We first focus the discussion on the resulting mean grain size in the different sample states, which is depicted in **Fig. 6.2–Fig. 6.6** and stated in **Tab. 6.2**, for 63% cold rolled samples, or **Tab. 6.3**, for 35% cold rolled samples, respectively.

Comparing the different results for the line intercept method from LOM, BSE and EBSD micrographs in **Fig. 6.2 (a),(c)**, the importance of well-designed grain size analysis becomes clear. Although LOM and BSE imaging and evaluation are more easily executed, the EBSD technique is less user-biased and was reported in [78] to have advantages especially in the detection of smaller sized grains. This is verified by the results in **Tab. 6.2**, where the average grain size is significantly smaller for experimentally observed data by the EBSD technique. Therefore, especially for further calculations, the usage of EBSD is beneficial to avoid error propagations [78]. However, the standard deviation is higher for EBSD results.

The influence of the processing parameters on the final grain size is denotable from **Tab. 6.2** and the respective figures. The refinement of the grains and the microstructural features obtained for the NR-C (near-rapid cooling) casting conditions [17] (comparing **Fig. 6.4** and **Fig. 6.5**) will improve the mechanical properties of the Al sheets, since the smaller average grain size is still preserved in the final sheet, to some extent [14]. Furthermore, the combination of the solidification rate and Fe, Mn and Si alloying contents determine the size, shape and composition of the primary phase particles [7–9, 12]. With the high number density of rather small and blocky Al-Fe-Mn(-Si) precipitates, as in, for example, the HFe-HMn alloys (**Fig. 6.3** and **Fig. 6.4 (b)**), the NR-C conditions can reduce the adverse effects caused by stress concentrations of needle-shaped Fe bearing phases and thus increase the mechanical properties, such as r value, yield strength or ultimate tensile strength [11, 67].

The comparison of **Tab. 6.2** to **Tab. 6.3** clarifies the impacts of the cold rolling degree on the resulting grain size. According to the classical recrystallization theory, the higher pressure for recrystallization in the 63% cold rolled alloys leads to distinct refinement of the microstructure in the soft annealed state (**Fig. 6.3** and **Fig. 6.4**) and might therefore improve the mechanical properties [14].

The effect of the homogenization temperature on the final sheets microstructure is discussed in light of **Tab. 6.2**, as well as **Tab. 6.4** and **Tab. 6.5**. As reported in Part I of the present study, the shape and constitution of the primary Al-Fe-Mn(-Si) and Mg_2Si particles alter with the high temperature heat treatment [15, 79, 80]. Furthermore, secondary phase particles undergo distinct coarsening at the higher homogenization temperature for LFe-HMn and HFe-HMn alloys (see **Fig. 6.2** and **Fig. A6.6 (d)** as well as **Fig. 6.5** and **Fig. 6.6 (d)**; compare **Tab. 6.4** and **Tab. 6.5**) [13, 79]. Although the results in the average grain size for 500 °C and 550 °C homogenization in **Tab. 6.2** are ambiguous concerning the exerted pinning forces by the dispersoids, the homogenization treatment plays a

fundamental role in the microstructure evolution in multiphase materials, as it predominantly initiates the dispersoid formation [16, 79, 80].

Alongside the processing parameters, the Fe and Mn alloying levels are crucial for the microstructure evolution in deformation and recrystallization processes [14, 67]. Concerning the results in **Tab. 6.2** or the micrographs given in **Fig. 6.2** and **Fig. 6.3**, either high Fe and/or Mn contents yield significant grain refinement for the HFe-HMn in comparison to the LFe-LMn alloy. However, in reference to the primary and secondary phase volume fractions obtained for the different alloys [15], the effect of Zener pinning requires consideration and sophisticated discussion in this context [10, 14, 66].

With the formation of $Al_6(Fe,Mn)$ dispersoids during homogenization found mainly in the high Mn containing alloys, the effective Zener pinning is clearly denoted by the obvious reduction in the average grain size. Besides the verification of the general Zener pinning effect [26], the results for the limiting grain size given in **Tab. 6.4** and **Tab. 6.5** vary significantly with the different model parameters for (Equ. 6.1 [26, 32, 33]). The large discrepancies between the approaches of Smith–Zener or Ryum and Manohar occur from the differently chosen pinning and driving pressures for grain growth [28]. However, while [28] stated the good applicability of the Manohar model parameters [33] to predict the resulting grain size in materials with dispersoid volume fractions below $f_v = 0.05$, the data for LFe-HMn and HFe-HMn in **Tab. 6.4** and **Tab. 6.5**, as well as **Fig. 6.7**, show best conformity with the original Smith–Zener approach [26].

Although the grain size predictions by the Ryum model [32] do not match the experimentally observed data as well as the Smith–Zener approach, the implementation of the dispersoids ellipsoidal shape in (Equ. 6.1) seems a necessary improvement for the present study. With the often obtained rod- or plate-like shape of the dispersoids in Mn and Fe containing 5xxx alloys [13, 19, 79] and their (banded) alignment with RD in subsequent processing (**Fig. 6.2** and **Fig. 6.3 (d)**), the resulting Zener drag will be different for the individual sample directions [27, 35, 41, 45]. The aspect ratios of the dispersoids in the high Mn containing alloys given in **Tab. 6.4** and **Tab. 6.5** affect the pinning efficiency in RD and ND and further cause the discrepancies in the grain size in those directions [14].

Concerning the resulting grain size in the LFe-LMn and HFe-LMn alloys, **Fig. 6.7** clearly depicts that large discrepancies occur between the predictions of the Smith–Zener or Manohar model and the experimental data. On the other hand, the tentatively applied optimized fit, which follows model parameters obtained for computational studies using the exponent $m = 0.33$, shows high accordance to the experimental data. Nevertheless, the close match with LFe-LMn and HFe-LMn is unexpected, as the computational model is stated to be valid only for high volume fractions of dispersoids $f_v > 0.01$ [34–46]. Moreover, the reliability of the fit is questionable with the high value of $K = 25$, since most studies proposed this parameter to be around $4/3$, as in the original Smith–Zener approach, or even lower [28]. Possible explanations for the deviations in the grain size prediction for the low Mn containing alloys might be that the final soft annealed samples (even though fully recrystallized) either

i) did not reach the static limiting grain size by grain growth in the short-term soft annealing, or ii) additional (primary phase) particle-related effects reduced the resulting grain size [14].

As shown in **Fig. 6.8 (b)** for the HFe-HMn alloy, the final microstructure and grain size shows distinct influence of micron-sized fragmented primary phases. With the effect of particle stimulated nucleation, preferential nucleation around these fragmented phases may be partly responsible for grain refinement [14, 20, 22, 25]. However, since the coarse primary particles are favorably situated on grain boundaries and junctions of the final recrystallized grains, they should also be considered for pinning effects during recrystallization and grain growth. Because the particle pinning efficiency decreases with increasing particle dimensions, additional pinning effects are only obtained for high primary phase volume fraction containing alloys HFe-LMn and HFe-HMn [26–28]. Therefore, the refined grains for HFe-LMn in comparison to LFe-LMn in **Tab. 6.2** may be the result of combined effects of PSN and primary phase pinning. The similar trends of grain size reduction for S-C cast HFe-HMn in comparison to LFe-HMn suggest equivalent mechanisms; however, with the high fraction of pinning dispersoids weakening the effect of the primary phases, the difference in the resulting grain size is significantly smaller [69].

In general, the present study verifies the theories of Zener pinning by second phase dispersoid particles. Despite numerous sophisticated corrections and improvements that have included various parameters into the model for the resulting limiting grain size, the applicability for predicting the resulting grain size in experimental or industrial processes is still limited. Even though the present results confirm the conclusions of the original Smith–Zener relation, further investigations and combined implementation of various particle-grain boundary related effects in an all-encompassing model equation are still sought [14, 26, 28, 32].

We now discuss the texture evolution of the investigated alloys shown in the IPF maps in **Fig. 6.2–Fig. 6.6 (c)**, as well as **Fig. 6.9** and **Fig. A6.29**. All samples exhibit remarkably low fractions of typical aluminum recrystallization textures in the annealed condition. These overall minor intensities were similarly found for laboratory and industrially processed EN AW-5182 alloys [73]. The texture transformations to higher random fractions can be attributed to shear band formation, which is likely in high Mg containing Al alloys implicating Cube texture suppression and preferential nucleation of Goss, P and Q orientation, or to PSN effects [14, 58].

Fig. 6.9 (a),(b) highlight the small and ambiguous influence of the casting process on the final texture. The variation in the casting cooling conditions S-C and NR-C mainly influences the refinement of the primary phase and the casting grain and accompanying texture modifications will be observed in the comparison of the individual alloys. As both casting processes do not involve any special operations or directed solidification, the formation of pronounced texture components in the as-cast state is not promoted [21] and, thus, the transfer of orientations, such as Cube, to the final soft annealed states is unlikely to occur [54].

The influence of the maximum homogenization temperature on the resulting texture is hardly perceptible when comparing **Fig. 6.9 (b),(c)**. Although grain boundary pinning by dispersoid particles in general affects the texture evolution, the differences in average dispersoid size and amount at 500 °C and 550 °C homogenization do not produce significant texture transformations [23, 25, 68, 69].

It is well established that cold rolling significantly influences the recrystallization behavior of materials by altering the driving pressure for primary recrystallization and normal grain growth [14]. The results on the impact of the CRD on the recrystallization texture (comparing **Fig. 6.9 (c),(d)**) are in line with expectations, as the higher CRD of 63% promotes recrystallization during soft annealing and, hence, exhibit lower fractions of remaining β -fiber components but more pronounced recrystallization textures [14].

With the generally weak texture found in the present study, the texture modifications due to primary particles and dispersoids can only be assessed by trends and not by significant differences in the intensities. The impacts of the Zener drag on the recrystallization texture can be deduced from the behavior of the different alloys in **Fig. 6.9** and **Fig. A6.29**. The weaker transformation of the rolling components in the LFe-HMn and HFe-HMn alloys can be related to pinning effects by dispersoids, since the growth of emerging recrystallization nuclei with Goss, P and Cube_{ND} orientation is retarded [25, 66, 68, 69]. In turn, the intensities of those components are rather low in comparison to the LFe-LMn and HFe-LMn alloys. Furthermore, as the growth of Cube oriented grains is assumed to be least affected by pinning effects, slightly higher Cube fractions are obtained for some of the LFe-HMn and HFe-HMn alloys in various sample states, in agreement with the mechanisms described in literature [25, 68, 69].

For the formation of the recrystallization structures, the PSN mechanism also needs to be taken into account, as the occurring fragmentation of primary phase particles during rolling can significantly increase the number of potential PSN nuclei (**Fig. 6.2–Fig. 6.6 (b)**), thus altering the resulting texture [21]. The PSN related texture component P was slightly more favorably observed for the low Mn alloys; in the case of the high Mn alloys, however, the expansion of the P-oriented nuclei is likely to be retarded by dispersoid pinning effects [23–25, 68, 69]. In general, it has to be emphasized that due to the overall weak textures the change of the annealing texture towards a higher random fraction of orientations through PSN effects is very weakly pronounced [6, 58, 59].

With the large varieties in primary and secondary phase fractions in the four different alloys and the differences in the resulting grain size, the mechanical properties, as well as the forming behavior, will be affected. In addition to the commonly known increased strength with the reduction in the average grain size, recent studies also state that there can be beneficial effects of (coarse) Fe and Mn bearing primary phases on the mechanical properties, as well as the deep drawability, as the phases can beneficially refine the soft annealed grain structure and favor texture randomization [3, 11, 67]. Moreover, the detrimental effect of Lüdering in the AlMg(Mn) alloys can effectively be reduced by

the control of the primary and secondary phase number density, size and total volume fraction [70, 71].

Furthermore, whereas numerous publications mention the essential effects of PSN to reduce the mechanical anisotropy or surface effects, such as roping in other Al alloys series [6, 23, 24, 66], the high fraction of random texture components obtained in the 5xxx series will minimize the plastic anisotropy in the material [52, 73]. In light of these findings, in particular the Fe and Mn rich alloy HFe-HMn processed via NR-C is expected to exhibit interesting mechanical properties due to the particle distribution, small grain size and random annealing textures.

6.5 Conclusions

The present work investigates the influence of Fe and Mn bearing primary and secondary phase particles under various processing conditions on the resulting microstructure and texture. With regard to the findings in Part I on the details on primary and secondary particle characteristics, the following conclusions can be drawn.

- Effective Zener pinning was observed for $Al_6(Fe,Mn)$ containing high Mn alloys resulting in distinct refinement of the grains in soft annealed samples.
- Rapid cooling conditions in casting and higher cold rolling degrees significantly refine the final soft annealed microstructures in terms of grain size and fragmentation of primary phases.
- The impact of the maximum homogenization temperature on the resulting microstructure is rather small; despite the fact that homogenization is essential for the formation of the secondary phase, i.e., the dispersoids.
- All investigated conditions showed very weak textures in 5xxx alloys. Nevertheless, trends of the influence of CRD, PSN and Zener related texture modifications were observed.
- When comparing different Zener pinning models with the experimental data, it has been shown that in the original Smith–Zener approach the dispersoid volume fraction is to be weighted with the exponent 0.33 (third root).
- Coarse primary phase particles can affect the microstructure by both PSN and pinning, although the effects are only well observable in combination with low fractions of dispersoids.

Acknowledgements

The authors gratefully thank Lisa Zwitnig for her valuable experimental work during her master thesis and further all involved colleagues at AMAG rolling GmbH, the Christian Doppler Laboratory for Advanced Aluminum Alloys and Chair of Nonferrous Metallurgy, Montanuniversitaet Leoben for their input.

Appendix to Section 6

Tab. A6.1. Volume fractions and morphological parameters of the dispersoids for S-C cast samples homogenized at 500 °C, cold rolled to a CRD of 35% and soft annealed; limiting grain sizes calculated using the models of Smith–Zener [26], Manohar [33] and Ryum [32].

Sample	Volume Fraction [vol. %]	r [nm]	AR	R_{lim} [μ m]			
				Smith–Zener	Manohar	Ryum RD	Ryum ND
LFe-LMn	0.01	78	1.67	1105.8	141.0	1753.0	981.3
LFe-HMn	0.96	81	2.02	11.3	1.4	21.5	9.5
HFe-LMn	0.01	45	1.77	462.8	59.0	773.9	404.2
HFe-HMn	0.64	62	1.82	12.8	1.63	22.1	11.1

r: average dispersoid radius; AR: aspect ratio of the ellipsoidal particles; R_{lim} : calculated limiting grain radius using different Zener pinning model parameters.

Tab. A6.2. Volume fractions and morphological parameters of the dispersoids for S-C cast samples homogenized at 550 °C, cold rolled to a CRD of 35% and soft annealed; limiting grain sizes calculated using the models of Smith–Zener [26], Manohar [33] and Ryum [32].

Sample	Volume Fraction [vol. %]	r [nm]	AR	R_{lim} [μ m]			
				Smith–Zener	Manohar	Ryum RD	Ryum ND
LFe-LMn	0.01	78	1.67	1105.8	141.0	1753.0	981.3
LFe-HMn	0.96	81	2.02	11.3	1.4	21.5	9.5
HFe-LMn	0.01	45	1.77	462.8	59.0	773.9	404.2
HFe-HMn	0.64	62	1.82	12.8	1.63	22.1	11.1

r: average dispersoid radius; AR: aspect ratio of the ellipsoidal particles; R_{lim} : calculated limiting grain radius using different Zener pinning model parameters.

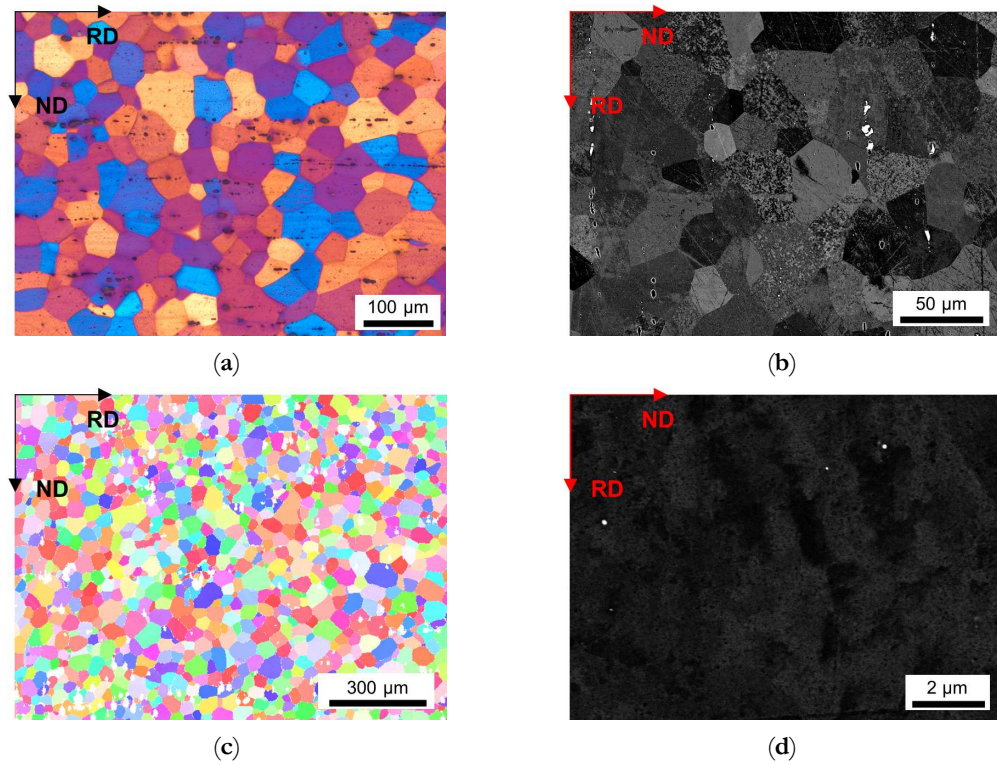


Fig. A6.1. Microstructure of the soft annealed LFe-LMn cast under S-C condition, homogenized at 500 °C and cold rolled to a CRD of 35%. (a) LOM. (b) BSE image. (c) EBSD IPF map in RD–ND plane. (d) BSE micrograph showing dispersoids.

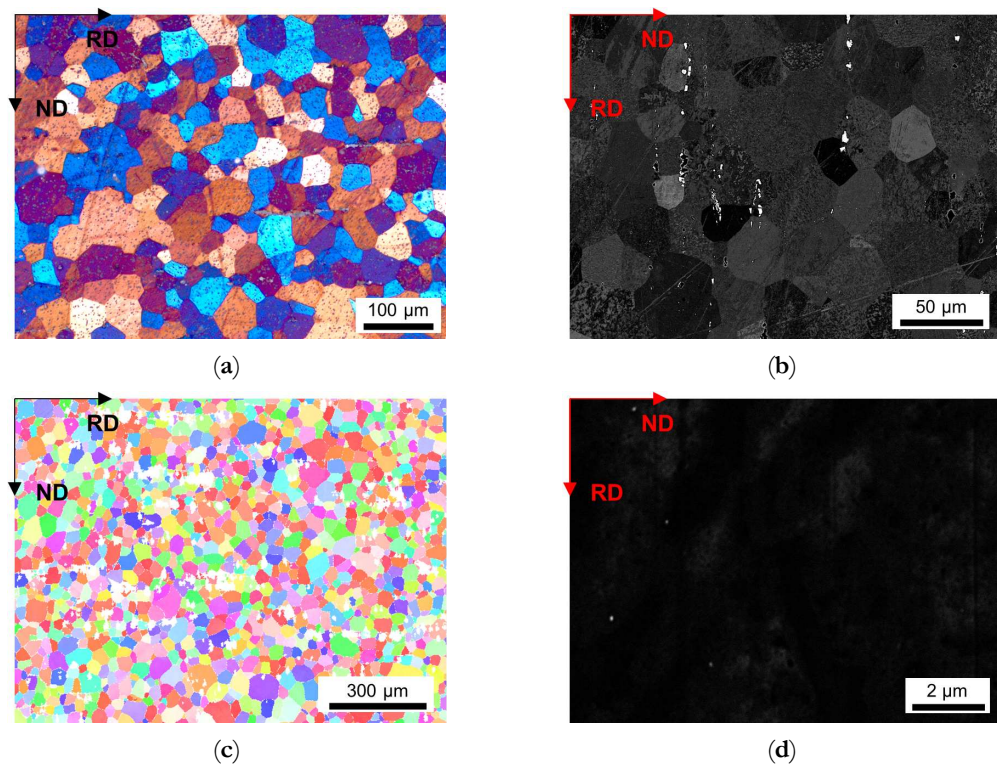


Fig. A6.2. Microstructure of the soft annealed LFe-LMn cast under S-C condition, homogenized at 500 °C and cold rolled to a CRD of 63%. (a) LOM. (b) BSE image. (c) EBSD IPF map in RD–ND plane. (d) BSE micrograph showing dispersoids.

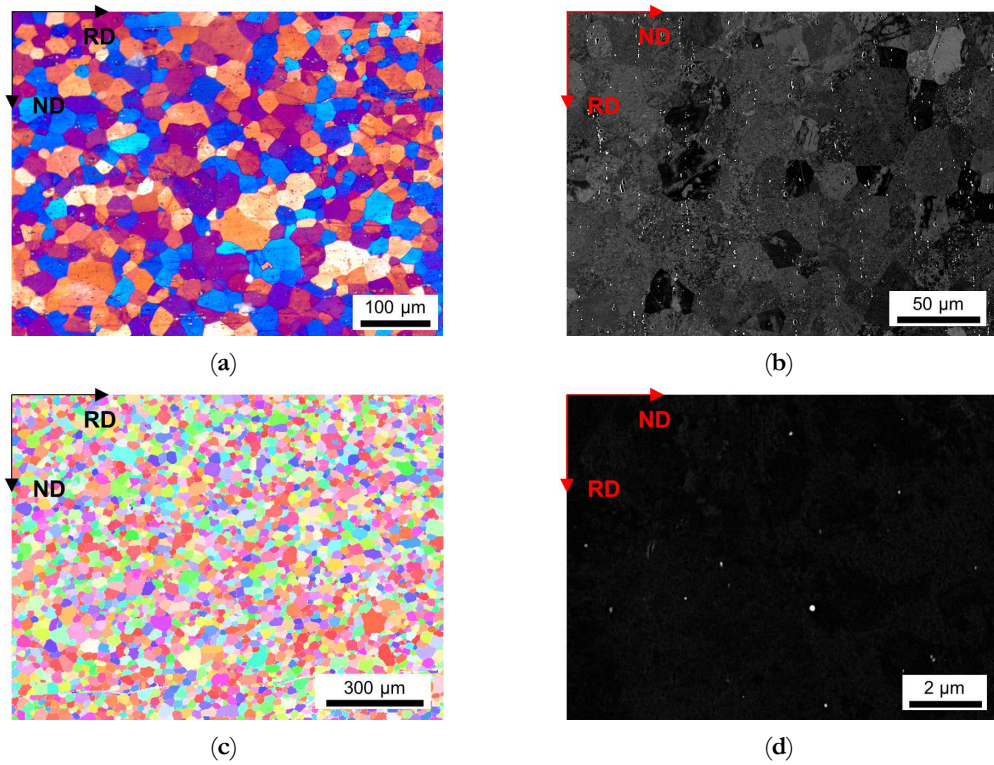


Fig. A6.3. Microstructure of the soft annealed LFe-LMn cast under NR-C condition, homogenized at 500 °C and cold rolled to a CRD of 63%. (a) LOM. (b) BSE image. (c) EBSD IPF map in RD-ND plane. (d) BSE micrograph showing dispersoids.

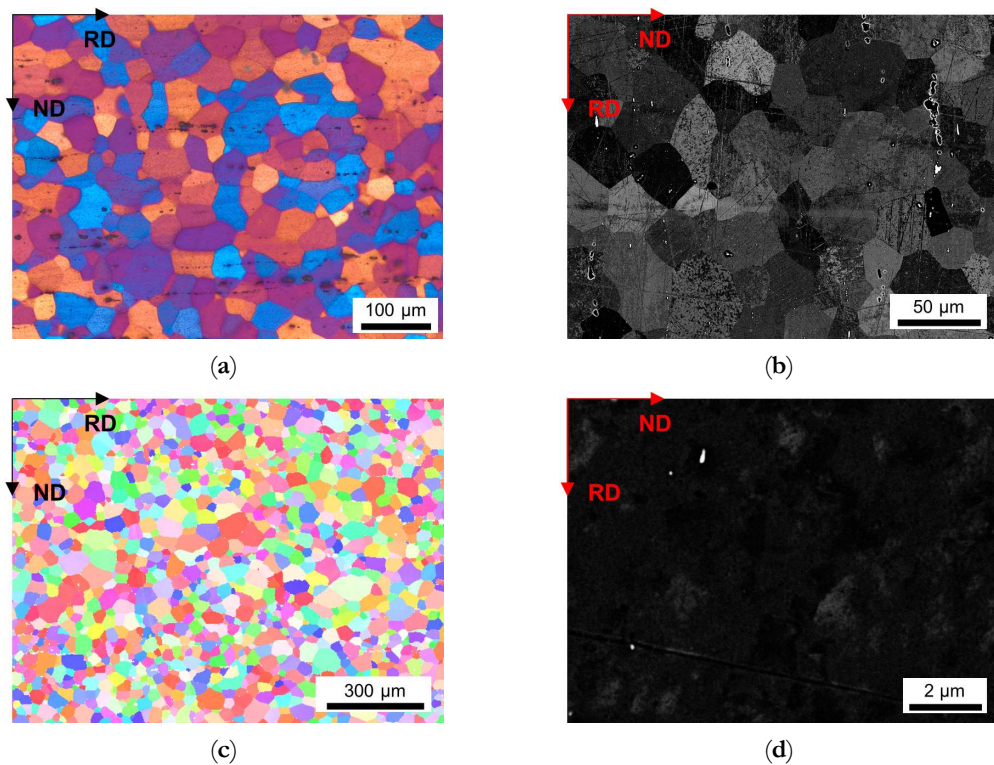


Fig. A6.4. Microstructure of the soft annealed LFe-LMn cast under S-C condition, homogenized at 550 °C and cold rolled to a CRD of 35%. (a) LOM. (b) BSE image. (c) EBSD IPF map in RD-ND plane. (d) BSE micrograph showing dispersoids.

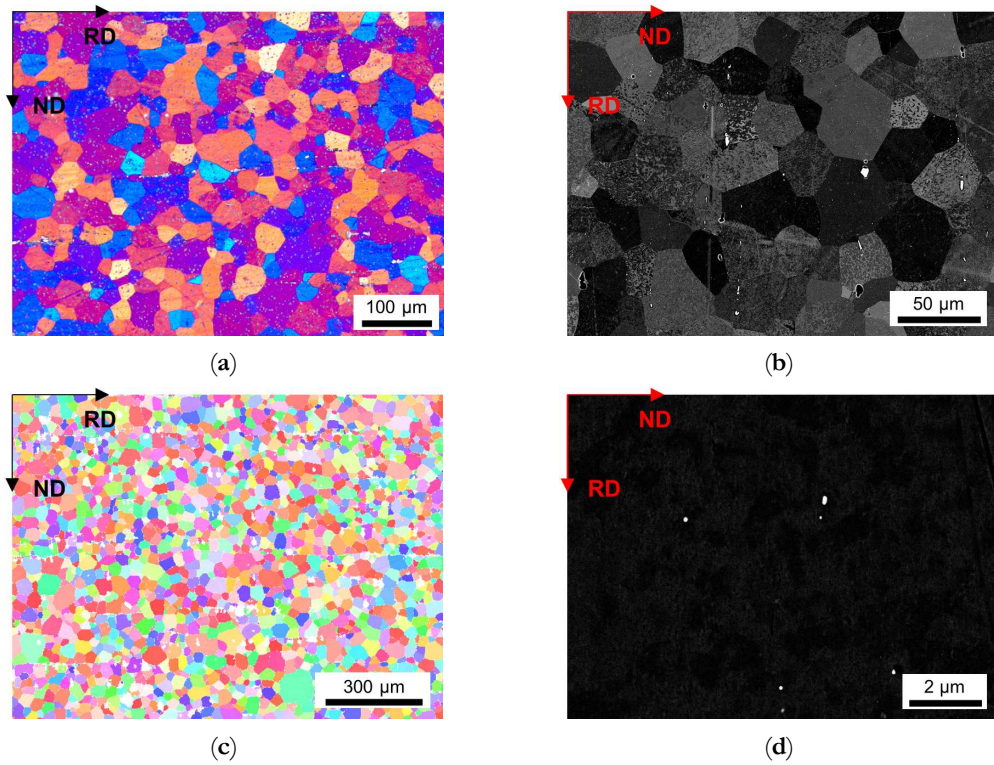


Fig. A6.5. Microstructure of the soft annealed LFe-LMn cast under S-C condition, homogenized at 550 °C and cold rolled to a CRD of 63%. (a) LOM. (b) BSE image. (c) EBSD IPF map in RD–ND plane. (d) BSE micrograph showing dispersoids.

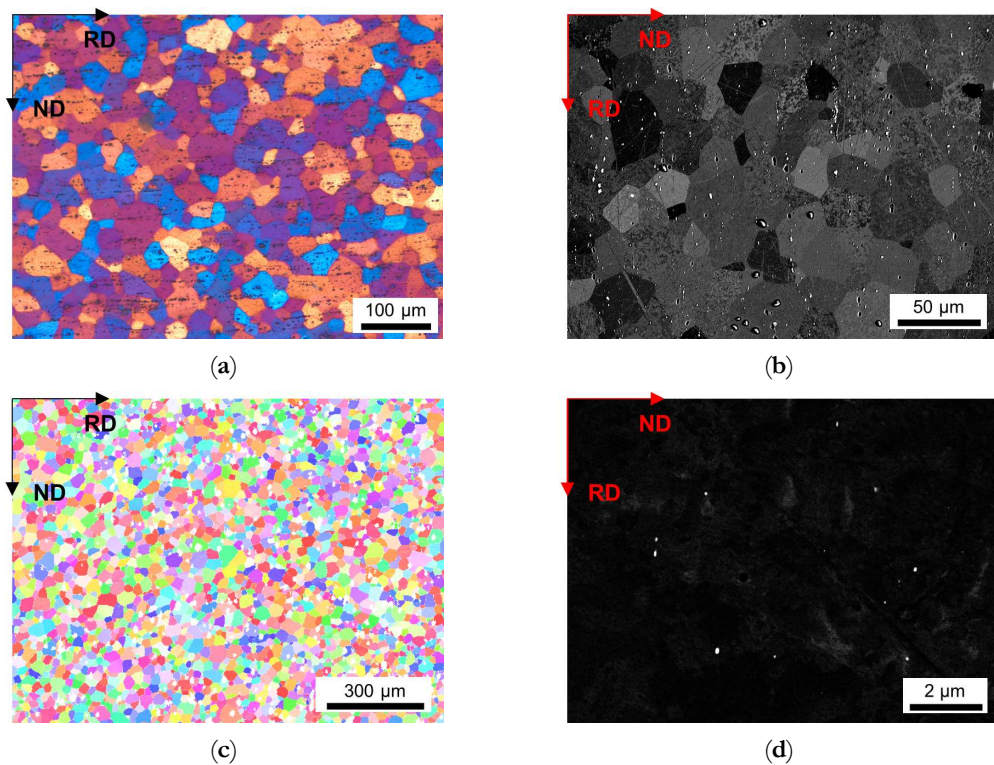


Fig. A6.6. Microstructure of the soft annealed LFe-LMn cast under NR-C condition, homogenized at 550 °C and cold rolled to a CRD of 35%. (a) LOM. (b) BSE image. (c) EBSD IPF map in RD–ND plane. (d) BSE micrograph showing dispersoids.

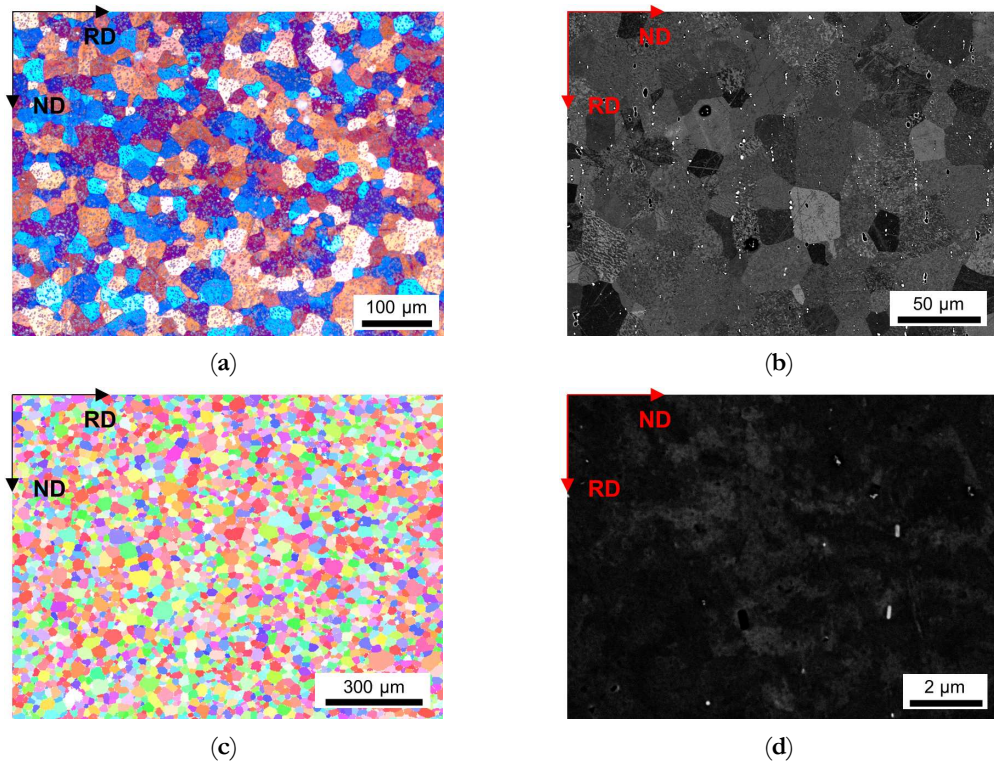


Fig. A6.7. Microstructure of the soft annealed LFe-LMn cast under NR-C condition, homogenized at 550 °C and cold rolled to a CRD of 63%. (a) LOM. (b) BSE image. (c) EBSD IPF map in RD–ND plane. (d) BSE micrograph showing dispersoids.

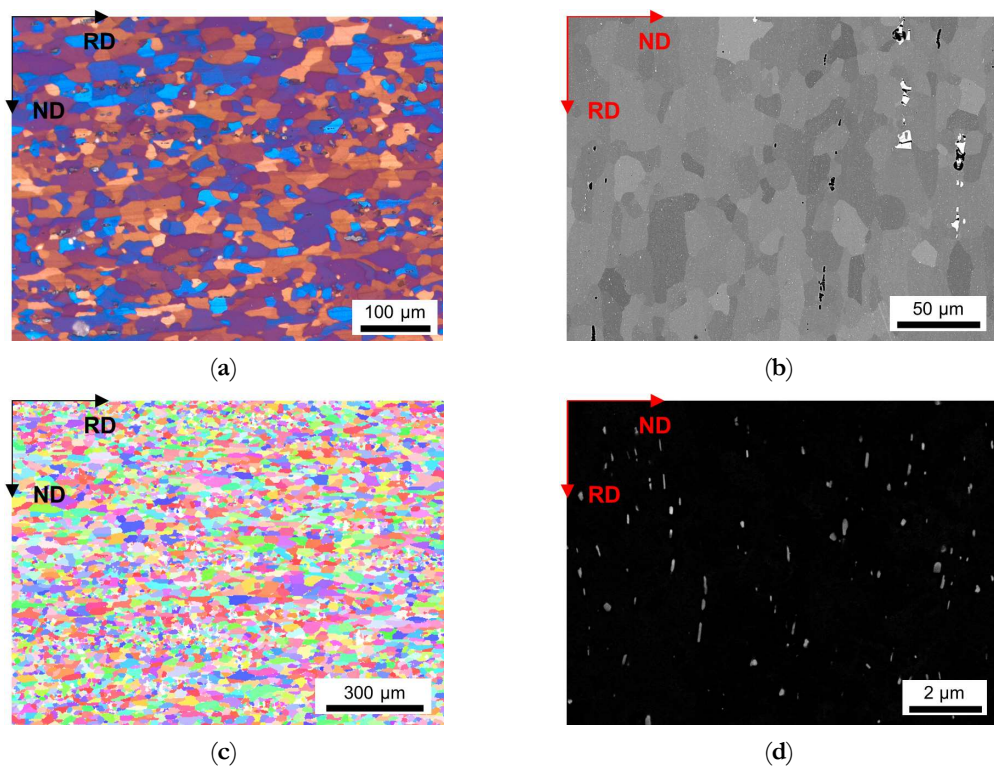


Fig. A6.8. Microstructure of the soft annealed LFe-HMn cast under S-C condition, homogenized at 500 °C and cold rolled to a CRD of 35%. (a) LOM. (b) BSE image. (c) EBSD IPF map in RD–ND plane. (d) BSE micrograph showing dispersoids.

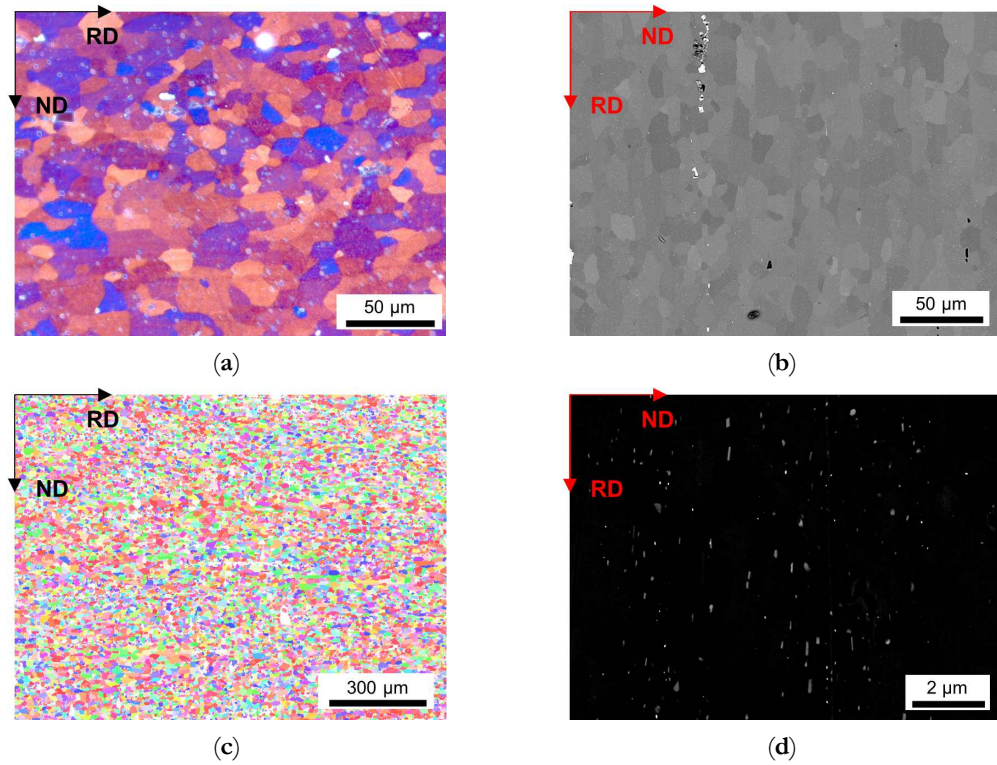


Fig. A6.9. Microstructure of the soft annealed LFe-HMn cast under S-C condition, homogenized at 500 °C and cold rolled to a CRD of 63%. (a) LOM. (b) BSE image. (c) EBSD IPF map in RD–ND plane. (d) BSE micrograph showing dispersoids.

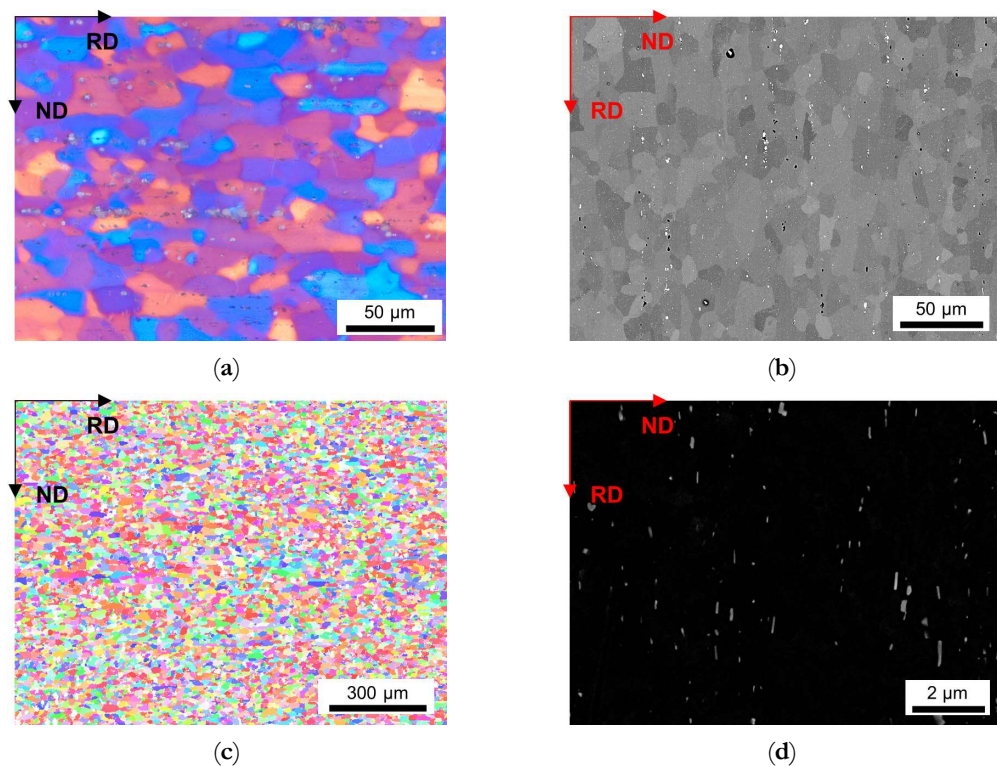


Fig. A6.10. Microstructure of the soft annealed LFe-HMn cast under NR-C condition, homogenized at 500 °C and cold rolled to a CRD of 35%. (a) LOM. (b) BSE image. (c) EBSD IPF map in RD–ND plane. (d) BSE micrograph showing dispersoids.

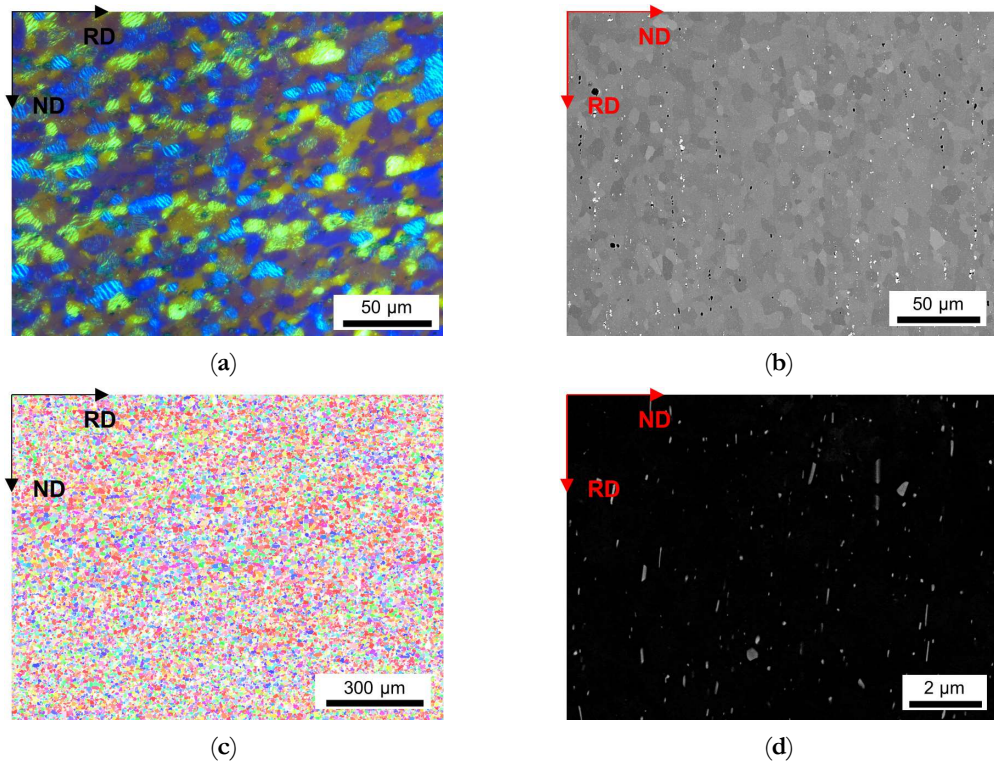


Fig. A6.11. Microstructure of the soft annealed LFe-HMn cast under NR-C conditions, homogenized at 500 °C and cold rolled to a CRD of 63%. (a) LOM. (b) BSE image. (c) EBSD IPF map in RD–ND plane. (d) BSE micrograph showing dispersoids.

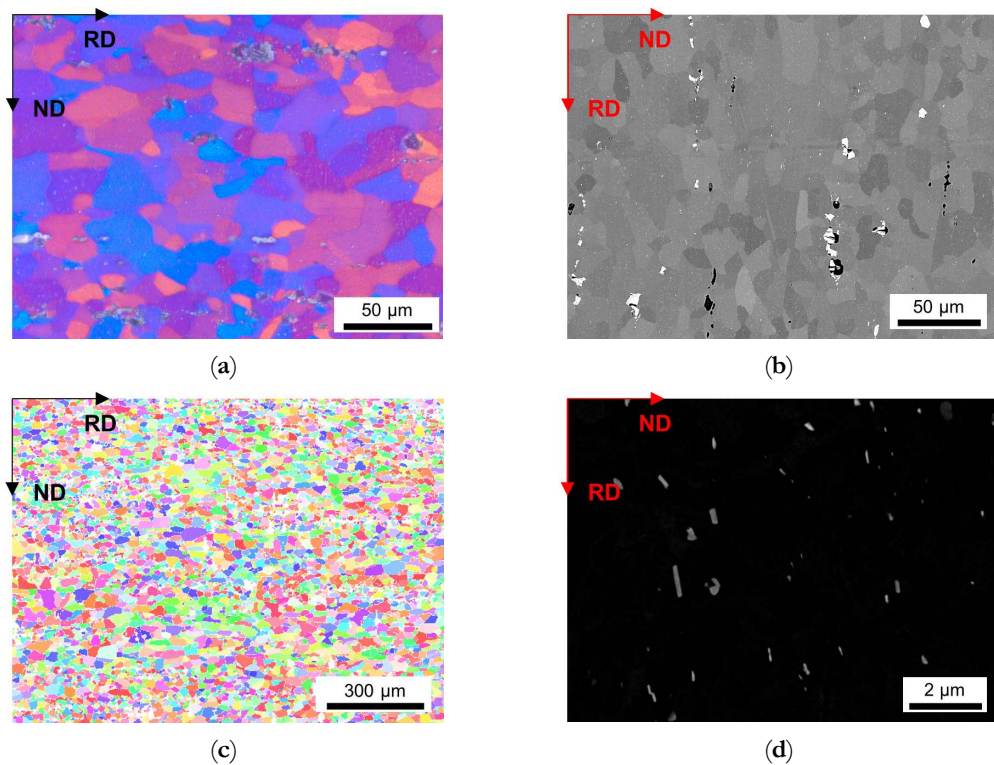


Fig. A6.12. Microstructure of the soft annealed LFe-HMn cast under S-C conditions, homogenized at 550 °C and cold rolled to a CRD of 35%. (a) LOM. (b) BSE image. (c) EBSD IPF map in RD–ND plane. (d) BSE micrograph showing dispersoids.

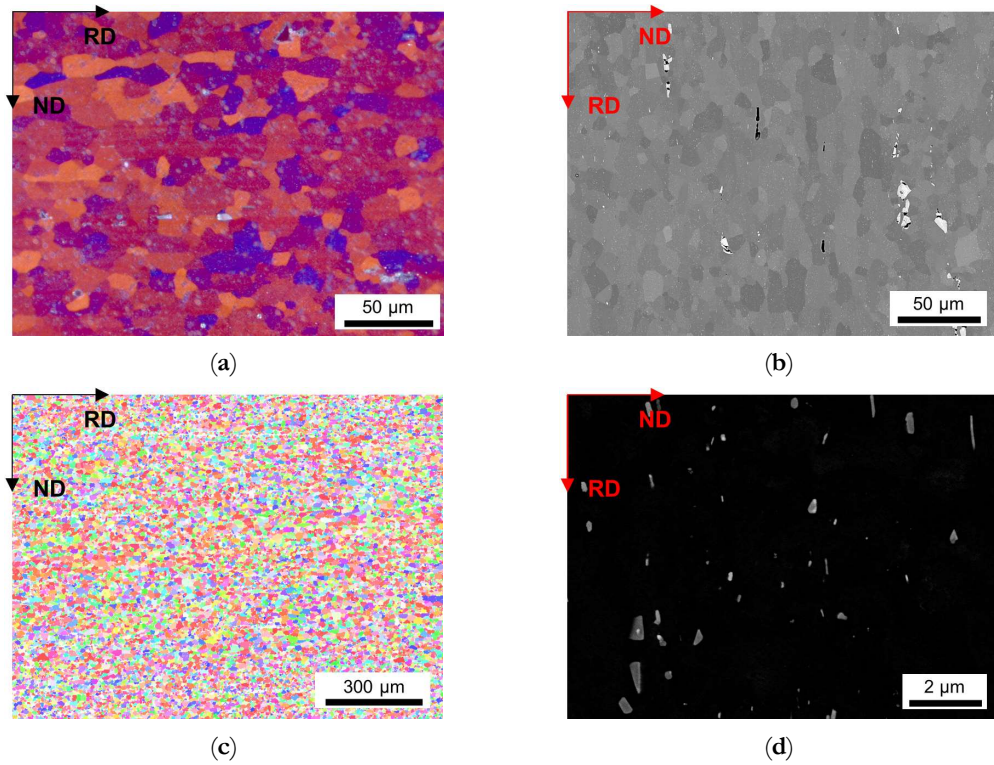


Fig. A6.13. Microstructure of the soft annealed LFe-HMn cast under S-C conditions, homogenized at 550 °C and cold rolled to a CRD of 63%. (a) LOM. (b) BSE image. (c) EBSD IPF map in RD-ND plane. (d) BSE micrograph showing dispersoids.

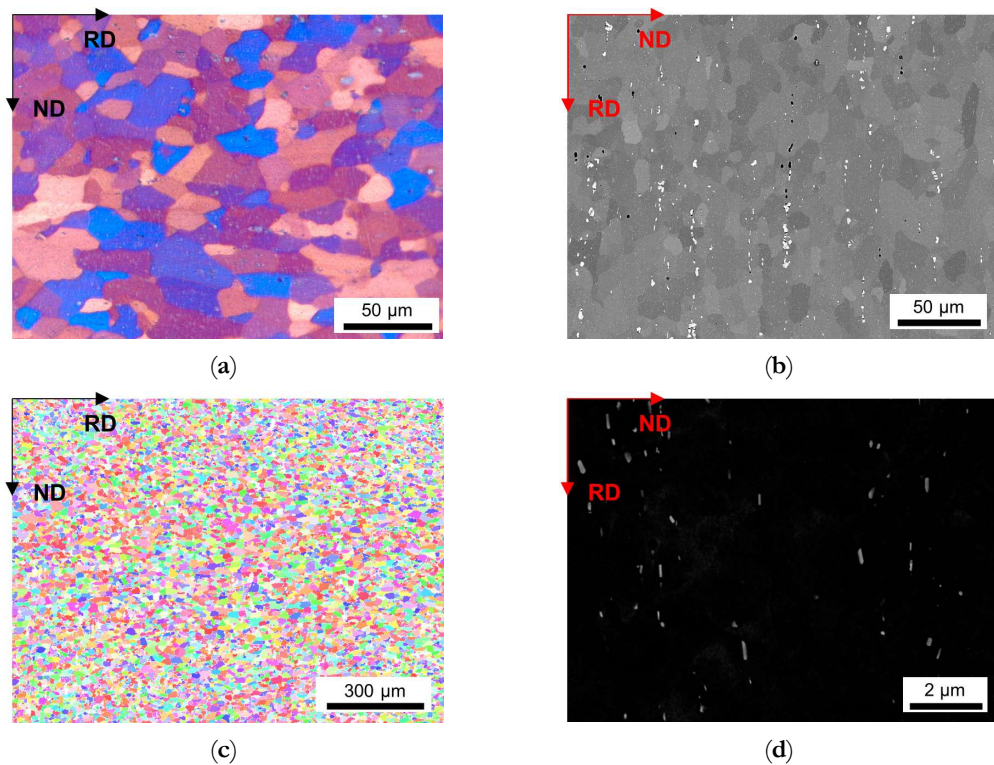


Fig. A6.14. Microstructure of the soft annealed LFe-HMn cast under NR-C conditions, homogenized at 550 °C and cold rolled to a CRD of 35%. (a) LOM. (b) BSE image. (c) EBSD IPF map in RD-ND plane. (d) BSE micrograph showing dispersoids.

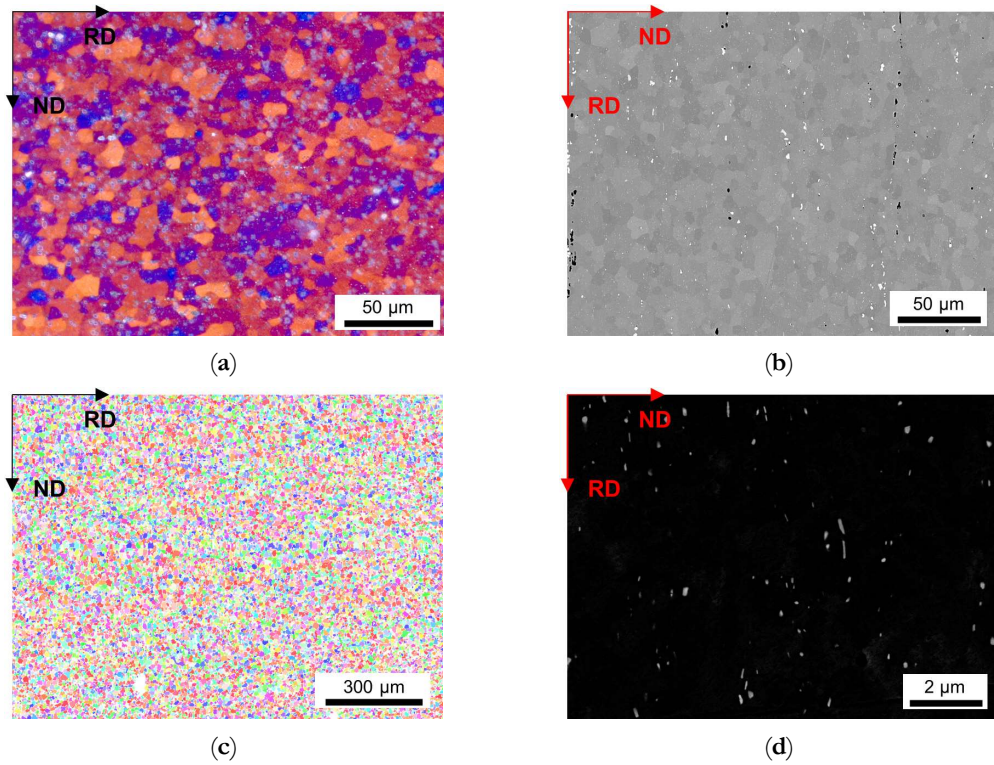


Fig. A6.15. Microstructure of the soft annealed LFe-HMn cast under NR-C conditions, homogenized at 550 °C and cold rolled to a CRD of 63%. (a) LOM. (b) BSE image. (c) EBSD IPF map in RD–ND plane. (d) BSE micrograph showing dispersoids.

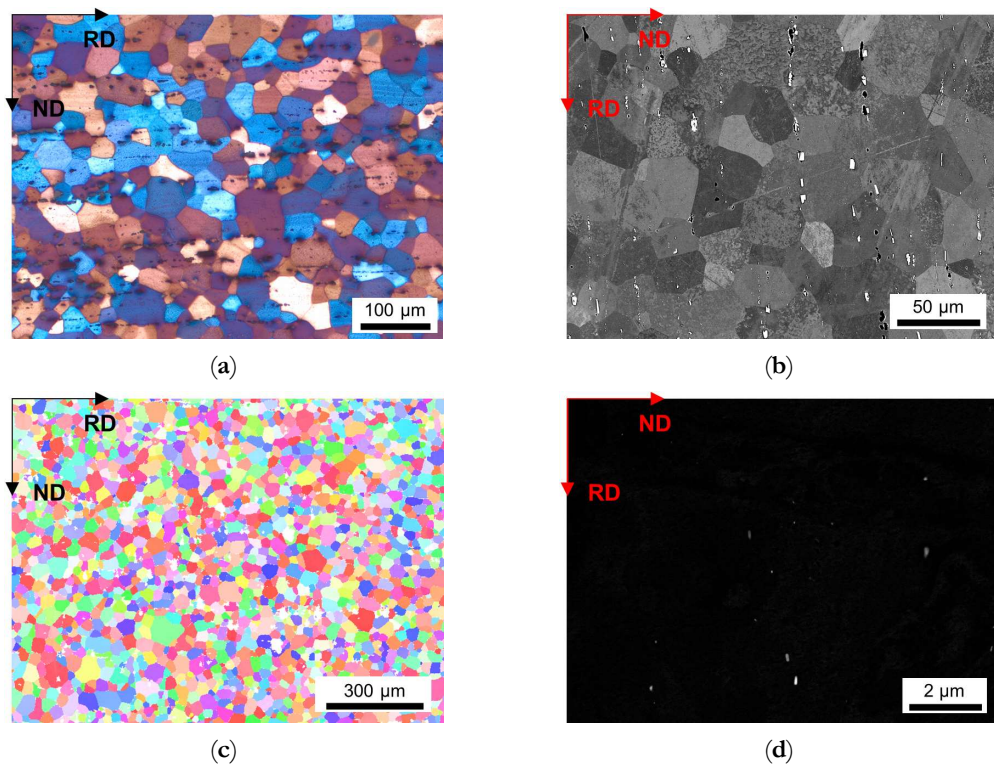


Fig. A6.16. Microstructure of the soft annealed HFe-LMn cast under S-C conditions, homogenized at 500 °C and cold rolled to a CRD of 35%. (a) LOM. (b) BSE image. (c) EBSD IPF map in RD–ND plane. (d) BSE micrograph showing dispersoids.

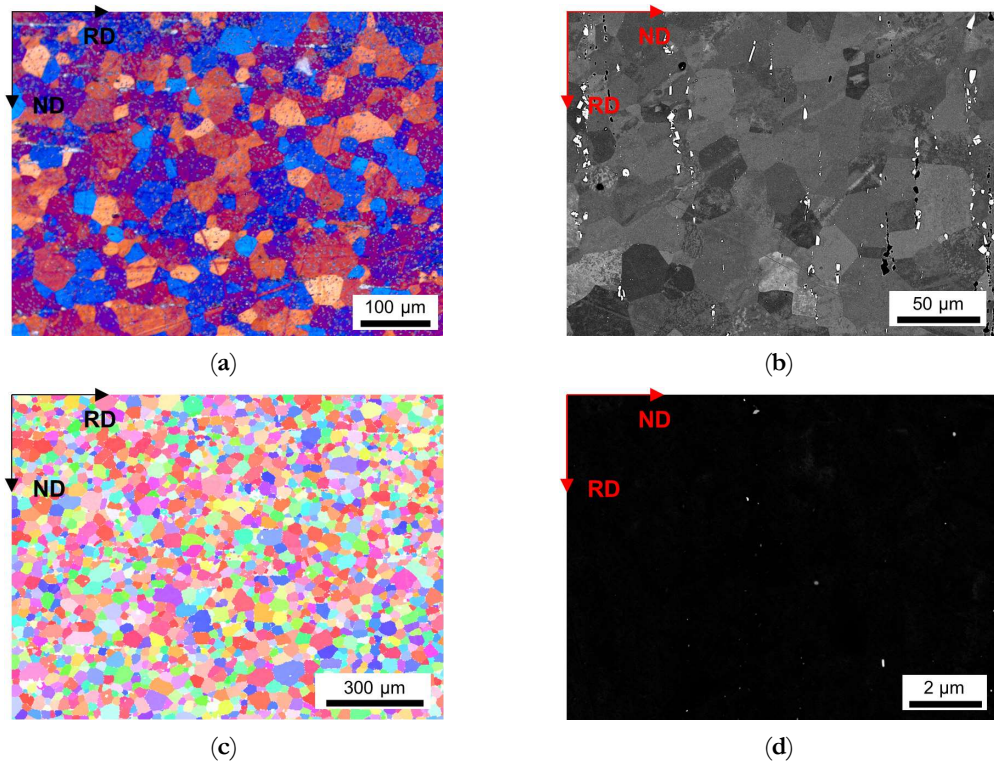


Fig. A6.17. Microstructure of the soft annealed HFe-LMn cast under S-C conditions, homogenized at 500 °C and cold rolled to a CRD of 63%. (a) LOM. (b) BSE image. (c) EBSD IPF map in RD-ND plane. (d) BSE micrograph showing dispersoids.

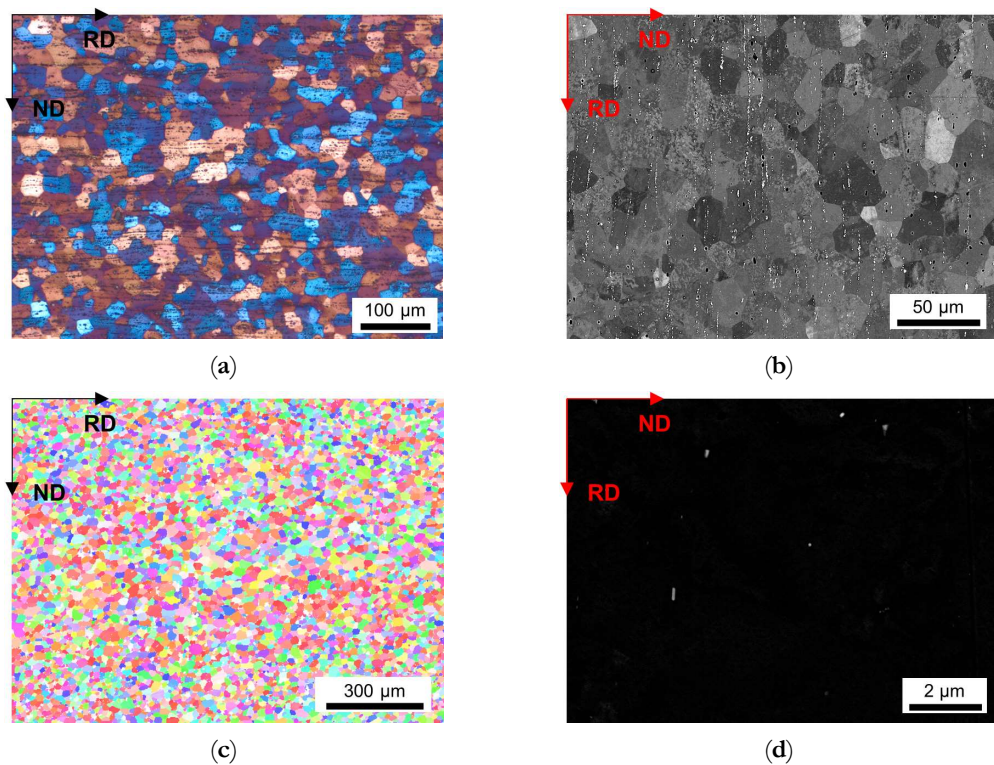


Fig. A6.18. Microstructure of the soft annealed HFe-LMn cast under NR-C conditions, homogenized at 500 °C and cold rolled to a CRD of 35%. (a) LOM. (b) BSE image. (c) EBSD IPF map in RD-ND plane. (d) BSE micrograph showing dispersoids.

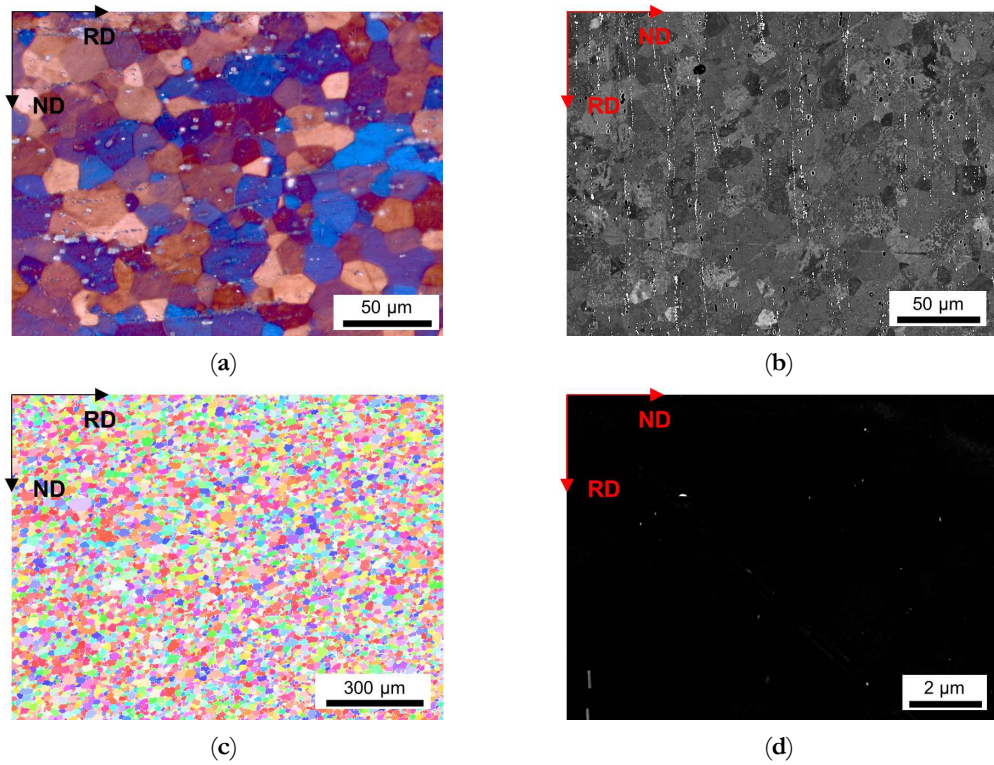


Fig. A6.19. Microstructure of the soft annealed HFe-LMn cast under NR-C conditions, homogenized at 500 °C and cold rolled to a CRD of 63%. (a) LOM. (b) BSE image. (c) EBSD IPF map in RD-ND plane. (d) BSE micrograph showing dispersoids.

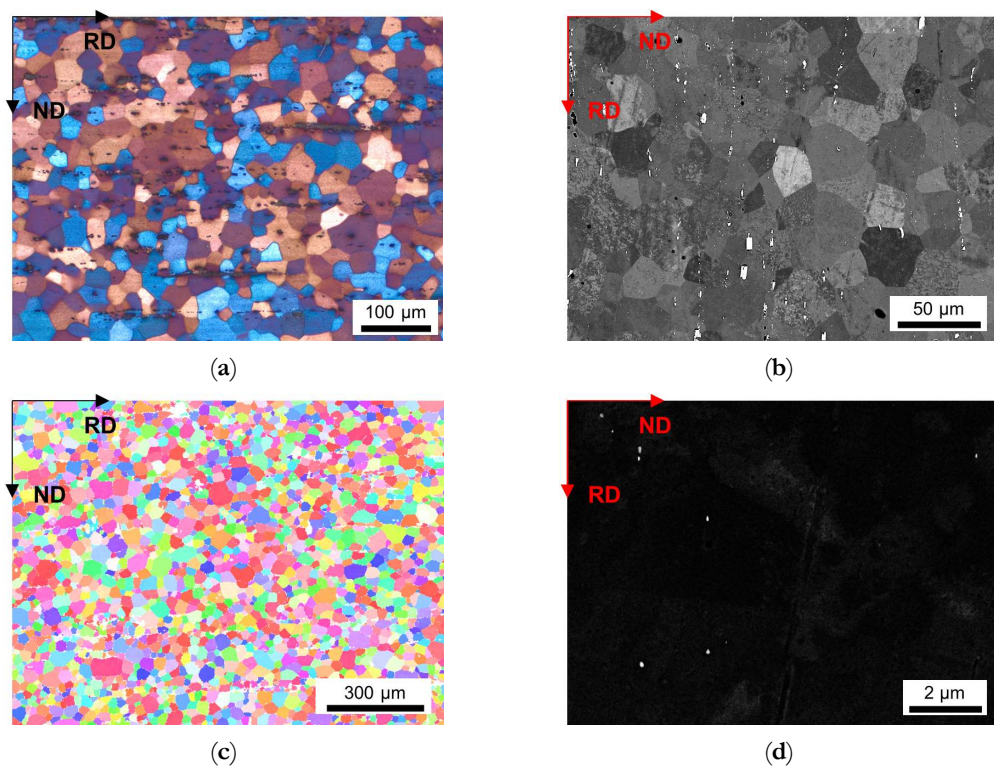


Fig. A6.20. Microstructure of the soft annealed HFe-LMn cast under S-C conditions, homogenized at 550 °C and cold rolled to a CRD of 35%. (a) LOM. (b) BSE image. (c) EBSD IPF map in RD-ND plane. (d) BSE micrograph showing dispersoids.

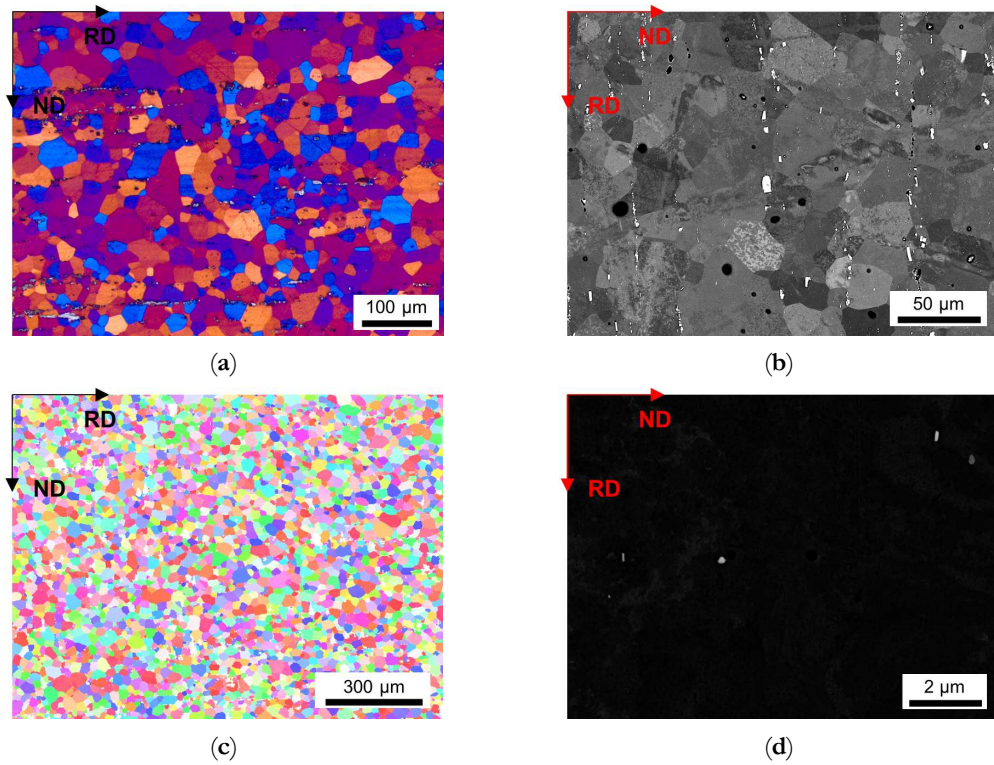


Fig. A6.21. Microstructure of the soft annealed HFe-LMn cast under S-C conditions, homogenized at 550 °C and cold rolled to a CRD of 63%. (a) LOM. (b) BSE image. (c) EBSD IPF map in RD–ND plane. (d) BSE micrograph showing dispersoids.

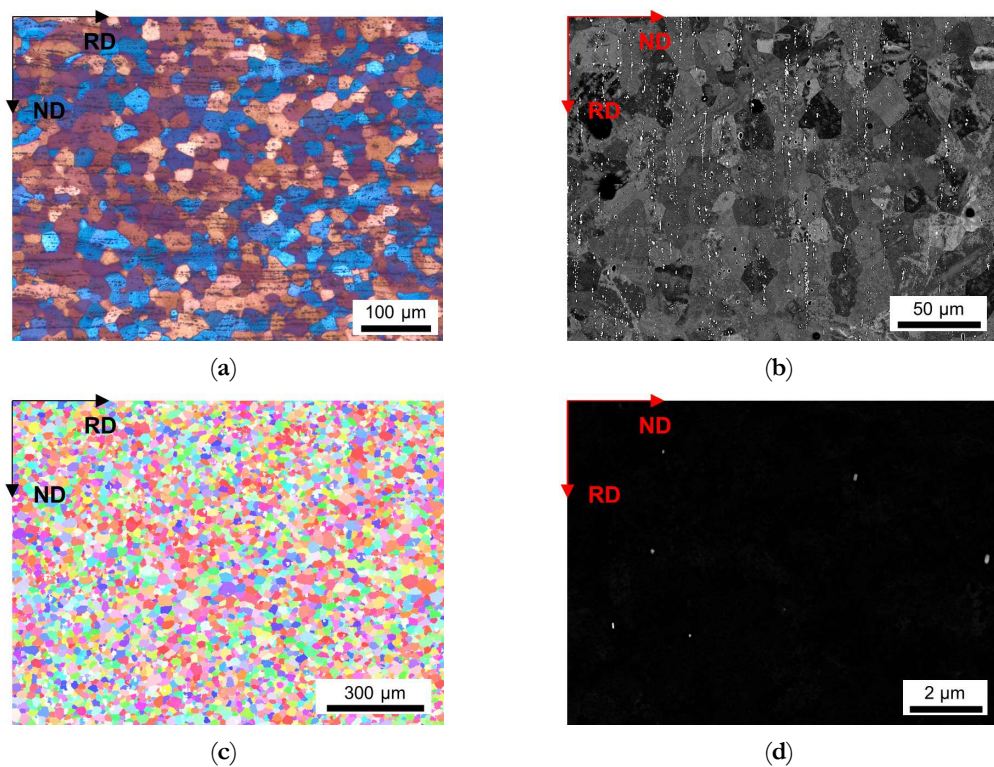


Fig. A6.22. Microstructure of the soft annealed HFe-LMn cast under NR-C conditions, homogenized at 550 °C and cold rolled to a CRD of 35%. (a) LOM. (b) BSE image. (c) EBSD IPF map in RD–ND plane. (d) BSE micrograph showing dispersoids.

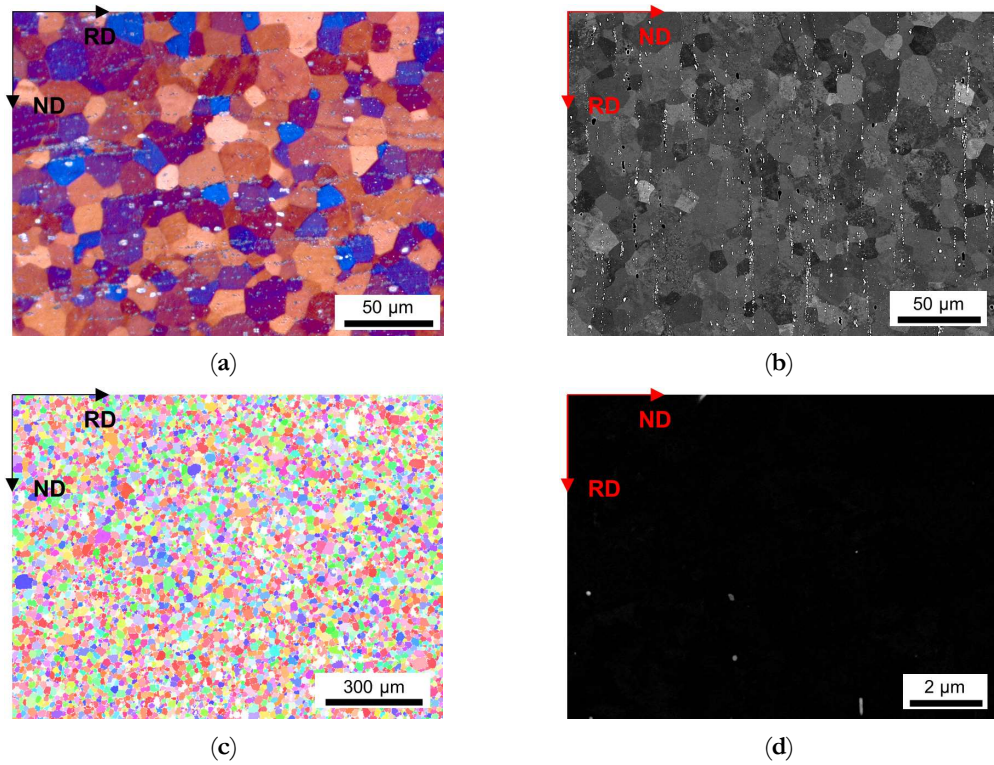


Fig. A6.23. Microstructure of the soft annealed HFe-LMn cast under NR-C conditions, homogenized at 550 °C and cold rolled to a CRD of 63%. (a) LOM. (b) BSE image. (c) EBSD IPF map in RD–ND plane. (d) BSE micrograph showing dispersoids.

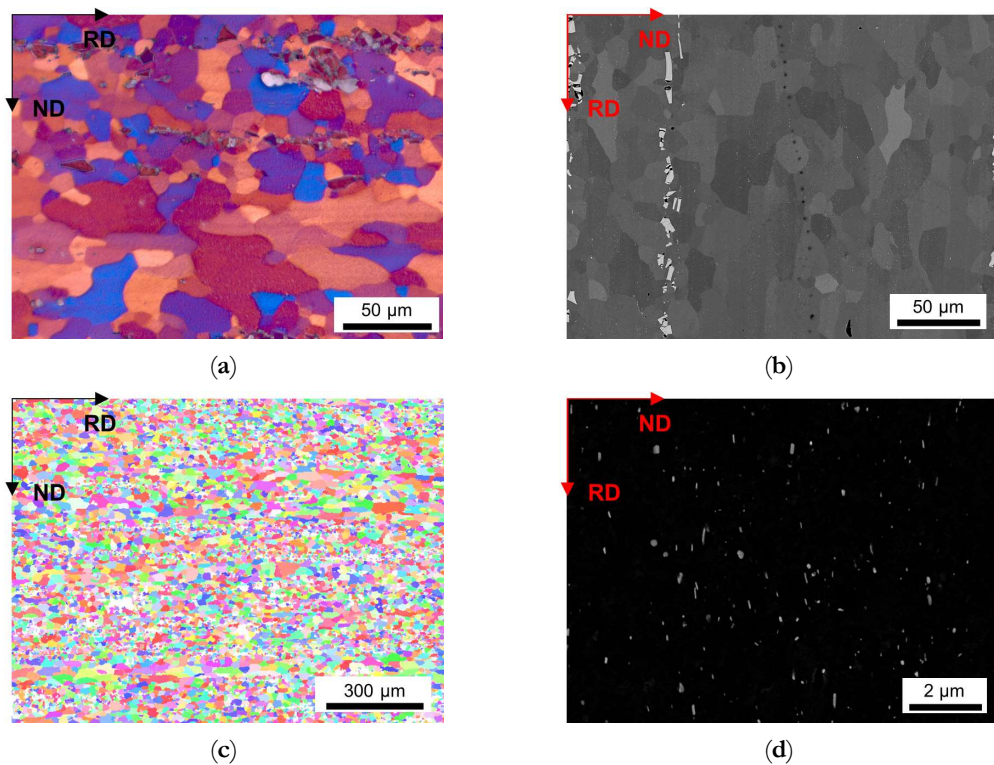


Fig. A6.24. Microstructure of the soft annealed HFe-HMn cast under S-C conditions, homogenized at 500 °C and cold rolled to a CRD of 35%. (a) LOM. (b) BSE image. (c) EBSD IPF map in RD–ND plane. (d) BSE micrograph showing dispersoids.

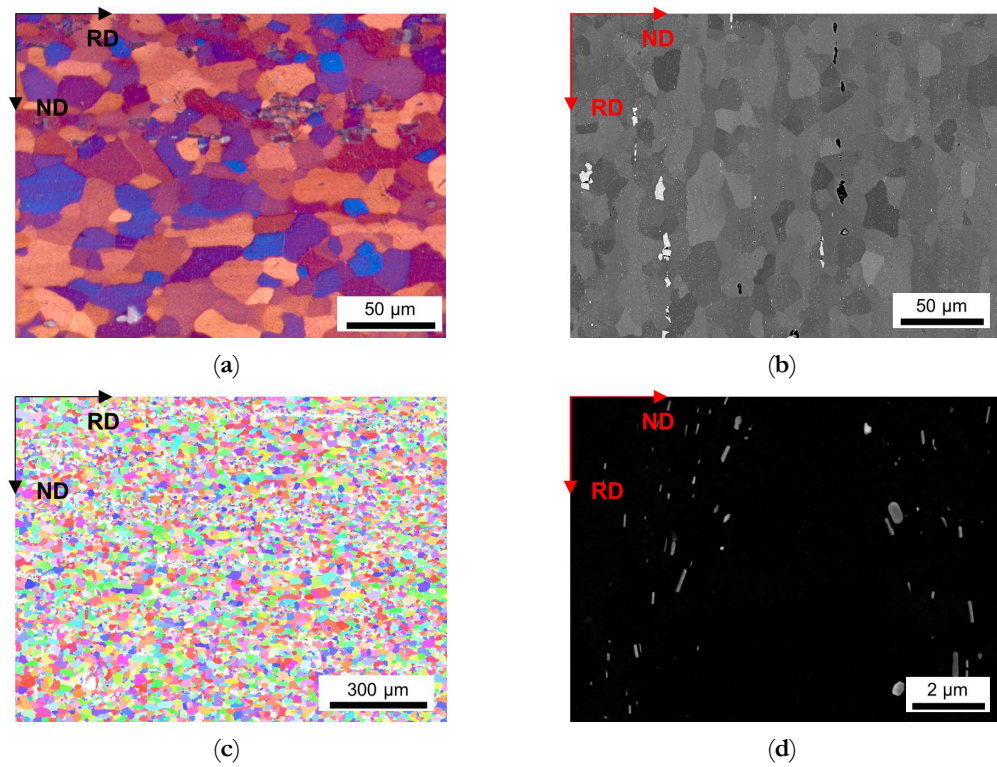


Fig. A6.25. Microstructure of the soft annealed HFe-HMn cast under S-C conditions, homogenized at 550 °C and cold rolled to a CRD of 35%. (a) LOM. (b) BSE image. (c) EBSD IPF map in RD–ND plane. (d) BSE micrograph showing dispersoids.

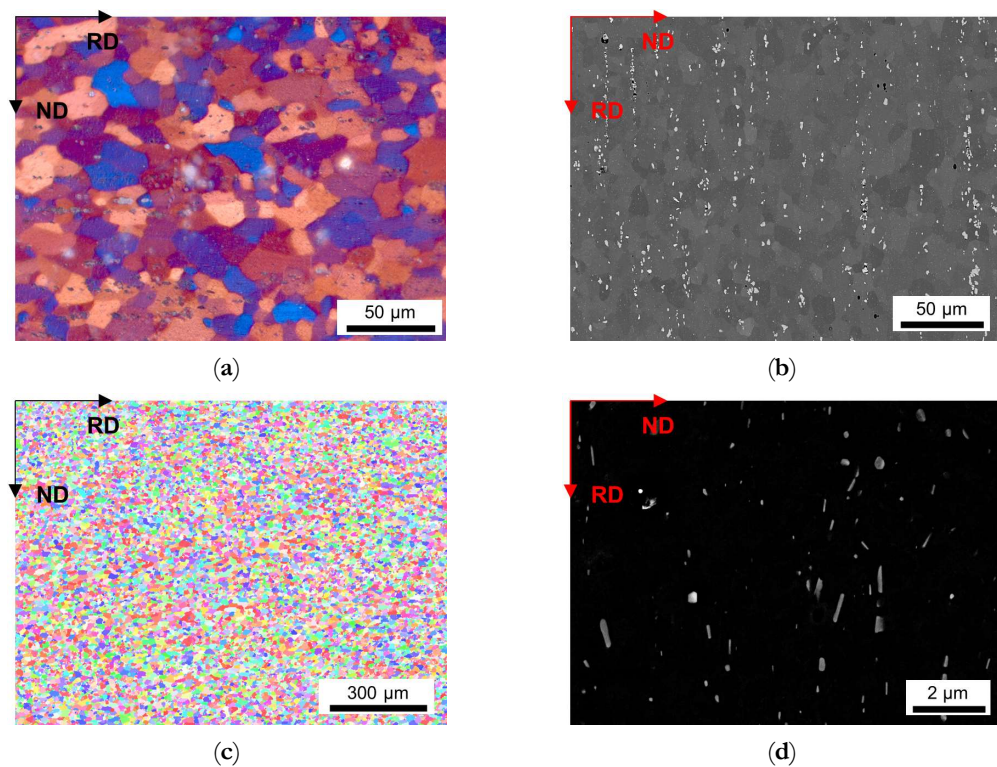


Fig. A6.26. Microstructure of the soft annealed HFe-HMn cast under NR-C conditions, homogenized at 550 °C and cold rolled to a CRD of 35%. (a) LOM. (b) BSE image. (c) EBSD IPF map in RD–ND plane. (d) BSE micrograph showing dispersoids.

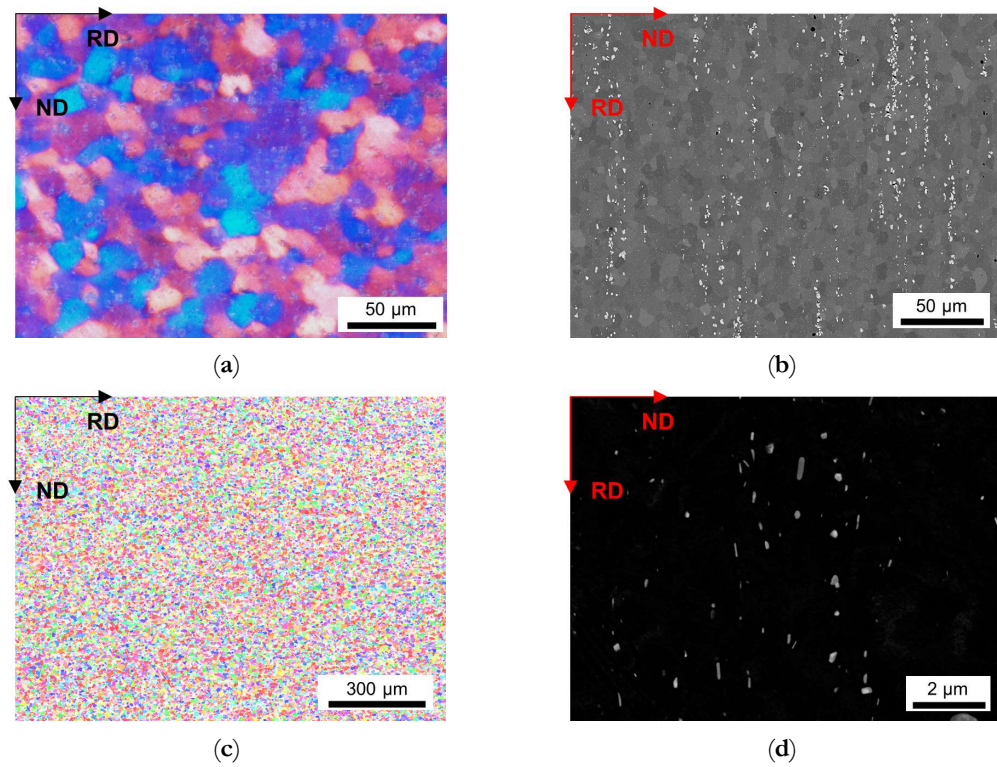


Fig. A6.27. Microstructure of the soft annealed HFe-HMn cast under NR-C conditions, homogenized at 550 °C and cold rolled to a CRD of 63%. (a) LOM. (b) BSE image. (c) EBSD IPF map in RD–ND plane. (d) BSE micrograph showing dispersoids.

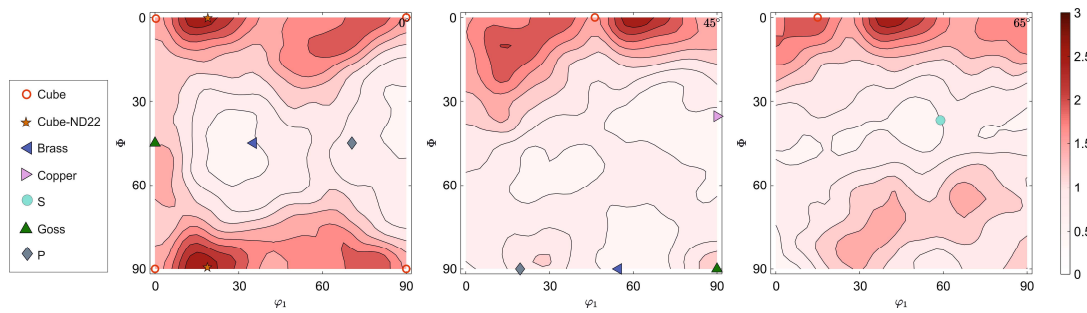


Fig. A6.28. ODF data of the soft annealed HFe-HMn cast under NR-C conditions, homogenized at 500 °C and cold rolled to a CRD of 63% plotted in sections of φ_2 and including the ideal orientations of specific texture components; left: $\varphi_2 = 0^\circ$, middle: $\varphi_2 = 45^\circ$ and right: $\varphi_2 = 65^\circ$.

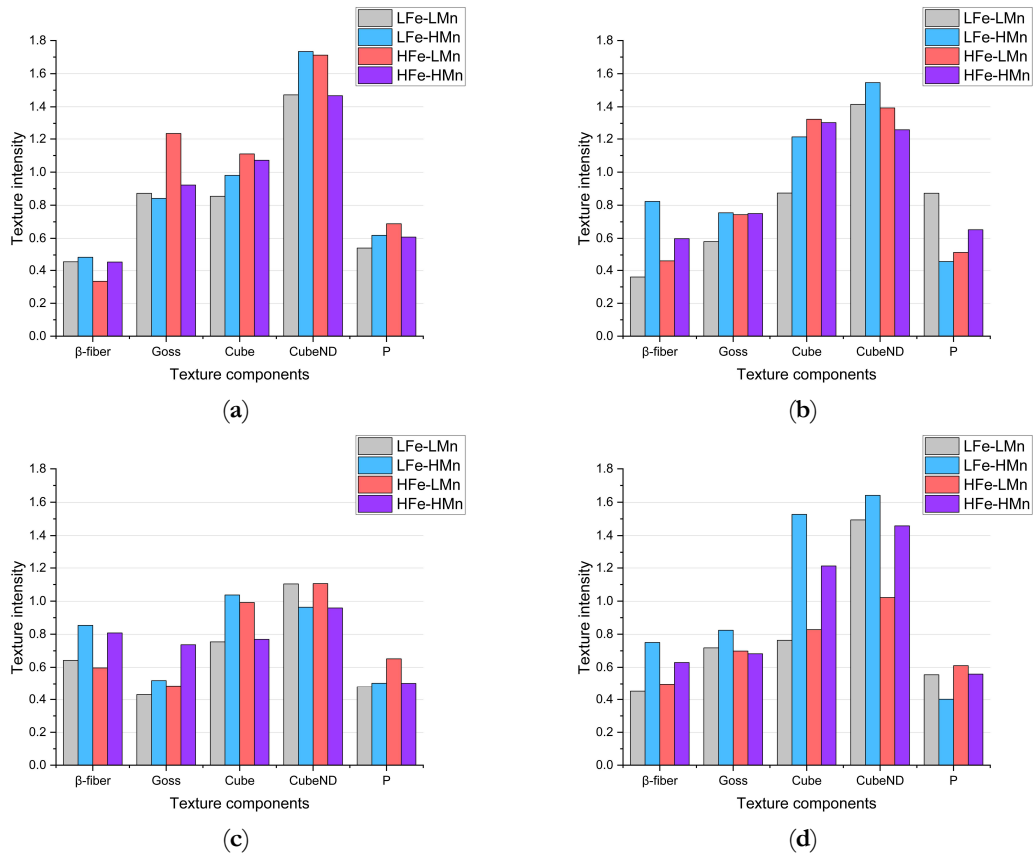


Fig. A6.29. Rolling and recrystallization texture components for the samples states not included in **Fig. 6.9**. (a) NR-C cast, 500 °C homogenized and 63% CRD. (b) S-C cast, 500 °C homogenized and 63% CRD. (c) S-C cast, 550 °C homogenized and 35% CRD. (d) S-C cast, 550 °C homogenized and 63% CRD.

References

- [1] Das S. K.: Designing Aluminium Alloys for a Recycling Friendly World. Aluminium Alloys 2006 - ICAA10, 519-521 (2006), 1239–1244.
- [2] Cole G. S. and A. M. Sherman: Light weight materials for automotive applications. Materials Characterization, 35 (1995), 3–9.
- [3] Ostermann F.: Anwendungstechnologie Aluminium. Springer, Berlin, Germany (2014).
- [4] Burger G. B. et al.: Microstructural control of aluminum sheet used in automotive applications. Materials Characterization, 35 (1995), 23–39.
- [5] Miller W. et al.: Recent development in aluminium alloys for the automotive industry. Materials Science and Engineering: A, 280 (2000), 37–49.
- [6] Hirsch J. and T. Al-Samman: Superior light metals by texture engineering: Optimized aluminum and magnesium alloys for automotive applications. Acta Materialia, 61 (2013), 818–843.
- [7] Davignon G. et al.: An isothermal section at 550 °C in the Al-Rich corner of the Al-Fe-Mn-Si system. Metallurgical and Materials Transactions A, 27 (1996), 3357–3361.
- [8] Algendy A. Y., K. Liu and X.-G. Chen: Formation of intermetallic phases during solidification in Al-Mg-Mn 5xxx alloys with various Mg levels. MATEC Web of Conferences, 326 (2020), 2002.
- [9] Allen C. M. et al.: Intermetallic phase selection in 1XXX Al alloys. Progress in Materials Science, 43 (1998), 89–170.

- [10] Marshall G. J.: Microstructural Control during Processing of Aluminium Canning Alloys. *Materials Science Forum*, 217-222 (1996), 19–30.
- [11] Zhu X. et al.: Strengthening die-cast Al-Mg and Al-Mg-Mn alloys with Fe as a beneficial element. *Materials Science and Engineering: A*, 732 (2018), 240–250.
- [12] Liu Y. et al.: Effect of Mn and Fe on the Formation of Fe- and Mn-Rich Intermetallics in Al-5Mg-Mn Alloys Solidified Under Near-Rapid Cooling. *Materials (Basel, Switzerland)*, 9 (2016), 88.
- [13] Engler O. and S. Miller-Jupp: Control of second-phase particles in the Al-Mg-Mn alloy AA 5083. *Journal of Alloys and Compounds*, 689 (2016), 998–1010.
- [14] Humphreys F. J., G. S. Rohrer and A. D. Rollett: *Recrystallization and related annealing phenomena*. Elsevier Science Ltd. (2017).
- [15] Grasserbauer J. et al.: Influence of Fe and Mn on the Microstructure Formation in 5xxx Alloys—Part I: Evolution of Primary and Secondary Phases. *Materials (Basel, Switzerland)*, 14 (2021), 3204.
- [16] Engler O., K. Kuhnke and J. Hasenclever: Development of intermetallic particles during solidification and homogenization of two AA 5xxx series Al-Mg alloys with different Mg contents. *Journal of Alloys and Compounds*, 728 (2017), 669–681.
- [17] Liu Y. et al.: Effect of Fe, Si and Cooling Rate on the Formation of Fe- and Mn-rich Intermetallics in Al-5Mg-0.8Mn Alloy. *Journal of Materials Science & Technology*, 32 (2016), 305–312.
- [18] Rakhmonov J. et al.: Effects of Al(MnFe)Si dispersoids with different sizes and number densities on microstructure and ambient/elevated-temperature mechanical properties of extruded Al-Mg-Si AA6082 alloys with varying Mn content. *Journal of Alloys and Compounds*, 861 (2021), 157937.
- [19] Ratchev P., B. Verlinden and P. van Houtte: Effect of preheat temperature on the orientation relationship of (Mn,Fe)Al₆ precipitates in an AA 5182 Aluminium—Magnesium alloy. *Acta Metallurgica et Materialia*, 43 (1995), 621–629.
- [20] Humphreys F. J.: The nucleation of recrystallization at second phase particles in deformed aluminium. *Acta Metallurgica*, 25 (1977), 1323–1344.
- [21] Aryshenskii E., J. Hirsch and S. Konovalov: Investigation of the Intermetallic Compounds Fragmentation Impact on the Formation of Texture during the as Cast Structure Thermomechanical Treatment of Aluminum Alloys. *Metals*, 11 (2021), 507.
- [22] Furu T., K. Marthinsen and E. Nes: Particle Effects on Recrystallization of Metals. *Materials Science Forum*, 113-115 (1993), 41–54.
- [23] Bennett T. A., R. H. Petrov and L. A. I. Kestens: Effect of particles on texture banding in an aluminium alloy. *Scripta Materialia*, 62 (2010), 78–81.
- [24] Bennett T. A. et al.: The effect of particle-stimulated nucleation on texture banding in an aluminium alloy. *Scripta Materialia*, 63 (2010), 461–464.
- [25] Vatne H. E., O. Engler and E. Nes: Influence of particles on recrystallisation textures and microstructures of aluminium alloy 3103. *Materials Science and Technology*, 13 (1997), 93–102.
- [26] Smith C. S.: Grains, phases, and interfaces: An introduction of microstructure. *Trans.AIME*, 175 (1948), 15–51.
- [27] Nes E., N. Ryum and O. Hunderi: On the Zener drag. *Acta Metallurgica*, 33 (1985), 11–22.
- [28] Manohar P. A., M. Ferry and T. Chandra: Five Decades of the Zener Equation. *ISIJ International*, 38 (1998), 913–924.
- [29] Li W.-B. and K. E. Easterling: The influence of particle shape on zener drag. *Acta Metallurgica et Materialia*, 38 (1990), 1045–1052.

- [30] Wang N. et al.: Two modes of grain boundary pinning by coherent precipitates. *Acta Materialia*, 135 (2017), 226–232.
- [31] Bate P.: The effect of deformation on grain growth in Zener pinned systems. *Acta Materialia*, 49 (2001), 1453–1461.
- [32] Ryum N., O. Hunderi and E. Nes: On grain boundary drag from second phase particles. *Scripta Metallurgica*, 17 (1983), 1281–1283.
- [33] Manohar P. A. et al.: Grain Growth Predictions in Microalloyed Steels. *ISIJ International*, 36 (1996), 194–200.
- [34] Hazzledine P. M. and R. D. J. Oldershaw: Computer simulation of Zener pinning. *Philosophical Magazine A*, 61 (1990), 579–589.
- [35] Kad B. K. and P. M. Hazzledine: Monte Carlo simulations of grain growth and Zener pinning. *Materials Science and Engineering: A*, 238 (1997), 70–77.
- [36] Anderson M. P. et al.: Inhibition of grain growth by second phase particles: Three dimensional Monte Carlo computer simulations. *Scripta Metallurgica*, 23 (1989), 753–758.
- [37] Nishizawa T., I. Ohnuma and K. Ishida: Examination of the Zener Relationship between Grain Size and Particle Dispersion. *Materials Transactions, JIM*, 38 (1997), 950–956.
- [38] Srolovitz D. J. et al.: Computer simulation of grain growth-III. Influence of a particle dispersion. *Acta Metallurgica*, 32 (1984), 1429–1438.
- [39] Agnoli A. et al.: Development of a level set methodology to simulate grain growth in the presence of real secondary phase particles and stored energy – Application to a nickel-base superalloy. *Computational Materials Science*, 89 (2014), 233–241.
- [40] Chakrabarti T. and S. Manna: Zener pinning through coherent precipitate: A phase-field study. *Computational Materials Science*, 154 (2018), 84–90.
- [41] Chang K., W. Feng and L.-Q. Chen: Effect of second-phase particle morphology on grain growth kinetics. *Acta Materialia*, 57 (2009), 5229–5236.
- [42] Phaneesh K. R. et al.: On the Zener limit of grain growth through 2D Monte Carlo simulation. *Computational Materials Science*, 58 (2012), 188–191.
- [43] Phaneesh K. R. et al.: 3D MC Simulation of Grain Growth Kinetics and the Zener Limit in Polycrystals. *Applied Mechanics and Materials*, 598 (2014), 8–12.
- [44] Vanherpe L. et al.: Pinning effect of spheroid second-phase particles on grain growth studied by three-dimensional phase-field simulations. *Computational Materials Science*, 49 (2010), 340–350.
- [45] Schwarze C., R. Darvishi Kamachali and I. Steinbach: Phase-field study of zener drag and pinning of cylindrical particles in polycrystalline materials. *Acta Materialia*, 106 (2016), 59–65.
- [46] Li Z., J. Wang and H. Huang: Influences of particle fractions on second-phase particles pinning grain coarsening processes. *Journal of Materials Science*, 55 (2020), 3434–3449.
- [47] Hillert M.: Inhibition of grain growth by second-phase particles. *Acta Metallurgica*, 36 (1988), 3177–3181.
- [48] Dillamore I. L. and W. T. Roberts: Preferred Orientation In Wrought And Annealed Metals. *Metallurgical Reviews*, 10 (1965), 271–380.
- [49] Alvi M. H. et al.: Cube texture in hot-rolled aluminum alloy 1050 (AA1050)—nucleation and growth behavior. *Acta Materialia*, 56 (2008), 3098–3108.
- [50] Hirsch J. and K. Lücke: Overview no. 76: Mechanism of deformation and development of rolling textures in polycrystalline f.c.c. metals—I. Description of rolling texture development in homogeneous CuZn alloys. *Acta Metallurgica*, 36 (1988), 2863–2882.

- [51] Weiland H. and J. Hirsch: Microstructure and Local Texture in Hot Rolled Aluminum. *Textures and Microstructures*, 14 (1991), 647–652.
- [52] Engler O. and J. Hirsch: Control of recrystallisation texture and texture-related properties in industrial production of aluminium sheet. *Int. J. Mat. Res.*, 100 (2009), 564–575.
- [53] Bate P. and A. Oscarsson: Deformation banding and texture in hot rolled Al-1.0Mn-1.2Mg alloy. *Materials Science and Technology*, 6 (1990), 520–527.
- [54] Hirsch J., E. Nes and K. Lücke: Rolling and recrystallization textures in directionally solidified aluminium. *Acta Metallurgica*, 35 (1987), 427–438.
- [55] Li S. et al.: A Review of Texture Evolution Mechanisms During Deformation by Rolling in Aluminum Alloys. *Journal of Materials Engineering and Performance*, 27 (2018), 3350–3373.
- [56] Liu W. C. and J. G. Morris: Kinetics of the formation of the b fiber rolling texture in continuous cast AA 5xxx series aluminum alloys. *Scripta Materialia*, 47 (2002), 743–748.
- [57] Liu W. C. and J. G. Morris: Comparison of the texture evolution in cold rolled DC and SC AA 5182 aluminum alloys. *Materials Science and Engineering: A* (2003), 183–193.
- [58] Engler O. and K. Lücke: Mechanisms of recrystallization texture formation in aluminium alloys. *Scripta Metallurgica et Materialia*, 27 (1992), 1527–1532.
- [59] Daaland O. and E. Nes: Recrystallization texture development in commercial Al-Mn-Mg alloys. *Acta Materialia*, 44 (1996), 1413–1435.
- [60] Dons A. L. and E. Nes: Nucleation of cube texture in aluminium. *Materials Science and Technology*, 2 (1986), 8–18.
- [61] Hamad K., H. W. Yang and Y. G. Ko: Interpretation of annealing texture changes of severely deformed Al-Mg-Si alloy. *Journal of Alloys and Compounds*, 687 (2016), 300–305.
- [62] Kashyap K. T. and R. George: Mechanism of cube grain nucleation during recrystallization of deformed commercial purity aluminium. *Bulletin of Materials Science*, 29 (2006), 197–200.
- [63] La Chapelle S. de: Cube recrystallization textures in a hot deformed Al-Mg-Si alloy. *Scripta Materialia*, 45 (2001), 1387–1391.
- [64] Theyssier M. C. and J. H. Driver: Recrystallization nucleation mechanism along boundaries in hot deformed Al bicrystals. *Materials Science and Engineering: A* (1999), 73–82.
- [65] Duckham A., R. Knutsen and O. Engler: Influence of deformation variables on the formation of copper-type shear bands in Al-1Mg. *Acta Materialia*, 49 (2001), 2739–2749.
- [66] Engler O. and J. Hirsch: Recrystallization Textures and Plastic Anisotropy in Al-Mg-Si Sheet Alloys. *Materials Science Forum*, 217 (1996), 479–486.
- [67] Yu L. et al.: Influence of Fe-rich particles on microstructure evolution, texture and mechanical properties of Al-Mg-Si-Cu alloys. *Metallurgical Research & Technology*, 117 (2020), 508.
- [68] Higginson R. L., M. Aindow and P. S. Bate: The effect of finely dispersed particles on primary recrystallisation textures in AlMnSi alloys. *Materials Science and Engineering: A*, 225 (1997), 9–21.
- [69] Engler O.: On the Influence of Dispersoids on the Particle Stimulated Nucleation of Recrystallization in an Al-Fe-Si Model Alloy. *International Conference On Textures and Anisotropy of Polycrystals*, Clausthal (1997).
- [70] Nie X. et al.: On the role of Zr content into Portevin-Le Chatelier (PLC) effect of selective laser melted high strength Al-Cu-Mg-Mn alloy. *Materials Letters*, 248 (2019), 5–7.
- [71] Ebenberger P. et al.: Processing-controlled suppression of Lüders elongation in AlMgMn alloys. *Scripta Materialia*, 166 (2019), 64–67.

- [72] Bennett T. A., R. H. Petrov and L. A. I. Kestens: Surface Texture Modification for Improved Roping Behaviour of Aluminium Alloy 6016. *Solid State Phenomena*, 160 (2010), 197–202.
- [73] Grasserbauer J. et al.: Evolution of Microstructure and Texture in Laboratory- and Industrial-Scaled Production of Automotive Al-Sheets. *Materials (Basel, Switzerland)*, 13 (2020), 469.
- [74] Petzow G. and V. Carle: Metallographisches, keramographisches, plastographisches Ätzen. In: *Materialkundlich-technische Reihe, Band: 1*. Borntraeger, Berlin (2006).
- [75] Han J.-H. and D.-Y. Kim: Analysis of the proportionality constant correlating the mean intercept length to the average grain size. *Acta Metallurgica et Materialia*, 43 (1995), 3185–3188.
- [76] Engler O. and V. Randle: *Introduction to texture analysis*. CRC Press, Boca Raton (2010).
- [77] Engler O., J. Hirsch and K. Lücke: Texture development in Al-1.8 wt% Cu depending on the precipitation state—II. Recrystallization textures. *Acta Metallurgica et Materialia*, 43 (1995), 121–138.
- [78] Gao N. et al.: A comparison of grain size determination by light microscopy and EBSD analysis. *Journal of Materials Science*, 40 (2005), 4971–4974.
- [79] Engler O., Z. Liu and K. Kuhnke: Impact of homogenization on particles in the Al–Mg–Mn alloy AA 5454 – Experiment and simulation. *Journal of Alloys and Compounds*, 560 (2013), 111–122.
- [80] Sheppard T. and N. Raghunathan: Modification of cast structures in Al–Mg alloys by thermal treatments. *Materials Science and Technology*, 5 (1989), 268–280.

7 SUMMARY AND OUTLOOK

The increasing demands for aluminum, especially in the automotive industry, demand a profound knowledge in the control of the final sheet's properties. The frequently used alloying classes of AlMg(Mn) and AlMgSi alloys were already studied to a large extent; however, microstructure and texture engineering of those alloys is still part of the ongoing discussions as it strongly affects the essential properties like strength and formability of the Al sheets. While intensive research focused on specific microstructure and texture effects (e.g. roping phenomenon) or on the improvements in simulation software, the aim of the present thesis was comprehensive experimental work on the comparability of laboratory- and industrial-scaled processing of 5xxx and 6xxx Al sheets as well as the specific microstructure and texture modification in aluminum alloys by additional alloying elements.

The initial research addressed the fundamental microstructure and texture evolution in an EN AW-5182 and EN AW-6016 alloy throughout the entire sheet fabrication process on laboratory and industrial scales. Although the basic mechanisms have been extensively studied for years, the comparability of the differently scaled processes is a recent challenge as the design of novel alloying systems, or the modification of processing parameters is often realized in laboratory facilities. Therefore, if possible promising results in microstructure and texture should be transferred to the industrial scale.

The resulting microstructures and textures for the EN AW-5182 showed good conformity in the rolling and recrystallization behavior, both qualitatively and quantitatively. Although the results for EN AW-6016 showed qualitative similarities during the rolling processing steps, the texture quantification revealed significant discrepancies. However, as the microstructures and textures in the final annealed sheets indicated an overall good comparability of the process, the small-scale laboratory processing route was approved for further research in texture and microstructure optimization.

The subsequently following two-part study investigated the influence of varied Fe and Mn levels in Al4.5Mg0.1Si alloys. Regarding the increasing importance of recycling of aluminum alloys, the impacts of higher "impurity" Fe levels on the phase formation and resulting microstructures and textures are crucial. Therefore, the studies followed the aspects of beneficial effects of additional Mn in the Fe containing 5xxx alloys. Part I of the study comprised extensive experimental work including different casting, homogenization, and rolling parameters in laboratory-scaled Al sheet fabrication and focused on the evolution of primary and secondary phases in four different Fe/Mn containing Al4.5Mg0.1Si alloys throughout their entire processing. The phase characterization showed the preferential precipitation of characteristically needle-like shaped $\text{Al}_3(\text{Fe},\text{Mn})$ primary phases in alloys with high Fe/Mn ratios. Increasing Mn levels coarsened the primary phases and more likely formed

$Al_6(Fe,Mn)$ or $Al_{15}(Fe,Mn)_3Si_2$. The primary phase size, volume fraction, and type is for the most part determined by the Fe contents and the casting cooling rates but remains nearly unaffected by the homogenization treatment. The formation of secondary phase dispersoids of types $Al_6(Fe,Mn)$ or $Al_{15}(Fe,Mn)_3Si_2$ was observed during homogenization. Whereas the volume fraction was strongly affected by the Mn levels, the average dispersoid size significantly increased with higher Fe levels and higher homogenization temperatures. Additional thermodynamic calculations affirmed both the observed types and volume fractions of the primary and secondary phases in the four alloys.

The impacts of the coarse primary and finely dispersed secondary phases were then discussed in Part II of the study. The final soft annealed microstructures in the Fe and Mn alloyed Al4.5Mg0.1Si sheets showed strong impacts of the different process parameters as well as the various Fe/Mn ratios. The grain size was significantly reduced by higher casting cooling rates as well as higher degrees of cold rolling, which further caused fragmentation and band-wise alignment of the primary phases. Higher Fe or Mn levels resulted in variations in the primary and secondary phase volume fractions, which distinctly altered the resulting microstructure and strongly reduced the average grain size. Effective Smith-Zener pinning was observed for the high Mn containing alloys and the experimental data were compared to well-established models for the Zener limiting grain size. Whereas reasonable conformity was obtained for the original Smith-Zener approach and the high Mn containing alloys, the implementation of further effects in the Zener limiting grain size formula seems indispensable for the development of a generally applicable model. Higher fractions of coarse primary particles also resulted in significantly reduced grain sizes by additional pinning or PSN effects. Although the weak textures in the Al4.5Mg0.1Si alloys complicated the accurate analysis of those effects, trends of the related texture modifications as the retardation of classical recrystallization and PSN components was observed.

In conclusion, this thesis highlighted the comparability of the established laboratory-scaled alloy processing to the common Al sheet production in terms of microstructure and texture evolution. The subsequent study on Fe and Mn alloyed 5xxx sheets correlated the microstructure and phase evolution to process parameters and highlighted the importance of the holistic consideration of various effects and their impacts on the final microstructure and texture. The comprehensive experimental work affirmed some well-established mechanisms of general microstructure evolution, especially concerning the substructure and phase formation; however, open questions concerning the precise mathematical description of the concurrent microstructural effects PSN and Smith-Zener pinning remain to be clarified.

8 APPENDIX

This chapter lists the authored or co-authored publications and given talks of the author while following his position as a PhD student.

8.1 Peer-reviewed publications

Grasserbauer J., Weißensteiner I., Falkinger G., Mitsche S., Uggowitzer P.J., and Pogatscher S. Evolution of Microstructure and Texture in Laboratory- and Industrial-Scaled Production of Automotive Al-Sheets. *Materials* 13 (2020) 469, doi:10.3390/ma13020469.

Grasserbauer J., Weißensteiner I., Falkinger G., Kremmer T.M., Uggowitzer P.J., and Pogatscher S. Influence of Fe and Mn on the Microstructure Formation in 5xxx Alloys—Part I: Evolution of Primary and Secondary Phases. *Materials* 14 (2021) 3204, doi.org/10.3390/ma14123204.

Grasserbauer J., Weißensteiner I., Falkinger G., Uggowitzer P.J., and Pogatscher S. Influence of Fe and Mn on the Microstructure Formation in 5xxx alloys—Part II: Evolution of Grain Size and Texture. *Materials* 14 (2021) 3312, <https://doi.org/10.3390/ma14123312>.

Tunes M.A., Quick, C.R., Stemper L., S.R. Coradini D., Grasserbauer J., Dumitraschkewitz P., Kremmer T.M., and Pogatscher S. A Fast and Implantation-Free Sample Production Method for Large Scale Electron-Transparent Metallic Samples Destined for MEMS-Based In Situ S/TEM Experiments. *Materials* 14 (2021) 1085, doi:10.3390/ma14051085.

8.2 Talks

Grasserbauer J. In-situ EBSD investigations during heating: recrystallization and recovery of hot rolled Al-Si-Mg-alloy. 15. International Metallographietagung, Leoben, Austria, 2018 (the presentation was given in place of Stefan Mitsche).

Grasserbauer J. Microstructure and texture evolution in laboratory scaled production of aluminum sheets. LightMAT 2019, Manchester, England, 2019.

Grasserbauer J. Particle related texture and microstructure modifications in Al-Mg alloys with Fe and Mn additions. ICOTOM19, Online Conference, 2021.

Grasserbauer J. Influence of primary- and secondary-phase particles on the texture and microstructure evolution in laboratory-scaled production of aluminum alloys. Thermec'2021, Online Conference, 2021.